Theoretical and numerical aspects of wave propagation phenomena in complex domains and applications to remote sensing

Pedro Ramaciotti Morales

NNT : 2016SACLX063

THESE DE DOCTORAT
DE L'UNIVERSITE PARIS-SACLAY

préparée à

L'ÉCOLE POLYTECHNIQUE

ÉCOLE DOCTORALE N°574

École Doctorale de Mathématiques Hadamard (EDMH)

Spécialité de doctorat : Mathématiques

par

Mr. Pedro Ramaciotti Morales

Aspects Théoriques et Numériques des Phénomènes de Propagation d'Ondes dans Domaines de Géométrie Complexe et Applications à la Télédétection

Thèse présentée et soutenue à Palaiseau, le 17 Octobre 2016, après avis des rapporteurs :

Xavier ANTOINE
Ralf HIPTMAIR

Composition du jury :

Grégoire ALLAIRE	Examinateur
François ALOUGES	Président du Jury
Xavier ANTOINE	Rapporteur
Mario DURÁN	Co-Directeur de Thèse
Jean-Claude NÉDÉLEC	Directeur de Thèse

NNT : 2016SACLX063

THESE DE DOCTORAT

DE L'UNIVERSITE PARIS-SACLAY

préparée à

L'ÉCOLE POLYTECHNIQUE

ÉCOLE DOCTORALE N°574

École Doctorale de Mathématiques Hadamard (EDMH)

Spécialité de doctorat : Mathématiques

par

Mr. Pedro Ramaciotti Morales

Aspects Théoriques et Numériques des Phénomènes de Propagation d'Ondes dans Domaines de Géométrie Complexe et Applications à la Télédétection

Thèse présentée et soutenue à Palaiseau, le 17 Octobre 2016, après avis des rapporteurs :

Xavier ANTOINE	(IECL)
Ralf HIPTMAIR	(SAM)

Composition du jury :

Grégoire ALLAIRE	(CMAP)	Examinateur
François ALOUGES	(CMAP)	Président du Jury
Xavier ANTOINE	(IECL)	Rapporteur
Mario DURÁN	(PUC)	Co-Directeur de Thèse
Jean-Claude NÉDÉLEC	(CMAP)	Directeur de Thèse

To my parents,
for their generous gift of love and education.

L'infinito

Sempre caro mi fu quest'ermo colle,
e questa siepe, che da tanta parte
dell'ultimo orizzonte il guardo esclude.
Ma sedendo e mirando, interminati
spazi di là da quella, e sovrumani
silenzi, e profondissima quiete
io nel pensier mi fingo; ove per poco
il cor non si spaura. E come il vento
odo stormir tra queste piante, io quello
infinito silenzio a questa voce
vo comparando: e mi sovvien l'eterno,
e le morte stagioni, e la presente
e viva, e il suon di lei. Così tra questa
immensità s'annega il pensier mio:
e il naufragar m'è dolce in questo mare.

Giacomo Leopardi
Autumn of 1819
Recanati, Italia

Acknowledgements

This thesis is the result of much work and many transformative experiences, first and most obviously, in relation to the skills and knowledge linked to research. Second, from the view of personal change, I have been exposed to different work environments, a variety of people, different cities, a new country, a new continent, and I have had the great opportunity to view the world from a place of privileged access. These are all things for which I am grateful, in which many people have been involved, and for which I would like to expand.

I would like to thank the members of the thesis committee (*examinateurs et rapporteurs*) for their participation in the evaluation of the manuscript and the oral dissertation. I appreciate the time they have taken away from their daily tasks, from their work, and from their objectives, even if just for a brief time, to help with the revision, discussion, and enrichment of my work.

I cannot thank Jean-Claude Nédélec and Mario Durán enough. I thank them mainly for motivating me and inviting me to pursue a doctoral research project under their guidance and for the trust and freedom that they have granted me to pursue a wide gamut of interests and subjects. It is from these explorations that my work has sprung. Not only have they been generous in sharing their knowledge and experience with me, but they have also shared their new ideas, their motivations, and their own projects. It is in great part because of their energy, their motivation, and their unwavering commitment to creating inviting and challenging environments, that I chose to pursue a thesis, as I am sure many doctoral students felt inspired to do before me.

I thank Jean-Claude Nédélec for his patience in my transition from electrical engineering to mathematics and for sharing his knowledge and insights while making himself available to listen to my ideas, questions, and doubts. I also thank him for his humor and his friendship. I value greatly being able to share our visions and opinions about science, history, politics, France, Chile, and the world. I thank Mario Durán for his great energy and his ambitious vision for science and technology. I believe the trust he granted me through my transition between subjects can be explained in great part to that energy. I am also thankful for our friendship over the last many years attested by the countless conversations and arguments we have shared. I thank them both for having motivated me to pursue a binational doctoral project. This experience has been enormously enriching and I could not imagine the results of my work another way.

I would like to take this opportunity to thank many other professors that have contributed to my doctoral years. From École Polytechnique, I especially thank professors Grégoire Allaire, Frédérique Coquel, and Toufic Abboud for the influence their courses had in changing my vision of mathematics. From Pontificia Universidad Católica, I would like to thank two professors especially. To Marcelo Guarini, I am thankful for his motivation, his constant fascination with new and diverse subjects, and for his excellent disposition in working with students. With him I've learned subjects as diverse as processor architecture and design, electromagnetic theory, and ground-penetrating radars. The latter of which is part of the work here presented. To Sergio Gutiérrez, I am thankful for his vision of mathematics, of science, and of the academic life. The coincidence of his own binational research projects between Chile and France with my stay at École Polytechnique allowed us to share many discussions on a wide variety of subjects. It is fair to say that part of the formation that I received as a doctoral student came from his openness, his sincerity, and his conviction in many of the subjects we discussed, especially in those regarding academic life. I also thank the valuable exchanges with professor Ralf Hiptmair, that provided me with new and valuable insight about my own work.

I am very grateful to my fellow doctoral students, both in Chile and in France, together we have shared mutual support and company. We have shared what can be called *lab life*,

friendship, and it has been a pleasure to exchange opinions, references, code, lunches and laughs with all of you. There are too many of you to mention here but it is safe to say that I will remember you always. I would like to make a special mention of the colleague with whom I shared (intermittently) an office for almost three years: Thi Phong. I will always remember our constant strategies and negotiations over the temperature and heat settings in our office, even in spring!

My deepest gratitude to Nasséra and Alex from the Centre de Mathématiques Appliqués, and Emmanuel and Audrey from the Graduate School of École Polytechnique. Without them I might still be lost navigating a web of procedures and even if the web were never fully understood, their kindness and dedication would be enough to guide us through it. My gratitude goes also to Fernanda Kattan, Nicole Betti, Debbie Meza and María de Lourdes Troncoso from the Escuela de Ingeniería of the Pontificia Universidad Católica de Chile. I appreciate all the help provided in solving the particularities of a binational thesis project. I am thankful to my valued friends in Chile and France as well as others scattered around the world. Many were involved in some way or another in my work. Thank you for listening to my arguments, my doubts, accompanying me to think, and for sometimes just listening to my ramblings on the state of the world, physical idealism, or the perfect way to cook *pancia di maiale con finocchio*. Thanks to Julio, Diego, Andrea, Fernando, Juan Pablo and Matías. Special thanks to my friend Gabriel, to whom I thank, above all else, for his generosity with his time. Without him, the logistical difficulties of this binational project (which are many and considerable) would simply have been too overwhelming. Many thanks to Marissa Comstock for proofreading my manuscript. If you have ever had to proofread a 200-page thesis, then you can begin to grasp her generosity. Many thanks to everyone.

It is impossible to thank my family enough. The unconditional company and the care given to me by my family is surely among the greatest things life has given me. The more I get to know the world and the diversity of life experiences it offers, the more thankful I am to my parents for the very early gift of education. It is much less of a given than one would like it to be, and it has been without a doubt the most explicative factor of what I am today.

I want to thank Mónica, the person to whom I've been the closest in what I've lived so far. I want to thank her the love she gives me so constantly and so naturally, which is already fairly extraordinary in itself. But I am quickly distracted by more strange things: our desire to accompany each other thinking freely, as boundlessly as possible, without fear (or at least overcoming it as quickly as possible), as far as we have wanted to, and most often to the edge of our growing capacities. There is maybe only one thing I think of systematically about every day: that's her. In these thoughts there's always gratitude. She has been next to me throughout the years dedicated to this thesis.

The experience of coming to France for my doctoral project has been a positive and decisive one. I am thankful for my time at the Centre de Mathématiques Appliquées, where I have been exposed to an enriching vision of mathematics and its possibilities for application. My stay at École Polytechnique, and the now Université Paris-Saclay has also been invaluable. Such a concentrated diversity of subjects, at such advanced stages of development, available through friends, colleagues, workshops and conferences, could not pass through anyone's life without changing one's perception of the world. Even more generally, living in the Paris area, arguably one of Western Hemisphere's beacons of diversity, immediately puts the whole world at closer reach. I am truly thankful for all the experiences I have had and the discussions with such a wide range of people in vastly different situations. They cannot be disassociated from my doctoral experience. In a more concrete sense, I am grateful for what could be called a welcoming from a country and even a continent, and for that I owe my thanks to École Polytechnique, Fondation Mathématique Jacques Hadamard, and the French Embassy in Chile.

Contents

Acknowledgements **i**

List of Figures **ix**

List of Tables **xiii**

Abstract **xvi**

Résumé **xviii**

Resumen **xx**

1 Wave Propagation, Boundary Integral Equations, Boundary Element Methods, and Computational Complexity **1**

1.1 The Helmholtz equation in physics 2

1.1.1 Acoustic waves 2

1.1.2 Elastic waves 3

1.1.3 Electromagnetic waves 4

1.2 Problem domains, boundaries, and Sobolev spaces 6

1.2.1 Domains and boundaries 6

1.2.2 Elementary differential geometry 7

1.2.3 Sobolev spaces 8

1.2.4 Traces and jumps 11

1.3 Laplace and Helmholtz problems 12

1.3.1 Boundary and infinity conditions 12

1.3.2 Exterior partial differential equation problems for Lipschitz-regular obstacles 12

1.3.3 Exterior partial differential problems for screen obstacles 13

1.4 Fundamental solutions and boundary integral operators 16

1.4.1 Fundamental solutions and Green's functions 16

1.4.2 Boundary integral operators 17

1.5 Boundary integral equations and variational formulations for Lipschitz-regular obstacles 19

1.5.1 Boundary integral equations for the exterior problems 19

1.5.2 Bilinear forms and variational formulation 21

1.6 Surface discretization, boundary element method, and Galerkin matrices 23

1.6.1 Primal and dual meshes 23

1.6.2 Boundary element spaces and discrete variational formulations 25
1.6.3 Boundary element computations and Galerkin matrices 27
1.7 Memory complexity, algorithmic complexity and accuracy 28
1.7.1 Wave frequency and mesh refinement 28
1.7.2 Memory complexity 29
1.7.3 Algorithmic complexity 29
1.7.4 Accuracy 30
1.7.5 Overall complexity and accuracy 30
1.7.6 An illustrative example 31

2 Operator Preconditioning and Screen Obstacles 33
2.1 Operator preconditioning 34
2.2 Preconditioning for Lipschitz-regular obstacles 36
2.2.1 Laplace problem 36
2.2.2 Helmholtz problem 37
2.3 Boundary integral equations for the screen problem 40
2.4 Preconditioning for the segment obstacle in $\mathbb{R}^2$ 43
2.4.1 Geometrical and functional setting 43
2.4.2 Direct and inverse operators and kernels for the symmetric Dirichlet and the anti-symmetric Neumann problems 43
2.4.3 Series form of the integral kernels for the direct and inverse operators . 44
2.4.4 Series expansions of functions belonging to the Sobolev trace spaces . . 44
2.5 Geometrical and functional setting for the disk screen in $\mathbb{R}^3$ 46
2.5.1 Geometrical definitions 46
2.5.2 Functional setting 49
2.6 Existence of inverse operators for the Dirichlet and Neumann problems 51
2.6.1 Dirichlet Problems 51
2.6.2 Neumann problems 55
2.6.3 Inverses 56
2.7 Series forms for the boundary integral operators and their inverses 58
2.7.1 Spherical Harmonics: symmetry and parity 58
2.7.2 Disk basis functions 60
2.7.3 Some identities on the disk 61
2.7.4 Weighted spaces and series representations 65
2.7.5 Series forms for the boundary integral operators 67
2.7.6 Variational formulations and norms 82
2.7.7 Spectral method and preconditioning of the Laplace problem for the disk screen 84

3 Preconditioning for Screen Obstacles with Modified Integral Operators 89
3.1 Modified boundary integral operators with explicit closed variational form . . . 90
3.1.1 Integral kernels for the weakly singular and hypersingular boundary integral operators on the sphere 90
3.1.2 Modified integral kernels and operators 91

3.1.3 Variational problems and norms . . . 98
3.2 Boundary elements method implementation . . . 101
3.2.1 Domain discretization . . . 101
3.2.2 Mesh sets . . . 103
3.2.3 Boundary element spaces and basis functions . . . 105
3.2.4 Finite-dimensional variational problems . . . 106
3.2.5 Boundary element computations . . . 107
3.2.6 Galerkin matrices . . . 110
3.2.7 Benchmarks . . . 110
3.3 Preconditioning . . . 116
3.3.1 Mutual preconditioning of the Galerkin matrices for the modified boundary integral operators . . . 116
3.3.2 Preconditioning the matrices for the symmetric Dirichlet and anti-symmetric Neumann problems on the disk . . . 119
3.3.3 The Helmholtz problem for the unit disk in three dimensions as a compact perturbation . . . 125
3.3.4 Generalization to planar polygonal screens . . . 126

4 Applications to the Design and Testing of Remote Perception Technologies 131
4.1 Ground-penetrating radars . . . 132
4.1.1 Types of ground-penetrating radars . . . 132
4.1.2 Airborne ground-penetrating radars . . . 134
4.2 Simulating time-harmonic radio signals . . . 136
4.2.1 General setting and assumptions . . . 136
4.2.2 Radar targets . . . 139
4.2.3 Computational cost and conditioning . . . 140
4.2.4 Air-ground interface, hologram recording surfaces, and imaging surfaces 143
4.2.5 Simulating single domain and interface problems . . . 145
4.3 A type of subsurface holographic radar . . . 150
4.3.1 Holographic radar imaging and principles . . . 150
4.3.2 Imaging method for single underground domain scenarios . . . 151
4.3.3 Imaging method for double domains scenarios . . . 154
4.3.4 A simplified imaging method for double domain scenarios . . . 156
4.3.5 Simulated examples . . . 157

References 169

Synthèse en Français 173

List of Figures

1.1 Illustration of the collapse of a Lipschitz-regular obstacle into a screen. 7
1.2 Conformal triangular approximation Γ_h of a surface Γ in $\mathbb{R}^3$ 23
1.3 Sub-triangles of a triangle from a conformal triangular approximation. 24
1.4 Evolution of the alogirthmic and memory complexity of the boundary element method for an example case. 31
1.5 Evolution of the condition number and the relative error of a linear system using boundary element methods for an example case. 32

2.1 Optimal preconditioning for the Laplace problem on the exterior of a sphere. . 37
2.2 Optimal preconditioning for the Laplace problem on the exterior of a sphere. . 38
2.3 Geometrical setting for the disk screen in $\mathbb{R}^3$. 47

3.1 Detail of the construction of primary dual mesh $\widetilde{\mathcal{T}}_h$ and secondary dual mesh $\widetilde{\mathcal{T}}_h^0$ 102
3.2 Specimens of $\mathcal{T}_h$, $\widetilde{\mathcal{T}}_h$ and $\widetilde{\mathcal{T}}_h^0$ for $\mathbb{D}_h$ and fixed minimum edge h. 102
3.3 Example of discretized domains $\mathbb{D}_h$ and $\mathbb{S}_h^+$ in Mesh set #1 104
3.4 Example of discretized domains $\mathbb{D}_h$ and $\mathbb{S}_h^+$ in Mesh set #2 104
3.5 Example of discretized domains $\mathbb{D}_h$ and $\mathbb{S}_h^+$ in Mesh set #3 105
3.6 Relative error convergence for the benchmark cases using mesh set of type Mesh set #1 and Sobolev norms 112
3.7 Relative error convergence for the benchmark cases using mesh set of type Mesh set #2 and Sobolev norms 112
3.8 Relative error convergence for the benchmark cases using mesh set of type Mesh set #3 and Sobolev norms 113
3.9 Relative error convergence for the benchmark cases using mesh set of type Mesh set #1 and modified norms 114
3.10 Relative error convergence for the benchmark cases using mesh set of type Mesh set #2 and modified norms 114
3.11 Relative error convergence for the benchmark cases using mesh set of type Mesh set #3 and modified norms 115
3.12 Preconditioning of matrices $\boldsymbol{S}_s^h$ and $\boldsymbol{N}_{as}^h$ by matrices $\boldsymbol{M}_D^h$ and $\boldsymbol{M}_N^h$ for mesh set of type Mesh set #1 117
3.13 Preconditioning of matrices $\boldsymbol{S}_s^h$ and $\boldsymbol{N}_{as}^h$ by matrices $\boldsymbol{M}_D^h$ and $\boldsymbol{M}_N^h$ for mesh set of type Mesh set #2 118
3.14 Preconditioning of matrices $\boldsymbol{S}_s^h$ and $\boldsymbol{N}_{as}^h$ by matrices $\boldsymbol{M}_D^h$ and $\boldsymbol{M}_N^h$ for mesh set of type Mesh set #3 118
3.15 Preconditioning of matrices $\boldsymbol{S}^h$ and $\boldsymbol{N}^h$ by matrices $\boldsymbol{M}_D^h$ and $\boldsymbol{M}_N^h$ for mesh set of type Mesh set #1 119

3.16 Preconditioning of matrices $\boldsymbol{S}^h$ and $\boldsymbol{N}^h$ by matrices $\boldsymbol{M}_D^h$ and $\boldsymbol{M}_N^h$ for mesh set of type Mesh set #2 . . . 120
3.17 Preconditioning of matrices $\boldsymbol{S}^h$ and $\boldsymbol{N}^h$ by matrices $\boldsymbol{M}_D^h$ and $\boldsymbol{M}_N^h$ for mesh set of type Mesh set #3 . . . 120
3.18 No-continuity of $\widetilde{b}_s^{hs}$ in $H^{1/2}(\mathbb{D})$ . . . 121
3.19 Coercivity of $\widetilde{b}_s^{hs}$ for zero-mean functions of $H^{1/2}(\mathbb{D})$ . . . 122
3.20 Continuity of $\widetilde{b}_{as}^{ws}$ in $H^{-1/2}(\mathbb{D})$ . . . 123
3.21 No-coercivity of $\widetilde{b}_{as}^{ws}$ in $H^{-1/2}(\mathbb{D})$ . . . 124
3.22 Preconditioning of matrices $\boldsymbol{S}_k^h$ and $\boldsymbol{N}_k^h$ by matrices $\boldsymbol{M}_D^h$ and $\boldsymbol{M}_N^h$ for mesh set of type Mesh set #1 . . . 126
3.23 Example of a numerical simulation of wave propagation where a disk screen is the obstacle for an incoming wave . . . 126
3.24 Zone division of a square-shaped screen and an L-shaped screen. . . . 127
3.25 Discretized square-shaped screen Γ_h with its upper projection Γ_h^+ . . . 128
3.26 Discretized L-shaped screen Γ_h with its upper projection Γ_h^+ . . . 129
3.27 Evolution of the condition numbers for $\boldsymbol{S}^h$, $\boldsymbol{M}_D^h\boldsymbol{S}^h$, $\boldsymbol{N}^h$ and $\boldsymbol{M}_N^h\boldsymbol{N}^h$ for a squared-shaped screen . . . 129
3.28 Evolution of the condition numbers for $\boldsymbol{S}^h$, $\boldsymbol{M}_D^h\boldsymbol{S}^h$, $\boldsymbol{N}^h$ and $\boldsymbol{M}_N^h\boldsymbol{N}^h$ for an L-shaped screen . . . 130

4.1 Illustration of an airborne line-array of antennas taking multi-monostatic radar measurements over a given portion of land. . . . 135
4.2 Composition of the scalar wave fields at both sides of an interface Γ^I. . . . 137
4.3 General setting for a holographic ground-penetrating simulation for a single domain and a interface case . . . 137
4.4 General setting for a holographic ground-penetrating simulation for a single underground domain scenario showing the incident and the scattered wave field 138
4.5 General setting for a holographic ground-penetrating simulation for a double domain or interface scenario showing the incident and the scattered wave field . 138
4.6 Conformal triangular approximation Γ_h^T of the radar target Γ^T . . . 139
4.7 Evolution of $T_{MMS}^{\%}(h, N_{MMS})$ for the chosen radar target approximation Γ_h^T, for $h = 0.0049695$ and $N_T = 2872$ for an increasing number N_{MMS} of multi-monostatic radar measuring points in the hologram recording surface Γ^H . . . 143
4.8 Rectangular grid approximation of Γ_h^I of surface Γ^I, made of 400 elements (for illustrative purposes) for the function f_I from (4.11) . . . 144
4.9 Example computation of radio wave propagation in a single underground domain scenario . . . 146
4.10 Incident wave field example computation of radio wave propagation in a double domain scenario . . . 148
4.11 Scattered wave field example computation of radio wave propagation in a double domain scenario . . . 149
4.12 Scenario for the simulated multi-monostatic holographic radar acquisition using parameters of Table 4.5, showing the underground propagation domain, the radar target, and Γ^H with the magnitude of the values of $\mathcal{H}$ painted on. . . . 153
4.13 Magnitude of the values of the map $\mathcal{H}$ painted on Γ^H (left), and magnitude of the values of the map $\mathcal{R}$ painted on Γ^R (right) using parameters of Table 4.5. The known shape of the radar target Γ^T has been drawn on the reflectivity image on the right as a reference. . . . 153

4.14 Geometrical lengths and vectors for an arbitrary round-trip between points on the recording hologram surface and the imaging surface. 155
4.15 Geometrical lengths and vectors for the simplified round-trip passing between points on the interface surface surface and the imaging surface. 156
4.16 Three-dimensional depiction of Scenario A and recorded hologram $\mathcal{H}$ 160
4.17 Values of $|\mathcal{R}|$ reconstructed for Scenario A using AI-CPM and SPAI-CPM . . . 160
4.18 Three-dimensional depiction of Scenario B and recorded hologram $\mathcal{H}$ 161
4.19 Values of $|\mathcal{R}|$ reconstructed for Scenario B using AI-CPM and SPAI-CPM . . . 161
4.20 Three-dimensional depiction of Scenario C and recorded hologram $\mathcal{H}$ 162
4.21 Values of $|\mathcal{R}|$ reconstructed for Scenario C using AI-CPM and SPAI-CPM . . . 162
4.22 Three-dimensional depiction of Scenario D and recorded hologram $\mathcal{H}$ 163
4.23 Values of $|\mathcal{R}|$ reconstructed for Scenario D using AI-CPM and SPAI-CPM . . . 163
4.24 Three-dimensional depiction of Scenario E and recorded hologram $\mathcal{H}$ 164
4.25 Values of $|\mathcal{R}|$ reconstructed for Scenario E using AI-CPM and SPAI-CPM . . . 164
4.26 Three-dimensional depiction of Scenario F and recorded hologram $\mathcal{H}$ 165
4.27 Values of $|\mathcal{R}|$ reconstructed for Scenario F using AI-CPM and SPAI-CPM . . . 165
4.28 Three-dimensional depiction of Scenario G and recorded hologram $\mathcal{H}$ 166
4.29 Values of $|\mathcal{R}|$ reconstructed for Scenario G using AI-CPM and SPAI-CPM . . . 166

List of Tables

1.1 Summary of the computational complexity of an example case of boundary element method for a wave propagation problem 30

2.1 Explicit forms of the integral kernels of the operators linked to the boundary integral equations in two dimensions. 44
2.2 Series forms of the integral kernels of the operators linked to the boundary integral equations in two dimensions. 44
2.3 Relation between operators on the disk. 57
2.4 First values of $\mathbb{P}_l^m(w(\rho))$. 60
2.5 First values of α_l^m. 68
2.6 First values of β_l^m. 73
2.7 Summary of the operators over $\mathbb{D}$ in their different forms. 81

3.1 Types of mesh sets to be used in the numerical computations of boundary elements 104
3.2 Boundary integral equations for the modified integral operators to be used as benchmark cases. 111
3.3 Sobolev norms relative errors for the boundary integral equations for the modified integral operators. 111
3.4 Modified norms relative errors for the boundary integral equations for the modified integral operators.. 113

4.1 Condition number and number of iterations required so solve the linear system associated with unpreconditioned and the preconditioned matrix for progressively finer meshes for the L-shaped screen radar target. 140
4.2 Time duration of the different processes involved in matrix assembling, preconditining and solving for progressively finer triangular approximation of the screen radar target. 141
4.3 Parameters for the single underground domain example simulations 146
4.4 Parameters for double domain example simulations 148
4.5 Parameters used for a multi-monostatic simulation and image reconstruction using a single underground scenario 152
4.6 Parameters used for example cases of a multi-monostatic simulation and image reconstruction in double domain scenarios 158
4.7 Summary of the scenarios under which the two underground imaging method will be evaluated using numerical simulations 158

Abstract

This thesis is about some boundary integral operators defined on the unit disk in three-dimensional spaces, their relation with the exterior Laplace and Helmholtz problems, and their application to the preconditioning of the systems arising when solving these problems using the boundary element method.

We begin by describing the so-called integral method for the solution of the exterior Laplace and Helmholtz problems defined on the exterior of objects with Lipschitz-regular boundaries, or on the exterior of open two-dimensional surfaces in a three-dimensional space. We describe the integral formulation for the Laplace and Helmholtz problem in these cases, their numerical implementation using the boundary element method, and we discuss its advantages and challenges: its computational complexity (both algorithmic and memory complexity) and the inherent ill-conditioning of the associated linear systems.

In the second part we show an optimal preconditioning technique (independent of the chosen discretization) based on operator preconditioning. We show that this technique is easily applicable in the case of problems defined on the exterior of objects with Lipschitz-regular boundary surfaces, but that its application fails for problems defined on the exterior of open surfaces in three-dimensional spaces. We show that the integral operators associated with the resolution of the Dirichlet and Neumann problems defined on the exterior of open surfaces have inverse operators that would provide optimal preconditioners but they are not easily obtainable. Then we show a technique to explicitly obtain such inverse operators for the particular case when the open surface is the unit disk in a three-dimensional space. Their explicit inverse operators will be given, however, in the form of a series, and will not be immediately applicable in the use of boundary element methods.

In the third part we show how some modifications to these inverse operators allow us to obtain variational explicit and closed-form expressions, no longer expressed as series, that also conserve some characteristics that are relevant for their preconditioning effect. These explicit and closed forms expressions are applicable in boundary element methods. We obtain precise variational expressions for them and propose numerical schemes to compute the integrals needed for their use with boundary elements. The proposed numerical methods are tested using identities available within the developed theory and then used to build preconditioning matrices. Their performance as preconditioners for linear systems is tested for the case of the Laplace and Helmholtz problems for the unit disk. Finally, we propose an extension of this method that allows for the treatment of cases of open surfaces other than the disk. We exemplify and study this extension in its use on a square-shaped and an L-shaped surface screen in a three-dimensional space.

Finally, the methods developed are used in an application example. Based on techniques and assumptions from geometrical optics, we propose improvements to existing methods for the imaging of underground reflectivity using ground penetrating radar. Because they rely on assumptions from geometrical optics, these methods have to tested by means of computational simulations, resulting in the resolution of a massive number of direct problems. A complexity analysis shows how the proposed preconditioning techniques can significantly reduce the algorithmic complexity of the global problem. Finally, the resolution capability of the proposed imaging methods are tested in different scenarios of practical interest.

Keywords: Exterior Laplace problem, exterior Helmholtz problem, boundary integral equations, boundary element methods, operator preconditioning, optimal preconditioning, screen problems, crack problems.

Résumé

Cette thèse s'inscrit dans le sujet des opérateurs intégraux de frontière définis sur le disque unitaire en trois dimensions, leurs relations avec les problèmes externes de Laplace et Helmholtz, et leurs applications au préconditionnement des systèmes linéaires obtenus en utilisant la méthode des éléments finis de frontière.

On décrit d'abord les méthodes intégrales pour résoudre les problèmes de Laplace et de Helmholtz en dehors des objets à frontière régulière lipschitzienne, et en dehors des surfaces bidimensionnelles ouvertes dans un espace tridimensionnel. La formulation intégrale des problèmes de Laplace et de Helmholtz pour ces cas est décrite formellement. La mise en œuvre d'une méthode numérique utilisant la méthode des éléments finis de frontière est également décrite. Les avantages et les défis inhérents à la méthode sont abordés : la complexité du calcul numérique (de mémoire et algorithmique) et le mauvais conditionnement inhérent des systèmes linéaires associés.

Dans une deuxième partie on expose une technique optimale de préconditionnement (indépendante de la discrétisation) sur la base des opérateurs intégraux de frontière. On montre comment cette technique est facilement réalisable dans le cas de problèmes définis en dehors d'un objet régulier à frontière lipschitzienne, mais qu'elle pose des problèmes quand ils sont définis en dehors d'une surface ouverte dans un espace tridimensionnel. On montre que les opérateurs intégraux de frontière associés à la résolution des problèmes de Dirichlet et Neumann définis en dehors des surfaces ont des inverses bien définies. On montre également que celles-ci pourraient conduire à des techniques de préconditionnement optimales, mais que ses formes explicites ne sont pas faciles à obtenir. Ensuite, on montre une méthode pour obtenir de tels opérateurs inverses de façon explicite lorsque la surface sur laquelle ils sont définis est un disque unitaire dans un espace tridimensionnel. Ces opérateurs inverses explicites seront, cependant, sous forme de séries, et n'auront pas une adaptation immédiate pour leur utilisation dans des méthodes des éléments finis de frontière.

Dans une troisième partie on montre comment certaines modifications aux opérateurs inverses mentionnés permettent d'obtenir des expressions variationnelles explicites et fermées, non plus sous la forme de séries, en conservant certaines caractéristiques importantes pour l'effet de préconditionnement cherché. Ces formes explicites sont applicables aux méthodes des éléments finis frontière. On obtient des expressions variationnelles précises et on propose des calculs numériques pour leur utilisation avec des éléments finis frontière. Ces méthodes numériques sont testées en utilisant différentes identités obtenues dans la théorie développée, et sont ensuite utilisées pour produire des matrices préconditionnantes. Leur performance en tant que préconditionneurs de systèmes linéaires associés à des problèmes de Laplace et Helmholtz à l'extérieur du disque est ainsi testée. Enfin, on propose une extension de cette méthode pour couvrir les cas des surfaces diverses. Ceci est étudié dans les cas précis des problèmes extérieurs à des surfaces en forme de carré et en forme de L dans un espace tridimensionnel.

Finalement, les méthodes développées sont utilisées dans un exemple d'application. Sur la base de techniques et hypothèses de l'optique géométrique, on propose des améliorations à des méthodes existantes pour l'imagerie de la réflectivité du sous-sol en utilisant le radar à pénétration de sol. Étant basées sur des hypothèses de l'optique géométrique, ces méthodes doivent être évaluées par simulations numériques, ce qui entraîne la résolution d'un nombre très important de problèmes directs. Une analyse de complexité montre comment les techniques de préconditionnement proposées peuvent réduire la complexité algorithmique du problème global. Enfin, la capacité de résolution des méthodes proposées pour la formation des images du sous-sol est évaluée pour différents scénarios d'intérêt.

Mots-clés : Problème extérieur de Laplace, problème extérieur de Helmholtz, équations intégrales de frontière, méthode des éléments finis de frontière, préconditionnement par opérateurs, préconditionnement optimal, problèmes des surfaces ouvertes, problèmes de fissures.

Resumen

Esta tesis trata sobre operadores integrales de contorno definidos sobre el disco unitario en tres dimensiones, su relación con los problemas exteriores de Laplace y de Helmholtz, y su aplicación al precondicionamiento de sistemas lineales generados utilizando el método de los elementos finitos de frontera.

Inicialmente se describen los llamados métodos integrales para la resolución de problemas de Laplace y Helmholtz en el exterior de objetos de frontera regular Lischitziana y de superficies abiertas bi-dimensionales. Se describe la formulación integral de los problemas de Laplace y Helmholtz para estos casos, su implementación numérica utilizando el método de elementos finitos de frontera, y se discuten las ventajas y los desafíos intrínsecos a método: su complejidad computacional (de memoria y algortímica), y el inherente mal condicionamiento de los sistemas lineales asociados.

En una segunda parte se expone una técnica de precondicionamiento óptimo (independiente de la discretización), basado en operadores integrales de contorno, y se muestra como esta técnica es fácilmente realizable en el caso de problemas definidos en el exterior de un objeto de frontera regular Lipschitziana, pero no así cuando el problema se define en el exterior de una superficie abierta en tres dimensiones. Se mostrará que los operadores integrales de contorno asociados a la resolución de los problemas de Dirichlet y de Neumann definidos en el exterior de superficies tienen inversas bien definidas. Se mostrará también que estas inversas podrían dar origen a técnicas de precondicionamiento óptimo, pero que su forma explícita no es fácil de obtener. A continuación se mostrarán formas de obtener dichos operadores inversos de forma explícita cuando la superficie es un disco unitario en un espacio tridimensional. Estos operadores inversos explícitos estarán dados, sin embargo, en forma de series, y no serán apropiados para el uso inmediato en métodos de elementos finitos de frontera.

En una tercera parte mostraremos cómo algunas modificaciones a los operadores inversos mencionados permiten obtener expresiones variaciones explícitas y cerradas, ya no en forma de series, conservando algunas características relevantes para el efecto precondicionador. Estas formas explícitas cerradas sí son aplicables en métodos de elementos finitos de frontera. Se obtienen expresiones variaciones precisas y se proponen cálculos numéricos para su uso con elementos finitos de frontera. Estos métodos numéricos se prueban utilizando distintas identidades aseguradas en la teoría desarrollada y se utilizan para producir matrices precondicionantes. Su desempeño en la mejora del condicionamiento de los sistemas lineales asociados a los problemas de Laplace y Helmholtz en el exterior del disco es exhibido. Finalmente, se propone una extensión de este método que permite cubrir casos de dominios exteriores a superficies de diversos tipos, la que se ejemplifica y estudia en problemas exteriores a superficies cuadradas y en forma de L en un espacio en tres dimensiones.

Finalmente, los métodos desarrollados se utilizan en un ejemplo de aplicación. Basados técnicas y supuestos de la óptica geométrica, se proponen mejoras a métodos existentes para la formación de imágenes de reflectividad del subsuelo utilizando radares de penetración de suelo. Al basarse en supuestos de la óptica geométrica, estos métodos deben evaluarse mediante simulaciones físicas computacionales, lo que resulta en la resolución de un número masivo de problemas directos. Un análisis de complejidad muestra cómo las técnicas propuestas de precondicionamiento reducen significativamente la complejidad algóritmica del problema global. Finalmente, la capacidad de resolución de los métodos propuestos para hacer imágenes se evalúan en distintas situaciones de interés.

Palabras clave: Problema exterior de Laplace, problema exterior de Helmoltz, ecuaciones integrales de contorno, método de elementos finitos de frontera, precondicionamiento por operadores, precondicionamiento óptimo, problemas de superficies abiertas, problemas de fisuras.

Chapter 1

Wave Propagation, Boundary Integral Equations, Boundary Element Methods, and Computational Complexity

In this chapter we will treat the subject of wave propagation, its mathematical modeling in some specific cases, some common numerical strategies to solve wave propagation problems, their advantages and challenges.

In this chapter we lay down the framework for the results of the following chapters. The chapter covers a wide range of subjects in a succinct manner aiming to provide a summarized view of the domains relevant to the research work undertaken in this thesis. It contains definitions, notations, and results from previous research to be used in later chapters. It also serves to illustrate the motivation of this research through highlighting the advantages, and especially the challenges, this approach poses. The reader can skip the different sections of this chapter depending on its familiarity with the subjects treated.

We will begin by establishing the Helmholtz equation and its relation to the Laplace equation and to wave propagation phenomena in several areas of physics providing motivation and examples. We will then state a precise formulation of a relevant family of problems arising in wave propagation along with some geometrical and functional framework. Next, we will present the integral equation approach, that allows to solve some partial differential equations recasting them as integral equations on the boundaries of the propagation domains. We will present variational formulations for the boundary integral equations, a boundary discretization method, and the boundary element method which will give rise to discrete variational formulations posed on finite-dimensional spaces. We will show how this allows for the construction of Galerkin matrices leading to linear systems that can solve the discrete variational problem. Finally, we will address the main difficulties of this method, regarding computational complexity and accuracy, which will serve as an introduction to the following chapter where we provide a strategy to tackle these issues.

The definitions, propositions and theorems have been taken from different classic sources on the subject, such as [51], [57], [48]. Notation follows roughly that of [51]. Notation and results concerning the surface discretization, triangular meshes, and boundary elements spaces presented in this chapter have also been taken from [61].

1.1 The Helmholtz equation in physics

We will briefly provide a few examples of the use of the Helmholtz equation in the mathematical modeling of wave propagation phenomena. These examples will quickly show a wide range of possible applications in science and engineering, which will serve as motivation and background for the work undertaken and reported in this document. These examples follow those presented in [51, Section 1.2] and [64, Section 1.2].

Wave propagation phenomena in three-dimensional space are governed at each point by the hyperbolic wave equation,

$$-\frac{\partial^2 u}{\partial t^2}(\boldsymbol{x},t) + c^2 \Delta u(\boldsymbol{x},t) = 0 \text{ for } \boldsymbol{x} \in \mathbb{R}^3, \text{ and } t \in \mathbb{R}^+, \tag{1.1}$$

where u is a function describing a quantity that is preserved over time and over $\mathbb{R}^3$, and c the wave velocity of the propagation medium.

A time-harmonic solution, of frequency f, to the wave equation can be sought using Fourier transforms, slightly abusing notation, with the time dependency convention

$$u(\boldsymbol{x},t) = \mathrm{Re}\left\{u(\boldsymbol{x})e^{-\mathrm{i}\omega t}\right\}, \tag{1.2}$$

where the quantity $\omega = 2\pi f$ is called the pulsation of the time-harmonic wave. Function u is now a solution to the Helmholtz equation:

$$-\left(\Delta u(\boldsymbol{x}) + k^2 u(\boldsymbol{x})\right) = 0 \text{ for } \boldsymbol{x} \in \mathbb{R}^3, \tag{1.3}$$

where $k = \omega/c$ is called the wave number.

The Laplace equation is a limit case of the Helmholtz equation, in which the frequency f is zero. Thus, k is also zero, yielding:

$$-\Delta u(\boldsymbol{x}) = 0 \text{ for } \boldsymbol{x} \in \mathbb{R}^3. \tag{1.4}$$

The Helmholtz equation arises naturally in the mathematical modeling of numerous wave propagation phenomena that are intrinsically time-harmonic. Additionally, the use of Fourier transforms allows us to perform time-harmonic calculations for frequencies f over a given band so we can then compute the transient wave behavior. In the rest of this section we develop examples of some of the most classic physical models for wave phenomena using the Helmholtz equation.

1.1.1 Acoustic waves

Let us consider a gas in which a pressure wave is traveling. The total pressure on each point is described by a function $p_T(\boldsymbol{x},t)$, the total density by a function $\rho_T(\boldsymbol{x},t)$, and the total velocity by a function $\boldsymbol{v}_T(\boldsymbol{x},t)$. The conservation of mass can be expressed as

$$\frac{d\rho_T}{dt}(\boldsymbol{x},t) + \mathrm{div}\,(\rho_T\,\boldsymbol{v}_T)\,(\boldsymbol{x},t) = 0, \tag{1.5}$$

and the conservation of momentum as

$$\frac{d}{dt}\,(\rho_t\,\boldsymbol{v}_t)\,(\boldsymbol{x},t) + \overrightarrow{\mathrm{grad}}\,(p_t)\,(\boldsymbol{x},t) = 0. \tag{1.6}$$

Being interested in the perturbations of the pressure, we express the total pressure, density, and wave velocity as background values p_0, ρ_0, and $\boldsymbol{v}_0$ plus perturbations p, ρ, and $\boldsymbol{v}$:

$$\boldsymbol{v}_T = \boldsymbol{v}_0 + \boldsymbol{v}, \quad p_T = p_0 + p, \quad \text{and} \quad \rho_T = \rho_0 + \rho. \tag{1.7}$$

We will assume that the gas is perfect. Assuming that the gas is also at rest, i.e. that $\boldsymbol{v}_0 = 0$, and using a first order linearization of (1.5) and (1.6) (refer to [64, Section 1.2.1] or [39, Sections 1.1.1 & 1.1.2]) yields the system of equations

$$\begin{cases} \rho_0 \dfrac{\partial \boldsymbol{v}}{\partial t}(\boldsymbol{x},t) + \overrightarrow{\operatorname{grad}}\, p(\boldsymbol{x},t) = 0, \\ \\ \dfrac{1}{c^2}\dfrac{\partial p}{\partial t}(\boldsymbol{x},t) + \rho_0 \operatorname{div} \boldsymbol{v}(\boldsymbol{x},t) = 0, \end{cases} \tag{1.8}$$

where $c = \sqrt{\gamma R_s T}$ is the wave velocity, γ the adiabatic index of the gas, R_s its specific constant, and T its absolute pressure. Assuming that the propagating wave is time-harmonic, and using (1.2) as $p(\boldsymbol{x},t) = \operatorname{Re}\left\{p(\boldsymbol{x})e^{-\mathrm{i}\omega t}\right\}$ and as $\boldsymbol{v}(\boldsymbol{x},t) = \operatorname{Re}\left\{\boldsymbol{v}(\boldsymbol{x})e^{-\mathrm{i}\omega t}\right\}$ we can rewrite the system (1.8) as

$$\begin{cases} -\mathrm{i}\omega\rho_0 \boldsymbol{v}(\boldsymbol{x}) + \overrightarrow{\operatorname{grad}}\, p(\boldsymbol{x}) = 0, \\ \\ -\dfrac{\mathrm{i}\omega}{c^2} p(\boldsymbol{x}) + \rho_0 \operatorname{div} \boldsymbol{v}(\boldsymbol{x}) = 0. \end{cases} \tag{1.9}$$

Applying divergence to the first equation and eliminating $\operatorname{div} \boldsymbol{v}$ yields a Helmholtz equation for the pressure variation p:

$$-\left(\Delta p(\boldsymbol{x}) + k^2 p(\boldsymbol{x})\right) = 0, \tag{1.10}$$

where $k = \omega/c$ is the wave number.

1.1.2 Elastic waves

The elastic equation describes the displacement of points inside an elastic object when a linear approximation is used in the case of small displacements. Let $\boldsymbol{u}(\boldsymbol{x},t) = (u_1(\boldsymbol{x},t), u_2(\boldsymbol{x},t), u_3(\boldsymbol{x},t))$ be the three-dimensional displacement at point $\boldsymbol{x}$ and time t. Let the strain tensor ε for the object be

$$\varepsilon_{ij}(\boldsymbol{u}) = \frac{1}{2}\left(\frac{\partial u_j}{\partial x_i} + \frac{\partial u_j}{\partial x_i}\right). \tag{1.11}$$

The strain tensor is related to the stress tensor σ by the Lamé parameters μ and λ as

$$\sigma_{ij}(\boldsymbol{u}) = 2\mu\varepsilon_{ij}(\boldsymbol{u}) + \delta_i^j \lambda \sum_{k=1}^{3} \varepsilon_{kk}(\boldsymbol{u}), \tag{1.12}$$

where δ_i^j is the Kronecker delta.

Given the density ρ, the conservation of momentum can be expressed as

$$\rho \frac{\partial u_i}{\partial t^2}(\boldsymbol{x},t) - \sum_{j=1}^{3} \frac{\partial \sigma_{ij}}{\partial x_j}(\boldsymbol{u})(\boldsymbol{x},t) = 0. \tag{1.13}$$

Using (1.2) as $\boldsymbol{u}(\boldsymbol{x},t) = \operatorname{Re}\left\{\boldsymbol{u}(\boldsymbol{x},t)e^{-\mathrm{i}\omega t}\right\}$, if the displacement is time-harmonic, we can rewrite the last equation as

$$\rho\omega^2 u_i(\boldsymbol{x}) + \sum_{j=1}^{3} \frac{\partial \sigma_{ij}}{\partial x_j}\boldsymbol{u}(\boldsymbol{x}) = 0, \tag{1.14}$$

which, in vectorial notation, can be expressed as

$$\rho\omega^2\boldsymbol{u}(\boldsymbol{x}) + \mu\Delta\boldsymbol{u}(\boldsymbol{x}) + (\lambda+\mu)\overrightarrow{\text{grad}}\,\text{div}\,\boldsymbol{u}(\boldsymbol{x}) = 0. \tag{1.15}$$

If the displacement $\boldsymbol{u}$ has null divergence, i.e. $\text{div}\,\boldsymbol{u} = 0$, the object is incompressible and the previous equation can be rewritten as a Helmholtz equation for the time-harmonic displacement:

$$\Delta\boldsymbol{u}(\boldsymbol{x}) + k^2\boldsymbol{u}(\boldsymbol{x}) = 0, \tag{1.16}$$

where the wave number is $k = \omega\sqrt{\rho/\mu}$. These are the so-called shearing waves, or S waves.

An interesting type of solutions is the irrotational time-harmonic waves, thus writable as $\boldsymbol{u} = \overrightarrow{\text{grad}}\,\varphi$. Using the vectorial identity $\Delta\boldsymbol{v} = \overrightarrow{\text{grad}}\,\text{div}\,\boldsymbol{v} - \overrightarrow{\text{curl}}\,\overrightarrow{\text{curl}}\,\boldsymbol{v}$, equation (1.15) can be written as

$$\rho\omega^2\boldsymbol{u}(\boldsymbol{x}) + (\lambda+2\mu)\overrightarrow{\text{grad}}\,\text{div}\,(\boldsymbol{u}(\boldsymbol{x})) - \mu\overrightarrow{\text{curl}}\,\overrightarrow{\text{curl}}\,\boldsymbol{u}(\boldsymbol{x}) = 0, \tag{1.17}$$

which means that, if $\boldsymbol{u} = \overrightarrow{\text{grad}}\,\varphi$, then φ must necessarily satisfy

$$\rho\omega^2\varphi + (\lambda+2\mu)\Delta\varphi = 0. \tag{1.18}$$

This is a Helmholtz equation for a wave number $k = \omega\sqrt{\rho/(\lambda+2\mu)}$. These are the so-called pressure wave, or P waves.

1.1.3 Electromagnetic waves

We will show that the Helmholtz equation can also model an interesting range of electromagnetic wave propagation phenomena. Let us consider a homogeneous medium free of charges with electrical permittivity ϵ and magnetic permeability μ. The behavior of the electric and magnetics fields $\boldsymbol{E}$ and $\boldsymbol{H}$ is then governed by Maxwell's equations:

$$\begin{cases} -\epsilon\dfrac{\partial\boldsymbol{E}}{\partial t}(\boldsymbol{x},t) + \overrightarrow{\text{curl}}\,\boldsymbol{H}(\boldsymbol{x},t) = 0, \\ \\ \mu\dfrac{\partial\boldsymbol{H}}{\partial t}(\boldsymbol{x},t) + \overrightarrow{\text{curl}}\,\boldsymbol{E}(\boldsymbol{x},t) = 0. \end{cases} \tag{1.19}$$

Taking the divergence of both equations yields

$$\frac{\partial}{\partial t}\text{div}\,\boldsymbol{E}(\boldsymbol{x},t) = \frac{\partial}{\partial t}\text{div}\,\boldsymbol{H}(\boldsymbol{x},t) = 0, \tag{1.20}$$

which implies that

$$\text{div}\,\boldsymbol{E}(\boldsymbol{x},t) = \text{div}\,\boldsymbol{H}(\boldsymbol{x},t) = 0, \tag{1.21}$$

if $\text{div}\,\boldsymbol{E}(\boldsymbol{x},0) = \text{div}\,\boldsymbol{H}(\boldsymbol{x},0) = 0$. Using again the identity $\Delta\boldsymbol{v} = \overrightarrow{\text{grad}}\,\text{div}\,\boldsymbol{v} - \overrightarrow{\text{curl}}\,\overrightarrow{\text{curl}}\,\boldsymbol{v}$, and taking $\overrightarrow{\text{curl}}$ on both equations, we can obtain

$$\begin{cases} \dfrac{\partial^2\boldsymbol{E}}{\partial t^2}(\boldsymbol{x},t) - c^2\Delta\boldsymbol{E}(\boldsymbol{x},t) = 0, \\ \\ \dfrac{\partial^2\boldsymbol{H}}{\partial t^2}(\boldsymbol{x},t) - c^2\Delta\boldsymbol{H}(\boldsymbol{x},t) = 0, \end{cases} \tag{1.22}$$

where $c = 1/\sqrt{\epsilon\mu}$ is the wave velocity.

Using (1.2) as $\boldsymbol{E}(\boldsymbol{x},t) = \text{Re}\left\{\boldsymbol{E}(\boldsymbol{x})e^{-\text{i}\omega t}\right\}$ and $\boldsymbol{H}(\boldsymbol{x},t) = \text{Re}\left\{\boldsymbol{H}(\boldsymbol{x})e^{-\text{i}\omega t}\right\}$, we obtain Helmholtz equations for the electric and the magnetic fields when they are considered to be time-harmonic:

$$\begin{cases} \Delta \boldsymbol{E}(\boldsymbol{x}) + k^2 \boldsymbol{E}(\boldsymbol{x}) = 0, \\ \\ \Delta \boldsymbol{H}(\boldsymbol{x}) + k^2 \boldsymbol{H}(\boldsymbol{x}) = 0. \end{cases}, \tag{1.23}$$

where $k = \omega/c = \omega\sqrt{\epsilon\mu}$ is the wave number.

1.2 Problem domains, boundaries, and Sobolev spaces

In this section, we will provide a geometrical and a functional setting for much of the rest of this document. We will begin by describing the types of domains that will be considered for the development of the results that will be treated in the subsequent chapters. These domains will be mainly classified according to the regularity of their boundaries, for which we will provide a precise definition. We will also provide a characterization of the functional spaces that will be relevant to the analysis of the problems to be considered in these domains.

1.2.1 Domains and boundaries

Throughout this thesis we will consider a precise range of problems, those consisting of a wave propagating on the exterior of a connected and bounded obstacle embedded in three-dimensional space. This obstacle will be most notably distinguished by the regularity of its boundary. If the obstacle is represented by the set of points $\mathcal{O} \subset \mathbb{R}^3$ with boundary $\Gamma = \partial\mathcal{O}$, we will distinguish between obstacles with Lipschitz-regular boundary Γ and obstacles whose boundary isn't Lipschitz-regular. Roughly speaking, a Lipschitz-regular boundary Γ of an obstacle $\mathcal{O} \subset \mathbb{R}^3$ is a surface that can be represented locally by the graph of a Lipschitz-regular function [48, page 89]. We will provide a more precise description of this notion in the following definition.

Definition 1.2.1 (Lipschitz-regular surfaces [48, Definition 3.28])**.** *A Lipschitz-regular surface $\Gamma = \partial\mathcal{O}$, boundary of an obstacle $\mathcal{O}$ in $\mathbb{R}^3$, is a surface for which exist finite families of sets $\{W_i\}_{i=1}^N$ and $\{\Omega_i\}_{i=1}^N$ having the following properties:*

1. *The family $\{W_i\}_{i=1}^N$ is a finite open cover of Γ, i.e., each W_i is an open subset of $\mathbb{R}^3$ and $\Gamma \subseteq \bigcup_{i=1}^N W_i$.*
2. *Each Ω_i can be transformed to a Lipschitz hypograph by a rigid motion, i.e., by a rotation plus a translation.*
3. *The set $\mathcal{O}$ satisfies $W_i \cap \mathcal{O} = W_i \cap \Omega_i$ for $i = 1...N$.*

We will also speak of a Lipschitz-regular obstacle whenever an obstacle has a boundary that is a Lipschitz-regular surface. This kind of object allows for the use of special analysis tools that will provide significant advantages in modeling wave propagation phenomena, and in developing numerical methods able to produce numerical simulations.

Cusps, cracks, and screens are examples of surfaces that are not Lipschitz-regular. The screens are the focus of much of the work presented in this thesis, and will be described in more detail. A large family of surfaces that are not Lipschitz-regular is produced when, locally, parts of two Lipschitz-regular surfaces are joined with an angle of zero degrees. Surfaces that are not Lipschitz-regular appear naturally when modeling many problems of practical interest, but unfortunately they deprive us of many of the useful analytical tools that are available for cases that consider only Lipschitz-regular surfaces. These domains that are not Lipschitz-regular have a more complex geometry when applied to the modeling of physical phenomena. This will be a major subject in the next chapters of this document.

A particular case of obstacles that are not Lipschitz-regular, especially relevant for the work presented here, are the so-called screens. They are open surfaces in $\mathbb{R}^3$. These obstacles can be viewed as objects that have collapsed and thus have no interior ($\text{int}(\mathcal{O}) = \varnothing$) but only external boundary. The boundary will in turn have a one-dimensional manifold (a curve) as boundary ($\partial\Gamma \neq \varnothing$) . We will consider an orientation for surfaces Γ definable a.e. We will denote with signs + and - this orientation, respectively signaling the exterior and interior sides if Γ is a closed surface (in the case of the boundary of an obstacle), or an upper and lower side in the case of an open surface, i.e., in the case of a screen. We will also define, a.e., a

unit vector, denoted by $\boldsymbol{n}$, normal to surface Γ and pointing towards the exterior or the upper side, according to the case. Figure 1.1 illustrates a transformation that can give rise to screen obstacles and the elements identified so far.

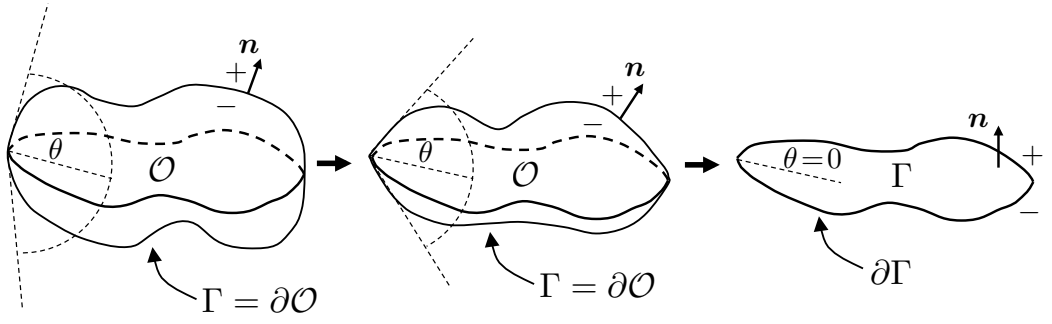

Figure 1.1: Illustration of the collapse of a Lipschitz-regular obstacle $\mathcal{O}$ into a screen Γ, showing its orientation and unit normal vector.

Two cases are of special interest: Lipschitz-regular obstacles $\mathcal{O}$ of boundary Γ, and screen obstacles Γ. We will take interest in what is called the exterior problem. In the case of Lipschitz-regular obstacles $\mathcal{O}$ with Lipschitz-regular boundaries $\Gamma = \partial\mathcal{O}$, the problem domain will be $\Omega_{\mathcal{O}} = \mathbb{R}^3 \setminus \overline{\mathcal{O}}$ with boundaries Γ, and what will be called the infinity. Similarly, in the case of screen obstacles Γ , the problem domain will be denoted by $\Omega_\Gamma = \mathbb{R}^3 \setminus \overline{\Gamma}$ with boundaries Γ and the infinity. Many problems in physics can be modeled specifying conditions at the boundaries of the problem's domain, i.e. on Γ and at infinity, the latter one meaning a specification of the behavior of a solution asymptotically far from the obstacle.

It will be useful to consider a notion of regularity wider than that of Lipshitz-regularity. In the context of Definition 1.2.1 a surface Γ will be further called of class C^k, or k-regular, if there is a diffeomorphism ξ_i of class C^k with inverse of class C^k mapping each covering set W_i onto the unit ball such that the set $W_i \cap \Gamma$ is mapped onto its equatorial plane [51, Section 2.5.2].

1.2.2 Elementary differential geometry

It will be useful to define certain surface differential operators for functions defined on sufficiently smooth surfaces, as the ones that will be used in the rest of this document. These operators will appear later in the study of variational forms of boundary integral operators that will be relevant for the treatment of the Laplace and Helmholtz problems. Let us begin defining the distance from a point to a given set in $\mathbb{R}^3$.

Definition 1.2.2 (Distance function)**.** *For every point $\boldsymbol{x}$ in $\mathbb{R}^3$, we denote by $dist(\boldsymbol{x}, A)$ the distance of $\boldsymbol{x}$ to the set A:*

$$dist(\boldsymbol{x}, A) = \inf_{\boldsymbol{y}\in A} \|\boldsymbol{x} - \boldsymbol{y}\| . \tag{1.24}$$

The most relevant application for this function will be the measurement of the distance from a point $\boldsymbol{x}$ to a surface Γ, i.e. $\operatorname{dist}(\boldsymbol{x}, \Gamma)$, and the distance from a point on the surface, $\boldsymbol{x} \in \Gamma$, to the edge of that surface whenever it is open, i.e. $\operatorname{dist}(\boldsymbol{x}, \partial\Gamma)$. We will use this notion of distance to define the tubular neighborhood of a surface.

Definition 1.2.3 (Tubular neighborhood [51, Section 2.5.6])**.** *A collection of points, denoted Γ_ε, whose distance to a surface Γ is less than $\varepsilon > 0$ is a tubular neighborhood of Γ defined as*

$$\Gamma_\varepsilon = \left\{ \boldsymbol{x} \in \mathbb{R}^3 : dist(\boldsymbol{x}, \Gamma) \leq \varepsilon \right\} . \tag{1.25}$$

The imposition of regularity conditions on Γ will allow us to define orthogonal projections and liftings that will be needed in the definition of some surface differential operators.

Proposition 1.2.1 (Orthogonal surface projection [57, Example 8.1.8] [22, Lemma 14.16])**.** *If Γ is a k-regular surface with $k \geq 2$, then there exists $\varepsilon > 0$ and a tubular neighborhood Γ_ε of Γ such that the mapping*

$$\psi : \Gamma \times (-\varepsilon, \varepsilon) \to \Gamma_\varepsilon, \quad \psi(\boldsymbol{x}, s) = \boldsymbol{x} + s\boldsymbol{n}_{\boldsymbol{x}} \ \text{ for } \boldsymbol{x} \in \Gamma, \tag{1.26}$$

is a C^{k-1} diffeomorphism. Thus, the orthogonal projection $P_\Gamma : \Gamma_\varepsilon \to \Gamma$ is well defined by

$$P_\Gamma(\boldsymbol{x} + s\boldsymbol{n}_{\boldsymbol{x}}) = \boldsymbol{x} \quad \text{for } \boldsymbol{x} \in \Gamma, \text{ and } s \in (-\varepsilon, \varepsilon). \tag{1.27}$$

For a function u defined on a 2-regular surface Γ, we will consider the lifting $u \circ P_\Gamma$. We denote this function, in the scope of this section, by $\widetilde{u} = u \circ P_\Gamma$.

Definition 1.2.4 (Surface differential operators $\overrightarrow{\operatorname{curl}}_\Gamma$ and $\overrightarrow{\operatorname{grad}}_\Gamma$)**.** *We introduce the tangential gradient, $\overrightarrow{grad}_\Gamma$, defined by*

$$\overrightarrow{grad}_\Gamma u = \overrightarrow{grad}\,(\widetilde{u}), \tag{1.28}$$

and the tangential curl, $\overrightarrow{curl}_\Gamma$, defined by

$$\overrightarrow{curl}_\Gamma u = \overrightarrow{curl}\,(\widetilde{u}\boldsymbol{n}), \tag{1.29}$$

for a function u defined on a surface Γ with $\boldsymbol{n}$ being its unit normal.

Remark 1.2.1 (Alternative expression for $\overrightarrow{\operatorname{curl}}_\Gamma$)**.** *Considering the vector calculus identity $\overrightarrow{curl}(\psi\boldsymbol{v}) = \overrightarrow{grad}\,\psi \times \boldsymbol{v} + \psi\overrightarrow{curl}\,\boldsymbol{v}$ for a field $\boldsymbol{v}$ and a scalar field ψ on $\mathbb{R}^3$, the definition of the tangential curl is equivalent to*

$$\overrightarrow{curl}_\Gamma u = \overrightarrow{grad}_\Gamma u \times \boldsymbol{n}, \tag{1.30}$$

where $\boldsymbol{n}$ is the unit normal to Γ (and thus $\overrightarrow{curl}\,\boldsymbol{n} = 0$).

1.2.3 Sobolev spaces

In this subsection we will define the functional spaces in which the different problems to be treated will be considered. These functional spaces are called Sobolev spaces and are the natural spaces of functions in which to solve variational formulations of partial differential equations [4, Section 4.1]. This is due to the fruitful energy analysis in mathematical physical modeling and the capacity of the Sobolev spaces to treat this concept together with a formal framework for integration.

We will consider a variety of Sobolev spaces defined on propagation domains and in the surface of obstacles, either Lipschitz-regular or screens. We will focus on definitions directly applicable to the cases to be treated in the next chapter. For results of wider reach and greater detail, the reader is referred to [48, Chapter 3], [19, Chapter 7], and [51, Section 2.5.2]. The following exposition follows that of [61, Section 1.1].

Let us consider the following norms.

Definition 1.2.5 (L^2-norm)**.** *Let us consider a function u measurable on a set $S \in \mathbb{R}^3$. The L^2-norm $\|\cdot\|_{L^2(S)}$ of u on S is defined as*

$$\|u\|_{L^2(S)} = \left(\int_S |u|^2 dS \right)^{1/2}. \tag{1.31}$$

Definition 1.2.6 (Sobolev-Slobodeckii norm)**.** *Let u be a function defined on a surface Γ in $\mathbb{R}^3$, the Sobolev-Slobodeckii norm $|\cdot|_{H^{1/2}(\Gamma)}$ of u is defined as*

$$|u|_{H^{1/2}(\Gamma)} = \left(\int_\Gamma \int_\Gamma \frac{|u(\boldsymbol{x}) - u(\boldsymbol{y})|^2}{\|\boldsymbol{x} - \boldsymbol{y}\|^3} d\Gamma(\boldsymbol{x}) d\Gamma(\boldsymbol{y}) \right)^{1/2}. \tag{1.32}$$

Definition 1.2.7 ($H^{1/2}$ Sobolev norm for functions defined on surfaces)**.** *Let u be a function defined on a surface Γ in $\mathbb{R}^3$. The $H^{1/2}(\Gamma)$ Sobolev norm $\|\cdot\|_{H^{1/2}(\Gamma)}$ of u is defined as*

$$\|u\|_{H^{1/2}(\Gamma)} = \left(\|u\|^2_{L^2(\Gamma)} + |u|^2_{H^{1/2}(\Gamma)} \right)^{1/2}. \tag{1.33}$$

Before proceeding to the definition of the Sobolev spaces that will be used in the rest of this document, let us consider the extension of an open surface on $\mathbb{R}^3$.

Definition 1.2.8 (Closed extension $\widetilde{\Gamma}$ of an open surface Γ in $\mathbb{R}^3$)**.** *Given an open surface Γ (i.e. $\partial\Gamma \neq \varnothing$) embedded in $\mathbb{R}^3$, let us consider the closed extension $\widetilde{\Gamma}$ as the Lipschitz-regular, closed surface (i.e. $\partial\widetilde{\Gamma} = \varnothing$) such that $\Gamma \subset \widetilde{\Gamma}$.*

Let us now define the Sobolev spaces that will be directly relevant for definitions to be presented in the rest of this chapter, and for the results presented in subsequent ones.

Definition 1.2.9 (Positive order Sobolev spaces defined on surfaces in $\mathbb{R}^3$)**.** *For an open or closed surface Γ embedded in $\mathbb{R}^3$ we define the following spaces:*

1. *The Sobolev space $H^{1/2}(\Gamma)$ is the closure of space $C^\infty(\Gamma)$ using the norm $\|\cdot\|_{H^{1/2}(\Gamma)}$.*
2. *The Sobolev space $H_0^{1/2}(\Gamma)$ is the closure of space $C_0^\infty(\Gamma)$ using the norm $\|\cdot\|_{H^{1/2}(\Gamma)}$.*
3. *The Sobolev space $\widetilde{H}^{1/2}(\Gamma)$ is the subspace of $H^{1/2}(\widetilde{\Gamma})$ of functions with support on $\overline{\Gamma}$: $\widetilde{H}^{1/2}(\Gamma) = \left\{ u \in H^{1/2}(\widetilde{\Gamma}) : \mathrm{supp}(u) \subseteq \overline{\Gamma} \right\}$. If Γ is closed, $\widetilde{\Gamma} = \Gamma$ and $H^{1/2}(\Gamma) = \widetilde{H}^{1/2}(\Gamma)$.*

Remark 1.2.2. *It follows from the previous definition that $\widetilde{H}^{1/2}(\Gamma) \subseteq H_0^{1/2}(\Gamma)$.*

We will define negative order Sobolev spaces using duality, for which we will define the duality pairing. It is a standard practice to represent the duality pairing of Sobolev spaces as inner products in L^2 even if the elements are no longer L^2-integrable [19, Section 7.4].

Definition 1.2.10 (Duality pairing)**.** *Let $f \in V'$ and $g \in V$ be functions in dual spaces, with V and V' defined over a surface Γ, and possibly $f \notin L^2(\Gamma)$. We will compute the duality pairing between dual Sobolev spaces as inner products in $L^2(\Gamma)$ using density as*

$$\langle f, g \rangle_{V',V} = \lim_{n\to\infty} (f_n, g)_{L^2(\Gamma)} = \lim_{n\to\infty} \int_\Gamma f_n(\boldsymbol{x}) \overline{g(\boldsymbol{x})} d\Gamma(\boldsymbol{x}), \tag{1.34}$$

where $\{f_n\}_{n=1}^\infty \subset L^2(\Gamma)$ is a sequence such that

$$\lim_{n\to\infty} \|f - f_n\|_{V'} = 0. \tag{1.35}$$

Notation 1.2.1. *We also use the following notation for duality pairings referring only to the domain of integration:*

$$\langle f, g \rangle_\Gamma = \langle f, g \rangle_{V',V}. \tag{1.36}$$

We now use the duality pairing to define negative order Sobolev spaces on surfaces.

Definition 1.2.11 (Negative order Sobolev spaces defined on surfaces in $\mathbb{R}^3$)**.** *For an open or closed surface Γ embedded in $\mathbb{R}^3$ we use duality pairing to define the following spaces:*

1. *The Sobolev space $H^{-1/2}(\Gamma) = \left(\widetilde{H}^{1/2}(\Gamma)\right)'$, with norm*

$$\|u\|_{H^{-1/2}(\Gamma)} = \sup_{0\neq v\in\widetilde{H}^{1/2}(\Gamma)} \frac{|\langle u\,,\, v\rangle_{L^2(\Gamma)}|}{\|v\|_{H^{1/2}(\Gamma)}}. \tag{1.37}$$

2. *The Sobolev space $\widetilde{H}^{-1/2}(\Gamma) = \left(H^{1/2}(\Gamma)\right)'$, with norm*

$$\|u\|_{\widetilde{H}^{-1/2}(\Gamma)} = \sup_{0\neq v\in H^{1/2}(\Gamma)} \frac{|\langle u\,,\, v\rangle_{L^2(\Gamma)}|}{\|v\|_{H^{1/2}(\Gamma)}}. \tag{1.38}$$

If Γ is closed, $\widetilde{\Gamma} = \Gamma$ and $\widetilde{H}^{-1/2}(\Gamma) = H^{-1/2}(\Gamma)$.

Proposition 1.2.2 (Tilde spaces' inclusions [61, Equation (1.6)])**.** *It is easy to use the definition of the norms to state the following inclusions:*

1. $\widetilde{H}^{1/2}(\Gamma) \subset H^{1/2}(\Gamma)$;
2. $\widetilde{H}^{-1/2}(\Gamma) \subset H^{-1/2}(\Gamma)$.

When Γ is an open surface (a screen) spaces $H^{1/2}(\Gamma)$ and $H^{-1/2}(\Gamma)$ are no longer dual to each other. This will prove to be challenging to some preconditioning methods based on operator preconditioning with opposite order operators for first kind boundary integral equations. It is this fact that deprives us from using well established operator preconditioning techniques in the case of screen obstacles. Its implications will be made clearer during this chapter, and will be formally stated in the next one.

When studying problems on unbounded domains, exterior to Lipschitz-regular obstacle $\mathcal{O}$ or screen Γ, it will be natural to consider weighted Sobolev spaces that will take into account prescribed behaviors on functions asymptotically far from $\mathcal{O}$. Let us consider the following spaces.

Definition 1.2.12 (The weighted Sobolev space $W^{1,-1}(\Omega)$ [51, Section 2.5.4])**.** *Given an unbounded exterior domain, $\Omega = \mathbb{R}^3 \setminus \overline{\mathcal{O}}$ for a bounded Lipschitz-regular obstacle $\mathcal{O}$ or $\Omega = \mathbb{R}^3 \setminus \overline{\Gamma}$ for a screen Γ, we define the space*

$$W^{1,-1}(\Omega) = \left\{u : \frac{u}{f} \in L^2(\Omega),\ \frac{\partial u}{\partial x_i} \in L^2(\Omega)\right\}, \tag{1.39}$$

with $f(\boldsymbol{x}) = \sqrt{1+\|\boldsymbol{x}\|^2}$.

Definition 1.2.13 (The weighted Sobolev space $W^H(\Omega)$ [51, Section 2.6.2])**.** *Given an unbounded exterior domain, $\Omega = \mathbb{R}^3 \setminus \overline{\mathcal{O}}$ for a bounded Lipschitz-regular obstacle $\mathcal{O}$ or $\Omega = \mathbb{R}^3 \setminus \overline{\Gamma}$ for a screen Γ, we define the space*

$$W^H(\Omega) = \left\{u : \frac{u}{f} \in L^2(\Omega),\ \frac{1}{f}\frac{\partial u}{\partial x_i} \in L^2(\Omega), \frac{\partial u}{\partial r} - \mathrm{i}ku \in L^2(\Omega)\right\}, \tag{1.40}$$

with $f(\boldsymbol{x}) = \sqrt{1+\|\boldsymbol{x}\|^2}$.

Remark 1.2.3 (Restriction to bounded domains)**.** *For a bounded subset Ω_B of the exterior domain Ω from Definition 1.2.13, the restriction of functions from the weighted Sobolev spaces to Ω_B coincides with $H^1(\Omega_B)$. That is, for a bounded part of Ω, $W^{1,-1}(\Omega)$ and $W^H(\Omega)$ coincide with $H^1_{loc}(\Omega)$*

The weighted Sobolev spaces are Hilbert spaces, unlike $H^1_{loc}(\Omega)$ which is only of Fréchet type. Coinciding locally with $H^1_{loc}(\Omega)$ will be an important feature of the weighted Sobolev space that will provide us with a meaningful way of referring to the value of the limits of functions on Ω as they approach surface Γ. This will be treated formally in the next subsection.

1.2.4 Traces and jumps

In this subsection we will summarize some results about the relation between a function defined on an exterior propagation domain and the limit of its value approaching the boundary of an obstacle, be it Lipschitz-regular or a screen. We will define the so-called trace operator, which will provide this limit value. The main tool presented in this subsection will be the trace theorem, which will provide regularity estimates for a function defined on surface Γ as a result of this limit process. We will begin by giving a simple definition for the trace operator, following [19, Section 7.5]. Definitions and results with greater reach, beyond the scope of the work presented in this document, can be found in [48, page 100] and [38, Section 4.2].

Definition 1.2.14 (Trace operator)**.** *Given a Lipschitz-regular surface Γ in $\mathbb{R}^3$, we define the external and internal zeroth order trace operators $\gamma_\Gamma^\pm : H^1_{loc}(\mathbb{R}^3 \setminus \overline{\Gamma}) \to H^{1/2}(\Gamma)$ as*

$$\gamma_\Gamma^\pm u(\boldsymbol{x}) = \lim_{\varepsilon \to 0^\pm} u(\boldsymbol{x} \pm \varepsilon \boldsymbol{n}_{\boldsymbol{x}}) \tag{1.41}$$

for $\boldsymbol{x}$ in Γ, and $\boldsymbol{n}_{\boldsymbol{x}}$ the external unit normal at $\boldsymbol{x}$. Similarly, we define the first order trace operator, $\gamma_\Gamma^\pm \circ \frac{\partial}{\partial \boldsymbol{n}} : H^1_{loc}(\mathbb{R}^3 \setminus \overline{\Gamma}) \to H^{-1/2}(\Gamma)$ as

$$\gamma_\Gamma^\pm \frac{\partial u}{\partial \boldsymbol{n}_{\boldsymbol{x}}}(\boldsymbol{x}) = \lim_{\varepsilon \to 0^\pm} \frac{\partial}{\partial \boldsymbol{n}_{\boldsymbol{x}}} u(\boldsymbol{x} \pm \varepsilon \boldsymbol{n}_{\boldsymbol{x}}). \tag{1.42}$$

Theorem 1.2.1 (Trace theorem [19, Section 7.5] [51, Theorem 2.5.3])**.** *The trace operator $\gamma_\Gamma^\pm$ maps continuously the space $H^1_{loc}(\mathbb{R}^3 \setminus \overline{\Gamma})$, onto $H^{1/2}(\Gamma)$. The trace operator $\gamma_\Gamma^\pm \circ \frac{\partial}{\partial \boldsymbol{n}}$ maps continuously the space $H^1_{loc}(\mathbb{R}^3 \setminus \overline{\Gamma})$, onto $H^{-1/2}(\Gamma)$.*

We will be interested in the difference of the traces of opposite sides of a surface. The jump operators will provide us with the functions describing this quantity.

Definition 1.2.15 (Jump operator)**.** *Given an oriented surface Γ in $\mathbb{R}^3$ we define the jump operator $[\gamma_\Gamma \cdot]$ as*

$$[\gamma_\Gamma u] = \gamma_\Gamma^+(u) - \gamma_\Gamma^-(u), \tag{1.43}$$

and the jump operator $\left[\gamma_\Gamma \frac{\partial}{\partial \boldsymbol{n}} \cdot\right]$ as

$$\left[\gamma_\Gamma \frac{\partial u}{\partial \boldsymbol{n}}\right] = \gamma_\Gamma^+ \frac{\partial u}{\partial \boldsymbol{n}} - \gamma_\Gamma^- \frac{\partial u}{\partial \boldsymbol{n}}. \tag{1.44}$$

The trace operator and the trace theorem will allow us to define boundary conditions on Γ for the problems of interest. Imposing boundary conditions on the limit values of a function will give rise to the so-called Dirichlet problems, while imposing boundary conditions on the limits of the normal derivatives of a function will give rise to the so-called Neumann problems. We will detail the Dirichlet and Neumann problems for the Laplace and Helmholtz equations in the following section.

1.3 Laplace and Helmholtz problems

In this section we will define the problems that will be treated in the rest of this document. These problems will be, for a propagation domain $\Omega_{\mathcal{O}}$ on the exterior of a Lipschitz-regular object $\mathcal{O}$, the Dirichlet or Neumann, Laplace or Helmholtz partial differential equation problems. Likewise, for a propagation domain Ω_Γ on the exterior of a screen obstacle Γ, the symmetric or anti-symmetric, Dirichlet or Neumann, Laplace or Helmholtz partial differential equation problems. We will use the domain characterization, functional framework, and the trace operators defined on previous Section 1.2 to provide precise definitions of these problems. Before proceeding to the formal definition of the aforementioned partial differential equation problems, we will describe the different kinds of boundary conditions that can be prescribed on functions, and in particular the conditions for a searched solution asymptotically far from an obstacle.

1.3.1 Boundary and infinity conditions

Definition 1.3.1 (Dirichlet boundary conditions)**.** *Given an orientable surface Γ embedded in $\mathbb{R}^3$, a function defined on a domain $\Omega_\Gamma = \mathbb{R}^3 \setminus \overline{\Gamma}$, can be set to comply with Dirichlet boundary conditions, on either side of Γ by prescribing the identities*

$$\gamma_\Gamma^+ u = g^+ \quad \text{and} \quad \gamma_\Gamma^- u = g^- \quad \text{on } \Gamma, \tag{1.45}$$

for functions $g^\pm$ defined on Γ.

Definition 1.3.2 (Neumann boundary conditions)**.** *Given an orientable surface Γ embedded in $\mathbb{R}^3$, a function defined on a domain $\Omega_\Gamma = \mathbb{R}^3 \setminus \overline{\Gamma}$, can be set to comply with Neumann boundary conditions on either side of Γ by prescribing the identities*

$$\gamma_\Gamma^+ \frac{\partial u}{\partial \boldsymbol{n}} = \varphi^+ \quad \text{and } \gamma_\Gamma^- \frac{\partial u}{\partial \boldsymbol{n}} = \varphi^- \quad \text{on } \Gamma, \tag{1.46}$$

for functions $\varphi^\pm$ defined on Γ.

Definition 1.3.3 (Conditions at infinity [51, Section 2.2] [19, Section 11.3])**.** *Let us consider a function u defined on an exterior domain $\Omega_{\mathcal{O}}$ (for Lipschitz-regular obstacles) or Ω_Γ (for screen obstacles). For a point $\boldsymbol{x}$ far from the origin, let us express it as $u(r)$, with $r = \|x\|$. We will say that it complies with the Sommerfeld radiation condition, or outgoing wave condition, if*

$$\lim_{r\to\infty} r \left\| \frac{\partial u}{\partial r} - \mathrm{i}ku \right\| = 0. \tag{1.47}$$

Remark 1.3.1 (Radiation condition and physical solutions)**.** *Commonly, given Dirichlet or Neumann boundary conditions on the surface of an obstacle, two possible solutions complying with the Helmholtz equation on the exterior domain. Being a time-harmonic formulation, both incoming and outgoing waves satisfy it. The imposition of a condition like that of Definition 1.3.3, called the Sommerfeld radiation condition, eliminates one of them, leaving only the one that physically represents an outgoing wave of field.*

1.3.2 Exterior partial differential equation problems for Lipschitz-regular obstacles

We will precisely define the problems that will treated throughout the rest of this document. In this subsection we will specify the ones posed on domains exterior to a Lipschitz-regular obstacle $\mathcal{O}$.

Laplace problems

Let us define the following problems related to the Laplace partial differential equation posed on the exterior of a Lipschitz-regular obstacle $\mathcal{O}$ of boundary $\Gamma = \partial\mathcal{O}$, i.e. on $\Omega_{\mathcal{O}} = \mathbb{R}^3 \setminus \overline{\mathcal{O}}$.

Problem 1.3.1 (Dirichlet Laplace problem for a Lipschitz-regular obstacle)**.**

Given $g \in H^{1/2}(\Gamma)$*, find* $u \in W^{1,-1}(\Omega_{\mathcal{O}})$ *such that*

$$\begin{cases} -\Delta u(\boldsymbol{x}) = 0, & \text{for } \boldsymbol{x} \in \Omega_{\mathcal{O}}, \\ \gamma_{\Gamma}^{+} u(\boldsymbol{x}) = g(\boldsymbol{x}), & \text{for } \boldsymbol{x} \in \Gamma. \end{cases} \tag{1.48}$$

Problem 1.3.2 (Neumann Laplace problem for a Lipschitz-regular obstacle)**.**

Given $\varphi \in H^{-1/2}(\Gamma)$*, find* $u \in W^{1,-1}(\Omega_{\mathcal{O}})/\mathbb{R}$ *such that*

$$\begin{cases} -\Delta u(\boldsymbol{x}) = 0, & \text{for } \boldsymbol{x} \in \Omega_{\mathcal{O}}, \\ \gamma_{\Gamma}^{+} \dfrac{\partial u}{\partial \boldsymbol{n}_{\boldsymbol{x}}}(\boldsymbol{x}) = \varphi(\boldsymbol{x}), & \text{for } \boldsymbol{x} \in \Gamma. \end{cases} \tag{1.49}$$

Helmholtz problems

Let us define the following problems related to the Helmholtz partial differential equation posed on the exterior of a Lipschitz-regular obstacle $\mathcal{O}$ of boundary $\Gamma = \partial\mathcal{O}$, i.e. on $\Omega_{\mathcal{O}} = \mathbb{R}^3 \setminus \overline{\mathcal{O}}$.

Problem 1.3.3 (Dirichlet Helmholtz problem for a Lipschitz-regular obstacle)**.**

Given $g \in H^{1/2}(\Gamma)$ *and* $k \in \mathbb{C}$*, find* $u \in W^{H}(\Omega_{\mathcal{O}})$ *such that*

$$\begin{cases} -\big(\Delta u(\boldsymbol{x}) + k^2 u(\boldsymbol{x})\big) = 0, & \text{for } \boldsymbol{x} \in \Omega_{\mathcal{O}}, \\ \gamma_{\Gamma}^{+} u(\boldsymbol{x}) = g(\boldsymbol{x}), & \text{for } \boldsymbol{x} \in \Gamma, \\ (1.47) \text{ is satisfied.} \end{cases} \tag{1.50}$$

Problem 1.3.4 (Neumann Helmholtz problem for a Lipschitz-regular obstacle)**.**

Given $\varphi \in H^{-1/2}(\Gamma)$ *and* $k \in \mathbb{C}$*, find* $u \in W^{H}(\Omega_{\mathcal{O}})$ *such that*

$$\begin{cases} -\big(\Delta u(\boldsymbol{x}) + k^2 u(\boldsymbol{x})\big) = 0, & \text{for } \boldsymbol{x} \in \Omega_{\mathcal{O}}, \\ \gamma_{\Gamma}^{+} \dfrac{\partial u}{\partial \boldsymbol{n}_{\boldsymbol{x}}}(\boldsymbol{x}) = \varphi(\boldsymbol{x}), & \text{for } \boldsymbol{x} \in \Gamma, \\ (1.47) \text{ is satisfied.} \end{cases} \tag{1.51}$$

1.3.3 Exterior partial differential problems for screen obstacles

In this subsection we will specify the partial differential equation problems that will be posed on domains exterior to screen a Γ, i.e., on exterior domains $\Omega_{\Gamma} = \mathbb{R}^3 \setminus \overline{\Gamma}$. These problems will have a wider variety of interesting definitions because of the physical relevance of the cases where the given Dirichlet or Neumann trace data are set symmetrically or anti-symmetrically on opposite sides of Γ.

Laplace problems

Let us define the following problems related to the Laplace partial differential equation posed on the exterior of screen Γ, i.e. on $\Omega_\Gamma = \mathbb{R}^3 \setminus \overline{\Gamma}$.

Problem 1.3.5 (Symmetric Dirichlet Laplace problem for a screen obstacle)**.**

Given $g \in H^{1/2}(\Gamma)$ *find* $u \in W^{1,-1}(\Omega_\Gamma)$ *such that*

$$\begin{cases} -\Delta u(\boldsymbol{x}) = 0, & \text{for } \boldsymbol{x} \in \Omega_\Gamma, \\ \gamma_\Gamma^{\pm} u(\boldsymbol{x}) = g(\boldsymbol{x}), & \text{for } \boldsymbol{x} \in \Gamma. \end{cases} \tag{1.52}$$

Problem 1.3.6 (Anti-symmetric Dirichlet Laplace problem for a screen obstacle)**.**

Given $g \in \widetilde{H}^{1/2}(\Gamma)$ *find* $u \in W^{1,-1}(\Omega_\Gamma)$ *such that*

$$\begin{cases} -\Delta u(\boldsymbol{x}) = 0, & \text{for } \boldsymbol{x} \in \Omega_\Gamma, \\ \gamma_\Gamma^{\pm} u(\boldsymbol{x}) = \pm g(\boldsymbol{x}), & \text{for } \boldsymbol{x} \in \Gamma. \end{cases} \tag{1.53}$$

Problem 1.3.7 (Symmetric Neumann Laplace problem for a screen obstacle)**.**

Given $\varphi \in \widetilde{H}^{-1/2}(\Gamma)$ *find* $u \in W^{1,-1}(\Omega_\Gamma)/\mathbb{R}$ *such that*

$$\begin{cases} -\Delta u(\boldsymbol{x}) = 0, & \text{for } \boldsymbol{x} \in \Omega_\Gamma, \\ \left[\gamma_\Gamma \dfrac{\partial u}{\partial \boldsymbol{n}_{\boldsymbol{x}}}(\boldsymbol{x})\right] = \varphi(\boldsymbol{x}), & \text{for } \boldsymbol{x} \in \Gamma. \end{cases} \tag{1.54}$$

Problem 1.3.8 (Anti-Symmetric Neumann Laplace problem for a screen obstacle)**.**

Given $\varphi \in H^{-1/2}(\Gamma)$ *find* $u \in W^{1,-1}(\Omega_\Gamma)/\mathbb{R}$ *such that*

$$\begin{cases} -\Delta u(\boldsymbol{x}) = 0, & \text{for } \boldsymbol{x} \in \Omega_\Gamma, \\ \gamma_\Gamma^{\pm} \dfrac{\partial u}{\partial \boldsymbol{n}_{\boldsymbol{x}}}(\boldsymbol{x}) = \varphi(\boldsymbol{x}), & \text{for } \boldsymbol{x} \in \Gamma. \end{cases} \tag{1.55}$$

Helmholtz problems

Let us now define the following problems related to the Helmholtz partial differential equation posed on the exterior of screen Γ, i.e. on $\Omega_\Gamma = \mathbb{R}^3 \setminus \overline{\Gamma}$.

Problem 1.3.9 (Symmetric Dirichlet Helmholtz problem for a screen obstacle)**.**

Given $g \in H^{1/2}(\Gamma)$ *and* $k \in \mathbb{C}$ *find* $u \in W^H(\Omega_\Gamma)$ *such that*

$$\begin{cases} -\left(\Delta u(\boldsymbol{x}) + k^2 u(\boldsymbol{x})\right) = 0, & \text{for } \boldsymbol{x} \in \Omega_\Gamma, \\ \gamma_\Gamma^{\pm} u(\boldsymbol{x}) = g(\boldsymbol{x}), & \text{for } \boldsymbol{x} \in \Gamma, \\ (1.47) \text{ is satisfied.} \end{cases} \tag{1.56}$$

Problem 1.3.10 (Anti-symmetric Dirichlet Helmholtz problem for a screen obstacle)**.**

Given $g \in \widetilde{H}^{1/2}(\Gamma)$ *and* $k \in \mathbb{C}$ *find* $u \in W^H(\Omega_\Gamma)$ *such that*

$$\begin{cases} -\big(\Delta u(\boldsymbol{x}) + k^2 u(\boldsymbol{x})\big) = 0, & \text{for } \boldsymbol{x} \in \Omega_\Gamma, \\ \gamma_\Gamma^{\pm} u(\boldsymbol{x}) = \pm g(\boldsymbol{x}), & \text{for } \boldsymbol{x} \in \Gamma, \\ (1.47) \text{ is satisfied.} \end{cases} \tag{1.57}$$

Problem 1.3.11 (Symmetric Neumann Helmholtz problem for a screen obstacle)**.**

Given $\varphi \in \widetilde{H}^{-1/2}(\Gamma)$ *and* $k \in \mathbb{C}$ *find* $u \in W^H(\Omega_\Gamma)$ *such that*

$$\begin{cases} -\big(\Delta u(\boldsymbol{x}) + k^2 u(\boldsymbol{x})\big) = 0, & \text{for } \boldsymbol{x} \in \Omega_\Gamma, \\ \left[\gamma_\Gamma \dfrac{\partial u}{\partial \boldsymbol{n}_{\boldsymbol{x}}}(\boldsymbol{x})\right] = \varphi(\boldsymbol{x}), & \text{for } \boldsymbol{x} \in \Gamma, \\ (1.47) \text{ is satisfied.} \end{cases} \tag{1.58}$$

Problem 1.3.12 (Anti-Symmetric Neumann Helmholtz problem for a screen obstacle)**.**

Given $\varphi \in H^{-1/2}(\Gamma)$ *and* $k \in \mathbb{C}$ *find* $u \in W^H(\Omega_\Gamma)$ *such that*

$$\begin{cases} -\big(\Delta u(\boldsymbol{x}) + k^2 u(\boldsymbol{x})\big) = 0, & \text{for } \boldsymbol{x} \in \Omega_\Gamma, \\ \gamma_\Gamma^{\pm} \dfrac{\partial u}{\partial \boldsymbol{n}_{\boldsymbol{x}}}(\boldsymbol{x}) = \varphi(\boldsymbol{x}), & \text{for } \boldsymbol{x} \in \Gamma, \\ (1.47) \text{ is satisfied.} \end{cases} \tag{1.59}$$

In the rest of this chapter, we will focus on the problems defined on exterior domains for Lipschitz-regular obstacles. These results will later be extended for the screen obstacles in the next chapter, where we will deal with the challenges posed by the screen geometry.

1.4 Fundamental solutions and boundary integral operators

This section will mark a depart from the pure partial differential equations approach to introduce Green's functions and their associated boundary integral equations. These are the main tools that will allow us to recast the considered problems, posed on exterior domains, as integral equation problems posed on boundary surfaces or screens. These tools characterize the framework for the results of this thesis, that is, the so-called integral equation methods.

We will begin by defining the Green's function for the two partial differential operators considered, the Laplace and the Helmholtz partial differential operators (following the exposition presented in [19, Section 11.1]). We will then use this Green's function to define boundary integral operators. We will show relevant properties of these operators that will later allow us to formulate the exhibited problems as integral equation ones. The presentation of the results for the boundary integral operators follow the exposition of [51, Chapter 3].

1.4.1 Fundamental solutions and Green's functions

A fundamental solution for a partial differential operator $\mathcal{P}$, linear, with constant coefficients and defined in the space of distributions $\left(C_0^\infty(\mathbb{R}^3)\right)'$, is a distribution E that satisfies

$$\mathcal{P}E = \delta_0 \text{ in } \left(C_0^\infty(\mathbb{R}^3)\right)', \tag{1.60}$$

together with radiation or decay conditions, where δ_0 is the Dirac delta function located at the origin. Fundamental solutions are of interest because their convolution with a data function f, i.e. $u = E * f$, when it has sense, is a solution to $\mathcal{P}u = f$. If we no longer consider the Dirac delta function centered at the origin, but at a point $\boldsymbol{x} \in \mathbb{R}^3$, i.e. $\delta_{\boldsymbol{x}}$, the solution $G(\boldsymbol{x}, \boldsymbol{y})$ to $\mathcal{P}G(\boldsymbol{x}, \boldsymbol{y}) = \delta_{\boldsymbol{x}}(\boldsymbol{y})$ is called the Green's function for the operator $\mathcal{P}$.

The Green's functions for the Laplace and Helmholtz operators are of great interest because they allow us to express functions in $\Omega_{\mathcal{O}}$ (the exterior of a Lipschitz-regular obstacle) or in Ω_Γ (the exterior of a screen) using their traces on boundary Γ. Let us consider the free space Green's function for the Helmholtz differential operator for wave number $k \in \mathbb{C}$ as the function that solves:

$$-\left(\Delta_{\boldsymbol{y}} G^k(\boldsymbol{x}, \boldsymbol{y}) + k^2 G^k(\boldsymbol{x}, \boldsymbol{y})\right) = \delta_{\boldsymbol{x}}(\boldsymbol{y}). \tag{1.61}$$

The solution to (1.61) that satisfies conditions at infinity given in Definition 1.3.3 is

$$G^k(\boldsymbol{x}, \boldsymbol{y}) = \frac{e^{\mathrm{i}k\|\boldsymbol{y}-\boldsymbol{x}\|}}{4\pi \|\boldsymbol{y} - \boldsymbol{x}\|}. \tag{1.62}$$

The Green's function for the Laplace operator results from taking $k = 0$, as

$$G^0(\boldsymbol{x}, \boldsymbol{y}) = \frac{1}{4\pi \|\boldsymbol{y} - \boldsymbol{x}\|}. \tag{1.63}$$

Likewise, the derivatives of the Green's function for the Helmholtz operator is

$$\overrightarrow{\operatorname{grad}}_{\boldsymbol{y}} G^k(\boldsymbol{x}, \boldsymbol{y}) = \frac{e^{\mathrm{i}k\|\boldsymbol{y}-\boldsymbol{x}\|}}{4\pi} \left(1 - \mathrm{i}k \|\boldsymbol{y} - \boldsymbol{x}\|\right) \frac{\boldsymbol{y} - \boldsymbol{x}}{\|\boldsymbol{y} - \boldsymbol{x}\|^3}, \tag{1.64}$$

and for the Laplace operator, making $k = 0$,

$$\overrightarrow{\operatorname{grad}}_{\boldsymbol{y}} G^0(\boldsymbol{x}, \boldsymbol{y}) = \frac{\boldsymbol{y} - \boldsymbol{x}}{4\pi \|\boldsymbol{y} - \boldsymbol{x}\|^3}. \tag{1.65}$$

We have that $\overrightarrow{\operatorname{grad}}_{\boldsymbol{x}} G(\boldsymbol{x}, \boldsymbol{y}) = -\overrightarrow{\operatorname{grad}}_{\boldsymbol{y}} G(\boldsymbol{x}, \boldsymbol{y})$, for all k, including $k = 0$.

Remark 1.4.1 (The Green's function in $\mathbb{R}^2$)**.** *In $\mathbb{R}^2$, the Green's function for the Helmholtz operator is*

$$G^k(\boldsymbol{x},\boldsymbol{y}) = \frac{\mathrm{i}}{4} H_0^{(1)}\left(k\left\|\boldsymbol{y}-\boldsymbol{x}\right\|\right), \tag{1.66}$$

where $H_0^{(1)}$ is the Hankel function of the first kind [19, Section 6.4]. The Green's function for the Laplace operator in $\mathbb{R}^2$ is

$$G^0(\boldsymbol{x},\boldsymbol{y}) = -\frac{1}{2\pi}\ln\left\|\boldsymbol{y}-\boldsymbol{x}\right\|. \tag{1.67}$$

Equation (1.66) *satisfies conditions at infinity prescribed for $\mathbb{R}^2$ [19, Equation 11.25].*

1.4.2 Boundary integral operators

Using the Green's function for the Helmholtz differential operators, we will define the following boundary integral operators.

Definition 1.4.1 (Boundary integral operators defined on a surface Γ)**.** *Let Γ be a surface embedded in $\mathbb{R}^3$ and q be a function defined on Γ. We will define the following boundary integral operators:*

1. *The single layer or weakly singular operator:*

$$\left(\mathcal{S}^k q\right)(\boldsymbol{y}) = \int_\Gamma G^k(\boldsymbol{x},\boldsymbol{y}) q(\boldsymbol{x}) d\Gamma(\boldsymbol{x}). \tag{1.68}$$

2. *The double layer operator:*

$$\left(\mathcal{D}^k q\right)(\boldsymbol{y}) = \int_\Gamma \frac{\partial}{\partial \boldsymbol{n}_{\boldsymbol{x}}} G^k(\boldsymbol{x},\boldsymbol{y}) q(\boldsymbol{x}) d\Gamma(\boldsymbol{x}). \tag{1.69}$$

3. *The transpose double layer operator:*

$$\left((\mathcal{D}^k)^* q\right)(\boldsymbol{y}) = \int_\Gamma \frac{\partial}{\partial \boldsymbol{n}_{\boldsymbol{y}}} G^k(\boldsymbol{x},\boldsymbol{y}) q(\boldsymbol{x}) d\Gamma(\boldsymbol{x}) \tag{1.70}$$

4. *The hypersingular operator:*

$$\left(\mathcal{N}^k q\right)(\boldsymbol{y}) = \int_\Gamma \frac{\partial^2}{\partial \boldsymbol{n}_{\boldsymbol{x}} \partial \boldsymbol{n}_{\boldsymbol{y}}} G^k(\boldsymbol{x},\boldsymbol{y}) q(\boldsymbol{x}) d\Gamma(\boldsymbol{x}). \tag{1.71}$$

Theorem 1.4.1 (Traces of the weakly singular or single layer operator [51, Theorem 3.1.2, part 1])**.** *Let q be a function defined on Γ and let $u(\boldsymbol{y}) = (\mathcal{S}q)(\boldsymbol{y})$ for $\boldsymbol{y} \in \mathbb{R}^3$. Then:*

1. *Function u is continuous across Γ: $\gamma_\Gamma^+ u = \gamma_\Gamma^- u$ and $[\gamma_\Gamma u] = 0$.*
2. *The normal derivates of u at Γ are*

$$\gamma_\Gamma^\pm \frac{\partial u}{\partial \boldsymbol{n}_{\boldsymbol{y}}}(\boldsymbol{y}) = \mp\frac{q(\boldsymbol{y})}{2} + \int_\Gamma \frac{\partial}{\partial \boldsymbol{n}_{\boldsymbol{y}}} G(\boldsymbol{x},\boldsymbol{y}) q(\boldsymbol{x}) d\Gamma(\boldsymbol{x}), \text{ for } \boldsymbol{y} \in \Gamma. \tag{1.72}$$

Theorem 1.4.2 (Traces of the double layer operator [51, Theorem 3.1.2, part 2])**.** *Let φ be a function defined on Γ and let $u(\boldsymbol{y}) = (\mathcal{D}\varphi)(\boldsymbol{y})$ for $\boldsymbol{y} \in \mathbb{R}^3$. Then :*

1. *The normal derivate of function u is continuous across Γ:* $\gamma_\Gamma^+ \frac{\partial u}{\partial \boldsymbol{n}} = \gamma_\Gamma^- \frac{\partial u}{\partial \boldsymbol{n}}$, *and* $\left[\gamma_\Gamma \frac{\partial u}{\partial \boldsymbol{n}}\right] = 0$.

2. *The traces of u at Γ are*

$$\gamma_\Gamma^\pm u(\boldsymbol{y}) = \pm\frac{\varphi(\boldsymbol{y})}{2} + \int_\Gamma \frac{\partial}{\partial \boldsymbol{n}_{\boldsymbol{x}}} G(\boldsymbol{x},\boldsymbol{y})\varphi(\boldsymbol{x}) d\Gamma(\boldsymbol{x}), \text{ for } \boldsymbol{y} \in \Gamma. \tag{1.73}$$

Remark 1.4.2 (Normal derivative of $\mathcal{D}u$)**.** *The normal derivate of $\mathcal{D}u$ from Theorem 1.4.2 is given by operator $\mathcal{N}$ from Definition 1.4.1. Its associated kernel admits a strong singularity equivalent to $\|\boldsymbol{x}-\boldsymbol{y}\|^{-3}$ and it is not integrable. We will consider it to be an improper integral to be calculated as a finite part integral or in a weak sense.*

Finally, let us state the Calderón Identities for the defined boundary integral operators.

Theorem 1.4.3 (Calderón Identities [51, Theorem 3.1.3])**.** *When a surface Γ is closed and Lipschitz-regular, the boundary integral operators from Definition 1.4.1 satisfy the following operator identities:*

$$\mathcal{D}^k \circ \mathcal{S}^k = \mathcal{S}^k \circ (\mathcal{D}^k)^*, \tag{1.74}$$

$$\mathcal{N}^k \circ \mathcal{D}^k = (\mathcal{D}^k)^* \circ \mathcal{N}^k, \tag{1.75}$$

$$\mathcal{D}^k \circ \mathcal{D}^k - \mathcal{S}^k \circ \mathcal{N}^k = \frac{1}{4}\mathcal{I}, \tag{1.76}$$

$$(\mathcal{D}^k)^* \circ (\mathcal{D}^k)^* - \mathcal{N}^k \circ \mathcal{S}^k = \frac{1}{4}\mathcal{I}, \tag{1.77}$$

where $\mathcal{I}$ is the identity operator.

Remark 1.4.3 (Laplace as a special case of the Helmholtz case)**.** *All the results presented in this subsection apply to the Laplace case by setting $k = 0$.*

1.5 Boundary integral equations and variational formulations for Lipschitz-regular obstacles

Using the previously defined boundary integral operators from Definition 1.4.1, the partial differential equation problems can be recast as boundary integral equation problems posed on bounded surfaces instead of on unbounded propagation domains. This becomes a crucial advantage when seeking computational methods to solve these problems, as the domain to be discretized now becomes finite. Without recourse to these so-called boundary integral equation methods, the alternatives are the use of the so-called domain methods. These domain methods discretize the propagation domain after truncating it at an often large distance from the obstacle and imposing absorbing boundary conditions of perfectly matched layers on this new fictitious boundary. This poses additional difficulties when estimating the existence and properties of the searched solutions and often require greater computational resources. The integral equation approach does eliminate these problems for a wide range of relevant cases, but introduces new ones that will be addressed in the final section of this chapter, and treated in the rest of this thesis.

1.5.1 Boundary integral equations for the exterior problems

Using the properties of the defined boundary integral operators, we can pose the partial differential equation problems as integral equation problems for the case of Lipschitz-regular obstacles. The case of screen obstacles will require special treatment and will be introduced in the next chapter. Let $\mathcal{O}$ be a Lipschitz-regular obstacle of boundary $\Gamma = \partial\mathcal{O}$. In order to solve the exterior partial differential equation problem, we will associate it with an internal problem posed on the interior of $\mathcal{O}$. Let us denote by μ the jump of the Dirichlet trace and by λ the jump of the Neumann trace across Γ:

$$\mu(\boldsymbol{y}) = [\gamma_\Gamma u](\boldsymbol{y}) \quad \text{and} \quad \lambda(\boldsymbol{y}) = \left[\gamma_\Gamma \frac{\partial u}{\partial \boldsymbol{n}}\right](\boldsymbol{y}), \quad \text{for } \boldsymbol{y} \in \Gamma. \tag{1.78}$$

The properties of the boundary integral operators $\mathcal{S}$ and $\mathcal{D}$ from Theorems 1.4.1 and 1.4.2 will allow us to establish important identities. Let us consider the following function defined on $\mathbb{R}^3 \setminus \overline{\Gamma}$:

$$u(\boldsymbol{y}) = \mathcal{S}^k\lambda(\boldsymbol{y}) - \mathcal{D}^k\mu(\boldsymbol{y}), \quad \text{for } \boldsymbol{y} \in \mathbb{R}^3 \setminus \Gamma. \tag{1.79}$$

This function has an interesting property, as stated by the following theorem.

Theorem 1.5.1 (Integral representation theorem [51, Theorem 3.1.1])**.** *For a Lipschitz-regular obstacle $\mathcal{O}$, for a given wave number $k \in \mathbb{C}$, let u be a function such that*

$$\begin{cases} -\left(\Delta u + k^2 u\right) = 0, & \text{in } \mathcal{O}, \\ \\ -\left(\Delta u + k^2 u\right) = 0, & \text{in } \mathbb{R}^3 \setminus \overline{\mathcal{O}}. \end{cases} \tag{1.80}$$

Let us denote the jump of the traces of u across Γ as in (1.78). Then, for $\boldsymbol{y} \notin \Gamma$, u can be written as

$$u(\boldsymbol{y}) = \mathcal{S}^k\lambda(\boldsymbol{y}) - \mathcal{D}^k\mu(\boldsymbol{y}). \tag{1.81}$$

We will use this theorem, central to the so-called boundary integral equation approach and methods, to reformulate the exterior Dirichlet and Neumann problems for the Laplace and Helmholtz equations. We will do so for the case of Lipschitz-regular obstacles. When used for the case of screen obstacles, its use will demand more specificity, especially regarding the spaces used. This will be a starting point of the subsequent chapters.

Dirichlet problem for a Lipschitz-regular obstacle

Let us focus on the Dirichlet exterior Laplace or Helmholtz problem, i.e. Problem 1.3.1 or Problem 1.3.3. Let us propose the following associated interior problem:

Problem 1.5.1 (Associated interior Dirichlet problem)**.** *Given $g \in H^{1/2}(\Gamma)$, and $k \in \mathbb{C}$ (possibly zero), find $u \in W^{1,-1}(\mathcal{O})$ such that*

$$\begin{cases} -\left(\Delta u(\boldsymbol{x}) + k^2 u(\boldsymbol{x})\right) = 0, & \text{for } \boldsymbol{x} \in \mathcal{O}, \\ \\ \gamma_\Gamma^- u(\boldsymbol{x}) = g(\boldsymbol{x}), & \text{for } \boldsymbol{x} \in \Gamma. \end{cases} \tag{1.82}$$

If we consider the previous interior Problem 1.5.1 together with the exterior one, Problem 1.3.3 or Problem 1.3.1 for $k = 0$, we get that the jump of the Dirichlet traces is

$$\left[\gamma_\Gamma u\right](\boldsymbol{x}) = \mu(\boldsymbol{x}) = 0, \quad \text{for } \boldsymbol{x} \in \Gamma. \tag{1.83}$$

If we consider the jump of the Neumann traces,

$$\left[\gamma_\Gamma \frac{\partial u}{\partial \boldsymbol{n}}\right](\boldsymbol{x}) = \lambda(\boldsymbol{x}), \quad \text{for } \boldsymbol{x} \in \Gamma, \tag{1.84}$$

Theorem 1.5.1 tells us that

$$u(\boldsymbol{x}) = \left(\mathcal{S}^k \lambda\right)(\boldsymbol{x}), \quad \text{for } \boldsymbol{x} \notin \Gamma, \tag{1.85}$$

is a solution to the interior Problem 1.5.1, and particularly to the exterior Problem 1.3.3 or Problem 1.3.1 when $k = 0$. Also, Theorem 1.4.1 assures the continuity of u across Γ, which tells us that

$$\gamma_\Gamma^+ u = g. \tag{1.86}$$

This provides us with an integral equation for λ, which we can later used to find the solution to the exterior problem. This allows us to recast Problem 1.3.3, or Problem 1.3.3 if $k = 0$, as a new integral equation problem.

Problem 1.5.2 (Boundary integral equation problem for the Dirichlet exterior partial differential equation problem)**.** *Given $g \in H^{1/2}(\Gamma)$, and $k \in \mathbb{C}$ (possibly zero), find $\lambda \in H^{-1/2}(\Gamma)$ such that*

$$\mathcal{S}^k \lambda(\boldsymbol{x}) = g(\boldsymbol{x}), \quad \text{for } \boldsymbol{x} \in \Gamma, \tag{1.87}$$

and use it to determine

$$u(\boldsymbol{x}) = \left(\mathcal{S}^k \lambda\right)(\boldsymbol{x}), \quad \text{for } \boldsymbol{x} \in \mathbb{R}^3 \setminus \overline{\mathcal{O}}. \tag{1.88}$$

This assures us that the solution to Problem 1.5.2 is also the solution to Problem 1.3.3 or Problem 1.3.1 when $k = 0$.

Neumann problem for a Lipschitz-regular obstacle

Let us focus on the Neumann exterior Laplace or Helmholtz problem, i.e. Problem 1.3.2 or Problem 1.3.4. Let us propose the following associated interior problem:

Problem 1.5.3 (Associated interior Neumann problem)**.** *Given $\varphi \in H^{-1/2}(\Gamma)$, and $k \in \mathbb{C}$ (possibly zero), find $u \in W^{1,-1}(\mathcal{O})$ such that*

$$\begin{cases} -\left(\Delta u(\boldsymbol{x}) + k^2 u(\boldsymbol{x})\right) = 0, & \text{for } \boldsymbol{x} \in \mathcal{O}, \\ \\ \gamma_\Gamma^- \dfrac{\partial u}{\partial \boldsymbol{n}_{\boldsymbol{x}}}(\boldsymbol{x}) = \varphi(\boldsymbol{x}) & \text{for } \boldsymbol{x} \in \Gamma. \end{cases} \tag{1.89}$$

If we consider the previous interior problem, Problem 1.5.3, together with the exterior one, Problem 1.3.4 or Problem 1.3.2 if $k = 0$, we get that the jump of the Neumann traces is

$$\left[\gamma_\Gamma \frac{\partial u}{\partial \boldsymbol{n}}\right](\boldsymbol{x}) = \lambda(\boldsymbol{x}) = 0, \quad \text{for } \boldsymbol{x} \in \Gamma. \tag{1.90}$$

If we consider the jump of the Dirichlet traces,

$$[\gamma_\Gamma u](\boldsymbol{x}) = \mu(\boldsymbol{x}) \quad \text{for } \boldsymbol{x} \in \Gamma, \tag{1.91}$$

Theorem 1.5.1 tells us that

$$u(\boldsymbol{x}) = -\left(\mathcal{D}^k \mu\right)(\boldsymbol{x}) \quad \text{for } \boldsymbol{x} \notin \Gamma, \tag{1.92}$$

is a solution to the interior Problem 1.5.3, and particularly to the exterior Problem 1.3.4 or Problem 1.3.2 if $k = 0$. Also, Theorem 1.4.2 assures the continuity of the normal derivative of $\mathcal{D}^k$, which tells us that

$$\gamma_\Gamma^+ \frac{\partial u}{\partial \boldsymbol{n}} = \varphi, \tag{1.93}$$

This provides us with an integral equation for μ, which we can later use in (1.92) to find the solution to the exterior problem. This allows us to recast Problem 1.3.4 as a new integral equation problem.

Problem 1.5.4 (Boundary integral equation problem for the Neumann exterior partial differential equation problem)**.** *Given $\varphi \in H^{-1/2}(\Gamma)$, and $k \in \mathbb{C}$ (possibly zero), find $\mu \in H^{1/2}(\Gamma)$ such that*

$$-\frac{\partial}{\partial \boldsymbol{n}_{\boldsymbol{x}}} \mathcal{D}^k \mu(\boldsymbol{x}) = -\mathcal{N}^k \mu(\boldsymbol{x}) = \varphi(\boldsymbol{x}), \quad \textit{for } \boldsymbol{x} \in \Gamma, \tag{1.94}$$

and use it to determine

$$u(\boldsymbol{x}) = -\left(\mathcal{D}^k \mu\right)(\boldsymbol{x}), \quad \textit{for } \boldsymbol{x} \in \mathbb{R}^3 \setminus \overline{\mathcal{O}}. \tag{1.95}$$

This assures us that the solution to Problem 1.5.4 is also the solution Problem 1.3.4 or Problem 1.3.2 if $k = 0$.

1.5.2 Bilinear forms and variational formulation

Let us define the bilinear forms induced by the boundary integral operators associated with the Dirichlet and Neumann exterior problems.

Definition 1.5.1 (Bilinear forms for $\mathcal{S}^k$ and $\mathcal{N}^k$)**.** *Let us define the following bilinear forms induced by the weakly singular operator $\mathcal{S}^k$ and the hypersingular operator $\mathcal{N}^k$:*

$$a_k^{ws}(\lambda, \lambda^t) = \left\langle \mathcal{S}^k \lambda \,,\, \lambda^t \right\rangle_\Gamma, \tag{1.96}$$

$$a_k^{hs}(\mu, \mu^t) = \left\langle -\mathcal{N}^k \mu \,,\, \mu^t \right\rangle_\Gamma. \tag{1.97}$$

These bilinear forms are suitable for variational formulations for Problems 1.5.2 & 1.5.4, as the following theorems will show.

Theorem 1.5.2 (The bilinear form induced by $\mathcal{S}^k$ is coercive [51, Theorems 3.3.1 & 3.4.1])**.** *The boundary integral equation (1.87) from Problem 1.5.2 admits the following variational formulation*

$$\begin{cases} \textit{Given } g \in H^{1/2}(\Gamma), \textit{ find } \lambda \in H^{-1/2}(\Gamma) \textit{ such that} \\ \\ \forall \lambda^t \in H^{-1/2}(\Gamma) \left(a_k^{ws}(\lambda, \lambda^t) = \left\langle g \,,\, \lambda^t \right\rangle_\Gamma\right). \end{cases} \tag{1.98}$$

The associated operator $\mathcal{S}^k$ is an isomorphism from $H^{-1/2}(\Gamma)$ onto $H^{1/2}(\Gamma)$ when $-k^2$ is not an eigenvalue of the interior Dirichlet Problem 1.5.1 for the Laplacian. This also holds for $k = 0$.

Theorem 1.5.3 (The bilinear form induced by $\mathcal{N}^k$ is coercive [51, Theorems 3.3.2 & 3.4.2])**.** *The boundary integral equation (1.94) from Problem 1.5.4 admits the following variational formulation*

$$\begin{cases} \text{Given } \varphi \in H^{-1/2}(\Gamma), \text{ find } \mu \in H^{1/2}(\Gamma) \text{ such that} \\ \\ \forall \mu^t \in H^{1/2}(\Gamma) \left(a_k^{hs}(\mu, \mu^t) = \left\langle \varphi \, , \, \mu^t \right\rangle_\Gamma \right). \end{cases} \tag{1.99}$$

The kernel of $\mathcal{N}^k$ is not integrable, but can be computed as an improper integral and has the following expression:

$$\begin{aligned} a_k^{hs}(\mu, \mu^t) = & \int_\Gamma \int_\Gamma G^k(\boldsymbol{x}, \boldsymbol{y}) \left(\overrightarrow{curl}_\Gamma \mu, \overrightarrow{curl}_\Gamma \mu^t \right) d\Gamma(\boldsymbol{x}) d\Gamma(\boldsymbol{y}) \\ & -k^2 \int_\Gamma \int_\Gamma G^k(\boldsymbol{x}, \boldsymbol{y}) \mu(\boldsymbol{x}) \overline{\mu^t(\boldsymbol{y})} \, (\boldsymbol{n}_{\boldsymbol{x}}, \boldsymbol{n}_{\boldsymbol{y}}) \, d\Gamma(\boldsymbol{x}) d\Gamma(\boldsymbol{y}). \end{aligned} \tag{1.100}$$

The associated operator $\mathcal{N}^k$ is an isomorphism from $H^{1/2}(\Gamma)$ onto $H^{-1/2}(\Gamma)$ when $-k^2$ is not an eigenvalue of the interior Neumann Problem 1.5.3 for the Laplacian and $k \neq 0$. For $k = 0$ operator $\mathcal{N}^0$ is an isomorphism from $H^{1/2}(\Gamma)/\mathbb{R}$ onto $H_0^{-1/2}(\Gamma)$, the subspace of $H^{-1/2}(\Gamma)$ whose elements satisfy $\langle \varphi \, , \, 1 \rangle_\Gamma = 0$.

In the following section we will see how to discretize the integration domain Γ in order to consider subspaces of the Sobolev trace spaces and formulate finite-dimensional variational formulations.

1.6 Surface discretization, boundary element method, and Galerkin matrices

In this section we will define the way in which a surface Γ is discretized in order to form the boundary element spaces. These spaces will be finite-dimensional subspaces of the Sobolev trace spaces $H^{1/2}(\Gamma)$ and $H^{-1/2}(\Gamma)$, and will serve to define finite-dimentional variational formulations that will provide approximations to the solutions of the infinite-dimensional variational formulations associated with the boundary integral equations for $\mathcal{S}^k$ and $\mathcal{N}^k$.

1.6.1 Primal and dual meshes

Let Γ be a surface, open or closed, embedded in $\mathbb{R}^3$. Let us also consider a triangular approximation Γ_h indexed by a discretization parameter h. Figure 1.2 illustrates a triangular approximation for an open and a closed surface.

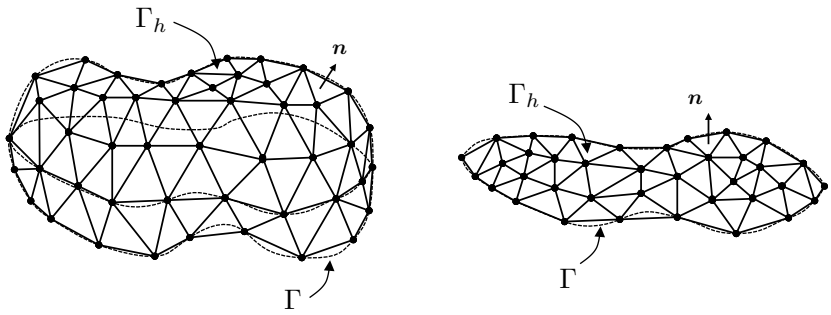

Figure 1.2: Conformal triangular approximation Γ_h of a closed (left) and an open (right) surface embedded in $\mathbb{R}^3$.

Notation 1.6.1 (Indexing by the discretization parameter h)**.** *We will index a triangular approximation of a surface Γ either by Γ_h or Γ_{N_T}, referencing the discretization parameter h or the number of triangles N_T.*

Definition 1.6.1 (Conformal triangular approximation)**.** *A triangular approximation Γ_h of a surface Γ is conformal if it is a connected set, and if the intersection of any two different triangles of Γ_h is either void, a set triangle vertices, or a full triangle edge.*

Definition 1.6.2 (Triangular mesh)**.** *A triangular mesh $\mathcal{T}_h$ (or $\mathcal{T}_{N_T}$) for the conformal triangular approximation Γ_h (or Γ_{N_T}) of a surface Γ embedded in $\mathbb{R}^3$, open or closed, is the set of:*

- *The set of N_T triangles t_i (indexed by i) that compose its triangular approximation Γ_h: $\{t_i\}_{i=1}^{N_T}$.*
- *The set of N_E edges e_i (indexed by i) that compose its triangular approximation Γ_h: $\{e_i\}_{i=1}^{N_E}$.*
- *The set of N_V vertices $\boldsymbol{v}_i$ (indexed by i) of the triangles that compose its triangular approximation Γ_h: $\{\boldsymbol{v}_i\}_{i=1}^{N_V}$.*

If surface Γ is open, i.e. $\partial\Gamma \neq \varnothing$, the triangular mesh $\mathcal{T}_h$ will also include the set of N_V^0 internal vertices $\boldsymbol{v}_i^0$ (indexed by i): $\{\boldsymbol{v}_i^0\}_{i=1}^{N_V^0}$.

Notation 1.6.2 (Triangular mesh indexing)**.** *We will denote indistinctly a triangular mesh indexing it by a discretization parameter h, or by the number N_T of triangles that composes it as $\mathcal{T}_{N_T}$.*

Notation 1.6.3 (Referencing elements of a triangular mesh)**.** *We will adopt the simplified notation: $t_i \in \mathcal{T}_h$ will reference the i-th triangle from $\mathcal{T}_h$, $e_i \in \mathcal{T}_h$ will reference the i-th edge from $\mathcal{T}_h$, $\boldsymbol{v}_i \in \mathcal{T}_h$ will reference the i-th vertex from $\mathcal{T}_h$, and $\boldsymbol{v}_i^0 \in \mathcal{T}_h$ will reference the i-th internal vertex from $\mathcal{T}_h$ if surface Γ is open.*

Definition 1.6.3 (Triangle elements)**.** *For each triangle t_i of a triangular mesh $\mathcal{T}_h$ we identify the following elements:*

- *The set of its three vertices $T_{t\to\boldsymbol{v}}(t_i) := \{\boldsymbol{v}_1^i, \boldsymbol{v}_2^i, \boldsymbol{v}_3^i\}$.*
- *The set of the six non-intersecting sub-triangles resulting from dividing t_i using all its medians as delimiters (barycentric refinement): $T_{t\to\hat{t}}(t_i) := \left\{\hat{t}_j^i\right\}_{j=1}^6$.*
- *The set of the six pairwise non-intersecting sub-triangles resulting from dividing t_i in halves using its medians as delimiters: $T_{t\to\tilde{t}}(\tau_i) := \left\{\tilde{t}_j^i\right\}_{j=1}^6$.*

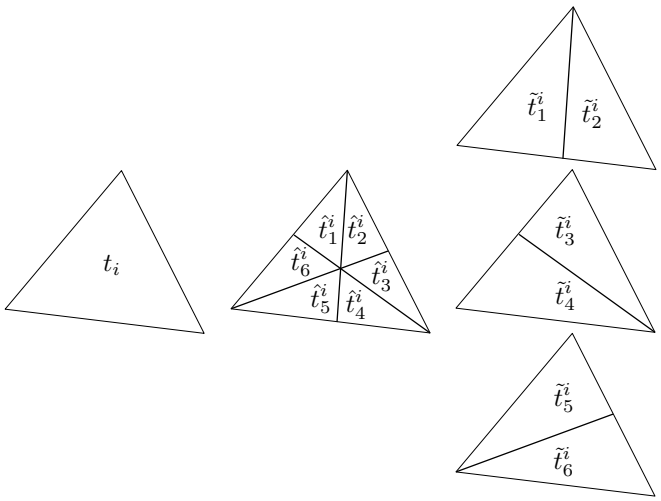

Figure 1.3: Example of a triangle t_i (left) of a triangular mesh with its sub-triangles $\hat{t}_j^i$ (center) and sub-triangles $\tilde{t}_j^i$ (right).

Definition 1.6.4 (Vertex elements)**.** *For each vertex $\boldsymbol{v}_i$ of a triangular mesh $\mathcal{T}_h$ we identify the following elements:*

- *The set of triangles t for which $\boldsymbol{v}_i$ is a vertex: $T_{\boldsymbol{v}\to t}(\boldsymbol{v}_i) = \{t \in \mathcal{T}_h : \boldsymbol{v}_i \text{ is a vertex of } t\}$.*
- *The set of sub-triangles $\hat{t}$ for which $\boldsymbol{v}_i$ is a vertex: $T_{\boldsymbol{v}\to\hat{t}}(\boldsymbol{v}_i) = \{\hat{t} \in \mathcal{T}_h : \boldsymbol{v}_i \text{ is vertex of } \hat{t}\}$.*

Definition 1.6.5 (Triangle measurements)**.** *Let us define the following measurements related to a triangle t_i of a triangular mesh $\mathcal{T}_h$:*

- *Its area A_i:*

$$A_i = \int_{t_i} dt_i(\boldsymbol{x}). \tag{1.101}$$

- *Its cell size h_i:*

$$h_i = \sqrt{A_i}. \tag{1.102}$$

- *Its diameter d_i:*

$$d_i = \sup_{\boldsymbol{x},\boldsymbol{y}\in t_i} \|\boldsymbol{x}-\boldsymbol{y}\|. \tag{1.103}$$

Definition 1.6.6 (Maximal and minimal cell sizes)**.** *For a triangular mesh $\mathcal{T}_h$ we define the maximal and minimal cell sizes as*

$$h_{max} = \max_{i=1\ldots N_T} h_i \quad \textit{and} \quad h_{min} = \min_{i=1\ldots N_T} h_i. \tag{1.104}$$

Definition 1.6.7 (Regular triangular mesh)**.** *A family of triangular meshes $\mathcal{T}_h$ is said to be regular if for every triangle t_i for every mesh there is always a constant C_R such that*

$$0 < C_R \leq \frac{h_i}{d_i} \leq 1. \tag{1.105}$$

Definition 1.6.8 (Locally quasi-uniform triangular mesh)**.** *A family of triangular meshes $\mathcal{T}_h$ is said to be locally quasi-uniform if for every pair of triangles t_i and t_j, there is a constant C_L such that for every mesh in the family*

$$\frac{h_i}{h_j} \leq C_L, \tag{1.106}$$

whenever triangles t_i and t_j are adjacent, i.e., when they share an edge or a vertex.

Definition 1.6.9 (Globally quasi-uniform triangular mesh)**.** *A family of triangular meshes $\mathcal{T}_h$ is said to be globally quasi-uniform if there is a constant C_G such that for every mesh in the family*

$$\frac{h_{max}}{h_{min}} \leq C_G. \tag{1.107}$$

We will use the defined mesh to build a new one called dual mesh. The name is motivated by the fact that we will use it to define spaces that will be subspaces of the space dual to the one that we will define on the first and primal mesh.

Definition 1.6.10 (Dual mesh)**.** *We will call $\widetilde{\mathcal{T}}_h$ the dual mesh of the triangular mesh $\mathcal{T}_h$ to the set of polygonal-wise elements associated with the N_V vertices of $\mathcal{T}_h$, $\{L_i\}_{i=1}^{N_V}$, where an element L_i associated with the vertex $\boldsymbol{r}_i$ is defined as the union of the subtriangles $\hat{t}$ that have $\boldsymbol{r}_i$ as vertex:*

$$L_i = \bigcup_{\hat{t}\in T_{\boldsymbol{v}\to\hat{t}}(\boldsymbol{r}_i)} \hat{t}. \tag{1.108}$$

We will use mesh $\mathcal{T}_h$ to define subspaces of $H^{1/2}(\Gamma_h)$ and $\widetilde{\mathcal{T}}_h$ to define subspaces of $H^{-1/2}(\Gamma_h)$.

1.6.2 Boundary element spaces and discrete variational formulations

In this section we will use the discretized surface Γ_h of Γ and the triangular meshes $\mathcal{T}_h$ and $\widetilde{\mathcal{T}}_h$ to define finite-dimensional subspaces of $H^{1/2}(\Gamma_h)$ and $H^{-1/2}(\Gamma_h)$, which we will use to compute approximations to the solutions to the integral equations associated with $\mathcal{S}^k$ and $\mathcal{N}^k$. The space discretization for the case of open surfaces, i.e. screen obstacles, will be treated in the next chapters.

Let $\mathbb{P}_n$ denote the space of bivariate polynomials of a degree less than or equal to n. Let us also consider the triangular mesh $\mathcal{T}_h$ for the triangular approximation Γ_h of Γ.

Definition 1.6.11 (The V_h finite-dimensional space)**.** *Let $V_h \subset H^{1/2}(\Gamma_h)$ be the finite-dimensional space*

$$V_h = \{v \subset C(\Gamma_h) : \textit{ for every triangle } t \in \mathcal{T}_h \, (v|_t \in \mathbb{P}_1)\}. \tag{1.109}$$

Definition 1.6.12 (A basis for V_h)**.** *Let us consider as basis for V_h the set*

$$\{\chi_i\}_{i=1}^{N_V} \text{ such that, for } i = 1...N_V \text{ we have } \chi_i(\boldsymbol{v}_j) = \begin{cases} 1 \text{ if } j = i, \\ 0 \text{ if } j \neq i. \end{cases} \tag{1.110}$$

Definition 1.6.13 (The W_h finite-dimensional space)**.** *Let $W_h \subset H^{-1/2}(\Gamma_h)$ be the space*

$$W_h = \left\{ w \subset L^2(\Gamma_h) : \text{ for every element } L \in \widetilde{\mathcal{T}}_h \left(w|_L \in \mathbb{P}_0 \right) \right\}. \tag{1.111}$$

Definition 1.6.14 (A basis for W_h)**.** *Let us consider as basis for W_h the set*

$$\{\kappa_i\}_{i=1}^{N_V} \text{ such that, for } i = 1...N_V \text{ we have } \kappa_i(\boldsymbol{x}) = \begin{cases} 1 \text{ if } \boldsymbol{x} \in L_i, \\ 0 \text{ if } \boldsymbol{x} \notin L_i, \end{cases} \tag{1.112}$$

where L_i is the element of $\widetilde{\mathcal{T}}_h$ associated with the vertex $\boldsymbol{v}_i$.

Definition 1.6.15 (Local mesh size associated with basis functions)**.** *For a basis function associated with a vertex $\boldsymbol{v}_i \in \mathcal{T}_h$, be it χ_i or κ_i, we will denote by $\hat{h}_i$ its local mesh size, defined as*

$$\hat{h}_i = \frac{1}{|T_{\boldsymbol{v}\to t}(\boldsymbol{v}_i)|} \sum_{t_l \in T_{\boldsymbol{v}\to t}(\boldsymbol{v}_i)} h_l, \tag{1.113}$$

the average of the cell size of the triangles making up its support.

Using the defined basis functions, a function $\mu_h \in V_h(\Gamma_h)$ can be determined by the set of coefficients $\{\mu_i^h\}_{i=1}^{N_V}$:

$$\mu_h(\boldsymbol{x}) = \sum_{i=1}^{N_V} \mu_i^h \chi_i(\boldsymbol{x}), \quad \text{for } \boldsymbol{x} \in \Gamma_h. \tag{1.114}$$

Likewise, a function $\lambda_h \in W_h(\Gamma_h)$ can be determined by the set of coefficients $\{\lambda_i^h\}_{i=1}^{N_V}$:

$$\lambda_h(\boldsymbol{x}) = \sum_{i=1}^{N_V} \lambda_i^h \kappa_i(\boldsymbol{x}), \quad \text{for } \boldsymbol{x} \in \Gamma_h. \tag{1.115}$$

We can use this decomposition to define finite-dimensional versions of the variational formulations established for the boundary integral equations associated with operators $\mathcal{S}^k$ and $\mathcal{N}^k$.

Definition 1.6.16 (Finite dimensional variational formulations)**.** *Let us define the following finite-dimensional variational formulation associated with the variational formulation (1.98), associated with the boundary integral equation for $\mathcal{S}^k$:*

$$\begin{cases} \text{Given } g_h \in V_h, \text{ find the set of coefficients } \{\lambda_i^h\}_{i=1}^{N_V} \text{ such that} \\ \\ \text{for } j = 1...N_V : \displaystyle\sum_{i=1}^{N_V} \lambda_i^h a_k^{ws}(\kappa_i, \kappa_j) = \langle g_h \, , \, \kappa_j \rangle_{\Gamma_h}. \end{cases} \tag{1.116}$$

Similarly, let us define the following finite-dimensional variational formulation associated with the variational formulation (1.98), associated with the boundary integral equation for $\mathcal{N}^k$:

$$\begin{cases} \text{Given } \varphi_h \in W_h, \text{ find the set of coefficients } \{\mu_i^h\}_{i=1}^{N_V} \text{ such that} \\ \\ \text{for } j = 1...N_V : \displaystyle\sum_{i=1}^{N_V} \mu_i^h a_k^{hs}(\chi_i, \chi_j) = \langle \varphi_h \, , \, \chi_j \rangle_{\Gamma_h}. \end{cases} \tag{1.117}$$

Slightly abusing notation, we have kept the notation a_k^{ws} and a_k^{hs} although they now refer to bilinear forms induced by operators $\mathcal{S}^k$ and $\mathcal{N}^k$ defined over the discretized surface Γ_h. Additionally, finite-variational formulation (1.117) has to be augmented with a parameters $\alpha \in \mathbb{R}^+$ when $k = 0$ to assure that the solution μ_h belongs to a subspace of $H_0^{1/2}(\Gamma_h)$:

$$\begin{cases} \text{Given } \varphi_h \in W_h, \text{ find the set of coefficients } \{\mu_i^h\}_{i=1}^{N_V} \text{ such that} \\ \\ \text{for } j = 1...N_V : \displaystyle\sum_{i=1}^{N_V} \mu_i^h a_0^{hs}(\chi_i, \chi_j) + \alpha \left\langle \chi_i \, , \, 1 \right\rangle_{\Gamma_h} \left\langle \chi_j \, , \, 1 \right\rangle_{\Gamma_h} = \left\langle \varphi_h \, , \, \chi_j \right\rangle_{\Gamma_h}. \end{cases} \tag{1.118}$$

1.6.3 Boundary element computations and Galerkin matrices

In this subsection we will define the way in which the Galerkin matrices associated with finite-dimensional variational formulations (1.116) and (1.117) are computed.

Definition 1.6.17 (Galerkin matrices associated with $\mathcal{S}^k$ and $\mathcal{N}^k$)**.** *Let us define the Galerkin matrices associated with boundary integral operators $\mathcal{S}^k$ and $\mathcal{N}^k$ on the conformal triangular approximation Γ_h for a surface Γ. We denote by N_V the number of vertices of the mesh $\mathcal{T}_h$ for Γ_h. We define $\boldsymbol{S}^h \in \mathbb{C}^{N_V \times N_V}$ as*

$$\boldsymbol{S}_k^h[i,j] = a_k^{ws}(\kappa_i, \kappa_j) = \left\langle \mathcal{S}^k \kappa_i \, , \, \kappa_j \right\rangle_{\Gamma_h}, \quad \text{for } i,j = 1...N_V. \tag{1.119}$$

We define $\boldsymbol{N}_k^h \in \mathbb{C}^{N_V \times N_V}$ as

$$\boldsymbol{N}_k^h[i,j] = a_k^{hs}(\chi_i, \chi_j) = \left\langle -\mathcal{N}^k \chi_i \, , \, \chi_j \right\rangle_{\Gamma_h}, \quad \text{for } i,j = 1...N_V. \tag{1.120}$$

In the case of the Laplace problem, when $k = 0$ matrix $\boldsymbol{N}_k^h$ has to be augmented, as indicated in (1.118) to account for the kernel space of operator $\mathcal{N}^0$. In that case, we define $\boldsymbol{N}_0^h \in \mathbb{C}^{N_V \times N_V}$ as

$$\boldsymbol{N}_0^h[i,j] = a_0^{hs}(\chi_i, \chi_j) = \left\langle -\mathcal{N}^0 \chi_i \, , \, \chi_j \right\rangle_{\Gamma_h} + \alpha \left\langle \chi_i \, , \, 1 \right\rangle_{\Gamma_h} \left\langle \chi_j \, , \, 1 \right\rangle_{\Gamma_h}, \quad \text{for } i,j = 1...N_V. \tag{1.121}$$

with a parameter $\alpha \in \mathbb{R}^+$.

These Galerkin matrices allow us to pose linear systems to solve the finite-dimensional variational formulations for the integral equations that allow us to find solutions to Laplace and Helmholtz problems, on the exterior of a Lipschitz-regular obstacle, with Dirichlet or Neumann boundary conditions. Despite the advantages that this approach brings to the treatment of such problems, most particularly in unbounded domains, we will see that it comes at a cost. In the next section we will explain and quantify this cost. It will become evident that the challenges posed by the boundary integral equation approach must be addressed, which will end this introductory chapter by motivating the work undertaken in the subsequent ones.

1.7 Memory complexity, algorithmic complexity and accuracy

The main advantage of the approach outlined in this chapter, that of the boundary integral equations and the boundary element method, is that they can tackle partial differential equation problems posed on unbounded domains in a more natural way. They also need less degrees of freedom, in comparison to domain methods, when used to solve cases with small boundary surface to propagation volume ratios. However, other problems inherent to the boundary integral equation and boundary element methods are introduced. In this section we will discuss and quantify these disadvantages.

Through this section we will consider the case of a Lipschitz-regular obstacle Ω, of boundary $\partial\Omega = \Gamma$ that has been discretized in a mesh Γ_h. The number of basis functions spanning the discrete boundary element spaces used, i.e. the number of degrees of freedom of the linear equation to be solved, will be denoted as N_{dof}. We will consider the case of a numerical simulation where the maximum frequency of the propagating wave is f_{max}, in a linear homogeneous medium with wave propagation velocity v. Three quantities of a given mesh are of interest when determining the size of the linear system, the number of unknowns N_{dof}: the number of triangles N_T, the number of vertices N_V and the number of edges N_E. The presented variational formulations will give rise to a linear system with Galerkin matrix $\boldsymbol{A}$ and right-hand side vector $\boldsymbol{b}$, thus giving to consideration the system $\boldsymbol{Ax} = \boldsymbol{b}$.

The approach presented is intended for single frequency problems, but the concept of a maximum frequency f_{max} comes into consideration when a Fourier analysis is used for solving transient waves using several frequencies on a frequency range.

1.7.1 Wave frequency and mesh refinement

The relation between maximum wave frequency and mesh refinement comes from the necessity to accurately represent the oscillatory behavior of the computed solution of the traces defined on surface Γ_h. Depending on the application, different criteria are used.

If f_{max} is the maximum wave frequency and v is the wave velocity, the shortest wavelength λ_{min} in the simulated scenario will be

$$\lambda_{min} = \frac{v}{f_{max}}. \tag{1.122}$$

Depending on the application (simulation of near-field or far-field phenomena, for example) a number n_λ of basis functions, typically between 5 and 10, must be assured by each wavelength [64, Section 6.2.1]. This means that the largest edge h_{max} on the mesh must comply with

$$h_{max} \leq \frac{\lambda_{min}}{n_\lambda} = \frac{v}{n_\lambda f_{max}}. \tag{1.123}$$

In the limit case of compliance with the basis-per-wavelength criterion ($h_{max} = v/(n_\lambda f_{max})$), and if the mesh is regular in the sense of Definition 1.6.9 ($h_{max} \leq C_G h_{min}$), the following inequality holds:

$$h_{max} = \frac{c}{n_\lambda f_{max}} \leq C_G h_{min}. \tag{1.124}$$

The number N_T of triangles of mesh Γ_h is bounded by

$$N_T \leq \frac{|\Gamma_h|}{h_{min}^2/2}, \tag{1.125}$$

where $|\Gamma_h|$ is the area of the discretized mesh surface Γ_h. Again in the limit case of compliance with the basis-per-wavelength criterion ($h_{max} = v/(n_\lambda f_{max})$), and if the mesh is regular in the

sense of Definition 1.6.9, the number of triangles can be further bounded by

$$N_T \leq \frac{2C_G^2 \left|\Gamma_h\right| n_\lambda^2}{v^2} f_{max}^2. \tag{1.126}$$

If the mesh is conformal, counting three edges for each triangle gives a global counting of edges where each one has been taken into consideration twice, thus relating the number triangles N_T and the number of edges N_E like $N_E = 3/2\, N_T$. If Γ_h is non-intersecting polyhedral mesh in $\mathbb{R}^3$, the Euler Characteristic applies, i.e.,

$$N_V - N_E + N_T = 2, \tag{1.127}$$

thus providing the number of nodes of the mesh:

$$N_V = \frac{1}{2} N_T + 2. \tag{1.128}$$

These two results provide us with limits to the number of edges and nodes for a frequency f_{max}:

$$N_E \leq \frac{C_G^2 \left|\Gamma_h\right| n_\lambda^2}{3v^2} f_{max}^2 \quad \text{and} \quad N_E \leq \frac{C_G^2 \left|\Gamma_h\right| n_\lambda^2}{v^2} f_{max}^2 + 2. \tag{1.129}$$

Since the number of basis functions N_{dof} will be a combination of multiples of N_V, N_E and/or N_T, the size of the linear system can always be limited in order by f_{max}^2.

1.7.2 Memory complexity

The Galerkin matrices produced by the boundary element method are symmetric and can be stored by saving the elements in, .e.g., the upper triangular part of the matrix. If the linear system has N_{dof} degrees of freedom and the computations use a data type that requires an amount m_t of memory to be stored, then the amount of memory N_{mem} required to store the matrix is

$$N_{mem} = m_t \frac{N_{dof}(N_{dof}+1)}{2}. \tag{1.130}$$

1.7.3 Algorithmic complexity

The algorithmic complexity of the resolution of the linear system is the amount of individual number operations N_{solve} required to solve it. Using iterative methods, the algorithmic complexity is then the number of operations involved in a matrix-vector multiplication $N_{M\times v}$ times the number of iterations N_{item} required by the iterative solver.

The number of individual number operations $N_{M\times v}$ involved in the multiplication of a $N_{dof} \times N_{dof}$ matrix by a N_{dof} vector is N_{dof}^2 multiplications and $(N_{dof}-1)^2$ sums, adding up to $N_{M\times v} = 2N_{dof}^2 - 2N_{dof} + 1$ individual operations.

The number of iterations N_{iter} required by an iterative method depends on the condition number of the matrix of the linear system; it grows with it.

Definition 1.7.1 (Condition number of a matrix)**.** *The condition number a matrix is a measure of how much can the result of a multiplication by a vector change, for a small changes in this vector. It depends on the norm used to measure this change. For a matrix $\boldsymbol{A} \in \mathbb{C}^{N\times N}$, the 2-norm condition number is defined as*

$$cond_2\left(\boldsymbol{A}\right) = \frac{\sigma_{max}(\boldsymbol{A})}{\sigma_{min}(\boldsymbol{A})}, \tag{1.131}$$

where $\sigma_{min}(\boldsymbol{A})$ and $\sigma_{max}(\boldsymbol{A})$ are the minimal and maximal singular values of $\boldsymbol{A}$.

The following theorem about the conditioning of the Galerkin matrices arising from the boundary element method will present us with a challenge.

Theorem 1.7.1 (Ill-conditioning of BEM matrices [57, Lemmas 4.5.1 & 4.5.2])**.** *Let Γ_h be a polygonal curve in $\mathbb{R}^2$ or polyhedral surface in $\mathbb{R}^3$, and $\mathcal{T}_h$ a conformal, regular mesh for it. The Galerkin matrices $\boldsymbol{S}_h^k$ and $\boldsymbol{N}_h^k$, associated with the boundary integral operators $\mathcal{S}^k$ and $\mathcal{N}^k$, are ill-conditioned in the sense that there exists a constant C_{cond} such that*

$$cond_2\left(\boldsymbol{S}_h^k\right) \leq C_{cond}\, h_{min}^{-1} \quad \text{and} \quad cond_2\left(\boldsymbol{N}_h^k\right) \leq C_{cond}\, h_{min}^{-1}. \tag{1.132}$$

It is known that for the conjugated gradient method, for example, to reach a relative reduction of ε, there is a constant $C_{cg}(\varepsilon)$ such that the number of iterations required is $N_{iter} = C_{cg}(\varepsilon)\sqrt{\mathrm{cond}_2(\boldsymbol{A})}$ [24, Theorem 11.3.3]. For other iterative methods for the resolution of the associated linear system, the dependency of the number of iterations on the condition number of system matrix $\boldsymbol{A}$ is harder to determine, although it grows with it as the mesh is refined. Some common iterative solvers used linear system arising from the boundary element method are the GMRES and the BiCGSTAB methods [43, 45, 66].

1.7.4 Accuracy

When computing the solution of a linear system $\boldsymbol{A}\boldsymbol{x} = \boldsymbol{b}$, the relative error of the computed solution will depend on the relative error in the numerical computation of $\boldsymbol{A}$ and $\boldsymbol{b}$, and the condition number of $\boldsymbol{A}$ as stated in the following theorem.

Theorem 1.7.2 (Accuracy lost due to ill-conditioning [24, Section 2.6.2])**.** *When solving the linear system $\boldsymbol{A}\boldsymbol{x} = \boldsymbol{b}$ but with a perturbed matrix and right hand vector, i.e.,*

$$\tilde{\boldsymbol{A}} = \boldsymbol{A} + \delta\boldsymbol{A} \quad \text{and} \quad \tilde{\boldsymbol{b}} = \boldsymbol{b} + \delta\boldsymbol{b}, \tag{1.133}$$

the relative error of the solution depends on the conditioning of matrix $\boldsymbol{A}$ and the perturbations as:

$$\frac{\|\boldsymbol{x} - \tilde{\boldsymbol{x}}\|}{\|\boldsymbol{x}\|} \leq \frac{cond_2(\boldsymbol{A})}{1 - cond_2(\boldsymbol{A})\frac{\|\delta\boldsymbol{A}\|}{\|\boldsymbol{A}\|}} \left(\frac{\|\delta\boldsymbol{A}\|}{\|\boldsymbol{A}\|} + \frac{\|\delta\boldsymbol{b}\|}{\|\boldsymbol{b}\|}\right), \tag{1.134}$$

where $\tilde{\boldsymbol{x}}$ is the solution of the perturbed system $\tilde{\boldsymbol{A}}\tilde{\boldsymbol{x}} = \tilde{\boldsymbol{b}}$.

1.7.5 Overall complexity and accuracy

The overall situation concerning the difficulties inherent to the boundary integral equation and boundary element method approach can be summarized in the following table, Table 1.1, using asymptotic notation (Big O, or Bachmann-Landau notation).

Table 1.1: Summary of the computational cost and relations between different quantities determining it, expressed in terms of the maximum frequency f_{max}, number of degrees of freedom N_{dof} and minimum mesh cell size h.

Computational Cost	f_{max}	N_{dof}	h
N_{dof}	$\mathcal{O}\left(f_{max}^2\right)$	1	$\mathcal{O}\left(h^{-2}\right)$
N_{mem}	$\mathcal{O}\left(f_{max}^4\right)$	$\mathcal{O}\left(N_{dof}^2\right)$	$\mathcal{O}\left(h^{-4}\right)$
$N_{M\times v}$	$\mathcal{O}\left(f_{max}^4\right)$	$\mathcal{O}\left(N_{dof}^2\right)$	$\mathcal{O}\left(h^{-4}\right)$

The situation depicted in the previous table stresses the challenges that the integral method introduces. Unaddressed, these difficulties greatly limit the applicability of this approach,

especially to endeavors that require the solution of multiple direct problems (automatic control, automated design, some inversion problems, etc.). Numerical accuracy will also prove to be a challenging point in the application of the integral approach, as the example from the next section will illustrate.

1.7.6 An illustrative example

In this subsection we will shortly illustrate the difficulties quantified in this section by means of an example. Let us consider the problem of computing the acoustic scattering by a rigid ball of one meter in radius in an unbounded scenario at normal propagation conditions: $v = 343.2$m/s at 1 atmosphere of pressure and 20ºC of temperature. The following figures will describe the evolution of the main quantities describing the complexity of the numerical problem for different required maximum frequencies within the audible range.

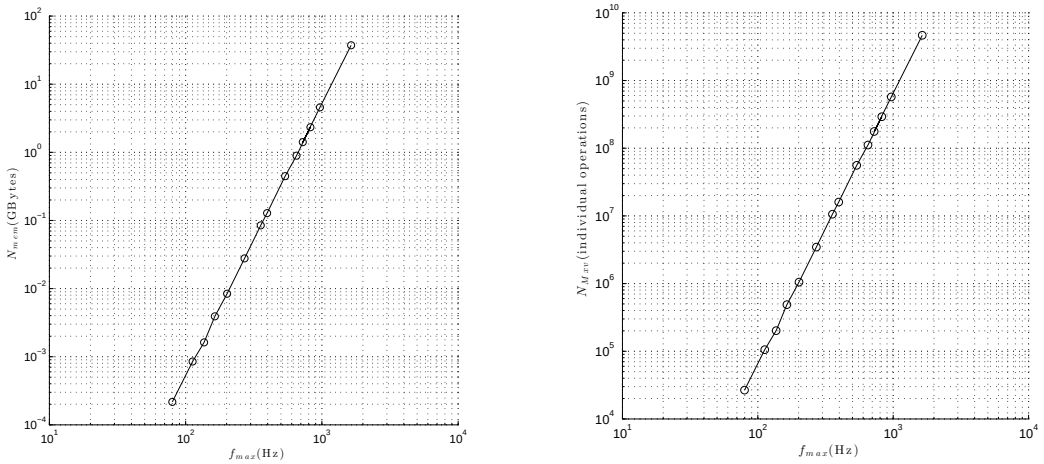

Figure 1.4: Evolution of the computational complexity with the rise of the required maximum frequency for the example problem: memory complexity N_{mem} (left) and algorithmic complexity $N_{M\times v}$ (right) versus maximum required frequency f_{max}.

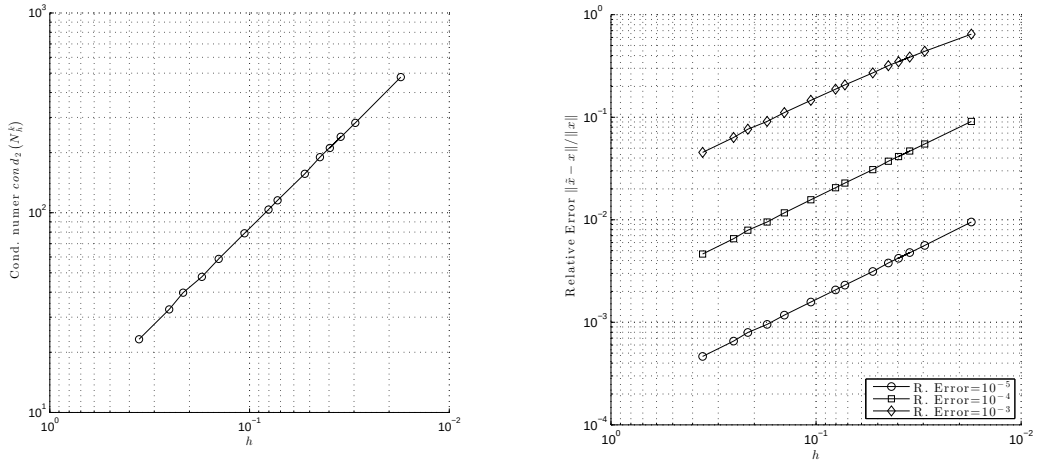

Figure 1.5: Evolution of the conditioning and the relative error of the linear system with the refinement of the mesh used for the example problem: condition number $\text{cond}_2(\boldsymbol{A})$ (left) and relative error $\|\boldsymbol{x}-\tilde{\boldsymbol{x}}\|/\|\boldsymbol{x}\|$ (right) versus the discretization parameters h considering different errors in the computation of the system matrix and right-hand side vector.

Algorithmic complexity $N_{M\times v}$ and memory complexity N_{mem} can be managed with acceleration/compression techniques, such as the Fast Multipoles Method [25, 26, 52, 55], the Panel Clustering Method [31,32,56,57], and the Hierarchical Matrix Method [9,28–30] with Adaptive Cross Approximations [5, 8, 10, 65]. The Hierarchical Matrix and ACA approach is very flexible, being able to tackle the problem for multiple integral kernels with the same computational implementation, and allows for reduced complexity:

$$N_{mem} = \mathcal{O}\left(N_{dof}\log N_{dof}\right) = \mathcal{O}\left(f_{max}^2 \log f_{max}\right), \tag{1.135}$$

$$N_{N\times v} = \mathcal{O}\left(N_{dof}\log N_{dof}\right) = \mathcal{O}\left(f_{max}^2 \log f_{max}\right). \tag{1.136}$$

However, conditioning and thus N_{iter} remains a problem, and thus, for the acceleration/compression given as example we still could encounter an elevated number of iterations and undesired inaccuracies.

Although it still allows for an increase in the frequency of simulation for a fixed computational capacity, this in turn stresses the importance of controlling the error due to ill-conditioning through preconditioning.

The subject of preconditioning will be treated in the next chapters. When the obstacle has a Lipschitz-regular surface there are robust and well-known methods. This isn't the situation for non-Lipschitz objects, for which we will propose a novel technique.

Chapter 2

Operator Preconditioning and Screen Obstacles

In this chapter we will develop a preconditioning strategy for the linear systems arising from Galerkin discretizations of boundary integral equations related to the Laplace and Helmholtz problems for a screen obstacle presented in Subsection 1.3.3. This present chapter can be roughly divided into two parts: 1) Sections 2.1, 2.2, 2.3 and 2.4, and 2) Sections 2.5, 2.6 and 2.7.

In the first part we will describe the main theoretical tool for the devising of preconditioning strategies in general, and for screen obstacles and Lipschitz-regular obstacles in particular. We will show how this tool immediately provides a viable preconditioning method for Lipschitz-regular domains and we will point out where it fails when applied to screens. Then, a brief explanation will be provided on previous results adapting this strategy for a curve screen embedded in $\mathbb{R}^2$. A geometrical and a functional framework will then be provided in the case of a canonical surface screen embedded in $\mathbb{R}^3$, the unit disk, which will be the main and starting case for further developments beyond this chapter.

In the second part we will establish the existence of operators that are the inverses to the boundary integral operators associated with the boundary integral equations that are used to solve the Dirichlet and Neumann problems. It will be also shown that their explicit form is not easily attainable, thus preventing their immediate use in building preconditioning methods using the boundary element method. We will develop tools to build basis functions for the functional trace spaces involved. This will lead to a rewriting, in the form of series expansions, of the involved integral operators, which in turn will allow for series representations of their inverses, whose existence will have been already proven. A spectral method for the resolution to the boundary integral equations will also be developed. Using the series expansions forms in a spectral method will illustrate, in a straightforward manner, how the devised preconditioning strategy yields an optimal preconditioning method and optimally preconditioned matrices, despite not being suited for the more versatile boundary element method. These results will pave the way for the introduction of new boundary integral operators, resulting from modifications made to the ones proposed in this chapter. These new and modified integral operators, to be developed in the next chapter, will have explicit variational forms that will be suited for use in boundary element methods.

2.1 Operator preconditioning

When solving a linear system $\boldsymbol{A}\boldsymbol{x} = \boldsymbol{b}$, where the matrix $\boldsymbol{A}$ is ill-conditioned, i.e., where the value $\text{cond}_2(\boldsymbol{A})$ is high (in a sense given by Theorem 1.7.2 according to the context), a preconditioning method must be used to tackle the problems that come with ill-conditioning (increased number of iterations required by an iterative solver and poor numerical accuracy). A preconditioning method provides a matrix $\boldsymbol{M}$ such that the matrix $\boldsymbol{M}\boldsymbol{A}$ has a much lower condition number and thus the linear system $\boldsymbol{M}\boldsymbol{A}\boldsymbol{x} = \boldsymbol{M}\boldsymbol{b}$ does not suffer from the aforementioned problems.

There are different strategies based on different rationales that deliver a wide gamut of preconditioning methods with different performances (a good collection of them can be found in [15]). In the context of Galerkin matrices arising from variational formulations such as the ones for the boundary integral equations described in the previous chapter, it was seen in Section 1.7 that conditioning worsens with mesh refinement (and thus higher frequencies in numerical wave simulations). The following theorem will suggest a strategy suitable for that context, and capable of providing optimal preconditioning.

Theorem 2.1.1 (Operator preconditioning [16], [35])**.** *Let V and W be reflexive Banach spaces. Let $a \in L(V \times V, \mathbb{C})$, $b \in L(W \times W, \mathbb{C})$ and $d \in L(V \times W, \mathbb{C})$ be continuous sesquilinear forms, with norms $\|a\|$, $\|b\|$, and $\|d\|$ respectively. Finally, let $V_h = \text{span}\left(\{\chi_i\}_{i=1}^N\right) \subset V$ and $W_h = \text{span}\left(\{\kappa_i\}_{i=1}^N\right) \subset W$ be finite-dimensional subspaces of the same dimension on which the following inf-sup conditions are fulfilled:*

$$\forall u_h \in V_h \sup_{v_h \in V_h} \frac{|a(u_h, v_h)|}{\|v_h\|_V} \geq c_a \|u_h\|_V, \tag{2.1}$$

$$\forall q_h \in W_h \sup_{w_h \in W_h} \frac{|b(q_h, w_h)|}{\|w_h\|_W} \geq c_b \|q_h\|_W, \tag{2.2}$$

$$\forall v_h \in V_h \sup_{w_h \in W_h} \frac{|d(v_h, w_h)|}{\|w_h\|_W} \geq c_d \|v_h\|_V. \tag{2.3}$$

Let us define the following Galerkin matrices: $\boldsymbol{A}[i,j] = a(\chi_i, \chi_j)$, $\boldsymbol{B}[i,j] = b(\kappa_i, \kappa_j)$, and $\boldsymbol{D}[i,j] = d(\chi_i, \kappa_j)$, and let us define the preconditioning matrix $\boldsymbol{M} = \boldsymbol{D}^{-1}\boldsymbol{B}\boldsymbol{D}^{-H}$. The spectral condition number of the preconditioned matrix $\boldsymbol{M}\boldsymbol{A}$ has the following bound:

$$cond_2\left(\boldsymbol{M}\boldsymbol{A}\right) \leq \frac{\|a\|\|b\|\|d\|^2}{c_a c_b c_d^2}, \tag{2.4}$$

where $\boldsymbol{D}^{-H}$ is the inverse of the conjugate transpose of matrix $\boldsymbol{D}$.

Remark 2.1.1 (Optimality of preconditioning)**.** *The bound from equation (2.4) is independent of the choice of bases for the spaces involved. In particular, the bound does not depend on the dimension of the chosen finite-dimensional subspaces.*

A general situation is attempting to solve a functional equation $\mathcal{P}v = w$ posed over a domain Ω, with $\mathcal{P} : V \to W$, when one space is the dual of the other. We take interest in the bilinear form $a(v, v^t) = \left\langle \mathcal{P}v, v^t \right\rangle_\Omega$ for the variational formulation, for functions $v, v^t \in V$. If $V_h = \text{span}\left(\{\chi_i\}_{i=1}^N\right) \subset V$ is an N-dimensional discretization of the space for the variational formulation, the problem can be solved via a linear system of equations $\boldsymbol{A}\boldsymbol{x} = \boldsymbol{b}$, with $\boldsymbol{A}[i,j] = a(\chi_i, \chi_j)$. Theorem 2.1.1 is a tool that allows us to formulate an optimal preconditioning strategy, as it will be stated in the following definition.

Definition 2.1.1 (Optimal preconditioning strategy)**.** *For a Galerkin matrix $\boldsymbol{A}$ arising from the variational formulation associated with the functional equation $\mathcal{P}v = w$ with $\mathcal{P} : V \to W$ (with V being the dual of W or vice versa), with variational formulation $a(v, v^t) = \left\langle \mathcal{P}v, v^t \right\rangle_\Omega$ using $V_h = \text{span}\left(\{\chi_i\}_{i=1}^N\right)$, an optimal preconditioning strategy is:*

1. *Find $\mathcal{Q} : W \to V$ that will induce a coercive bilinear form $b(w, w^t) = \langle \mathcal{Q}w, w^t \rangle_\Omega$, for $w, w^t \in W$.*

2. *Take the bilinear form d to be the duality pairing between V and W and find a N-dimensional discretization of the space W, $W_h = span\left(\{\kappa_i\}_{i=1}^N\right) \subset W$, such that it also renders the duality product $d(\chi, \kappa) = \langle \chi, \kappa \rangle_\Omega$ coercive for any $\chi \in V_h$ and $\kappa \in W_h$.*

3. *Build matrices $\boldsymbol{B}$ and $\boldsymbol{D}$ from bilinear forms b and d, and assemble $\boldsymbol{M} = \boldsymbol{D}^{-1}\boldsymbol{B}\boldsymbol{D}^{-H}$ as stated in the theorem.*

4. *Precondition the linear system yielding $\boldsymbol{M}\boldsymbol{A}\boldsymbol{x} = \boldsymbol{M}\boldsymbol{b}$.*

This particular preconditioning strategy is one among many other possibilities within the scope of Theorem 2.4.

Remark 2.1.2 (Candidates for $\mathcal{Q}$)**.** *Different problems naturally provide operators that will fulfill the role of operator $\mathcal{Q}$ as stated in the optimal preconditioning strategy. In the context of boundary integral equations linked to wave propagation phenomena, the weakly singular, and the hypersingular boundary integral operators fit the roles of $\mathcal{P}$ and $\mathcal{Q}$ if the obstacle is Lipschitz-regular. More generally, given an operator $\mathcal{P}$, an inverse $\mathcal{Q} = \mathcal{P}^{-1}$ (if available), is a useful choice.*

Remark 2.1.3 (Complexity of inversion)**.** *The computation of matrix $\boldsymbol{M}$ involves the inversion of matrix $\boldsymbol{D}$, for which the a priori algorithmic complexity is $\mathcal{O}\left(N^3\right)$. This consideration becomes especially relevant when the purpose of the preconditioning is the reduction of the overall algorithmic complexity of the resolution to a linear system. However, for many spectral and boundary element discretizations, using appropriate bases' numbering techniques can produce sparse and banded $\boldsymbol{D}$ matrices that are much easier to invert.*

2.2 Preconditioning for Lipschitz-regular obstacles

In this section we will show how the optimal preconditioning strategy can be used to yield methods that will achieve optimal preconditioning of the linear system associated with an integral equation in the context of a Helmholtz or Dirichlet problem for a Lipschitz-regular obstacle. We will see that when the obstacle is Lipschitz-regular, the second operator needed for the strategy is naturally available. We will also see that the preconditioning matrix built for the Laplace case, is also an optimal preconditioner for the Helmholtz case.

Let us begin by establishing the following result.

Proposition 2.2.1 (Stability of the pairing of the bases of finite-dimensional spaces [61, Section 2.2])**.** *Let Γ_h be conformal triangular approximation of a closed surface Γ and let $\mathcal{T}_h$ and $\widetilde{\mathcal{T}}_h$ be primary and dual triangular meshes for it. Let us consider the sets of basis functions $\{\chi_i\}_{i=1}^{N_T}$ and $\{\kappa_i\}_{i=1}^{N_T}$ as defined in Definition 1.6.12 and Definition 1.6.14. If we assume that $\mathcal{T}_h$ is locally quasi-uniform, and that for every triangle $t_l \in \mathcal{T}_h$ there is a constant C such that the associated local mesh sizes for the functions associated with its vertices (refer to Definition 1.6.15) satisfy*

$$\frac{51}{7} - \left(\sum_{\boldsymbol{v}_i \in T_{t\to\boldsymbol{v}}(t_l)} \hat{h}_i \sum_{\boldsymbol{v}_i \in T_{t\to\boldsymbol{v}}(t_l)} \frac{1}{\hat{h}_i} \right)^{1/2} \geq C > 0, \tag{2.5}$$

then, the following inf-sup condition is satisfied:

$$\sup_{j=1\ldots N_V} \frac{\left| \langle \chi_i \, , \, \kappa_j \rangle_{\Gamma_h} \right|}{\|\kappa_j\|_{H^{-1/2}(\Gamma_h)}} \geq c_d \, \|\chi_i\|_{H^{1/2}(\Gamma_h)} \, , \qquad \textit{for } i = 1\ldots N_V. \tag{2.6}$$

Remark 2.2.1 (The discretization from Subsection 1.6.2 satisfies conditions of Theorem 2.1.1)**.** *Condition (2.5) is easy to meet and, as we shall see indirectly in the next subsection, is met by the discretization described in Subsection 1.6.2. The consequence of the previous proposition is estimate (2.6), which allows to satisfy condition (2.3) from Theorem 2.1.1*

2.2.1 Laplace problem

For a Lipschitz-regular obstacle Ω of boundary $\Gamma = \partial\Omega$ let us consider a conformal triangular approximation Γ_h. It was shown in Theorem 1.5.3 that operator $\mathcal{N}^0 : H^{1/2}(\Gamma_h)/\mathbb{R} \to H^{-1/2}(\Gamma_h)$ defines an isomorphism, and that it induces coercive bilinear form in $H^{1/2}(\Gamma_h)/\mathbb{R}$. Similarly, it was shown in Theorem 1.5.2 that operator $\mathcal{S}^0 : H^{-1/2}(\Gamma_h) \to H^{1/2}(\Gamma_h)$ defines an isomorphism and that it induces a coercive bilinear form in $H^{-1/2}(\Gamma_h)$.

Additionally, it was shown in Subsection 1.2.3 that spaces $H^{1/2}(\Gamma_h)$ and $H^{-1/2}(\Gamma_h)$ are dual to each other if the surface is Lipschitz-regular, and that they can be discretized into N-dimensional spaces V_h and W_h using $\mathbb{P}_0$ Lagrange bases $\{\kappa_i\}_{i=1}^N$ and $\mathbb{P}_1$ bases $\{\chi_i\}_{i=1}^N$. Furthermore, it was shown in Proposition 2.2.1 that their basis functions comply with stability estimates specified in (2.3) from Theorem 2.1.1 if the bilinear form d is taken to be the duality product between $H^{1/2}(\Gamma_h)$ and $H^{1/2}(\Gamma_h)$.

Being in compliance with the hypotheses of Theorem 2.1.1, we follow the optimal preconditioning strategy from Definition 2.1.1 and consider the following matrices to perform a numerical experiment in the case of a spherical obstacle $\Omega = \{\boldsymbol{x} \in \mathbb{R}^3 : \|\boldsymbol{x}\| < 1\}$ with surface $\Gamma = \{\boldsymbol{x} \in \mathbb{R}^3 : \|\boldsymbol{x}\| = 1\}$ in $\mathbb{R}^3$, which we will mesh Γ into a triangular mesh Γ_h for a particular value of h as shown in Figure 2.1. We consider the following Galerkin matrices (cf. Definition 1.6.17):

$$\boldsymbol{A}_{S^0}[i,j] = \langle \mathcal{S}^0 \kappa_i \, , \, \kappa_j \rangle_{\Gamma_h}, \quad \boldsymbol{B}_{N^0}[i,j] = \langle \mathcal{N}^0 \chi_i \, , \, \chi_j \rangle_{\Gamma_h} + \alpha \langle \chi_i \, , \, 1 \rangle_{\Gamma_h} \langle \chi_j \, , \, 1 \rangle_{\Gamma_h} \, , \quad \text{for } \alpha \in \mathbb{R}^+, \tag{2.7}$$

and

$$\boldsymbol{D}[i,j] = \langle \chi_i \, , \, \kappa_j \rangle_{\Gamma_h} \, . \tag{2.8}$$

Using these Galerkin matrices, let us assemble the following preconditioning matrices as indicated by the theorem:

$$\boldsymbol{M}_{S^0} = \boldsymbol{D}^{-1} \boldsymbol{A}_{S^0} \boldsymbol{D}^{-H}, \quad \text{and} \quad \boldsymbol{M}_{N^0} = \boldsymbol{D}^{-1} \boldsymbol{B}_{N^0} \boldsymbol{D}^{-H}. \tag{2.9}$$

In the next figure, Figure 2.1, we show the evolution of the condition number for the Galerkin matrices $\boldsymbol{A}_{S^0}$ and $\boldsymbol{B}_{N^0}$ as a function of the discretization parameter together with the condition number for the preconditioned matrices $\boldsymbol{M}_{N^0}\boldsymbol{A}_{S^0}$ and $\boldsymbol{M}_{S^0}\boldsymbol{B}_{N^0}$.

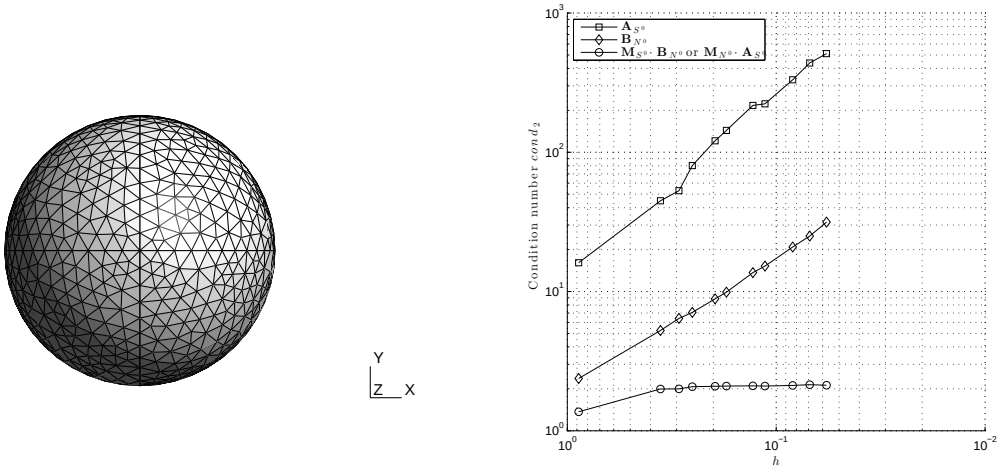

Figure 2.1: A triangular mesh discretization Γ_h of the spherical surface Γ taken as an example for a given discretization parameter h (left), and the evolution of the condition number of matrices $\boldsymbol{A}_{S^0}$, $\boldsymbol{B}_{N^0}$, and $\boldsymbol{M}_{N^0}\boldsymbol{A}_{S^0}$ (or $\boldsymbol{M}_{S^0}\boldsymbol{B}_{N^0}$) for diminishing values of h.

It is remarkable that, as predicted by Theorem 1.7.1, the condition number is roughly $\mathcal{O}\left(h^{-1}\right)$ for the unpreconditioned matrices, whereas the preconditioned matrices attain optimal, absolutely bounded, condition numbers.

2.2.2 Helmholtz problem

The Helmholtz case can be viewed as a perturbed case of the Laplace problem. We will use this fact to show that preconditioners built for the Laplace problem can also precondition the Galerkin matrices arising in the Helmholtz problem. Let us first note that the Green's function for the Helmholtz problem can be expressed as the integral kernel for the Laplace case plus a more regular function. Indeed, for $\boldsymbol{x}, \boldsymbol{y} \in \Gamma$:

$$G^k(\boldsymbol{x}, \boldsymbol{y}) = G^0(\boldsymbol{x}, \boldsymbol{y}) + R^k(\boldsymbol{x}, \boldsymbol{y}), \tag{2.10}$$

with

$$R^k(\boldsymbol{x}, \boldsymbol{y}) = \frac{e^{\mathrm{i}k\|\boldsymbol{x}-\boldsymbol{y}\|} - 1}{4\pi \, \|\boldsymbol{x} - \boldsymbol{y}\|}. \tag{2.11}$$

Thus, the weakly singular boundary integral operator can be written as the sum of two operators,

$$\mathcal{S}^k = \mathcal{S}^0 + \mathcal{P}^k, \tag{2.12}$$

with $\mathcal{P}^k$ being a convolution operator with kernel R^k, and thus a compact operator relative to $\mathcal{S}^0$ [57, Lemma 3.9.8]. Then, the bilinear form associated with $\mathcal{S}^k$ will be a compact perturbation of the one induced by $\mathcal{S}^0$, which will not affect the preconditioning strategy [36, Section 2.4].

Similarly, we know from Theorem 1.5.3 that the bilinear form induced by $\mathcal{N}^k$ can be rewritten using $\mathcal{S}^k$ as

$$\left\langle -\mathcal{N}^k u, v \right\rangle_{\Gamma_h} = \left\langle \mathcal{S}^k \overrightarrow{\operatorname{curl}}_{\Gamma_h} u, \overrightarrow{\operatorname{curl}}_{\Gamma_h} v \right\rangle_{\Gamma_h}, \tag{2.13}$$

which, by the same argument, can be written as a compact perturbation of the bilinear form associated with $\mathcal{N}^0$:

$$\left\langle -\mathcal{N}^k u, v \right\rangle_{\Gamma_h} = \left\langle \mathcal{S}^0 \overrightarrow{\operatorname{curl}}_{\Gamma_h} u, \overrightarrow{\operatorname{curl}}_{\Gamma_h} v \right\rangle_{\Gamma_h} + \left\langle \mathcal{P}^k \overrightarrow{\operatorname{curl}}_{\Gamma_h} u, \overrightarrow{\operatorname{curl}}_{\Gamma_h} v \right\rangle_{\Gamma_h}. \tag{2.14}$$

As before, the bilinear form induced by $\mathcal{N}^k$ is then a compact perturbation of the bilinear form induced by $\mathcal{N}^0$.

These results indicate that the preconditioning matrices $\boldsymbol{M}_{S^0}$ and $\boldsymbol{M}_{N^0}$ from the previous subsection can also be used to precondition the Galerkin matrices arising in the case of the Helmholtz problem. In what follows, we will put this idea to the test through a numerical example.

Let us consider the following two Galerkin matrices arising in the case of the Helmholtz problem:

$$\boldsymbol{A}_{S^k}[i,j] = \left\langle \mathcal{S}^k \kappa_i \, , \, \kappa_j \right\rangle_{\Gamma_h}, \quad \text{and} \quad \boldsymbol{B}_{N^k}[i,j] = \left\langle \mathcal{N}^k \chi_i \, , \, \chi_j \right\rangle_{\Gamma_h}. \tag{2.15}$$

Let us also take the previously considered preconditioning matrices built using the bilinear forms associated with operators $\mathcal{S}^0$ and $\mathcal{N}^0$. Figure 2.2 shows the condition number of the Galerkin matrices associated with the Helmholtz problem for, e.g., a wavenumber $k = 0.3$ and its evolution with diminishing discretization parameter h.

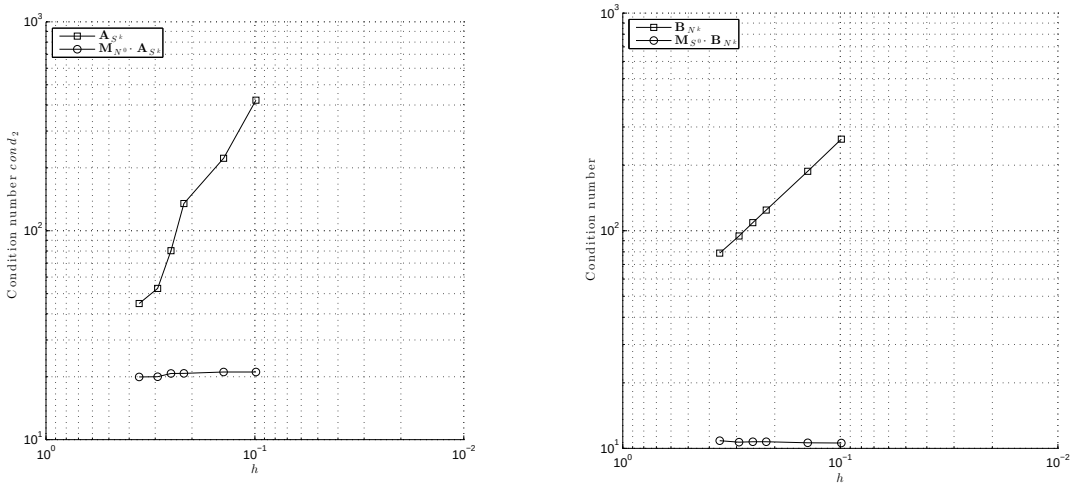

Figure 2.2: Evolution of the condition number of the Galerkin matrix for the Dirichlet Helmholtz problem $\boldsymbol{A}_{S^k}$ with and without preconditioning using the Neumann Galerkin matrix $\boldsymbol{M}_{N^0}$ (left). Evolution of the condition number of the Galerkin matrix for the Neumann Helmholtz problem $\boldsymbol{B}_{N^k}$ with and without preconditioning using the Dirichlet Galerkin matrix $\boldsymbol{M}_{S^0}$ (left).

Remark 2.2.2 (Optimality of the preconditioning after a transient)**.** *Figure 2.2 shows optimal preconditioning after an initial transient region due to the misrepresentation of the wave-like characteristics of the trace functions when using large cells in comparison to the wavelength.*

Given that the Laplace Galerkin matrices are enough to precondition the Helmholtz case we will drop the consideration for the Helmholtz case, and we will retake it at the end of this chapter when we test the developed preconditioning method for wave propagation phenomena. Consistently, we will change the notation to ease the exposition with focus on the Laplace case.

Notation 2.2.1 (Weakly singular and hypersingular kernel notation)**.** *In what follows, and unless specified otherwise, we will adopt the following simplifying notations. The weakly singular integral kernel for the Laplace case will be written as:*

$$K^{ws}(\boldsymbol{x}, \boldsymbol{y}) = G^0(\boldsymbol{x}, \boldsymbol{y}). \tag{2.16}$$

Similarly, the hypersingular integral kernel for the Laplace case will be written as:

$$K^{hs}(\boldsymbol{x}, \boldsymbol{y}) = \frac{\partial^2}{\partial \boldsymbol{n_x} \partial \boldsymbol{n_y}} G^0(\boldsymbol{x}, \boldsymbol{y}). \tag{2.17}$$

Consequently, the wavenumber superscript indicator will be dropped, implicitly indicating that $k = 0$*:*

$$\mathcal{S} = \mathcal{S}^0 \quad \textit{and} \quad \mathcal{N} = \mathcal{N}^0. \tag{2.18}$$

In what follows we will focus on the preconditioning of the matrices associated with the Laplace operator. In the next section we will make clear why this approach can't be used directly in the case of the screen obstacles. In this chapter we will describe this application problem, and in the next chapter we will develop a strategy to tackle it.

2.3 Boundary integral equations for the screen problem

In this section we will show some well established results that will provide the functional framework relevant to the integral equations associated with screen obstacles. We will underline the main difference between the case when Ω is a Lipschitz-regular obstacle and the case of screen obstacle, remarking the new and challenging mapping properties of the involved boundary integral operators.

We start by noting that between the four cases at hand for the screen problem, both the anti-symmetric Dirichlet (Problem 1.3.6) and symmetric Neumann (Problem 1.3.7), can be solved straightforwardly without need of recourse to boundary integral equations.

Proposition 2.3.1 (Solutions to the anti-symmetric Dirichlet problem and the symmetric Neumann problem)**.** *Given the symmetric Neumann data φ (i.e. $[\gamma_\Gamma \partial_{\boldsymbol{n}} u] = \varphi$), the solution to the Symmetric Neumann Problem 1.3.7 can be computed without solving a boundary integral equation. It can be computed by applying the weakly-singular operator to the Neumann data:*

$$u(\boldsymbol{y}) = (\mathcal{S}\varphi)(\boldsymbol{y}) = \int_\Gamma \frac{1}{4\pi \|\boldsymbol{x}-\boldsymbol{y}\|} \varphi(\boldsymbol{x}) d\Gamma(\boldsymbol{x}), \quad \forall \boldsymbol{y} \in \Omega_\Gamma. \tag{2.19}$$

Similarly, given anti-symmetric Dirichlet data g (i.e. $\gamma_\Gamma^{\pm} u = \pm g$), the solution to the Anti-symmetric Dirichlet Problem 1.3.6 can be computed without solving a boundary integral equation; it can be computed by applying the double layer operator to the Dirichlet data:

$$u(\boldsymbol{y}) = -(\mathcal{D}g)(\boldsymbol{y}) = -\int_\Gamma \frac{\partial}{\partial \boldsymbol{n}_{\boldsymbol{x}}} \left(\frac{1}{4\pi \|\boldsymbol{x}-\boldsymbol{y}\|} \right) g(\boldsymbol{x}) d\Gamma(\boldsymbol{x}), \quad \forall \boldsymbol{y} \in \Omega_\Gamma. \tag{2.20}$$

Proof The solution $u = \mathcal{S}\varphi$ is continuous across Γ, and the jump properties of the weakly singular operator (see Theorem 1.4.1) yields $[\gamma_\Gamma \partial u/\partial \boldsymbol{n}] = \varphi$, which satisfies boundary conditions of the Symmetric Neumann Problem 1.3.7.

The solution $u = -\mathcal{D}g$ has a discontinuity across Γ, given by Theorem 1.4.2: $[\gamma_\Gamma u] = g$, satisfying the boundary conditions given of the Anti-Symmetric Dirichlet Problem 1.3.6.

■

Remark 2.3.1 (Focus on the symmetric Dirichlet and the anti-symmetric Neumann problems)**.** *Given that the anti-symmetric Dirichlet and the symmetric Neumann problem do not require solving a boundary integral equation, and thus a linear system needing preconditioning, from now on we will focus only on the integral operator preconditioning associated with the symmetric Dirichlet and anti-symmetric Neumann problems.*

Lemma 2.3.1 (Jump of the trace for the solutions of the symmetric Dirichlet and anti-symmetric Neumann problems [62, Lemma 2.2])**.** *Let $u \in W^{1,-1}(\Omega_\Gamma)$ be the solution to the symmetric Dirichlet Laplace problem. Then, the jump of the Neumann trace on Γ is such that*

$$\lambda = \left[\frac{\partial u}{\partial \boldsymbol{n}} \right] \in \widetilde{H}^{-1/2}(\Gamma). \tag{2.21}$$

If $u \in W^{1,-1}(\Omega_\Gamma)$ is the solution to the anti-symmetric Neumann Laplace problem, then the jump of the Dirichlet trace on Γ is such that

$$\mu = [u] \in \widetilde{H}^{1/2}(\Gamma). \tag{2.22}$$

The next two theorems provide us with boundary integral equations that relate the traces of the searched solution with the given data. These integral equations are the same as for the case of Lipschitz-regular obstacles.

Theorem 2.3.1 (Boundary integral equation for the symmetric Dirichlet problem [62, Theorem 2.5]). *A function $u \in W^{1,-1}(\Omega_\Gamma)$ is the solution to the symmetric Dirichlet problem if and only if $\lambda = [\partial u/\partial \boldsymbol{n}] \in \widetilde{H}^{-1/2}(\Gamma)$ is the solution to boundary integral equation problem*

$$\mathcal{S}\lambda = g, \tag{2.23}$$

for $g \in H^{1/2}(\Gamma)$.

Theorem 2.3.2 (Boundary integral equation for the anti-symmetric Neumann problem [62, Theorem 2.6]). *A function $u \in W^{1,-1}(\Omega_\Gamma)$ is the solution to the anti-symmetric Neumann problem if and only if $\mu = [u] \in \widetilde{H}^{1/2}(\Gamma)$ is the solution to boundary integral equation problem*

$$-\mathcal{N}\mu = \varphi, \tag{2.24}$$

for $\varphi \in H^{-1/2}(\Gamma)$.

Theorem 2.3.3 (Potential computation of the solution to the Dirichlet and Neumann problems [62, Lemma 2.4]). *Once the jumps of the Dirichlet and Neumann traces have been found, the solution to the symmetric Dirichlet and anti-symmetric Neumann problems can be computed as*

$$u = \mathcal{S}\lambda - \mathcal{D}\mu. \tag{2.25}$$

Remark 2.3.2 (Vanishing jump of the traces). *In the case of the symmetric Dirichlet problem ($\gamma_\Gamma^{\pm} u = g$), the jump of the Dirichlet traces is zero, i.e. $\mu = 0$, and thus the solution to the problem becomes $u = \mathcal{S}\lambda$ once λ has been calculated. In the case of the anti-symmetric Neumann problem ($\gamma_\Gamma^{\pm}\partial u/\partial \boldsymbol{n} = \varphi$), the jump of the Neumann traces is zero, i.e. $\lambda = 0$, and thus the solution to the problem becomes $u = -\mathcal{D}\mu$ once μ has been calculated.*

The following theorem describes a key feature of the traces of the solutions to the symmetric Dirichlet and anti-symmetric Neumann problems for screen obstacles. This important feature will be present throughout this chapter and will be considered later as a hint for the proposal of many of the techniques involved in the preconditioning method.

Theorem 2.3.4 (Behavior of trace jumps at the edge of the screen [62, Theorem 2.9]). *The jump of the Neumann trace of the solution to the symmetric Dirichlet Laplace problem, i.e. $\lambda \in \widetilde{H}^{-1/2}(\Gamma)$, behaves, at edge $\partial\Gamma$ of the screen, like*

$$\lambda(\boldsymbol{y}) \sim 1/\sqrt{dist\,(\partial\Gamma, \boldsymbol{y})}, \tag{2.26}$$

and the jump of the Dirichlet trace of the solution to the anti-symmetric Neumann Laplace problem, i.e. $\mu \in \widetilde{H}^{1/2}(\Gamma)$, behaves, at edge $\partial\Gamma$ of the screen, like

$$\mu(\boldsymbol{y}) \sim \sqrt{dist\,(\partial\Gamma, \boldsymbol{y})}, \tag{2.27}$$

where $dist\,(\partial\Gamma, \boldsymbol{y})$ is the distance to the edge of the screen $\partial\Gamma$ from a point $\boldsymbol{y} \in \Gamma$ in the vicinity of the edge.

The core of the problem with operator preconditioning when a Lipschitz-regular obstacle Ω of boundary Γ collapses into a screen, an object of void interior and non-Lipschitz boundaries, is that the mapping properties of the weakly singular and the hypersingular boundary integral operators degenerate. They continue to map trace spaces onto their duals, but these spaces no longer coincide with the ones where the other operator induces coercive bilinear forms. When the boundary Γ is Lipschitz-regular, there are two spaces in consideration, 1) $H^{1/2}(\Gamma)$ where $\mathcal{N}$ induces a coercive bilinear form, and 2) $H^{-1/2}(\Gamma)$ where $\mathcal{S}$ also induces a coercive bilinear form. These are mutual dual spaces. When the obstacle collapses into a screen, and its boundary is no longer Lipschitz-regular, there are now four spaces in consideration, two associated with each boundary integral operator. Operator $\mathcal{S}$ maps $\widetilde{H}^{-1/2}(\Gamma)$ onto $H^{1/2}(\Gamma)$, to which it is the

dual. On the other hand $\mathcal{N}$ maps $\widetilde{H}^{1/2}(\Gamma)$ into its dual $H^{-1/2}(\Gamma)$. The two operators involved in the integral equations needed to solve the two problems, do not share spaces (either as image or pre-image) where they can induce coercive bilinear forms, and thus they no longer furnish optimal preconditioners. Additionally, Calderón Identities no longer hold, which were useful in achieving low condition numbers (besides being bounded) when the preconditioning strategy was applied in Section 2.2.

Different approaches have been tried to tackle or to bypass this problem. Despite the fact that the Calderón Identities no longer hold for screen boundaries, the weakly singular and the hypersingular boundary integral operators do precondition each other to some degree, as proposed in [49], although not in an asymptotically optimal manner, with the spectral condition number growing as $\mathcal{O}(|\log h|)$. Another approach, called generalized Calderón formula for open boundaries, provides good preconditioning tools [44], but no asymptotical estimations are available.

A family of strategies are based in the use of inverses to the boundary integral operators, when available. Finding the inverse operators to $\mathcal{S}$ and $\mathcal{N}$ is, in general, a difficult task. Recently, explicit variational expressions for the inverses have been found by Carlos Jerez-Hanckes and Jean-Claude Nédélec, along with precise space mapping properties and Calderón-type identities for the segment screen ($\Gamma = (-1, 1) \times \{0\}$) in $\mathbb{R}^2$ [41]. These inverse operators induce linear, continuous, and coercive bilinear variational forms in the dual spaces for each operator, and thus provide a means to build preconditioning Galerkin matrices [36]. These results have also been proven to be extensible to the boundary integral operators linked to the Helmholtz equation and to curves other than the segment via a sufficiently regular curve transformation. More recently, explicit expressions for the inverse have been found for the case where the screen obstacle is the unit disk in $\mathbb{R}^3$ but only for $\mathcal{N}$ [37]. In this chapter we will propose inverses for $\mathcal{S}$ and $\mathcal{N}$ in series form.

2.4 Preconditioning for the segment obstacle in $\mathbb{R}^2$

In this section, we will briefly describe how the optimal preconditioning strategy was developed in the past into a preconditioning method for the case of a straight segment screen in $\mathbb{R}^2$ for the symmetric Dirichlet and the anti-symmetric Neumann problems. This case will illustrate the difficulties encountered when dealing with screens and will provide insight and suggestions to the treatment of the tridimensional case. This aforementioned strategy was reported in [36].

2.4.1 Geometrical and functional setting

The canonical curve screen chosen in $\mathbb{R}^2$ was the straight segment, which was defined as the set $\Gamma = I \times \{0\}$, with $I = (-1, 1)$. The propagation domain is named Ω_Γ. Function $w(x) = \sqrt{1-x^2}$ was defined for $x \in I$, which captures the behavior of the jump of the traces at the edges of the screen (i.e. $x = -1, 1$) as revealed in Theorem 2.3.4.

Lemma 2.3.1 provides the relevant spaces where the boundary integral equations are posed: $\widetilde{H}^{1/2}(\Gamma)$ and $\widetilde{H}^{-1/2}(\Gamma)$. As a reminder, these spaces are defined as in [61, Section 1.1]:

$$\widetilde{H}^{-1/2}(\Gamma) \equiv \Big(H^{1/2}(\Gamma)\Big)' \quad \text{and} \quad H^{-1/2}(\Gamma) \equiv \Big(\widetilde{H}^{1/2}(\Gamma)\Big)'. \tag{2.28}$$

Gelfand triples [57, Proposition 2.5.2] provide us the following inclusion relations:

$$\widetilde{H}^{1/2}(\Gamma) \subset L^2(\Gamma) \subseteq H^{-1/2}(\Gamma), \quad H^{1/2}(\Gamma) \subset L^2(\Gamma) \subset \widetilde{H}^{-1/2}(\Gamma). \tag{2.29}$$

2.4.2 Direct and inverse operators and kernels for the symmetric Dirichlet and the anti-symmetric Neumann problems

Among the four original screen problems (Problems 1.3.5, 1.3.6, 1.3.7 and 1.3.8), the anti-symmetric Dirichlet and symmetric Neumann problems have straightforward solutions as shown in Proposition 2.3.1. The other two problems, the symmetric Dirichlet and anti-symmetric Neumann problems, can be rewritten as boundary integral equations. The direct operators associated with these integral equations are known to be $\mathcal{S}$ and $\mathcal{N}$, as stated in Theorems 2.3.1 and 2.3.2 respectively. For the symmetric Dirichlet boundary integral equation, the kernel of the integral operator is the same as for the $\mathcal{S}$ boundary integral operator in two dimensions:

$$K_s^{ws}(x,y) = -\frac{1}{2\pi}\log|x-y|, \text{ for } x, y \in I. \tag{2.30}$$

The variational formulation for the associated boundary integral equation is

$$\begin{cases} \text{For } g \in H^{1/2}(\Gamma), \text{ find } \lambda \in \widetilde{H}^{-1/2}(\Gamma) \text{ such that for all } \lambda^t \in \widetilde{H}^{-1/2}(\Gamma), \\ \big\langle \mathcal{S}\lambda, \lambda^t \big\rangle_\Gamma = -\int\limits_\Gamma \int\limits_\Gamma \frac{1}{2\pi}\log|x-y|\lambda(x)\lambda^t(y)dxdy = \int\limits_\Gamma g(y)\lambda^t(y)dy. \end{cases} \tag{2.31}$$

For the anti-symmetric Neumann boundary integral equation, the integral kernel of the integral operator is the same as for the $\mathcal{N}$ boundary integral operator in two dimensions:

$$K_{as}^{hs}(x,y) = \frac{1}{2\pi}\frac{1}{|x-y|^2}, \text{ for } x, y \in I. \tag{2.32}$$

The variational formulation for associated boundary integral equation is

$$\begin{cases} \text{For } \varphi \in H^{-1/2}(\Gamma), \text{ find } \mu \in \widetilde{H}^{1/2}(\Gamma) \text{ such that for all } \mu^t \in \widetilde{H}^{1/2}(\Gamma), \\ \\ \left\langle -\mathcal{N}\mu, \mu^t \right\rangle_\Gamma = -\int\limits_\Gamma \int\limits_\Gamma \frac{1}{2\pi} \frac{1}{|x-y|^2} \mu(x)\mu^t(y) dxdy = \int\limits_\Gamma \varphi(y)\mu^t(y) dy. \end{cases} \tag{2.33}$$

In the development of the preconditioning strategy for the segment screen, as reported in [41], explicit variational forms were developed for the inverse operators $\mathcal{S}^{-1}$ and $\mathcal{N}^{-1}$. For the symmetric Dirichlet problem, a symmetric hypersingular boundary integral operator $\mathcal{S}^{-1}$, with integral kernel K_s^{hs}, was determined. Likewise, for the anti-symmetric Neumann problem, a weakly-singular boundary integral operator $\mathcal{N}^{-1}$, with integral kernel K_{as}^{ws}, was found. The explicit forms of these kernels are shown in Table 2.1.

Table 2.1: Explicit forms of the integral kernels of the operators linked to the boundary integral equations in two dimensions.

Kernel	Symmetric Dirichlet	Anti-symmetric Neumann
Weakly singular	$K_s^{ws}(x,y) = -\frac{1}{2\pi}\log\lvert x-y\rvert$	$K_{as}^{ws}(x,y) = -\frac{1}{2\pi}\log\frac{2\lvert x-y\rvert}{(x-y)^2+(w(x)+w(y))^2}$
Hypersingular	$K_s^{hs}(x,y) = \frac{1-xy}{w(x)w(y)}\frac{1}{(x-y)^2}$	$K_{as}^{hs}(x,y) = \frac{1}{2\pi}\frac{1}{\lvert x-y\rvert^2}$

2.4.3 Series form of the integral kernels for the direct and inverse operators

These developments were achieved using polynomial bases (first kind T_n, and second kind U_n Tchebyshev polynomials), allowing for series expressions of the integral kernels. Table 2.2 shows the series expression of the integral kernels for the direct and inverse integral operators involved in the symmetric Dirichlet and anti-symmetric Neumann problems.

Table 2.2: Series forms of the integral kernels of the operators linked to the boundary integral equations in two dimensions.

Kernel	Symmetric Dirichlet	Anti-symmetric Neumann
Weakly singular	$K_s^{ws}(x,y) = \log 2 + \sum\limits_{n=1}^{\infty} \frac{2}{n} T_n(x)T_n(y)$	$K_{as}^{ws}(x,y) = \sum\limits_{n=1}^{\infty} \frac{w(x)w(y)}{n} U_{n-1}(x)U_{n-1}(y)$
Hypersingular	$K_s^{hs}(x,y) = \sum\limits_{n=1}^{\infty} 2n\frac{T_n(x)T_n(y)}{w(x)w(y)}$	$K_{as}^{hs}(x,y) = \sum\limits_{n=1}^{\infty} 2nU_{n-1}(x)U_{n-1}(y)$

Remark 2.4.1 (Kernel singularities at the edge of the screen)**.** *It is remarkable that the series expressions of the integral kernels explicitly show their behaviour near the edges of the segment screen. This will provide relevant hints in the development of similar inverse operators for the disk screen in* $\mathbb{R}^3$*, showing that the key feature is the relation between the singularities of the jump of the traces (the unknown of the integral equations) and the behavior of the kernel at the edge the screen.*

Having the integral kernels for the variational expressions of the inverse operators, Galerkin matrices can be built once the spaces have been discretized. These matrices act as mutual optimal preconditioners as has been reported in [36].

2.4.4 Series expansions of functions belonging to the Sobolev trace spaces

The polynomial bases mentioned in the previous subsection allow for the expression of the functions of the Sobolev trace spaces in the form of series expansions. This will become a key tool in the construction of bases for the trace spaces for disk screen in $\mathbb{R}^3$ in the next sections.

It has been shown separately by E. Stephan and co-workers in [20, 33, 60] and more recently in an more comprehensive exposition, in [41], that using polynomial bases for $L^2(I)$ and the weight function w allows for the creation of bases for the Sobolev trace spaces $\widetilde{H}^{1/2}(I)$, $\widetilde{H}^{-1/2}(I)$, $H^{1/2}(I)$, and $H^{-1/2}(I)$.

A function μ in the space $\widetilde{H}^{1/2}(I)$ can be expanded on the basis $\{wU_n\}_{n=0}^{\infty}$:

$$\mu(x) = \sum_{n=0}^{\infty} \mu_n w(x) U_n(x), \quad \mu_n = \frac{2}{\pi} \int_I \mu(x) U_n(x) dx. \tag{2.34}$$

A function g in the space $H^{1/2}(I)$ can be expanded on the basis $\{T_n\}_{n=0}^{\infty}$:

$$g(x) = \sum_{n=0}^{\infty} g_n T_n(x), \quad g_n = \frac{2}{\pi} \int_I \frac{g(x) T_n(x)}{w(x)} dx. \tag{2.35}$$

A function φ in the space $H^{-1/2}(I)$ can be expanded on the basis $\{U_n\}_{n=0}^{\infty}$:

$$\varphi(x) = \sum_{n=0}^{\infty} \varphi_n U_n(x), \quad \varphi_n = \frac{2}{\pi} \int_I \varphi(x) U_n(x) w(x) dx. \tag{2.36}$$

A function λ in the space $\widetilde{H}^{-1/2}(I)$ can be expanded on the basis $\{w^{-1}T_n\}_{n=0}^{\infty}$:

$$\lambda(x) = \sum_{n=0}^{\infty} \lambda_n w^{-1}(x) T_n(x), \quad \lambda_n = \frac{2}{\pi} \int_I \lambda(x) T_n(x) dx. \tag{2.37}$$

In the next sections we will adapt the results related to segment screen in $\mathbb{R}^2$ for the unit disk screen in $\mathbb{R}^3$. With that goal in mind, we will specify a geometrical and functional framework for that particular case and we will show the existence of operators that are inverses to the ones involved in the boundary integral equations associated with the symmetric Dirichlet and anti-symmetric Neumann problems.

2.5 Geometrical and functional setting for the disk screen in $\mathbb{R}^3$

From now on, we will focus on the case of a unit disk screen obstacle in $\mathbb{R}^3$. We will provide a geometrical and a functional setting appropriate for this case.

2.5.1 Geometrical definitions

Let $\boldsymbol{x} = (x_1, x_2, x_3) \in \mathbb{R}^3$, with canonical coordinate system $(\hat{\boldsymbol{e}}_1, \hat{\boldsymbol{e}}_2, \hat{\boldsymbol{e}}_3)$, be a point, and let us consider the split of the three-dimensional space into two half-spaces $\sigma_{\mp} = \{\boldsymbol{x} \in \mathbb{R}^3 : x_3 \lessgtr 0\}$, with interface plane Π given by $x_3 = 0$. We take interest in disk $\mathbb{D}$ in $\mathbb{R}^3$:

$$\mathbb{D} = \{\boldsymbol{x} \in \mathbb{R}^3 : x_3 = 0, x_1^2 + x_2^2 < 1\}. \tag{2.38}$$

We divide plane Π in open disjoint sections $\mathbb{D}$ and $\Pi_f = \Pi \setminus \overline{\mathbb{D}}$. The problem domain for the unit disk screen obstacle is denoted by $\Omega_{\mathbb{D}} = \mathbb{R}^3 \setminus \overline{\mathbb{D}}$.

We also consider the unit sphere $\mathbb{S}$ in $\mathbb{R}^3$. The plane Π divides the unit sphere into two half-spheres which we denote by $\mathbb{S}^+$ (upper half-sphere), and $\mathbb{S}^-$ (lower half-sphere). For a point on the sphere, we consider the cylindrical coordinate system (θ, ϕ), where θ and ϕ are the classic Euler angles ($\theta \in [0, \pi]$ and $\phi \in [0, 2\pi]$), and $\hat{\boldsymbol{e}}_r$, $\hat{\boldsymbol{e}}_\theta$ and $\hat{\boldsymbol{e}}_\phi$ the local spherical coordinate system for $\boldsymbol{x} \in \mathbb{S}$:

$$\begin{cases} x_1(\theta, \phi) = \sin\theta\cos\phi, \\ x_2(\theta, \phi) = \sin\theta\sin\phi, \\ x_3(\theta, \phi) = \cos\theta, \end{cases} \quad \begin{cases} \theta(\boldsymbol{x}) = \theta_{\boldsymbol{x}} = \arccos(x_3), \\ \phi(\boldsymbol{x}) = \phi_{\boldsymbol{x}} = \arctan(x_2/x_1), \end{cases} \tag{2.39}$$

$$\begin{cases} \hat{\boldsymbol{e}}_r(\boldsymbol{x}) = (\sin\theta\cos\phi, \sin\theta\sin\phi, \cos\theta), \\ \hat{\boldsymbol{e}}_\theta(\boldsymbol{x}) = (\cos\theta\cos\phi, \cos\theta\sin\phi, -\sin\theta), \\ \hat{\boldsymbol{e}}_\phi(\boldsymbol{x}) = (-\sin\phi, \cos\phi, 0). \end{cases} \tag{2.40}$$

For a point on the disk, represented in bi-dimensional Cartesian coordinates $(x_1, x_2) \in \mathbb{R}^2$, we consider the polar coordinate system (ρ, ϕ), where $\rho \in [0, 1)$ is the radius, and $\hat{\boldsymbol{e}}_\rho$ and $\hat{\boldsymbol{e}}_\phi$ the local cylindrical coordinate system of a point $\boldsymbol{x} \in \mathbb{D}$.

$$\begin{cases} x_1(\theta, \phi) = \rho\cos\phi, \\ x_2(\theta, \phi) = \rho\sin\phi, \end{cases} \quad \begin{cases} \rho(\boldsymbol{x}) = \rho_{\boldsymbol{x}} = \sqrt{x_1^2 + x_2^2} = \sin\theta, \\ \phi(\boldsymbol{x}) = \phi_{\boldsymbol{x}} = \arctan(x_2/x_1), \end{cases} \tag{2.41}$$

$$\begin{cases} \hat{\boldsymbol{e}}_\rho(\boldsymbol{x}) = (\cos\phi, \sin\phi), \\ \hat{\boldsymbol{e}}_\phi(\boldsymbol{x}) = (-\sin\phi, \cos\phi). \end{cases} \tag{2.42}$$

For a point $\boldsymbol{x} \in \mathbb{D}$ we denote as $\boldsymbol{x}^\pm \in \mathbb{S}^\pm$ its vertical projection onto the upper and lower half-spheres. Likewise, points $\boldsymbol{x}^\pm \in \mathbb{S}^\pm$ have a vertical projection $\boldsymbol{x} \in \mathbb{D}$ onto the disk.

It is noteworthy that with this definition, $\rho = \sin\theta$ is always non-negative. It will become useful to define a weight function w relating the radius ρ of a point $\boldsymbol{x} \in \mathbb{D}$ with the distance to its vertical projections on unit sphere $\mathbb{S}$,

$$w(\rho) = \sqrt{1 - \rho^2} = |\cos\theta|, \tag{2.43}$$

such that, for $\boldsymbol{x} = (\rho, \phi) \in \mathbb{D}$,

$$\boldsymbol{x}^\pm(\rho, \phi) = (\rho\cos\phi, \rho\sin\phi, \pm w(\rho)). \tag{2.44}$$

Finally, we will denote by $(\cdot, \cdot)$ the inner product in $\mathbb{R}^2$ and $\mathbb{R}^3$. When taking the inner products of complex valued functions, we will use the conventions of taking the conjugate on the second argument.

Figure 2.3 resumes the definitions and relations comprising the elements of the geometrical setting for the unit disk screen in $\mathbb{R}^3$.

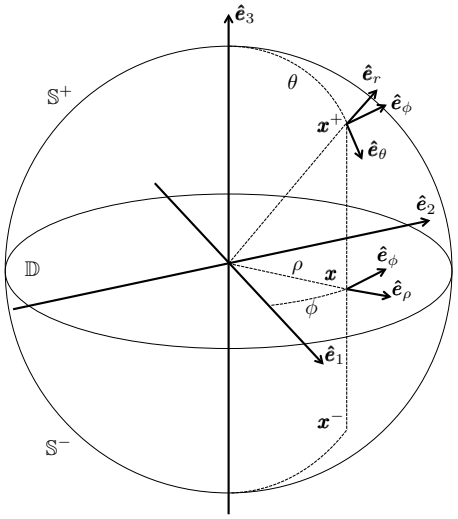

Figure 2.3: Geometrical setting for disk screen $\mathbb{D}$, upper $\mathbb{S}^+$, and lower $\mathbb{S}^-$ half-spheres and other geometrical elements considered in this chapter.

Proposition 2.5.1 (Hypersingular integral kernel on disk $\mathbb{D}$)**.** *The kernel of the hypersingular boundary integral operator $\mathcal{N}$ has the following expression when $\boldsymbol{x}, \boldsymbol{y} \in \mathbb{D}$:*

$$K^{hs}(\boldsymbol{x}, \boldsymbol{y}) = \frac{\partial^2}{\partial \boldsymbol{n}_{\boldsymbol{x}} \partial \boldsymbol{n}_{\boldsymbol{y}}} \left(\frac{1}{4\pi \left\| \boldsymbol{x} - \boldsymbol{y} \right\|} \right) = \frac{1}{4\pi \left\| \boldsymbol{x} - \boldsymbol{y} \right\|^3}. \tag{2.45}$$

Proof

$$\overrightarrow{\operatorname{grad}}_{\boldsymbol{x}} \left(\frac{1}{4\pi \left\| \boldsymbol{x} - \boldsymbol{y} \right\|} \right) = -\frac{\boldsymbol{x} - \boldsymbol{y}}{4\pi \left\| \boldsymbol{x} - \boldsymbol{y} \right\|^3}. \tag{2.46}$$

$$\frac{\partial}{\partial \boldsymbol{n}_{\boldsymbol{x}}} \left(\frac{1}{4\pi \left\| \boldsymbol{x} - \boldsymbol{y} \right\|} \right) = \boldsymbol{n}_{\boldsymbol{x}} \cdot \overrightarrow{\operatorname{grad}}_{\boldsymbol{x}} \left(\frac{1}{4\pi \left\| \boldsymbol{x} - \boldsymbol{y} \right\|} \right) = -\frac{\boldsymbol{n}_{\boldsymbol{x}} \cdot (\boldsymbol{x} - \boldsymbol{y})}{4\pi \left\| \boldsymbol{x} - \boldsymbol{y} \right\|^3}. \tag{2.47}$$

$$\overrightarrow{\operatorname{grad}}_{\boldsymbol{y}} \frac{\partial}{\partial \boldsymbol{n}_{\boldsymbol{x}}} \left(\frac{1}{4\pi \left\| \boldsymbol{x} - \boldsymbol{y} \right\|} \right) = -3\frac{(\boldsymbol{n}_{\boldsymbol{x}} \cdot \boldsymbol{x})(\boldsymbol{x} - \boldsymbol{y})}{4\pi \left\| \boldsymbol{x} - \boldsymbol{y} \right\|^5} + 3\frac{(\boldsymbol{n}_{\boldsymbol{x}} \cdot \boldsymbol{y})(\boldsymbol{x} - \boldsymbol{y})}{4\pi \left\| \boldsymbol{x} - \boldsymbol{y} \right\|^5} + \frac{\boldsymbol{n}_{\boldsymbol{x}}}{4\pi \left\| \boldsymbol{x} - \boldsymbol{y} \right\|^3}. \tag{2.48}$$

$$\boldsymbol{n}_{\boldsymbol{y}} \cdot \overrightarrow{\operatorname{grad}}_{\boldsymbol{y}} \frac{\partial}{\partial \boldsymbol{n}_{\boldsymbol{x}}} \left(\frac{1}{4\pi \left\| \boldsymbol{x} - \boldsymbol{y} \right\|} \right) = \frac{\boldsymbol{n}_{\boldsymbol{x}} \cdot \boldsymbol{n}_{\boldsymbol{y}}}{4\pi \left\| \boldsymbol{x} - \boldsymbol{y} \right\|^3} - 3\frac{(\boldsymbol{n}_{\boldsymbol{x}} \cdot (\boldsymbol{x} - \boldsymbol{y}))\,(\boldsymbol{n}_{\boldsymbol{y}} \cdot (\boldsymbol{x} - \boldsymbol{y}))}{4\pi \left\| \boldsymbol{x} - \boldsymbol{y} \right\|^5}. \tag{2.49}$$

This identity gives the desired results for the case of the disk, when $\boldsymbol{x}, \boldsymbol{y} \in \mathbb{D}$, an thus $x_3 = y_3 = 0$ and $\boldsymbol{n}_{\boldsymbol{x}} = \boldsymbol{n}_{\boldsymbol{y}} = (0, 0, 1)^T$. ∎

Proposition 2.5.2 (Hypersingular kernel on sphere $\mathbb{S}$)**.** *The kernel of the hypersingular boundary integral operator $\mathcal{N}$ has the following expression when $\boldsymbol{x}, \boldsymbol{y} \in \mathbb{S}$:*

$$K^{hs}(\boldsymbol{x}, \boldsymbol{y}) = \frac{1}{4\pi \left\| \boldsymbol{x} - \boldsymbol{y} \right\|^3} + \frac{1}{16\pi \left\| \boldsymbol{x} - \boldsymbol{y} \right\|}. \tag{2.50}$$

Proof We know from the proof of Proposition 2.5.1 that

$$\frac{\partial^2}{\partial \boldsymbol{n}_{\boldsymbol{x}} \partial \boldsymbol{n}_{\boldsymbol{y}}} \left(\frac{1}{4\pi \left\| \boldsymbol{x} - \boldsymbol{y} \right\|} \right) = \frac{\boldsymbol{n}_{\boldsymbol{x}} \cdot \boldsymbol{n}_{\boldsymbol{y}}}{4\pi \left\| \boldsymbol{x} - \boldsymbol{y} \right\|^3} - 3\frac{\boldsymbol{n}_{\boldsymbol{x}} \cdot (\boldsymbol{x} - \boldsymbol{y}) \boldsymbol{n}_{\boldsymbol{y}} \cdot (\boldsymbol{x} - \boldsymbol{y})}{4\pi \left\| \boldsymbol{x} - \boldsymbol{y} \right\|^5}. \tag{2.51}$$

We remark the fact that, particularly for $\boldsymbol{x}, \boldsymbol{y} \in \mathbb{S}$, we have that $\boldsymbol{n_x} = \boldsymbol{x}$, $\boldsymbol{n_y} = \boldsymbol{y}$ and $\|\boldsymbol{x}\| = \|\boldsymbol{y}\| = 1$. This allows for the following expressions for the distance $\|\boldsymbol{x} - \boldsymbol{y}\|$:

$$\|\boldsymbol{x} - \boldsymbol{y}\|^2 = 2 - 2(\boldsymbol{x} \cdot \boldsymbol{y}) \quad \text{and} \quad \|\boldsymbol{x} - \boldsymbol{y}\|^4 = 4 - 8(\boldsymbol{x} \cdot \boldsymbol{y}) + 4(\boldsymbol{x} \cdot \boldsymbol{y})^2. \tag{2.52}$$

We write the hypersingular kernel as,

$$\frac{\partial^2}{\partial \boldsymbol{n_x} \partial \boldsymbol{n_y}} \left(\frac{1}{4\pi \|\boldsymbol{x} - \boldsymbol{y}\|} \right) = \frac{(\boldsymbol{x} \cdot \boldsymbol{y}) \|\boldsymbol{x} - \boldsymbol{y}\|^2 - 3\boldsymbol{x} \cdot (\boldsymbol{x} - \boldsymbol{y}) \boldsymbol{y} \cdot (\boldsymbol{x} - \boldsymbol{y})}{4\pi \|\boldsymbol{x} - \boldsymbol{y}\|^5}. \tag{2.53}$$

The development of the numerator using the previous identities gives the desired result:

$$\begin{aligned}
(\boldsymbol{x} \cdot \boldsymbol{y}) \|\boldsymbol{x} - \boldsymbol{y}\|^2 - 3\boldsymbol{x} \cdot (\boldsymbol{x} - \boldsymbol{y}) \boldsymbol{y} \cdot (\boldsymbol{x} - \boldsymbol{y}) &= 3 - 4(\boldsymbol{x} \cdot \boldsymbol{y}) + (\boldsymbol{x} \cdot \boldsymbol{y})^2 && (2.54)\\
&= 2 - 2(\boldsymbol{x} \cdot \boldsymbol{y}) + \left(1 - 2(\boldsymbol{x} \cdot \boldsymbol{y}) + (\boldsymbol{x} \cdot \boldsymbol{y})^2\right) && (2.55)\\
&= \|\boldsymbol{x} - \boldsymbol{y}\|^2 + \frac{1}{4} \|\boldsymbol{x} - \boldsymbol{y}\|^4. && (2.56)
\end{aligned}$$

■

Proposition 2.5.3 (Relation between the weakly singular and the hypersingular integral kernels on the disk)**.** *For $\boldsymbol{x}, \boldsymbol{y} \in \mathbb{D}$, the kernels K^{ws} and K^{hs} of the boundary integral operators $\mathcal{S}$ and $\mathcal{N}$ on disk $\mathbb{D}$ are linked by the Laplace-Beltrami operator:*

$$\Delta_{\mathbb{D}} K^{ws} = K^{hs}. \tag{2.57}$$

$$\Delta_{\mathbb{D}} \left(\frac{1}{4\pi \|\boldsymbol{x} - \boldsymbol{y}\|} \right) = \frac{1}{4\pi \|\boldsymbol{x} - \boldsymbol{y}\|^3}. \tag{2.58}$$

Proof

$$\Delta_{\mathbb{D}} \left(G(\boldsymbol{x}, \boldsymbol{y}) \right) = \operatorname{div}_{\mathbb{D}} \left(\overrightarrow{\operatorname{grad}}_{\mathbb{D}} G(\boldsymbol{x}, \boldsymbol{y}) \right) = \left(\frac{\partial^2}{\partial y_1^2} + \frac{\partial^2}{\partial y_2^2} \right) G(\boldsymbol{x}, \boldsymbol{y}) \tag{2.59}$$

$$\frac{\partial}{\partial x_i} G(\boldsymbol{x}, \boldsymbol{y}) = -\frac{x_i - y_i}{4\pi \|\boldsymbol{x} - \boldsymbol{y}\|^3} \tag{2.60}$$

$$\frac{\partial^2}{\partial x_i^2} G(\boldsymbol{x}, \boldsymbol{y}) = -\frac{1}{4\pi \|\boldsymbol{x} - \boldsymbol{y}\|^3} - (x_i - y_i) \frac{\partial}{\partial x_i} \left(\frac{1}{4\pi \|\boldsymbol{x} - \boldsymbol{y}\|^3} \right) \tag{2.61}$$

$$\frac{\partial}{\partial x_i} \left(\frac{1}{4\pi \|\boldsymbol{x} - \boldsymbol{y}\|^3} \right) = -\frac{3(x_i - y_i)}{4\pi \|\boldsymbol{x} - \boldsymbol{y}\|^5} \tag{2.62}$$

$$\Rightarrow \frac{\partial^2}{\partial x_i^2} G(\boldsymbol{x}, \boldsymbol{y}) = -\frac{1}{4\pi \|\boldsymbol{x} - \boldsymbol{y}\|^3} + \frac{3(x_i - y_i)^2}{4\pi \|\boldsymbol{x} - \boldsymbol{y}\|^5} \tag{2.63}$$

$$\Rightarrow \left(\frac{\partial^2}{\partial x_1^2} + \frac{\partial^2}{\partial x_2^2} \right) G(\boldsymbol{x}, \boldsymbol{y}) = -\frac{2}{4\pi \|\boldsymbol{x} - \boldsymbol{y}\|^3} + \frac{3\left((x_1 - y_1)^2 + (x_2 - y_2)^2\right)}{4\pi \|\boldsymbol{x} - \boldsymbol{y}\|^5} \tag{2.64}$$

$$\left((x_1 - y_1)^2 + (x_2 - y_2)^2\right) = \|\boldsymbol{x} - \boldsymbol{y}\|^2. \tag{2.65}$$

$$\Rightarrow \left(\frac{\partial^2}{\partial x_1^2} + \frac{\partial^2}{\partial x_2^2} \right) G(\boldsymbol{x}, \boldsymbol{y}) = \frac{1}{4\pi \|\boldsymbol{x} - \boldsymbol{y}\|^3}. \tag{2.66}$$

■

Remark 2.5.1 (Change of variables between the disk and the upper half-sphere for the surface vector curl operator)**.** *The inner product in $\mathbb{C}^3$ for the curl of two functions u and v defined on $\mathbb{S}$ is, in spherical coordinates:*

$$\begin{aligned}
\left(\overrightarrow{curl}_{\mathbb{S}} u(\boldsymbol{x}), \overrightarrow{curl}_{\mathbb{S}} v(\boldsymbol{y}) \right) = \; & \frac{\partial u(\boldsymbol{x})}{\partial \phi_{\boldsymbol{x}}} \frac{\partial \overline{v}(\boldsymbol{y})}{\partial \phi_{\boldsymbol{y}}} \\
& + \cos\left(\phi_{\boldsymbol{x}} - \phi_{\boldsymbol{y}}\right) \left(\frac{\partial u(\boldsymbol{x})}{\partial \theta_{\boldsymbol{x}}} \frac{\partial \overline{v}(\boldsymbol{y})}{\partial \theta_{\boldsymbol{y}}} + \frac{\cos\theta_{\boldsymbol{x}} \cos\theta_{\boldsymbol{y}}}{\sin\theta_{\boldsymbol{x}} \sin\theta_{\boldsymbol{y}}} \frac{\partial u(\boldsymbol{x})}{\partial \phi_{\boldsymbol{x}}} \frac{\partial \overline{v}(\boldsymbol{y})}{\partial \phi_{\boldsymbol{y}}} \right) \\
& + \sin\left(\phi_{\boldsymbol{x}} - \phi_{\boldsymbol{y}}\right) \left(\frac{\cos\theta_{\boldsymbol{y}}}{\sin\theta_{\boldsymbol{y}}} \frac{\partial u(\boldsymbol{x})}{\partial \theta_{\boldsymbol{x}}} \frac{\partial \overline{v}(\boldsymbol{y})}{\partial \phi_{\boldsymbol{y}}} - \frac{\cos\theta_{\boldsymbol{x}}}{\sin\theta_{\boldsymbol{x}}} \frac{\partial u(\boldsymbol{x})}{\partial \phi_{\boldsymbol{x}}} \frac{\partial \overline{v}(\boldsymbol{y})}{\partial \theta_{\boldsymbol{y}}} \right).
\end{aligned} \tag{2.67}$$

The inner product in $\mathbb{C}^2$ for the curl of two functions u and v defined on $\mathbb{D}$ is, in cylindrical coordinates:

$$\begin{aligned}\left(\overrightarrow{curl}_{\mathbb{D}}u(\boldsymbol{x}),\overrightarrow{curl}_{\mathbb{D}}v(\boldsymbol{y})\right) = &\cos\left(\phi_{\boldsymbol{x}}-\phi_{\boldsymbol{y}}\right)\left(\frac{\partial u(\boldsymbol{x})}{\partial\rho_{\boldsymbol{x}}}\frac{\partial\overline{v}(\boldsymbol{y})}{\partial\rho_{\boldsymbol{y}}}+\frac{1}{\rho_{\boldsymbol{x}}\rho_{\boldsymbol{y}}}\frac{\partial u(\boldsymbol{x})}{\partial\phi_{\boldsymbol{x}}}\frac{\partial\overline{v}(\boldsymbol{y})}{\partial\phi_{\boldsymbol{y}}}\right)\\ &+\sin\left(\phi_{\boldsymbol{x}}-\phi_{\boldsymbol{y}}\right)\left(\frac{\partial u(\boldsymbol{x})}{\partial\rho_{\boldsymbol{x}}}\frac{1}{\rho_{\boldsymbol{y}}}\frac{\partial\overline{v}(\boldsymbol{y})}{\partial\phi_{\boldsymbol{y}}}-\frac{1}{\rho_{\boldsymbol{x}}}\frac{\partial u(\boldsymbol{x})}{\partial\phi_{\boldsymbol{x}}}\frac{\partial\overline{v}(\boldsymbol{y})}{\partial\rho_{\boldsymbol{y}}}\right)\end{aligned} \tag{2.68}$$

The change of variables $u(\boldsymbol{x}) = U(\boldsymbol{x}^+)$ gives $\partial U/\partial\phi = \partial u/\partial\phi$, and $\rho = \sin\theta$ gives

$$\frac{\partial u}{\partial\rho} = \frac{1}{\cos\theta}\frac{\partial U}{\partial\theta} = \frac{1}{w(\rho)}\frac{\partial U}{\partial\theta}. \tag{2.69}$$

Expressing one of the identities in the variables of the other through a change of variables allows for the identification of the following identity linking both:

$$\left(\overrightarrow{curl}_{\mathbb{D}}u(\boldsymbol{x}),\overrightarrow{curl}_{\mathbb{D}}v(\boldsymbol{y})\right) = \frac{1}{\cos\theta_{\boldsymbol{x}}\cos\theta_{\boldsymbol{y}}}\left(\left(\overrightarrow{curl}_{\mathbb{S}}U(\boldsymbol{x}^+),\overrightarrow{curl}_{\mathbb{S}}v(\boldsymbol{y}^+)\right)-\frac{\partial U(\boldsymbol{x}^+)}{\partial\phi_{\boldsymbol{x}}}\frac{\partial\overline{V}(\boldsymbol{y}^+)}{\partial\phi_{\boldsymbol{y}}}\right). \tag{2.70}$$

2.5.2 Functional setting

In this section we will recall some results from Section 1.2 for the particular case of disk screen $\mathbb{D}$ embedded in $\mathbb{R}^3$.

Let us define a function's restrictions over a half-space:

$$u^{\pm} = u|_{\sigma^{\pm}}. \tag{2.71}$$

Let us also introduce the trace operators $\gamma_{\Pi}^{\pm} : C_0^{\infty}\left(\overline{\sigma^{\pm}}\right) \to \Pi$ as

$$\gamma_{\Pi}^{\pm}u = \lim_{\epsilon\to 0^{\pm}} u(x_1,x_2,\epsilon). \tag{2.72}$$

Operators $\gamma_{\Pi}^{\pm}$ can be uniquely extended to the space of bounded linear operators from $H^1_{loc}(\sigma^{\pm})$ to $H^{1/2}_{loc}(\Pi)$ [48, Chapter 3]. Then, the trace operator of a subdomain Γ of Π can be defined as:

$$\gamma_{\Gamma}^{\pm}u = \left(\gamma_{\Pi}^{\pm}u\right)\big|_{\Gamma}. \tag{2.73}$$

Let $[\gamma_\Gamma] = \gamma_\Gamma^+ - \gamma_\Gamma^-$ be the jump operator across a surface Γ subset of plane Π. We will take particular interest in the case where Γ is $\mathbb{D}$.

Additionally, we define an orientation for the surface Γ, and denote by $\boldsymbol{n_x}$ the unit normal at $\boldsymbol{x} \in \Gamma$ on the positive part of the surface, according to Subsection 1.2.1. In the case of screen $\mathbb{D}$ the unit normal becomes $\boldsymbol{n_x} = \hat{\boldsymbol{e}}_3 = (0,0,1)$ for $\boldsymbol{x} \in \mathbb{D}$, thus defining the directional derivative

$$\partial_{\boldsymbol{n_x}}u = \frac{\partial u}{\partial x_3}. \tag{2.74}$$

We take interest in the functional spaces relevant for the description of the solutions to the Laplace and Helmholtz problems in $\Omega_{\mathbb{D}} = \mathbb{R}^3 \setminus \overline{\mathbb{D}}$, and the trace spaces on screen $\mathbb{D}$.

The natural Sobolev spaces considered for the Laplace and Helmoltz problems [4, Section 4.1], for a general problem domain Ω, are $H^1(\Omega)$ if $\Omega \subset \mathbb{R}^3$ is a bounded domain, or $H^1_{loc}(\Omega)$ if not. Being the latter only of Fréchet type, and being $\Omega_{\mathbb{D}}$ unbounded, we define

$$W^{1,-1}(\Omega_{\mathbb{D}}) = \left\{u \in C_0^{\infty}(\Omega_{\mathbb{D}}) : \frac{u}{\sqrt{1+\|x\|^2}} \in L^2(\Omega_{\mathbb{D}}), \overrightarrow{\operatorname{grad}}\, u \in \left(L^2(\Omega_{\mathbb{D}})\right)^3\right\}, \tag{2.75}$$

defining a Hilbert space which coincides with $H^1_{loc}(\Omega_{\mathbb{D}})$ for bounded parts of $\Omega_{\mathbb{D}}$ [51, Section 2.5.4]. We will also consider the following subspace of $W^{1,-1}(\Omega_{\mathbb{D}})$:

$$W_0^{1,-1}(\Omega_{\mathbb{D}}) = \left\{ u \in W^{1,-1}(\Omega_{\mathbb{D}}) : \gamma_{\mathbb{D}}^{\pm} u = 0 \right\}. \tag{2.76}$$

Gelfand triples [57, Proposition 2.5.2] provide us the following inclusion relations:

$$\widetilde{H}^{1/2}(\mathbb{D}) \subset L^2(\mathbb{D}) \subseteq H^{-1/2}(\mathbb{D}), \quad H^{1/2}(\mathbb{D}) \subset L^2(\mathbb{D}) \subset \widetilde{H}^{-1/2}(\mathbb{D}). \tag{2.77}$$

It is also remarkable that $\widetilde{H}^{1/2}(\mathbb{D}) \subset H_0^{1/2}(\mathbb{D})$.

Using these geometrical definitions and the outlined functional framework, we will show in the next section that boundary integral operators $\mathcal{S}$ and $\mathcal{N}$ do have inverses. Their existence will be guaranteed by the Lax-Mailgram theorem, and thus an explicit form will not be readily available. Their explicit form will then be the subject of the subsequent sections.

2.6 Existence of inverse operators for the Dirichlet and Neumann problems

As it was shown in Section 2.3, the Laplace problem for a screen can be posed as a boundary integral equation on the surface of the screen. For the Dirichlet (Neumann) problem, and given Dirichlet (Neumann) data, the problem amounts to finding the unknown jump of the Neumann (Dirichlet) trace solving the integral equation for the weakly-singular $\mathcal{S}$ (hypersingular $\mathcal{N}$) operator. In this section we will show that in the case of disk screen $\mathbb{D}$ in $\mathbb{R}^3$, integral operators $\mathcal{S}$ and $\mathcal{N}$ have inverses. We will also show, however, that these inverses do not have a straightforward explicit form. We will undertake the task of finding series expressions in the following sections of this chapter.

This section regarding the existence of inverse operators is an adaptation for $\mathbb{R}^3$ of the results derived for $\mathbb{R}^2$ in [41, Sections 2.6 & 2.7]. The exposition, order of the results and the notation follow that of the mentioned reference.

2.6.1 Dirichlet Problems

Instead of directly considering the symmetric Laplace problem, we start by tackling a more general Laplace problem with two different Dirichlet conditions $g^{\pm}$ from above and below on $\mathbb{D}$. These boundary data lie in the Hilbert space

$$\mathbb{X} = \left\{ \boldsymbol{g} = (g^+, g^-) \in H^{1/2}(\mathbb{D}) \times H^{1/2}(\mathbb{D}) : g^+ - g^- \in \widetilde{H}^{1/2}(\mathbb{D}) \right\} \tag{2.78}$$

with norm

$$\|\boldsymbol{g}\|_{\mathbb{X}}^2 = \left\|g^+\right\|_{H^{1/2}(\mathbb{D})}^2 + \left\|g^-\right\|_{H^{1/2}(\mathbb{D})}^2 + \left\|g^+ - g^-\right\|_{\widetilde{H}^{1/2}(\mathbb{D})}^2 . \tag{2.79}$$

We also define the Hilbert space for Neumann data as

$$\mathbb{Y} = \left\{ \boldsymbol{\varphi} = (\varphi^+, \varphi^-) \in H^{-1/2}(\mathbb{D}) \times H^{-1/2}(\mathbb{D}) : \varphi^+ - \varphi^- \in \widetilde{H}^{-1/2}(\mathbb{D}) \right\}, \tag{2.80}$$

with norm

$$\|\boldsymbol{\varphi}\|_{\mathbb{Y}}^2 = \left\|\varphi^+\right\|_{H^{-1/2}(\mathbb{D})}^2 + \left\|\varphi^-\right\|_{H^{-1/2}(\mathbb{D})}^2 + \left\|\varphi^+ - \varphi^-\right\|_{\widetilde{H}^{-1/2}(\mathbb{D})}^2 . \tag{2.81}$$

Let us consider the general Dirichlet problem for the disk screen.

Problem 2.6.1. *For $\boldsymbol{g} \in \mathbb{X}$, find $u \in W^{1,-1}(\Omega_{\mathbb{D}})$ such that:*

$$\begin{cases} -\Delta u \;=\; 0, & \boldsymbol{x} \in \Omega_{\mathbb{D}}, \\ \begin{pmatrix} \gamma_{\mathbb{D}}^+ \\ \gamma_{\mathbb{D}}^- \end{pmatrix} u \;=\; \boldsymbol{g}, & \boldsymbol{x} \in \mathbb{D}. \end{cases} \tag{2.82}$$

Uniqueness of solutions

Any function u in $W^{1,-1}(\Omega_{\mathbb{D}})$ can be split into its restrictions on $\pi_{\pm}$:

$$u^{\pm} \;=\; u|_{\sigma_{\pm}} \;\in\; W^{1,-1}(\sigma_{\pm}), \tag{2.83}$$

with well defined traces $\gamma_{\mathbb{D}}^{\pm} u^{\pm} \in H_{loc}^{1/2}(\mathbb{D})$. By definition, if u is a solution to Problem 2.6.1, then $\gamma_{\mathbb{D}}^{\pm} u^{\pm} = g^{\pm}$ with $[\gamma_{\mathbb{D}} u] \in \widetilde{H}^{1/2}(\mathbb{D})$. Due to the regularity of the solution in the interior of $\Omega_{\mathbb{D}}$, we have that

$$\left[\gamma_{\Pi_f} u\right] \;=\; 0, \qquad \text{and} \qquad \left[\gamma_{\Pi_f} \partial_n u\right] \;=\; 0. \tag{2.84}$$

By the extension theorem [48, Theorem 3.18], there exists a continuous operator $\mathcal{E}_\Pi^+ : H^{1/2}(\mathbb{D}) \to H^{1/2}(\Pi)$ extending g^+ over Π satisfying

$$\mathcal{E}_\Pi^+ g^+ \in H^{1/2}(\Pi)\,, \qquad \operatorname{supp}\left(\mathcal{E}_\Pi^+ g^+\right) \Subset \Pi \qquad \text{and} \qquad \left(\mathcal{E}_\Pi^+ g^+\right)\big|_{\mathbb{D}} \;=\; g^+. \tag{2.85}$$

Furthermore, $[g] \in \widetilde{H}^{1/2}(\mathbb{D})$ so that its extension by zero in Π_f, $\widetilde{[g]}$, belongs to $H^{1/2}(\Pi)$. Let us define $\mathcal{E}_\Pi^- g^- = \mathcal{E}_\Pi^+ g^+ - \widetilde{[g]}$, which is also continuous. $\mathcal{E}_\Pi^+ g^+$ and $\mathcal{E}_\Pi^- g^-$ also admit liftings with compact support in the upper and lower half-spaces, given by the continuous operators $\mathcal{R}^\pm : H^{1/2}(\Pi) \to W^{1,-1}(\sigma_\pm)$. Let us define $v^\pm \in W^{1,-1}(\sigma_\pm)$ using operator composition:

$$v^\pm \;=\; \left(\mathcal{R}^\pm \circ \mathcal{E}_\Pi^\pm\right) g^\pm, \tag{2.86}$$

which has compact support on $\sigma^\pm$. We consider

$$v \;= \begin{cases} v^+ & \text{if } \boldsymbol{x} \in \sigma^+, \\ v^- & \text{if } \boldsymbol{x} \in \sigma^-, \end{cases} \tag{2.87}$$

so that $v \in W^{1,-1}(\Omega_\mathbb{D})$. This allows the definition of an operator $\mathcal{A} : \mathbb{X} \to W^{1,-1}(\Omega_\mathbb{D})$ such that $v = \mathcal{A}\boldsymbol{g}$, and for which the following continuity inequality holds,

$$\|\mathcal{A}\boldsymbol{g}\|_{W^{1,-1}(\Omega_\mathbb{D})} \;\leq\; C_\mathcal{A}\, \|\boldsymbol{g}\|_\mathbb{X} \tag{2.88}$$

because of the continuity of all the composing operators. The continuity of the trace operators provides the following result.

Lemma 2.6.1. *If $u \in W^{1,-1}(\Omega_\mathbb{D})$ is such that $\gamma_\mathbb{D}^\pm u = g^\pm$ with $(g^+, g^-) \in \mathbb{X}$, there exists a real positive constant C_X such that*

$$\|\boldsymbol{g}\|_\mathbb{X} \;\leq\; C_X\, \|u\|_{W^{1,-1}(\Omega_\mathbb{D})}\,. \tag{2.89}$$

Since by construction $\gamma_\mathbb{D}^\pm v^\pm = g^\pm$, it holds $\gamma_\mathbb{D}^\pm (u - v) = 0$ and we can rewrite Problem 2.6.1 with a homogeneous Dirichlet condition:

Problem 2.6.2. *Given $v = \mathcal{A}\boldsymbol{g}$ and $f = \Delta\, v \in \left(W_0^{1,-1}(\Omega_\mathbb{D})\right)'$, find w in $W_0^{1,-1}(\Omega_\mathbb{D})$ such that*

$$\begin{cases} -\Delta\, w \;=\; f, & \boldsymbol{x} \in \Omega_\mathbb{D}, \\ \gamma_\mathbb{D}^\pm\, w \;=\; 0, & \boldsymbol{x} \in \mathbb{D}. \end{cases} \tag{2.90}$$

Proposition 2.6.1. *There is one and only one solution $w \in W_0^{1,-1}(\Omega_\mathbb{D})$ to Problem 2.6.2.*

Proof From (2.90), we have

$$-\left\langle \Delta\, w\,,\, w^t \right\rangle_{W_0^{1,-1}(\Omega_\mathbb{D})} \;=\; \left\langle f\,,\, w^t \right\rangle_{W_0^{1,-1}(\Omega_\mathbb{D})}, \quad \forall\, w^t \in W_0^{1,-1}(\Omega_\mathbb{D}). \tag{2.91}$$

Let B_R be the open ball of radius $R > 0$ centered at zero with boundary ∂B_R and such that $\operatorname{supp}(f) \Subset B_R$. Let $\Pi_R = \Pi \cap B_R$ and $B_R^\pm = \sigma_\pm \cap B_R$ be the upper and lower half-spheres with boundaries $\partial B_R^\pm = \Pi_R \cup (\partial B_R \cap \sigma_\pm)$. For every $w^t \in W_0^{1,-1}(\Omega_\mathbb{D})$, it holds

$$-\left\langle \Delta w\,,\, w^t \right\rangle_{W_0^{1,-1}(B_R^\pm)} \;=\; \left(\nabla w\,,\, \nabla w^t\right)_{B_R^\pm} \;-\; \left\langle \gamma_{\partial B_R^\pm} \partial_n w\,,\, \gamma_{\partial B_R^\pm} w^t \right\rangle_{H^{1/2}(\partial B_R^\pm)}, \tag{2.92}$$

and addition of both half-spheres contributions yields

$$\begin{aligned} -\left\langle \Delta\, w\,,\, w^t \right\rangle_{W_0^{1,-1}(B_R \cap \Omega_\mathbb{D})} \;=\; & \left(\nabla w\,,\, \nabla w^t\right)_{B_R \cap \Omega_\mathbb{D}} \;-\; \left\langle \gamma_{\partial B_R} \partial_n w\,,\, \gamma_{\partial B_R} w^t \right\rangle_{H^{1/2}(\partial B_R)} \\ & \sum_\pm \mp \left\langle \gamma_R^\pm \partial_n w\,,\, \gamma_R^\pm w^t \right\rangle_{H^{1/2}(\Pi_R)}, \end{aligned} \tag{2.93}$$

By definition of $W^{1,-1}(\Omega_{\mathbb{D}})$, when R tends to infinity, the second term on the right-hand side vanishes. The remaining boundary term over Π_R extends now over Π wherein the splitting into $\mathbb{D}$ and Π_f holds. Since $\gamma^{\pm}_{\mathbb{D}} w^t = 0$ and $\gamma^{\pm}_{\Pi_f} w^t = \gamma_{\Pi_f} w^t$, the duality products over $\mathbb{D}$ cancel out and yield:

$$-\left\langle \gamma^{+}_{\Pi}\partial_n w \,,\, \gamma^{+}_{\Pi} w^t \right\rangle_{H^{1/2}(\Pi)} + \left\langle \gamma^{-}_{\Pi}\partial_n w \,,\, \gamma^{-}_{\Pi} w^t \right\rangle_{H^{1/2}(\Pi)} \;=\; -\left\langle \left[\gamma_{\Pi_f}\partial_n w\right] \,,\, \gamma_{\Pi_f} w^t \right\rangle_{H^{1/2}(\Pi_f)}. \tag{2.94}$$

By the transmission conditions (2.84), the above contribution disappears to obtain:

$$\Phi_D(w, w^t) \;=\; \left(\nabla w \,,\, \nabla w^t\right)_{\Omega_{\mathbb{D}}} \;=\; \left\langle f \,,\, w^t \right\rangle_{W_0^{1,-1}(\Omega_{\mathbb{D}})} \qquad \forall\, w^t \;\in\; W_0^{1,-1}(\Omega_{\mathbb{D}}). \tag{2.95}$$

The associated bilinear form is continuous and coercive on $W_0^{1,-1}(\Omega_{\mathbb{D}})$. Indeed, using semi-norm properties for this space,

$$\Phi_D(w, w) = (\nabla w \,,\, \nabla w)_{\Omega_{\mathbb{D}}} \;=\; |w|^2_{1,-1,\Omega_{\mathbb{D}}} \;\geq\; c^{-2}\, \|w\|^2_{W_0^{1,-1}(\Omega_{\mathbb{D}})} \tag{2.96}$$

by [51, Theorem 2.5.11]. Thus, by the Lax-Milgram theorem, we have uniqueness of w since f belongs to the dual space of $W_0^{1,-1}(\Omega_{\mathbb{D}})$. ∎

This allows us to prove the following result.

Proposition 2.6.2. *If $\boldsymbol{g} \in \mathbb{X}$, then Problem 2.6.1 has a unique solution in $W^{1,-1}(\Omega_{\mathbb{D}})$.*

Proof Let w^* denote the solution to Problem 2.6.2. Then, the solution to the original Problem 2.6.1 is $u^* = w^* + v$ and is independent on the lifting $v \in W^{1,-1}(\Omega_{\mathbb{D}})$. Indeed, if we let $u_i^* = w_i^* + v_i$ denote the solution for two different liftings $i = 1, 2$, then it holds

$$\begin{cases} -\Delta\,(u_1^* - u_2^*) \;=\; 0 & \boldsymbol{x} \in \Omega_{\mathbb{D}}, \\ \gamma^{\pm}_{\mathbb{D}}\,(u_1^* - u_2^*) \;=\; 0 & \boldsymbol{x} \in \mathbb{D}, \end{cases} \tag{2.97}$$

which has as a unique solution $u_1^* - u_2^* = 0$ by Proposition 2.6.1. ∎

Average and jump decomposition

The solution to Problem 2.6.1 can be split as follows. To any function u in $W^{1,-1}(\Omega_{\mathbb{D}})$, we associate restrictions $u^{\pm}$ on $\sigma_{\pm}$ belonging to $W^{1,-1}(\sigma_{\pm})$. Denote by $\breve{u}^{\pm} \in W^{1,-1}(\mathbb{R}^d)$ the mirror reflection of $u^{\pm}$ over $\sigma_{\mp}$. Average and jump solutions defined over $\mathbb{R}^3$ are written as

$$\begin{cases} u_{\text{avg}} \;=\; \dfrac{\breve{u}^{+} + \breve{u}^{-}}{2}, \\ u_{\text{jmp}} \;=\; \dfrac{\breve{u}^{+} - \breve{u}^{-}}{2}, \end{cases} \qquad \text{associated with the data} \qquad \begin{cases} g_{\text{avg}} \;=\; \dfrac{g^{+} + g^{-}}{2}, \\ g_{\text{jmp}} \;=\; \dfrac{g^{+} - g^{-}}{2}. \end{cases} \tag{2.98}$$

Normal traces can also be similarly decomposed. Due to the orientation of the normal, define them as

$$\begin{cases} \gamma_{\mathbb{D}}\partial_n u_{\text{avg}} \;=\; \frac{1}{2}\hat{\boldsymbol{e}}_3 \cdot \nabla(\breve{u}^{+} - \breve{u}^{-}), \\ \gamma_{\mathbb{D}}\partial_n u_{\text{jmp}} \;=\; \frac{1}{2}\hat{\boldsymbol{e}}_3 \cdot \nabla(\breve{u}^{+} + \breve{u}^{-}), \end{cases} \quad \text{associated with the values} \quad \begin{cases} u_{\text{avg}}, \\ u_{\text{jmp}}, \end{cases} \tag{2.99}$$

and we have the associated Green's formula (as $(\nabla u_{\text{avg}} \,,\, \nabla v_{\text{jmp}})_{\Omega_{\mathbb{D}}} = 0$):

$$(\nabla u \,,\, \nabla v)_{\Omega_{\mathbb{D}}} = \left\langle \gamma_{\mathbb{D}}\partial_n u_{\text{avg}} \,,\, \gamma_{\mathbb{D}} v_{\text{avg}} \right\rangle_{H^{1/2}(\mathbb{D})} + \left\langle \gamma_{\mathbb{D}}\partial_n u_{\text{jmp}} \,,\, \gamma_{\mathbb{D}} v_{\text{jmp}} \right\rangle_{\widetilde{H}^{1/2}(\mathbb{D})}, \tag{2.100}$$

for $v \in W^{1,-1}(\mathbb{R}^2)$ split into average and jump parts.

Proposition 2.6.3. *The solution to the Dirichlet Problem 2.6.1, is such that its Neumann trace at $\mathbb{D}$ belongs to the space $\mathbb{Y}$. There exists a unique Dirichlet-to-Neumann map $DtN : \mathbb{X} \to \mathbb{Y}$ satisfying*

$$\langle DtN\boldsymbol{g}\,,\,\boldsymbol{g}\rangle_{\mathbb{X}} \;\geq\; C\,\|\boldsymbol{g}\|^2_{\mathbb{X}}\,, \tag{2.101}$$

for $\boldsymbol{g}$ in $\mathbb{X}$, and where the vector duality product is given by:

$$\langle DtN\boldsymbol{g}\,,\,\boldsymbol{g}\rangle_{\mathbb{X}} = \left\langle DtN\boldsymbol{g}_{avg}\,,\,\boldsymbol{g}_{avg}\right\rangle_{H^{1/2}(\mathbb{D})} + \left\langle DtN\boldsymbol{g}_{jmp}\,,\,\boldsymbol{g}_{jmp}\right\rangle_{\widetilde{H}^{1/2}(\mathbb{D})}. \tag{2.102}$$

Proof By Proposition 2.6.2, a unique continuous application $\mathcal{T}_D$ exists such that

$$\begin{array}{rccl} \mathcal{T}_D \;:\; & \mathbb{X} & \longrightarrow & W^{1,-1}(\Omega_{\mathbb{D}}), \\ & \boldsymbol{g} & \longmapsto & u = \mathcal{T}_D\boldsymbol{g}. \end{array} \tag{2.103}$$

Due to the trace theorem, Theorem 1.2.1, one can construct a continuous operator

$$DtN \;=\; \begin{pmatrix}\gamma^+_{\mathbb{D}}\\ \gamma^-_{\mathbb{D}}\end{pmatrix} \circ \partial_n \circ \mathcal{T}_D \;:\; \mathbb{X} \longrightarrow H^{-1/2}(\mathbb{D}) \times H^{-1/2}(\mathbb{D}),$$

belonging to $\mathbb{Y}$ since $\gamma^+_{\mathbb{D}}\partial_n u - \gamma^-_{\mathbb{D}}\partial_n u \in \widetilde{H}^{-1/2}(\mathbb{D})$. Parity decomposition follows by taking duality with v split into average and jump parts using formula (2.100). ∎

Corollary 2.6.1. *For $g^{\pm} = g \in H^{1/2}(\mathbb{D})$, the corresponding solution to Problem 2.6.1 in $\Omega_{\mathbb{D}}$ is symmetric with respect to Π. Moreover, there exists a unique Dirichlet-to-Neumann operator $DtN_s : H^{1/2}(\mathbb{D}) \to \widetilde{H}^{-1/2}(\mathbb{D})$ satisfying*

$$\langle DtN_s g\,,\,g\rangle_{H^{1/2}(\mathbb{D})} \;\geq\; C\,\|g\|^2_{H^{1/2}(\mathbb{D})}\,. \tag{2.104}$$

Proof Since $\boldsymbol{g} = (g, g)$, the difference $g^+ - g^- = 0$ lies trivially in $\widetilde{H}^{1/2}(\mathbb{D})$ and $\boldsymbol{g} \in \mathbb{X}$. Thus, Proposition 2.6.3 holds but now the norm is

$$\|\boldsymbol{g}\|_{\mathbb{X}} = 2\,\|g\|_{H^{1/2}(\mathbb{D})}\,,$$

and the duality product becomes

$$\sum_{\pm}\left\langle \gamma^{\pm}_{\mathbb{D}}\partial_n\mathcal{T}_D\boldsymbol{g}\,,\,g^{\pm}\right\rangle_{\mathbb{D}} \;=\; 2\,\langle[\gamma_{\mathbb{D}}\partial_n\mathcal{T}_D\boldsymbol{g}]\,,\,g\rangle_{\mathbb{D}}\,, \tag{2.105}$$

where $\mathcal{T}_D$ is given in (2.103) and factors two cancel out. We obtain the desired inequality by defining $DtN_s = [\gamma_{\mathbb{D}}\partial_n\mathcal{T}_D\mathcal{I}_{2\times 2}]$ where $\mathcal{I}_{n\times n}$ is the identity matrix of dimension n. ∎

Corollary 2.6.2. *For $g^{\pm} = \pm g \in \widetilde{H}^{1/2}(\mathbb{D})$, the associated solution to Problem 2.6.1 is anti-symmetric with respect to Π and there exists a unique Dirichlet-to-Neumann operator DtN_{as} : $\widetilde{H}^{1/2}(\mathbb{D}) \to H^{-1/2}(\mathbb{D})$. Moreover, the energy inequality holds*

$$\langle DtN_{as}g\,,\,g\rangle_{\widetilde{H}^{1/2}(\mathbb{D})} \;\geq\; C\,\|g\|^2_{\widetilde{H}^{1/2}(\mathbb{D})}\,. \tag{2.106}$$

Proof Let us define $\boldsymbol{g} = (g, -g)$. The difference $g^+ - g^-$ lies trivially in $\widetilde{H}^{1/2}(\mathbb{D})$ and $\boldsymbol{g} \in \mathbb{X}$. Thus, Proposition 2.6.3 holds with

$$\|\boldsymbol{g}\|_{\mathbb{X}} = 2\,\|g\|_{\widetilde{H}^{1/2}(\mathbb{D})}\,,$$

with duality product

$$\sum_{\pm}\left\langle \gamma^{\pm}_{\mathbb{D}}\partial_n\mathcal{T}_D\boldsymbol{g}\,,\,g^{\pm}\right\rangle_{\widetilde{H}^{1/2}(\mathbb{D})} \;=\; 2\,\langle\gamma_{\mathbb{D}}\partial_n\mathcal{T}_D\boldsymbol{g}\,,\,g\rangle_{\widetilde{H}^{1/2}(\mathbb{D})}\,, \tag{2.107}$$

so that factors cancel and we obtain the desired inequality. ∎

2.6.2 Neumann problems

As in the Dirichlet case, let us define the general problem:

Problem 2.6.3. *Given $\boldsymbol{\varphi} \in \mathbb{Y}$, find $u \in W^{1,-1}(\mathbb{R}^3)$ such that*

$$\begin{cases} -\Delta u \;=\; 0, & \boldsymbol{x} \in \Omega_{\mathbb{D}}, \\ \begin{pmatrix} \gamma_{\mathbb{D}}^{+}\partial_n u \\ \gamma_{\mathbb{D}}^{-}\partial_n u \end{pmatrix} \;=\; \boldsymbol{\varphi}, & \boldsymbol{x} \in \mathbb{D}. \end{cases} \tag{2.108}$$

Proposition 2.6.4. *The Neumann Problem 2.6.3 has a unique solution in the space $W^{1,-1}(\mathbb{R}^3)$ if and only if $\boldsymbol{\varphi} \in \mathbb{Y}$.*

Proof[cf. dem of Proposition 2.6.1] For $\boldsymbol{\varphi} = (\varphi^+, \varphi^-)$ and u satisfying (2.108), we have the following variational formulation:

$$\Phi_N(u,v) = \; (\nabla u\,,\, \nabla v)_{\mathbb{R}^3} \;= \sum_{\pm} \pm \left\langle \varphi^{\pm}\,,\, \gamma^{\pm} v \right\rangle_{H^{1/2}(\mathbb{D})}, \quad \forall\, v \in W^{1,-1}(\mathbb{R}^3). \tag{2.109}$$

Clearly, the bilinear form Φ_N is coercive and continuous. On the right hand side, the dual form is well defined only if $\varphi^+ - \varphi^- \in \widetilde{H}^{-1/2}(\mathbb{D})$, since $\gamma_{\mathbb{D}}^{\pm} v = \gamma_{\mathbb{D}} v \in H^{1/2}(\mathbb{D})$. Consequently, if $\boldsymbol{\varphi}$ belongs to $\mathbb{Y}$, by the Lax-Milgram theorem, the problem has a unique solution in $W^{1,-1}(\mathbb{R}^3)$. ■

Proposition 2.6.5. *The solution to the Neumann Problem 2.6.3, is such that its Dirichlet trace at $\mathbb{D}$ belongs to the space $\mathbb{X}$. There exists a unique Neumann-to-Dirichlet map $NtD : \mathbb{Y} \to \mathbb{X}$ satisfying*

$$\langle NtD\boldsymbol{\varphi}\,,\, \boldsymbol{\varphi}\rangle_{\mathbb{Y}} \;\geq\; C\,\|\boldsymbol{\varphi}\|_{\mathbb{Y}}^2, \tag{2.110}$$

for $\boldsymbol{\varphi}$ in $\mathbb{Y}$, and where the vector duality product is given by:

$$\langle NtD\boldsymbol{\varphi}\,,\, \boldsymbol{\varphi}\rangle_{\mathbb{Y}} = \left\langle NtD\boldsymbol{\varphi}_{avg}\,,\, \boldsymbol{\varphi}_{avg}\right\rangle_{\widetilde{H}^{-1/2}(\Pi_c)} + \left\langle NtD\boldsymbol{\varphi}_{jmp}\,,\, \boldsymbol{\varphi}_{jmp}\right\rangle_{H^{-1/2}(\mathbb{D})}. \tag{2.111}$$

Proof By Proposition 2.6.4, a unique continuous application $\mathcal{T}_N$ exists such that

$$\begin{array}{rccl} \mathcal{T}_N \;:\; & \mathbb{Y} & \longrightarrow & W^{1,-1}(\Omega_{\mathbb{D}}), \\ & \boldsymbol{\varphi} & \longmapsto & u = \mathcal{T}_N\boldsymbol{\varphi}. \end{array} \tag{2.112}$$

Due to the trace theorem, one can construct a continuous operator

$$NtD = \begin{pmatrix} \gamma_{\mathbb{D}}^{+} \\ \gamma_{\mathbb{D}}^{-} \end{pmatrix} \circ \mathcal{T}_D \;:\; \mathbb{Y} \longrightarrow H^{1/2}(\mathbb{D}) \times H^{1/2}(\mathbb{D}),$$

belonging to $\mathbb{X}$ since $\gamma_{\mathbb{D}}^{+} u - \gamma_{\mathbb{D}}^{-} u \in \widetilde{H}^{1/2}(\mathbb{D})$. Parity decomposition follows by taking the duality pairing with v split into average and jump parts using formula (2.100). ■

The symmetric and anti-symmetric Neumann problems for the disk can be stated as follows:

Problem 2.6.4. *Find $u_s, u_{as} \in W^{1,-1}(\mathbb{R}^3)$ such that*

$$\begin{cases} -\Delta u_s \;=\; 0, & \boldsymbol{x} \in \Omega_{\mathbb{D}}, \\ [\gamma_{\mathbb{D}}\partial_n u_s] \;=\; \varphi, & \boldsymbol{x} \in \mathbb{D}, \end{cases} \quad \textit{and} \quad \begin{cases} -\Delta u_{as} \;=\; 0, & \boldsymbol{x} \in \Omega_{\mathbb{D}}, \\ \gamma_{\mathbb{D}}^{\pm}\partial_n u_{as} = \varphi, & \boldsymbol{x} \in \mathbb{D}, \end{cases} \tag{2.113}$$

for data φ in the space $\widetilde{H}^{-1/2}(\mathbb{D})$ and φ in $H^{-1/2}(\mathbb{D})$ respectively.

Corollary 2.6.3. *The symmetric Neumann Problem 2.6.4 has a unique solution in* $W^{1,-1}(\mathbb{R}^3)$ *if and only if* $\varphi \in \widetilde{H}^{-1/2}(\mathbb{D})$*. Thus, there exists a unique continuous and invertible Neumann-to-Dirichlet operator, denoted* $NtD_s : \widetilde{H}^{-1/2}(\mathbb{D}) \to H^{1/2}(\mathbb{D})$*. Moreover, the energy inequality holds*

$$\langle NtD_s\varphi\,,\,\varphi\rangle_{\mathbb{D}} \;\geq\; C\,\|\varphi\|^2_{\widetilde{H}^{-1/2}(\mathbb{D})}\,. \tag{2.114}$$

The inverse of this application is the operator DtN_s *defined in Corollary 2.6.1.*

Proof Same as for Proposition 2.6.4 using

$$\Phi_N(u,v) \;=\; (\nabla u\,,\,\nabla v)_{\mathbb{R}^3} \;=\; \langle\varphi\,,\,\gamma_{\mathbb{D}}v\rangle_{\mathbb{D}}\,, \qquad \forall\, v \in W^{1,-1}(\mathbb{R}^3), \tag{2.115}$$

and replacing $\varphi^+ - \varphi^-$ with φ. ∎

Corollary 2.6.4. *The anti-symmetric Neumann problem 2.6.4 has a unique solution in* $W^{1,-1}(\mathbb{R}^3)$ *if and only if* $\varphi \in H^{-1/2}(\mathbb{D})$*. Hence, there exists a unique continuous and invertible operator* $NtD_{as} : H^{-1/2}(\mathbb{D}) \to \widetilde{H}^{1/2}(\mathbb{D})$ *satisfying*

$$\langle NtD_{as}\varphi\,,\,\varphi\rangle_{\mathbb{D}} \;\geq\; C\,\|\varphi\|^2_{H^{-1/2}(\mathbb{D})}\,. \tag{2.116}$$

The inverse of this application is the operator DtN_{as} *defined in Corollary 2.6.2.*

Proof Follows the one for Proposition 2.6.5. Operator $\mathcal{T}_N$ becomes

$$\begin{array}{rcl} \mathcal{T}_N \;:\; H^{-1/2}(\mathbb{D}) & \longrightarrow & W^{1,-1}(\mathbb{R}^3), \\ \varphi & \longmapsto & u \,=\, \mathcal{T}_N\varphi. \end{array}$$

and we can construct an operator $NtD_{as} = [\gamma_{\mathbb{D}} \circ \mathcal{T}_N]$ with range in $\widetilde{H}^{1/2}(\mathbb{D})$. Thus,

$$\langle NtD_{as}\varphi\,,\,\varphi\rangle_{\mathbb{D}} \;=\; (\nabla u\,,\,\nabla u)_{\mathbb{R}^3} \;=\; |u|^2_{1,-1,\mathbb{R}^3} \;\geq\; C_1\,\|\gamma_{\mathbb{D}}u\|^2_{\widetilde{H}^{1/2}(\mathbb{D})}\,, \tag{2.117}$$

by continuity of the lifting operator. This proves the invertibility of NtD_{as}. Moreover, since NtD_{as} is also continuous, it holds

$$\|\varphi\|_{H^{-1/2}(\mathbb{D})} \;=\; \left\|NtD_{as}^{-1}\gamma_{\mathbb{D}}u\right\|_{H^{-1/2}(\mathbb{D})} \;\leq\; C_2\,\|\gamma_{\mathbb{D}}u\|_{\widetilde{H}^{1/2}(\mathbb{D})}\,, \tag{2.118}$$

which combined with the previous inequality yields the desired result. ∎

2.6.3 Inverses

We will briefly state the main conclusions of the present section in the following remarks. They will state in further detail the fact that the boundary integral operators $\mathcal{S}$ and $\mathcal{N}$ are Neumann-to-Dirichlet and Dirichlet-to-Neumann operators, that they have inverses, but that they have so far been only expressed using abstract applications that solve the Dirichlet and Neumann problems, and thus do not have yet explicit form.

Remark 2.6.1 ($\mathcal{S}$ is NtD_s and $\mathcal{N}$ is DtN_{as})**.** *It can be seen from Theorem 2.3.1 and Corollary 2.6.1 that we can identify the boundary integral operator* $\mathcal{S}$ *with the Neumann-to-Dirichlet operator* NtD_s*. Likewise, it can be seen from Theorem 2.3.2 and Corollary 2.6.4 that we can identify the boundary integral operator* $\mathcal{N}$ *with the Dirichlet-to-Neumann operator* DtN_{as}*.*

Remark 2.6.2 (NtD_s has DtN_s as inverse and DtN_{as} has NtD_{as} as inverse)**.** *By construction, for the symmetric Dirichlet problem, the Dirichlet-to-Neumann operator* DtN_s *takes Dirichlet data and provides the Neumann traces of the solution. Also, for the symmetric Neumann problem, the Neumann-to-Dirichlet operator* NtD_s *takes Neumann data and provides the Dirichlet traces of the solution. Operators* DtN_{as} *and* NtD_{as} *are linked in the same manner for the anti-symmetric problems.*

Remark 2.6.3 (DtN_s and NtD_{as} don't have explicit forms so far)**.** *In the previous development presented in this chapter, operators DtN_s and NtD_{as} have been constructed using abstract operators that solve Dirichlet and Neumann problems from given boundary data via the Lax-Mailgram theorem, and thus do not have explicit form. Indeed, operator DtN_s is built using operator $\mathcal{T}_D$ from (2.103) that takes Dirichlet data on $\mathbb{D}$ and provides the solution in the problem domain $\Omega_{\mathbb{D}}$. Likewise, operator NtD_{as} is built using operator $\mathcal{T}_N$ from Equation 2.112 that takes Neumann data on $\mathbb{D}$ and provides the solution in the domain.*

In their present form, inverse operators do not contribute to the optimal preconditioning strategy because they do not have an explicit form usable in numerical methods resulting in a Galerkin matrix. In what follows in this chapter we will find suitable explicit forms that can be included in a preconditioning strategy. The following Table 2.3 summarizes the results so far.

Table 2.3: Boundary integral operators $\mathcal{S}$ and $\mathcal{N}$ are identified with NtD_s and DtN_{as} respectively, for which DtN_{as} and NtD_s are identified inverses, although not having explicit form.

BIO	Closed form kernel	D.-to-N./N-to-D.	Mappings
$\mathcal{S}$	K^{ws}	NtD_s	$\widetilde{H}^{-1/2}(\mathbb{D}) \to H^{1/2}(\mathbb{D})$
$\mathcal{N}$	K^{hs}	DtN_{as}	$\widetilde{H}^{1/2}(\mathbb{D}) \to H^{-1/2}(\mathbb{D})$
$\mathcal{S}^{-1}$		DtN_s	$H^{1/2}(\mathbb{D}) \to \widetilde{H}^{-1/2}(\mathbb{D})$
$\mathcal{N}^{-1}$		NtD_{as}	$H^{-1/2}(\mathbb{D}) \to \widetilde{H}^{1/2}(\mathbb{D})$

2.7 Series forms for the boundary integral operators and their inverses

In this section we will develop bases for the functional spaces involved in the Dirichlet and Neumann problems on the disk. This will allow us to rewrite boundary integral operators $\mathcal{S}$ and $\mathcal{N}$ in series form, using series expressions of the integral kernels. This will allow for an explicit expression for their inverses, also in series form.

The main tool for the development of disk basis functions will be the results for the case of a boundary integral operators on the unit sphere $\mathbb{S}$ in $\mathbb{R}^3$. Firstly, the referred results for the spherical case will be presented. Then, the basis disk functions will be defined in relation to the ones on the sphere. This will allow for the definition of series expressions of the functions in the spaces involved in the Dirichlet and Neumann problems. Finally, previously mentioned facts about the already developed two-dimensional case, and some other well established results, will suggest the construction of integral kernels that will define four new boundary integral operators. These boundary integral operators will be then identified as the four operators from the previous section, thus giving a series expression for $\mathcal{S}$, $\mathcal{N}$ and their inverses.

2.7.1 Spherical Harmonics: symmetry and parity

In the present subsection we will establish some useful facts about bases for functions defined on unit sphere $\mathbb{S}$.

Definition 2.7.1 (Spherical Harmonics)**.** *The $2l+1$ Spherical Harmonics of order $l > 0$ are the functions $Y_l^m : \mathbb{S} \to \mathbb{C}$ defined as*

$$Y_l^m(\theta, \phi) = \gamma_l^m e^{\mathrm{i}m\phi} I\!P_l^m(\cos\theta), \text{ for } -l \leq m \leq l, \tag{2.119}$$

where $I\!P_l^m$ is the Associated Legendre Function of order l and degree m, and γ_l^m is a normalization constant defined as

$$\gamma_l^m = (-1)^m \sqrt{\frac{l+1/2}{2\pi}} \sqrt{\frac{(l-m)!}{(l+m)!}}. \tag{2.120}$$

Proposition 2.7.1 (Hilbert basis for $L^2(\mathbb{S})$ [51, Theorem 2.4.4])**.** *The Spherical Harmonics are a Hilbert basis (i.e. orthogonal and normal) for the Hilbert space $L^2(\mathbb{S})$ endowed with the natural inner product*

$$(u, v)_{L^2(\mathbb{S})} = \int_{\mathbb{S}} u\bar{v} d\mathbb{S}. \tag{2.121}$$

It will be useful to define angular momentum differential operators that will later simplify the writing of many identities.

Definition 2.7.2 (Angular momenta on the sphere [51, Section 2.4.1])**.** *Let us consider the following differential operations, called angular momenta, for a function u defined on the unit sphere $\mathbb{S}$:*

$$L_\pm u = e^{\pm \mathrm{i}\phi} \left(\pm \frac{\partial u}{\partial \theta} + \mathrm{i} \frac{\cos\theta}{\sin\theta} \frac{\partial u}{\partial \phi} \right), \quad \text{and} \quad L_3 u = \frac{1}{\mathrm{i}} \frac{\partial u}{\partial \phi}. \tag{2.122}$$

Some properties regarding differential operators' action over Spherical Harmonics will also be used.

Lemma 2.7.1 (Angular momenta action on the Spherical Harmonics [51, Theorem 2.4.4])**.** *The action of the angular momentum operators on the Spherical Harmonics provide the following identities:*

$$L_\pm Y_l^m = \sqrt{(l \mp m)(l \pm m + 1)} Y_l^{m\pm 1}, \quad \text{and} \quad L_3 Y_l^m = m Y_l^m. \tag{2.123}$$

Proposition 2.7.2 (Derivaties of the Spherical Harmonics)**.** *A Spherical Harmonic Y_l^m has the following derivatives:*

$$\frac{\partial Y_l^m}{\partial \theta} = \frac{1}{2}\left(e^{-\mathrm{i}\phi}\sqrt{(l-m)(l+m+1)}Y_l^{m+1} - e^{\mathrm{i}\phi}\sqrt{(l+m)(l-m+1)}Y_l^{m-1}\right), \tag{2.124}$$

$$\frac{\partial Y_l^m}{\partial \phi} = -\frac{\mathrm{i}\sin\theta}{2\cos\theta}\left(e^{-\mathrm{i}\phi}\sqrt{(l-m)(l+m+1)}Y_l^{m+1} + e^{\mathrm{i}\phi}\sqrt{(l+m)(l-m+1)}Y_l^{m-1}\right). \tag{2.125}$$

Proof The computation of the derivatives of the Spherical Harmonics comes straightforwardly from the application of the previous Lemma 2.7.1. ∎

The parity of a Spherical Harmonics Y_l^m with respect to the variable x_3 is the same as the parity of $l+m$, and thus the spaces generated by the Spherical Harmonics can be split into two subspaces according to parity.

Definition 2.7.3 (Parity splitting of Spherical Harmonics)**.** *Let us define the two following subsets of the set of Spherical Harmonics according to their parity:*

$$Y_s = \{Y_l^m : l \geq 0,\ -l \leq m \leq l,\ \textit{and } l+m \textit{ is even}\}, \tag{2.126}$$

$$Y_{as} = \{Y_l^m : l \geq 0,\ -l \leq m \leq l,\ \textit{and } l+m \textit{ is odd}\}. \tag{2.127}$$

Remark 2.7.1 (Parity and symmetry)**.** *The Spherical Harmonics belonging to Y_s are symmetrical with respect to plane Π, and their value is not zero for all points on the equator ($x_3 = 0$) of sphere $\mathbb{S}$. The Spherical Harmonics belonging to Y_{as} are anti-symmetric with respect to plane Π, and their values are zero on the equator.*

Proposition 2.7.3 (Orthogonality in $\mathbb{S}^+$)**.** *If l_1+m_1 and l_2+m_2 have the same parity, the following orthogonality identity holds:*

$$\int_{\mathbb{S}^+} Y_{l_1}^{m_1}(\boldsymbol{x})\overline{Y_{l_2}^{m_2}(\boldsymbol{x})}d\mathbb{S}^+(\boldsymbol{x}) = \frac{1}{2}\delta_{m_2}^{m_1}\delta_{l_2}^{l_1}. \tag{2.128}$$

Proof

$$\int_{\mathbb{S}^+} Y_{l_1}^{m_1}(\boldsymbol{x})\overline{Y_{l_2}^{m_2}(\boldsymbol{x})}d\mathbb{S}^+(\boldsymbol{x}) = \gamma_{l_1}^{m_1}\gamma_{l_2}^{m_2}\int_0^{\pi/2} I\!P_{l_1}^{m_1}(\cos\theta)I\!P_{l_2}^{m_2}(\cos\theta)\sin\theta d\theta \int_0^{2\pi} e^{\mathrm{i}(m_1-m_2)\phi}d\phi \tag{2.129}$$

$$= \gamma_{l_1}^{m_1}\gamma_{l_2}^{m_2}2\pi\delta_{m_2}^{m_1}\int_0^1 I\!P_{l_1}^{m_1}(t)I\!P_{l_2}^{m_2}(t)dt. \tag{2.130}$$

Since l_1+m_1 and l_2+m_2 have the same parity, $I\!P_{l_1}^{m_1}$ and $I\!P_{l_2}^{m_2}$ will also have the same parity, and thus $I\!P_{l_1}^{m_1}I\!P_{l_2}^{m_2}$ will always be a pair function, which implies that

$$\int_0^1 I\!P_{l_1}^{m_1}(t)I\!P_{l_2}^{m_2}(t)dt = \frac{1}{2}\int_{-1}^1 I\!P_{l_1}^{m_1}(t)I\!P_{l_2}^{m_2}(t)dt, \tag{2.131}$$

from which we get

$$\int_{\mathbb{S}^+} Y_{l_1}^{m_1}(\boldsymbol{x})\overline{Y_{l_2}^{m_2}(\boldsymbol{x})}d\mathbb{S}^+(\boldsymbol{x}) = \frac{1}{2}\int_{\mathbb{S}} Y_{l_1}^{m_1}(\boldsymbol{x})\overline{Y_{l_2}^{m_2}(\boldsymbol{x})}d\mathbb{S}(\boldsymbol{x}) = \frac{1}{2}\delta_{m_2}^{m_1}\delta_{l_2}^{l_1}. \tag{2.132}$$

∎

The orthogonality property stated in the last proposition only works for pairs of Spherical Harmonic functions having the same parity. This feature will become a key aspect of the tools that will be developed in what follows.

2.7.2 Disk basis functions

Proposition 2.7.3 allows us to use orthogonality properties on the upper half-sphere, which will allow us to define similar properties for vertical projections onto the disk.

Definition 2.7.4 (The $\mathcal{Y}$ set)**.** *Let us consider the Spherical Harmonics Y_l^m on sphere $\mathbb{S}$. We define $\mathcal{Y}$, as the set of functions defined on $\mathbb{D}$ resulting from the composition of a projection from the disk onto the upper half-sphere, and the Spherical Harmonics:*

$$\mathcal{Y} = \left\{ y_l^m \in C^\infty(\mathbb{D}) : y_l^m(\boldsymbol{x}) = Y_l^m(\boldsymbol{x}^+),\ \textit{for } \boldsymbol{x} \in \mathbb{D} \right\}. \tag{2.133}$$

Notation 2.7.1 (Notation for arguments of the basis functions)**.** *Spherical Harmonics and disk basis functions can have their arguments expressed in the following equivalent ways:*

$$y_l^m(\boldsymbol{x}) = y_l^m(\rho,\phi) = \gamma_l^m e^{\mathrm{i}m\phi} I\!P_l^m(w(\rho)) = Y_l^m(\theta(\boldsymbol{x}^+),\phi(\boldsymbol{x}^+)) = Y_l^m(\boldsymbol{x}^+). \tag{2.134}$$

Remark 2.7.2 (First Associated Legendre Polynomials)**.** *The following table, Table 2.4, shows the first values of the Associated Legendre Polynomials involved in the functions of the set $\mathcal{Y}$, i.e., $I\!P_l^m(w(\rho))$. It is noteworthy that, when $l+m$ is even, $I\!P_l^m(w(\rho))$ is a polynomial, whereas $l+m$ odd renders $I\!P_l^m(w(\rho)) = w(\rho)p_l^m(\rho)$, where is p_l^m is a polynomial.*

Table 2.4: First values of the Associated Legendre Polynomials evaluated at $w(\rho)$, as used in the definition of the functions of $\mathcal{Y}$.

$I\!P_l^m(w(\rho))$	$m=-3$	$m=-2$	$m=-1$	$m=0$	$m=1$	$m=2$	$m=3$
$l=0$				1			
$l=1$			$\rho/2$	$\sqrt{1-\rho^2}$	$-\rho$		
$l=2$		$\frac{1}{8}\rho^2$	$\frac{1}{2}\rho\sqrt{1-\rho^2}$	$1-\frac{3\rho^2}{2}$	$-3\rho\sqrt{1-\rho^2}$	$3\rho^2$	
$l=3$	$\frac{1}{48}\rho^3$	$\frac{1}{8}\rho^2\sqrt{1-\rho^2}$	$\frac{1}{8}\rho\left(4-5\rho^2\right)$	$\sqrt{1-\rho^2}\left(1-\frac{5}{2}\rho^2\right)$	$-\frac{3\rho}{2}\left(4-5\rho^2\right)$	$15\rho^2\sqrt{1-\rho^2}$	$-15\rho^3$

Definition 2.7.5 (The $\mathcal{Y}_s$ and $\mathcal{Y}_{as}$ sets)**.** *We split the functions from $\mathcal{Y}$ into two subsets according to parity as follows:*

$$\mathcal{Y}_s = \{ y_l^m \in \mathcal{Y} : l+m \textit{ is even} \}, \tag{2.135}$$

$$\mathcal{Y}_{as} = \{ y_l^m \in \mathcal{Y} : l+m \textit{ is odd} \}. \tag{2.136}$$

Definition 2.7.6 (The $\mathcal{Y}_s^{1/w}$ and $\mathcal{Y}_{as}^{1/w}$ sets)**.** *Let us now define the following new sets based on the previous ones:*

$$\mathcal{Y}_s^{1/w} = \left\{ \frac{y_l^m}{w} : y_l^m \in \mathcal{Y}_s \right\}, \tag{2.137}$$

$$\mathcal{Y}_{as}^{1/w} = \left\{ \frac{y_l^m}{w} : y_l^m \in \mathcal{Y}_{as} \right\}. \tag{2.138}$$

Remark 2.7.3 (Behavior at the edge of $\mathbb{D}$)**.** *The properties of the Associated Legendre Functions determine that $I\!P_l^m(w(\rho))$ is a polynomial on ρ whenever $l+m$ is even, and a polynomial times function $\sqrt{1-\rho^2}$ whenever $l+m$ is odd. That means that they can be expressed as $p(\rho)\sqrt{1-\rho^2}$, where p is a polynomial. This determines the behavior of the disk basis functions near the border of $\mathbb{D}$:*

- *In the radial direction, functions belonging to $\mathcal{Y}_s$ behave as polynomials.*
- *In the radial direction, functions belonging to $\mathcal{Y}_{as}$ go to zero as $\sqrt{1-\rho^2}$ near $\rho=1$.*
- *In the radial direction, functions belonging to $\mathcal{Y}_s^{1/w}$ have a singularity that behaves as $1/\sqrt{1-\rho^2}$ near $\rho=1$.*
- *In the radial direction, functions belonging to $\mathcal{Y}_{as}^{1/w}$ behave as polynomials.*

2.7.3 Some identities on the disk

Proposition 2.7.4 (Orthogonality identity for $\mathbb{D}$)**.** *If l_1+m_1 and l_2+m_2 have the same parity, the following orthogonality identity holds:*

$$\int_{\mathbb{D}} \frac{y_{l_1}^{m_1}(\boldsymbol{x})\overline{y_{l_2}^{m_2}(\boldsymbol{x})}}{w(\boldsymbol{x})} d\mathbb{D}(\boldsymbol{x}) = \frac{1}{2}\delta_{m_2}^{m_1}\delta_{l_2}^{l_1}. \tag{2.139}$$

Proof The change of variable $\rho = \sin\theta$, along with the identity

$$y_l^m(\rho,\phi) = Y_l^m(\theta(\boldsymbol{x}^+),\phi(\boldsymbol{x}^+)), \tag{2.140}$$

implies that

$$\int_{\mathbb{D}} \frac{y_{l_1}^{m_1}(\boldsymbol{x})\overline{y_{l_2}^{m_2}(\boldsymbol{x})}}{w(\boldsymbol{x})} d\mathbb{D}(\boldsymbol{x}) = \int_{\mathbb{S}^+} Y_{l_1}^{m_1}(\boldsymbol{x})\overline{Y_{l_2}^{m_2}(\boldsymbol{x})} d\mathbb{S}^+(\boldsymbol{x}), \tag{2.141}$$

for which Proposition 2.7.3 finishes the proof. ∎

Lemma 2.7.2 (Conjugated disk basis functions)**.**

$$\overline{y_l^m(\boldsymbol{x})} = (-1)^m y_l^{-m}(\boldsymbol{x}). \tag{2.142}$$

Proof Direct application of the conjugation yields

$$\overline{y_l^m(\boldsymbol{x})} = \gamma_l^m e^{-\mathrm{i}m\phi} I\!P_l^m(w(\rho(\boldsymbol{x}))). \tag{2.143}$$

From the properties of the Associated Legendre Functions [3, Section 8.2], we know that:

$$I\!P_l^m(w(\rho(\boldsymbol{x}))) = (-1)^m \frac{(l+m)!}{(l-m)!} I\!P_l^{-m}(w(\rho(\boldsymbol{x}))) \tag{2.144}$$

$$\Rightarrow \overline{y_l^m(\boldsymbol{x})} = (-1)^m \frac{(l+m)!}{(l-m)!} \gamma_l^m e^{-\mathrm{i}m\phi} I\!P_l^{-m}(w(\rho(\boldsymbol{x}))) \tag{2.145}$$

$$= (-1)^m \frac{(l+m)!}{(l-m)!} (-1)^m \sqrt{\frac{l+1/2}{2\pi}} \sqrt{\frac{(l-m)!}{(l+m)!}} e^{-\mathrm{i}m\phi} I\!P_l^{-m}(w(\rho(\boldsymbol{x}))) \tag{2.146}$$

$$= (-1)^m \left((-1)^m \sqrt{\frac{l+1/2}{2\pi}} \sqrt{\frac{(l+m)!}{(l-m)!}} \right) e^{-\mathrm{i}m\phi} I\!P_l^{-m}(w(\rho(\boldsymbol{x}))) \tag{2.147}$$

$$= (-1)^m \gamma_l^{-m} e^{-\mathrm{i}m\phi} I\!P_l^{-m}(w(\rho(\boldsymbol{x}))). \tag{2.148}$$

∎

Corollary 2.7.1 (Variations to orthogonality on $\mathbb{D}$)**.** *If $l_1 + m_1$ and $l_2 + m_2$ have the same parity, the following orthogonality identity holds:*

$$\int_{\mathbb{D}} \frac{y_{l_1}^{m_1}(\boldsymbol{x}) y_{l_2}^{m_2}(\boldsymbol{x})}{w(\boldsymbol{x})} d\mathbb{D}(\boldsymbol{x}) = \int_{\mathbb{D}} \frac{\overline{y_{l_1}^{m_1}(\boldsymbol{x})}\,\overline{y_{l_2}^{m_2}(\boldsymbol{x})}}{w(\boldsymbol{x})} d\mathbb{D}(\boldsymbol{x}) = \frac{(-1)^m}{2}\delta_{l_2}^{l_1}\delta_{m_2}^{-m_1}, \tag{2.149}$$

with $m = |m_1| = |m_2|$ whenever $m_1 = -m_2$.

Definition 2.7.7 (Angular momenta on the disk)**.** *Similarly as in Definition 2.7.2, let us define the following differential operators over functions defined on $\mathbb{D}$:*

$$\mathcal{L}_\pm u = e^{\pm \mathrm{i}\phi}\left(\pm\frac{\partial u}{\partial \rho} + \mathrm{i}\frac{1}{\rho}\frac{\partial u}{\partial \phi}\right), \quad \mathcal{L}_3 u = \frac{1}{\mathrm{i}}\frac{\partial u}{\partial \phi}. \tag{2.150}$$

Proposition 2.7.5 (Conjugated angular momenta)**.**

$$\overline{\mathcal{L}_{\pm}u} = -\mathcal{L}_{\mp}\overline{u}, \quad \overline{\mathcal{L}_3 u} = -\mathcal{L}_3\overline{u}. \tag{2.151}$$

Proof The proof comes straightforwardly from the definition of the angular momenta operators on the disk. ∎

Proposition 2.7.6 (Laplace-Beltrami operators as a composition of angular momentum operators)**.** *The Laplace-Beltrami operator on disk $\mathbb{D}$ can be written using the angular momenta as*

$$\Delta_{\mathbb{D}}u = -\mathcal{L}_+ \circ \mathcal{L}_- u = -\mathcal{L}_- \circ \mathcal{L}_+ u. \tag{2.152}$$

Proof In cylindrical coordinates, the Laplace-Beltrami operators are known to have the following expression:

$$\Delta_{\mathbb{D}}u = \frac{\partial^2 u}{\partial\rho^2} + \frac{1}{\rho}\frac{\partial u}{\partial\rho} + \frac{1}{\rho^2}\frac{\partial^2 u}{\partial\phi^2}. \tag{2.153}$$

Using the partial derivates,

$$\frac{\partial}{\partial\rho}\left(\mathcal{L}_{\pm}u\right) = e^{\pm i\phi}\left(\pm\frac{\partial^2 u}{\partial\rho^2} - \frac{\mathrm{i}}{\rho^2}\frac{\partial u}{\partial\phi} + \frac{\mathrm{i}}{\rho}\frac{\partial^2 u}{\partial\rho\partial\phi}\right), \tag{2.154}$$

$$\frac{\partial}{\partial\phi}\left(\mathcal{L}_{\pm}u\right) = \pm\mathrm{i}e^{\pm i\phi}\left(\pm\frac{\partial u}{\partial\rho} + \frac{\mathrm{i}}{\rho}\frac{\partial u}{\partial\phi}\right) + e^{\pm i\phi}\left(\pm\frac{\partial^2 u}{\partial\rho\partial\phi} + \frac{\mathrm{i}}{\rho}\frac{\partial^2 u}{\partial\phi^2}\right), \tag{2.155}$$

we can calculate

$$\mathcal{L}_+\left(\mathcal{L}_- u\right) = \mathcal{L}_-\left(\mathcal{L}_+ u\right) = -\frac{\partial^2 u}{\partial\rho^2} - \frac{\mathrm{i}}{\rho^2}\frac{\partial u}{\partial\phi} + \frac{\mathrm{i}}{\rho}\frac{\partial^2 u}{\partial\rho\partial\phi} - \frac{1}{\rho}\frac{\partial u}{\partial\rho} + \frac{\mathrm{i}}{\rho^2}\frac{\partial u}{\partial\phi} - \frac{\mathrm{i}}{\rho}\frac{\partial^2 u}{\partial\phi\partial\rho} - \frac{1}{\rho^2}\frac{\partial^2 u}{\partial^2\phi}, \tag{2.156}$$

from which the desired result is straightforward. ∎

Notation 2.7.2 (Angular momenta for functions of two variables)**.** *When applied to a function of two variables, e.g. $\boldsymbol{x}$ and $\boldsymbol{y}$, the variable on which the angular momentum operators are applied is noted as a superscript:*

$$\mathcal{L}^{\boldsymbol{x}}_{\pm}u = e^{\pm\mathrm{i}\phi_{\boldsymbol{x}}}\left(\pm\frac{\partial u}{\partial\rho_{\boldsymbol{x}}} + \mathrm{i}\frac{1}{\rho_{\boldsymbol{x}}}\frac{\partial u}{\partial\phi_{\boldsymbol{x}}}\right), \quad \mathcal{L}^{\boldsymbol{x}}_3 u = \frac{1}{\mathrm{i}}\frac{\partial u}{\partial\phi_{\boldsymbol{x}}}. \tag{2.157}$$

Proposition 2.7.7 (Inner product representation for the $\overrightarrow{\mathrm{grad}}_{\mathbb{D}}$ and $\overrightarrow{\mathrm{curl}}_{\mathbb{D}}$ operators over complex functions)**.** *If u and v are complex functions defined on $\mathbb{D}$, we have that*

$$\left(\overrightarrow{curl}_{\mathbb{D}}u(\boldsymbol{x}), \overrightarrow{curl}_{\mathbb{D}}v(\boldsymbol{y})\right) = \left(\overrightarrow{grad}_{\mathbb{D}}u(\boldsymbol{x}), \overrightarrow{grad}_{\mathbb{D}}v(\boldsymbol{y})\right), \tag{2.158}$$

and that they are equal to

$$-\frac{1}{2}\left(\mathcal{L}_+u(\boldsymbol{x})\mathcal{L}_-\overline{v(\boldsymbol{y})} + \mathcal{L}_-u(\boldsymbol{x})\mathcal{L}_+\overline{v(\boldsymbol{y})}\right). \tag{2.159}$$

Proof We start by recalling the expressions for the $\overrightarrow{\mathrm{grad}}_{\mathbb{D}}$ and $\overrightarrow{\mathrm{curl}}_{\mathbb{D}}$ on the disk:

$$\overrightarrow{\mathrm{grad}}_{\mathbb{D}}u = \begin{pmatrix} \cos\phi\frac{\partial u}{\partial\rho} - \frac{\sin\phi}{\rho}\frac{\partial u}{\partial\phi} \\ \sin\phi\frac{\partial u}{\partial\rho} + \frac{\cos\phi}{\rho}\frac{\partial u}{\partial\phi} \end{pmatrix}, \tag{2.160}$$

$$\overrightarrow{\mathrm{curl}}_{\mathbb{D}}u = \begin{pmatrix} \sin\phi\frac{\partial u}{\partial\rho} + \frac{\cos\phi}{\rho}\frac{\partial u}{\partial\phi} \\ -\cos\phi\frac{\partial u}{\partial\rho} + \frac{\sin\phi}{\rho}\frac{\partial u}{\partial\phi} \end{pmatrix}. \tag{2.161}$$

We observe that

$$\mathcal{L}_+ u = \left(\cos\phi \frac{\partial u}{\partial \rho} - \frac{\sin\phi}{\rho} \frac{\partial u}{\partial \phi} \right) + \mathrm{i} \left(\sin\phi \frac{\partial u}{\partial \rho} + \frac{\cos\phi}{\rho} \frac{\partial u}{\partial \phi} \right), \tag{2.162}$$

$$\mathcal{L}_- u = \left(-\cos\phi \frac{\partial u}{\partial \rho} + \frac{\sin\phi}{\rho} \frac{\partial u}{\partial \phi} \right) + \mathrm{i} \left(\sin\phi \frac{\partial u}{\partial \rho} + \frac{\cos\phi}{\rho} \frac{\partial u}{\partial \phi} \right). \tag{2.163}$$

Using these expressions we can write the gradient and the curl operators as

$$\overrightarrow{\mathrm{grad}}_{\mathbb{D}} u = \frac{1}{2} \begin{pmatrix} \mathcal{L}_+ u - \mathcal{L}_- u \\ -\mathrm{i}\mathcal{L}_+ u - \mathrm{i}\mathcal{L}_- u \end{pmatrix}, \tag{2.164}$$

$$\overrightarrow{\mathrm{curl}}_{\mathbb{D}} u = -\frac{1}{2} \begin{pmatrix} \mathrm{i}\mathcal{L}_+ u + \mathrm{i}\mathcal{L}_- u \\ \mathcal{L}_+ u - \mathcal{L}_- u \end{pmatrix}. \tag{2.165}$$

We also recall the expression for the inner product of complex vectors on $\mathbb{D}$: $(\boldsymbol{x}\,,\,\boldsymbol{y}) = \boldsymbol{x}\overline{\boldsymbol{y}}^T$, giving us the expressions:

$$\left(\overrightarrow{\mathrm{grad}}_{\mathbb{D}} u(\boldsymbol{x})\,,\, \overrightarrow{\mathrm{grad}}_{\mathbb{D}} v(\boldsymbol{y}) \right) = \overrightarrow{\mathrm{grad}}_{\mathbb{D}} u(\boldsymbol{x}) \overline{\left(\overrightarrow{\mathrm{grad}}_{\mathbb{D}} v(\boldsymbol{y}) \right)}^T, \tag{2.166}$$

$$\left(\overrightarrow{\mathrm{curl}}_{\mathbb{D}} u(\boldsymbol{x})\,,\, \overrightarrow{\mathrm{curl}}_{\mathbb{D}} v(\boldsymbol{y}) \right) = \overrightarrow{\mathrm{curl}}_{\mathbb{D}} u(\boldsymbol{x}) \overline{\left(\overrightarrow{\mathrm{curl}}_{\mathbb{D}} v(\boldsymbol{y}) \right)}^T. \tag{2.167}$$

From the previous expressions it becomes evident that

$$\begin{aligned} \left(\overrightarrow{\mathrm{curl}}_{\mathbb{D}} u(\boldsymbol{x}), \overrightarrow{\mathrm{curl}}_{\mathbb{D}} v(\boldsymbol{y}) \right) &= \left(\overrightarrow{\mathrm{grad}}_{\mathbb{D}} u(\boldsymbol{x}), \overrightarrow{\mathrm{grad}}_{\mathbb{D}} v(\boldsymbol{y}) \right) && (2.168) \\ &= \frac{1}{4} \left((\mathrm{i}\mathcal{L}_+ u + \mathrm{i}\mathcal{L}_- u)(\mathrm{i}\mathcal{L}_- \overline{v} + \mathrm{i}\mathcal{L}_+ \overline{v}) \right. \\ &\quad \left. + (\mathcal{L}_+ u - \mathcal{L}_- u)(-\mathcal{L}_+ \overline{v} + \mathcal{L}_+ \overline{v}) \right) && (2.169) \\ &= -\frac{1}{2} \left(\mathcal{L}_+ u \mathcal{L}_- \overline{v} + \mathcal{L}_- u \mathcal{L}_+ \overline{v} \right). && (2.170) \end{aligned}$$

■

Lemma 2.7.3 (Adjoints of the angular momentum operators)**.** *For functions that are zero at the edge $\partial\mathbb{D}$, the angular momentum operators have the following adjoints:*

$$\langle \mathcal{L}_+ u\,,\, v \rangle_{\mathbb{D}} = \langle u\,,\, \mathcal{L}_- v \rangle_{\mathbb{D}}\,, \;\; \textit{i.e.,}\; \mathcal{L}_+^* = \mathcal{L}_-, \tag{2.171}$$

$$\langle \mathcal{L}_- u\,,\, v \rangle_{\mathbb{D}} = \langle u\,,\, \mathcal{L}_+ v \rangle_{\mathbb{D}}\,, \;\; \textit{i.e.,}\; \mathcal{L}_-^* = \mathcal{L}_+. \tag{2.172}$$

Proof Let us first address the adjoint of $\mathcal{L}_+$. We have that

$$\int_{\mathbb{D}} \mathcal{L}_+ u(\boldsymbol{x}) \overline{v(\boldsymbol{x})} d\mathbb{D}(\boldsymbol{x}) = \int_0^1 \int_0^{2\pi} e^{\mathrm{i}\phi} \left(\frac{\partial u}{\partial \rho}(\boldsymbol{x}) + \frac{\mathrm{i}}{\rho} \frac{\partial u}{\partial \phi}(\boldsymbol{x}) \right) \overline{v(\boldsymbol{x})} \rho d\rho d\phi. \tag{2.173}$$

Let us separate the integral in two parts:

$$I_1 = \int_0^1 \int_0^{2\pi} e^{\mathrm{i}\phi} \left(\frac{\partial u}{\partial \rho}(\boldsymbol{x}) \right) \overline{v(\boldsymbol{x})} \rho d\phi d\rho, \tag{2.174}$$

$$I_2 = \int_0^1 \int_0^{2\pi} e^{\mathrm{i}\phi} \left(\frac{\mathrm{i}}{\rho} \frac{\partial u}{\partial \phi}(\boldsymbol{x}) \right) \overline{v(\boldsymbol{x})} \rho d\phi d\rho. \tag{2.175}$$

Applying integration by parts to the first integral gives us

$$I_1 = \int_0^{2\pi} e^{\mathrm{i}\phi} \left(u(\boldsymbol{x})\overline{v(\boldsymbol{x})} \right) \Big|_{\rho=1} d\phi - \int_0^1 \int_0^{2\pi} e^{\mathrm{i}\phi} \left(\frac{u(\boldsymbol{x})\overline{v(\boldsymbol{x})}}{\rho} + \frac{\partial \overline{v}}{\partial \rho}(\boldsymbol{x}) u(\boldsymbol{x}) \right) \rho d\phi d\rho, \tag{2.176}$$

and applying integration by parts to the second integral gives us

$$I_2 = -\int_0^1 \int_0^{2\pi} e^{\mathrm{i}\phi} \left(-\frac{u(\boldsymbol{x})\overline{v(\boldsymbol{x})}}{\rho} + \frac{\mathrm{i}}{\rho} u(\boldsymbol{x}) \frac{\partial \overline{v}}{\partial \phi}(\boldsymbol{x}) \right) \rho d\phi d\rho. \tag{2.177}$$

$$\Rightarrow I_1 + I_2 = -\int_{\mathbb{D}} u(\boldsymbol{x}) \mathcal{L}_+ \overline{v(\boldsymbol{x})} d\mathbb{D} + \int_0^{2\pi} e^{\mathrm{i}\phi} \left(u(\boldsymbol{x})\overline{v(\boldsymbol{x})} \right) \Big|_{\rho=1} d\phi. \tag{2.178}$$

Proposition 2.7.5 tells us that $\mathcal{L}_+ \overline{v} = -\overline{\mathcal{L}_- v}$, so we can rewrite the previous expression as

$$\langle \mathcal{L}_+ u \, , \, v \rangle_{\mathbb{D}} = \langle u \, , \, \mathcal{L}_- v \rangle_{\mathbb{D}} + \int_0^{2\pi} e^{\mathrm{i}\phi} \left(u(\boldsymbol{x})\overline{v(\boldsymbol{x})} \right) \Big|_{\rho=1} d\phi. \tag{2.179}$$

Using the same procedure we also get

$$\langle \mathcal{L}_- u \, , \, v \rangle_{\mathbb{D}} = \langle u \, , \, \mathcal{L}_+ v \rangle_{\mathbb{D}} - \int_0^{2\pi} e^{\mathrm{i}\phi} \left(u(\boldsymbol{x})\overline{v(\boldsymbol{x})} \right) \Big|_{\rho=1} d\phi. \tag{2.180}$$

Since $u = v = 0$ for $\rho = 1$, we obtain the desired result. ∎

In the rest of this section we will develop a series of results related to application of derivatives and angular momenta to the disk basis functions that will prove useful in the proofs of the main results contained in the rest of the chapter.

Lemma 2.7.4 (Some properties of the Associated Legendre Functions [3, Section 8.5])**.** *For a given variable $\xi \in (-1, 1)$ we have the following recurrence relationships for the Associated Legendre Functions:*

$$(2l+1)\xi \mathbb{P}_l^m(\xi) = (l - m + 1)\ \mathbb{P}_{l+1}^m(\xi) - (l + m)\ \mathbb{P}_{l-1}^m(\xi), \tag{2.181}$$

$$(1-\xi^2)\frac{\partial \mathbb{P}_l^m}{\partial \xi}(\xi) = \frac{1}{2l+1}\left(((l+1)(l+m)\ \mathbb{P}_{l-1}^m(\xi) - l(l-m+1)\ \mathbb{P}_{l+1}^m(\xi)) \right), \tag{2.182}$$

$$\sqrt{(1-\xi^2)}\frac{\partial \mathbb{P}_l^m}{\partial \xi}(\xi) = \frac{1}{2}\left(((l-m+1)(l+m)\ \mathbb{P}_l^{m-1}(\xi) - \mathbb{P}_l^{m+1}(\xi)) \right). \tag{2.183}$$

This lemma and the application of the angular momentum operators easily allow to express several identities regarding the disk basis functions. We will list them in the following corollaries as they will be used later in subsequent proofs.

Corollary 2.7.2 (Angular momenta action on the disk basis functions)**.**

$$\mathcal{L}_+ y_l^m = \sqrt{(l-m)(l+m+1)}\frac{y_l^{m+1}}{w}, \tag{2.184}$$

$$\mathcal{L}_- y_l^m = \sqrt{(l+m)(l-m+1)}\frac{y_l^{m-1}}{w}, \tag{2.185}$$

$$\mathcal{L}_3 y_l^m = m y_l^m, \tag{2.186}$$

$$\mathcal{L}_+ \overline{y_l^m} = -\sqrt{(l+m)(l-m+1)}\frac{\overline{y_l^{m-1}}}{w}, \tag{2.187}$$

$$\mathcal{L}_- \overline{y_l^m} = -\sqrt{(l-m)(l+m+1)}\frac{\overline{y_l^{m+1}}}{w}, \tag{2.188}$$

$$\mathcal{L}_3 \overline{y_l^m} = -m\overline{y_l^m}, \tag{2.189}$$

$$\mathcal{L}_+ y_l^m = \frac{e^{i\phi}}{2\rho w(\rho)}\left((l-m)\ \frac{\sqrt{(l+1)^2-m^2}}{\sqrt{(l+1)^2-1/4}}\ y_{l+1}^m - (l+m+1)\ \frac{\sqrt{l^2-m^2}}{\sqrt{l^2-1/4}}\ y_{l-1}^m\right) \tag{2.190}$$

$$\mathcal{L}_- y_l^m = -\frac{e^{-i\phi}}{2\rho w(\rho)}\left((l+m)\ \frac{\sqrt{(l+1)^2-m^2}}{\sqrt{(l+1)^2-1/4}}\ y_{l+1}^m - (l-m+1)\ \frac{\sqrt{l^2-m^2}}{\sqrt{l^2-1/4}}\ y_{l-1}^m\right) \tag{2.191}$$

$$\mathcal{L}_+ \overline{y_l^m} = \frac{e^{i\phi}}{2\rho w(\rho)}\left((l+m)\ \frac{\sqrt{(l+1)^2-m^2}}{\sqrt{(l+1)^2-1/4}}\ \overline{y_{l+1}^m} - (l-m+1)\ \frac{\sqrt{l^2-m^2}}{\sqrt{l^2-1/4}}\ \overline{y_{l-1}^m}\right) \tag{2.192}$$

Corollary 2.7.3 (Recurrence relations for the disk basis functions)**.**

$$y_l^m(\boldsymbol{x}) = \frac{1}{2\sqrt{(1-\rho^2)}}\left(\frac{\sqrt{(l+1)^2-m^2}}{\sqrt{(l+1)^2-1/4}}\ y_{l+1}^m(\boldsymbol{x}) + \frac{\sqrt{l^2-m^2}}{\sqrt{l^2-1/4}}\ \ y_{l-1}^m(\boldsymbol{x})\right), \tag{2.193}$$

$$2\ \rho e^{i\phi}\ y_l^m(\boldsymbol{x}) = \sqrt{\frac{(l-m)(l-m-1)}{l^2-1/4}}\ y_{l-1}^{m+1}(\boldsymbol{x}) - \sqrt{\frac{(l+m+1)(l+m+2)}{(l+1)^2-1/4}}\ \ y_{l+1}^{m+1}(\boldsymbol{x}). \tag{2.194}$$

2.7.4 Weighted spaces and series representations

Definition 2.7.8 (Sesquilinear forms associated with w and $1/w$)**.** *Let us notate by $(\cdot,\cdot)_w$ the following sesquilinear form associated with w:*

$$(u,v)_w = \int_{\mathbb{D}} u(\boldsymbol{x})\overline{v(\boldsymbol{x})}w(\boldsymbol{x})d\mathbb{D}(\boldsymbol{x}). \tag{2.195}$$

Similarly, let us notate by $(\cdot,\cdot)_{1/w}$, the sesquilinear form associated with $1/w$:

$$(u,v)_{1/w} = \int_{\mathbb{D}} u(\boldsymbol{x})\overline{v(\boldsymbol{x})}w^{-1}(\boldsymbol{x})d\mathbb{D}(\boldsymbol{x}). \tag{2.196}$$

Definition 2.7.9 (The $L^2_w(\mathbb{D})$ and the $L^2_{1/w}(\mathbb{D})$ spaces)**.** *Let us define the space $L^2_w(\mathbb{D})$, associated with the inner product $(\cdot,\cdot)_w$ and with the norm $\|u\|_w = \sqrt{(u,u)_w}$, as*

$$L^2_w(\mathbb{D}) = \{u \text{ measurable } : \|u\|_w < \infty\}, \tag{2.197}$$

and the space $L^2_{1/w}(\mathbb{D})$, associated with the inner product $(\cdot,\cdot)_{1/w}$ and with the norm $\|u\|_{1/w} = \sqrt{(u,u)_{1/w}}$, as

$$L^2_{1/w}(\mathbb{D}) = \left\{u \text{ measurable } : \|u\|_{1/w} < \infty\right\}. \tag{2.198}$$

Proposition 2.7.8 (Bases for $L^2_w(\mathbb{D})$)**.** *The sets $\mathcal{Y}_s^{1/w}$ and $\mathcal{Y}_{as}^{1/w}$ form, each one, an orthogonal and complete basis for $L^2_w(\mathbb{D})$.*

Proof Orthogonality can be easily checked from Proposition 2.7.4. The sets $\mathcal{Y}_s^{1/w}$ and $\mathcal{Y}_{as}^{1/w}$ are subsets of $L^2_w(\mathbb{D})$, since it can be easily shown that each member has a finite norm (indeed equal to $1/\sqrt{2}$). If the set $\mathcal{Y}_s^{1/w}$ wasn't dense in $L^2_w(\mathbb{D})$, there would be a member $f \in L^2_w(\mathbb{D})$ not a.e. equal to zero and orthogonal to all members of $\mathcal{Y}_s^{1/w}$, i.e.,

$$\left(f\,,\,\frac{y_l^m}{w}\right)_w = \int_{\mathbb{D}} f(\boldsymbol{x})\overline{y_l^m(\boldsymbol{x})}d\mathbb{D}(\boldsymbol{x}) = 0 \;\text{ for } l \geq 0,\; -l \leq m \leq l,\, l+m \text{ even.} \tag{2.199}$$

But for $l+m$ even, functions y_l^m, i.e. the set $\mathcal{Y}_s$, is dense in $C^\infty(\mathbb{D})$, since it is a combination of polynomials in the radial direction (Remark 2.7.2) and trigonometric polynomials in the angular direction. This means that f must be equal to zero a.e., which contradicts the premises, thus implying that $\mathcal{Y}_s^{1/w}$ is dense in L^2_w. The same argument can be used for $l+m$ odd, except that y_l^m functions in the radial direction are of the form $w(\rho)p(\rho)$, where now p is polynomial (Remark 2.7.2). Being $w(\rho)$ regular on $\mathbb{D}$ the same argument stands, rendering the set of functions y_l^m for $l+m$ odd dense in $C^\infty(\mathbb{D})$, and thus $\mathcal{Y}_{as}^{1/w}$ is also dense in $L^2_w(\mathbb{D})$ ∎

Proposition 2.7.9 (Bases for $L^2_{1/w}(\mathbb{D})$)**.** *The sets $\mathcal{Y}_s$ and $\mathcal{Y}_{as}$ form, each one, an orthogonal and complete basis for $L^2_{1/w}(\mathbb{D})$.*

Proof This proof uses the same argument as the one from Proposition 2.7.8. Now, if the set $\mathcal{Y}_{as}$ was not dense in $L^2_{1/w}(\mathbb{D})$, there would be a member $f \in L^2_{1/w}(\mathbb{D})$ not a.e. equal to zero and orthogonal to all members of $\mathcal{Y}_{as}$, i.e.,

$$(f\,,\,y_l^m)_{1/w} = \int_{\mathbb{D}} \frac{f(\boldsymbol{x})\overline{y_l^m(\boldsymbol{x})}}{w(\boldsymbol{x})}d\mathbb{D}(\boldsymbol{x}) = 0 \;\text{ for } l \geq 0,\; -l \leq m \leq l,;l+m \text{ odd.} \tag{2.200}$$

But for $l+m$ odd, again in accordance with Remark 2.7.2, y_l^m/w are polynomials in ρ and thus the functions y_l^m/w are dense in $C^\infty(\mathbb{D})$. For $l+m$ even, functions y_l^m are polynomials in ρ, and thus f/w would have to be a.e. zero on $\mathbb{D}$. This means that f itself would also have to be a.e. zero on $\mathbb{D}$. By contradiction, there is not such a function f. ∎

We can expand functions in any of the four Sobolev spaces $\widetilde{H}^{1/2}(\mathbb{D})$, $H^{1/2}(\mathbb{D})$, $H^{-1/2}(\mathbb{D})$, and $\widetilde{H}^{-1/2}(\mathbb{D})$ using these bases. If u is the solution to the Laplace screen problem for the disk, the jump of the Neumann trace will behave as $\lambda \sim 1/\sqrt{1-\rho^2}$ near the edge, i.e., for $\rho \to 1$, and the jump of the Dirichlet trace will behave as $\mu \sim \sqrt{1-\rho^2}$ near the edge (cf. Theorem 2.3.4). This motivates the use of the weight function w and the expansion of functions in $\widetilde{H}^{1/2}(\mathbb{D})$ on the space $L^2_{1/w}$ on the basis $\mathcal{Y}_{as}$, functions in the space $H^{1/2}(\mathbb{D})$ on the space $L^2_{1/w}$ on the basis $\mathcal{Y}_s$, functions in the space $H^{-1/2}(\mathbb{D})$ on the space L^2_w on the basis $\mathcal{Y}_{as}^{1/w}$, and functions in the space $\widetilde{H}^{-1/2}(\mathbb{D})$ on the space L^2_w on the basis $\mathcal{Y}_s^{1/w}$. Given the properties of the basis sets, derived from the properties of the Associated Legendre Polynomials, this equates to use polynomial bases and the weight function w in the radial direction as it was done for the segment in $\mathbb{R}^2$ in Subsection 2.4.4, and the basis $\left\{e^{\mathrm{i}m\phi}\right\}_{m\in\mathbb{Z}}$ for $L^2([0,2\pi])$.

A function μ in the space $\widetilde{H}^{1/2}(\mathbb{D})$ will be expanded on the basis $\mathcal{Y}_{as}$ of space $L^2_{1/w}$:

$$\mu(\boldsymbol{x}) = \sum_{l=0}^{\infty}\sum_{\substack{m=-l\\ l+m \text{ odd}}}^{l} \mu_l^m y_l^m(\boldsymbol{x}), \quad \mu_l^m = (\mu, y_l^m)_{1/w} = \int_{\mathbb{D}} \frac{\mu(\boldsymbol{x})\overline{y_l^m}(\boldsymbol{x})}{\sqrt{(1-\rho(\boldsymbol{x})^2)}}d\mathbb{D}(\boldsymbol{x}). \tag{2.201}$$

A function g in the space $H^{1/2}(\mathbb{D})$ will be expanded on the basis $\mathcal{Y}_s$ of space $L^2_{1/w}$:

$$g(\boldsymbol{x}) = \sum_{l=0}^{\infty} \sum_{\substack{m=-l \\ l+m \text{ even}}}^{l} g_l^m y_l^m(\boldsymbol{x}), \quad g_l^m = (g, y_l^m)_{1/w} = \int_{\mathbb{D}} \frac{g(\boldsymbol{x})\overline{y_l^m}(\boldsymbol{x})}{\sqrt{(1-\rho(\boldsymbol{x})^2)}} d\mathbb{D}(\boldsymbol{x}). \tag{2.202}$$

A function φ in the space $H^{-1/2}(\mathbb{D})$ will be expanded on the basis $\mathcal{Y}_{as}^{1/w}$ of space L_w^2:

$$\varphi(\boldsymbol{x}) = \sum_{l=0}^{\infty} \sum_{\substack{m=-l \\ l+m \text{ odd}}}^{l} \varphi_l^m \frac{y_l^m(\boldsymbol{x})}{\sqrt{(1-\rho(\boldsymbol{x})^2)}}, \quad \varphi_l^m = \left(\varphi, \frac{y_l^m}{\sqrt{1-\rho(\boldsymbol{x})^2}}\right)_w = \int_{\mathbb{D}} \varphi(\boldsymbol{x})\overline{y_l^m}(\boldsymbol{x}) d\mathbb{D}(\boldsymbol{x}). \tag{2.203}$$

A function λ in the space $\widetilde{H}^{-1/2}(\mathbb{D})$ will be expanded on the basis $\mathcal{Y}_{s}^{1/w}$ of space L_w^2:

$$\lambda(\boldsymbol{x}) = \sum_{l=0}^{\infty} \sum_{\substack{m=-l \\ l+m \text{ even}}}^{l} \lambda_l^m \frac{y_l^m(\boldsymbol{x})}{\sqrt{(1-\rho(\boldsymbol{x})^2)}}, \quad \lambda_l^m = \left(\lambda, \frac{y_l^m(\boldsymbol{x})}{\sqrt{(1-\rho(\boldsymbol{x})^2)}}\right)_w = \int_{\mathbb{D}} \psi(\boldsymbol{x})\overline{y_l^m}(\boldsymbol{x}) d\mathbb{D}(\boldsymbol{x}). \tag{2.204}$$

2.7.5 Series forms for the boundary integral operators

In this section we will develop series expressions for the kernels of the integral operators related to boundary integral equations linked to the symmetric Dirichlet and anti-symmetric Neumann Laplace problems. This will be done in order to use the developed tools and identities concerning the disk basis functions to derive inverse integral operators. These inverse operators will be useful for solving the boundary integral equations and for building coercive bilinear forms in the function spaces relevant to these problems, thus compliant with the Theorem 2.1.1 on optimal preconditioning.

We will put forward a theorem about the mapping properties of the operator $\mathcal{N}$ acting on the disk basis functions, hinted by the results of Krenk [42] and Martin [46]. We will provide a proof later on this section. We will make use of the gamma function [19, Section 6.2], which we will denote, in the scope of this chapter, with the symbol Γ.

Theorem 2.7.1 (Hypersingular operator on the disk basis functions)**.** *For $l+m$ odd, the action of the hypersingular boundary integral operator on a disk basis function y_l^m is*

$$\left(\mathcal{N} y_l^m\right)(\boldsymbol{x}) = -\alpha_l^m \frac{y_l^m(\boldsymbol{x})}{w(\boldsymbol{x})}, \tag{2.205}$$

where the constant α_l^m is given by:

$$\alpha_l^m = \frac{\Gamma\left(\frac{l+m+2}{2}\right)\Gamma\left(\frac{l-m+2}{2}\right)}{\left(\frac{l+m-1}{2}\right)!\left(\frac{l-m-1}{2}\right)!}. \tag{2.206}$$

Remark 2.7.4 (Some of the first values of α_l^m)**.** *The values of α_l^m are real for $l+m$ odd, increasing with degree l, and decreasing with the absolute value of the order m. Table 2.5 shows some of the first values of α_l^m.*

We will now propose series expressions for the integral kernels of some integral operators intended to be related to the Dirichlet-to-Neumann and Neumann-to-Dirichlet operators for the symmetric Dirichlet and anti-symmetric Neumann Laplace problems.

We know from Theorem 2.3.4 that the behavior of the traces of the solutions for the symmetric Dirichlet and anti-symmetric resemble $1/\sqrt{\operatorname{dist}(\boldsymbol{x}, \partial\Gamma)}$ for the former and $\sqrt{\operatorname{dist}(\boldsymbol{x}, \partial\Gamma)}$ for the latter near the edge of the screen, and where $\operatorname{dist}(\boldsymbol{x}, \partial\Gamma)$ is the distance to the edge of

Table 2.5: Some of the first values of α_l^m, for degree $l \leq 4$, order $-4 \leq m \leq 4$ and $l+m$ odd.

α_l^m	$m=-4$	$m=-3$	$m=-2$	$m=-1$	$m=0$	$m=1$	$m=2$	$m=3$	$m=4$
l=0									
l=1					0.7854				
l=2				1.1781		1.1781			
l=3			1.4726		1.7671		1.4726		
l=4		1.7181		2.2089		2.2089		1.7181	

the screen from a given point $\boldsymbol{x}$ in the vicinity. We also know from the previous results obtained for the segment screen embedded in $\mathbb{R}^2$ that the integral kernels match those behaviors. Finally, from Theorem 2.7.1, the desired mapping properties of one of the integral operators, $\mathcal{N}$. We will propose new integral kernels that will match all these features in ρ.

Definition 2.7.10 (Some new integral kernels in series form)**.** *For $(\boldsymbol{x},\boldsymbol{y}) \in \mathbb{D}\times\mathbb{D}$, with $\boldsymbol{x}\neq\boldsymbol{y}$, let us define the anti-symmetric weakly singular and hypersingular integral kernels as the formal series*

$$K_{as}^{ws}(\boldsymbol{x},\boldsymbol{y}) = \sum_{l=0}^{\infty}\sum_{\substack{m=-l\\ l+m\ odd}}^{l} \frac{1}{\alpha_l^m}\left(y_l^m(\boldsymbol{x})\overline{y_l^m}(\boldsymbol{y}) + \overline{y_l^m}(\boldsymbol{x})y_l^m(\boldsymbol{y})\right), \tag{2.207}$$

$$K_{as}^{hs}(\boldsymbol{x},\boldsymbol{y}) = -\sum_{l=0}^{\infty}\sum_{\substack{m=-l\\ l+m\ odd}}^{l} \alpha_l^m\left(\frac{y_l^m(\boldsymbol{x})}{w(\boldsymbol{x})}\frac{\overline{y_l^m}(\boldsymbol{y})}{w(\boldsymbol{y})} + \frac{\overline{y_l^m}(\boldsymbol{x})}{w(\boldsymbol{x})}\frac{y_l^m(\boldsymbol{y})}{w(\boldsymbol{y})}\right), \tag{2.208}$$

where α_l^m is defined as in Theorem 2.7.1. Similarly for $(\boldsymbol{x},\boldsymbol{y}) \in \mathbb{D}\times\mathbb{D}$, with $\boldsymbol{x}\neq\boldsymbol{y}$, let us define the symmetric weakly singular and hypersingular integral kernels as the formal series

$$K_{s}^{ws}(\boldsymbol{x},\boldsymbol{y}) = \sum_{l=0}^{\infty}\sum_{\substack{m=-l\\ l+m\ even}}^{l} \frac{1}{\beta_l^m}\left(y_l^m(\boldsymbol{x})\overline{y_l^m}(\boldsymbol{y}) + \overline{y_l^m}(\boldsymbol{x})y_l^m(\boldsymbol{y})\right), \tag{2.209}$$

$$K_{s}^{hs}(\boldsymbol{x},\boldsymbol{y}) = -\sum_{l=0}^{\infty}\sum_{\substack{m=-l\\ l+m\ even}}^{l} \beta_l^m\left(\frac{y_l^m(\boldsymbol{x})}{w(\boldsymbol{x})}\frac{\overline{y_l^m}(\boldsymbol{y})}{w(\boldsymbol{y})} + \frac{\overline{y_l^m}(\boldsymbol{x})}{w(\boldsymbol{x})}\frac{y_l^m(\boldsymbol{y})}{w(\boldsymbol{y})}\right), \tag{2.210}$$

where β_l^m is a function of l and m yet to be defined.

Remark 2.7.5 (The behavior at the edge is the same as in the $\mathbb{R}^2$ case)**.** *From Remark 2.7.3, it becomes clear that the integral kernels of the four integral operators on the segment for the two-dimensional case, have the same behavior as the corresponding proposed integral kernels from the previous definition in the radial direction.*

Using these integral kernels we now define their corresponding boundary integral operators.

Definition 2.7.11 (Associated boundary integral operators)**.** *For a function u defined on $\mathbb{D}$, let us define the symmetric weakly singular integral operator*

$$\left(\mathcal{L}_s^{ws}u\right)(\boldsymbol{y}) = \int_{\mathbb{D}} K_s^{ws}(\boldsymbol{x},\boldsymbol{y})u(\boldsymbol{x})d\mathbb{D}(\boldsymbol{x}), \tag{2.211}$$

the anti-symmetric weakly singular integral operator

$$\left(\mathcal{L}_{as}^{ws}u\right)(\boldsymbol{y}) = \int_{\mathbb{D}} K_{as}^{ws}(\boldsymbol{x},\boldsymbol{y})u(\boldsymbol{x})d\mathbb{D}(\boldsymbol{x}), \tag{2.212}$$

the symmetric hypersingular integral operator

$$\left(\mathcal{L}_s^{hs} u\right)(\boldsymbol{y}) = \int_{\mathbb{D}} K_s^{hs}(\boldsymbol{x},\boldsymbol{y}) u(\boldsymbol{x}) d\mathbb{D}(\boldsymbol{x}), \tag{2.213}$$

and the anti-symmetric hypersingular integral operator

$$\left(\mathcal{L}_{as}^{hs} u\right)(\boldsymbol{y}) = \int_{\mathbb{D}} K_{as}^{hs}(\boldsymbol{x},\boldsymbol{y}) u(\boldsymbol{x}) d\mathbb{D}(\boldsymbol{x}). \tag{2.214}$$

Using the tools and identities developed in this section, the mapping properties of the associated boundary integral operators for the disk basis functions are easy to determine.

Proposition 2.7.10 (Integral operator action on the disk basis functions)**.** *The following mapping identities hold for the boundary integral operators from Definition 2.7.11:*

$$\mathcal{L}_s^{ws} \frac{y_l^m}{w} = \frac{1}{\beta_l^m} y_l^m, \ \textit{for } l+m \textit{ even}, \tag{2.215}$$

$$\mathcal{L}_{as}^{ws} \frac{y_l^m}{w} = \frac{1}{\alpha_l^m} y_l^m, \ \textit{for } l+m \textit{ odd}, \tag{2.216}$$

$$\mathcal{L}_s^{hs} y_l^m = -\beta_l^m \frac{y_l^m}{w}, \ \textit{for } l+m \textit{ even}, \tag{2.217}$$

$$\mathcal{L}_{as}^{hs} y_l^m = -\alpha_l^m \frac{y_l^m}{w}, \ \textit{for } l+m \textit{ odd}. \tag{2.218}$$

Proof Let us analyze the first case.

$$\left(\mathcal{L}_s^{ws} \frac{y_l^m}{w}\right)(\boldsymbol{y}) = \sum_{l=0}^{\infty} \sum_{\substack{m=-l \\ l+m \text{ even}}}^{l} \frac{1}{\beta_{l'}^{m'}} \left(\overline{y_{l'}^{m'}}(\boldsymbol{y}) \int_{\mathbb{D}} y_{l'}^{m'}(\boldsymbol{x}) \frac{y_l^m}{w}(\boldsymbol{x}) d\mathbb{D}(\boldsymbol{x}) + y_{l'}^{m'}(\boldsymbol{y}) \int_{\mathbb{D}} \overline{y_{l'}^{m'}}(\boldsymbol{x}) \frac{y_l^m}{w} d\mathbb{D}(\boldsymbol{x}) \right). \tag{2.219}$$

Using the orthogonality relations from Proposition 2.7.4 and Corollary 2.7.1 it follows that

$$\left(\mathcal{L}_s^{ws} \frac{y_l^m}{w}\right)(\boldsymbol{y}) = \sum_{l=0}^{\infty} \sum_{\substack{m=-l \\ l+m \text{ even}}}^{l} \frac{1}{\beta_{l'}^{m'}} \left(\overline{y_{l'}^{m'}}(\boldsymbol{y}) \frac{(-1)^{(m')}}{2} \delta_{-m}^{m'} \delta_l^{l'} + y_{l'}^{m'}(\boldsymbol{y}) \frac{1}{2} \delta_m^{m'} \delta_l^{l'} + y_{l'}^{m'} \right) \tag{2.220}$$

$$= \frac{(-1)^m}{2} \frac{1}{\beta_l^{-m}} \overline{y_l^{-m}}(\boldsymbol{y}) + \frac{1}{2} \frac{1}{\beta_l^m} y_l^m(\boldsymbol{y}). \tag{2.221}$$

Noting that $\beta_l^m = \beta_l^{-m}$ and that $\overline{y_l^{-m}} = (-1)^m y_l^m$, the desired result is obtained. The next three cases follow from similar analyses. ∎

Proposition 2.7.10 assures that the constructed boundary integral operator $\mathcal{L}_{as}^{hs}$ has the desired mapping qualities.

Remark 2.7.6 ($\mathcal{N}$ is identified $\mathcal{L}_{as}^{hs}$)**.** *Operator $\mathcal{N}$ is identified with operator $\mathcal{L}_{as}^{hs}$ as they map functions of $\widetilde{H}^{1/2}(\mathbb{D})$ onto the same images on $H^{-1/2}(\mathbb{D})$.*

The previous Proposition 2.7.10 allows us to extract two results that aim to show that the boundary integral operators defined using the series integral kernel fulfill the required conditions, i.e., they provide inverse operators that induce bilinear forms that we can use to build preconditioners.

Theorem 2.7.2 ($\mathcal{L}_s^{hs}$ is minus the inverse of $\mathcal{L}_s^{ws}$ and $\mathcal{L}_{as}^{ws}$ is minus the inverse of $\mathcal{L}_{as}^{hs}$)**.** *The operator $\mathcal{L}_s^{hs} : \mathcal{Y}_s \to \mathcal{Y}_s^{1/w}$ is the inverse of the operator $\mathcal{L}_s^{ws} : \mathcal{Y}_s^{1/w} \to \mathcal{Y}_s$ composed with a change of sign, and the operator $\mathcal{L}_{as}^{ws} : \mathcal{Y}_{as}^{1/w} \to \mathcal{Y}_{as}$ is the inverse of the operator $\mathcal{L}_{as}^{hs} : \mathcal{Y}_{as} \to \mathcal{Y}_{as}^{1/w}$ composed with a change of sign.*

Proof These results follow straightforwardly from Proposition 2.7.10. ∎

Corollary 2.7.4 (Bilinear forms induced by the new boundary integral operators on for the disk basis functions)**.** *For l_1+m_1 and l_2+m_2 odd, we have the following bilinear form identities:*

$$\left\langle \mathcal{L}_{as}^{ws} \frac{y_{l_1}^{m_1}}{w}, \frac{y_{l_2}^{m_2}}{w} \right\rangle_{\mathbb{D}} = \begin{cases} 0 & , \text{ if } l_1 \neq l_2 \text{ or } m_1 \neq m_2, \\ \frac{1}{2\alpha_l^m} & , \text{ if } l_1 = l_2 = l \text{ and } m_1 = m_2 = m, \end{cases} \tag{2.222}$$

$$\left\langle \mathcal{L}_{as}^{hs} y_{l_1}^{m_1}, y_{l_2}^{m_2} \right\rangle_{\mathbb{D}} = \begin{cases} 0 & , \text{ if } l_1 \neq l_2 \text{ or } m_1 \neq m_2, \\ -\frac{\alpha_l^m}{2} & , \text{ if } l_1 = l_2 = l \text{ and } m_1 = m_2 = m. \end{cases} \tag{2.223}$$

For $l_1 + m_1$ and $l_2 + m_2$ even, we have the following additional bilinear form identities:

$$\left\langle \mathcal{L}_{s}^{ws} \frac{y_{l_1}^{m_1}}{w}, \frac{y_{l_2}^{m_2}}{w} \right\rangle_{\mathbb{D}} = \begin{cases} 0 & , \text{ if } l_1 \neq l_2 \text{ or } m_1 \neq m_2, \\ \frac{1}{2\beta_l^m} & , \text{ if } l_1 = l_2 = l \text{ and } m_1 = m_2 = m, \end{cases} \tag{2.224}$$

$$\left\langle \mathcal{L}_{s}^{hs} y_{l_1}^{m_1}, y_{l_2}^{m_2} \right\rangle_{\mathbb{D}} = \begin{cases} 0 & , \text{ if } l_1 \neq l_2 \text{ or } m_1 \neq m_2, \\ -\frac{\beta_l^m}{2} & , \text{ if } l_1 = l_2 = l \text{ and } m_1 = m_2 = m. \end{cases} \tag{2.225}$$

Proof These results follow straightforwardly from the mapping properties of basis functions established in Proposition 2.7.10, and orthogonality properties from Proposition 2.7.4. ∎

Up until this point, we have matched $\mathcal{L}_{as}^{hs}$, for which $\mathcal{L}_{as}^{ws}$ was the inverse, with $\mathcal{N}$; their definitions depend on the coefficients α_l^m, which are known. The question remains how to choose β_l^m so that we can identify $\mathcal{L}_s^{ws}$ with $\mathcal{S}$, thus providing us with the inverse $\mathcal{L}_s^{hs}$. We noted in Remark 2.6.1 that the Neumann-to-Dirichlet operator for the symmetric Dirichlet problem, NtD_s, is in fact the operator $\mathcal{S}$. Thus, the choice of β_l^m must allow K_s^{ws} to be written as K^{ws}. Following (1.100) from Theorem 1.5.3, we impose special relations between $\mathcal{L}_{as}^{hs}$ and $\mathcal{L}_s^{ws}$, and between $\mathcal{L}_s^{hs}$ and $\mathcal{L}_{as}^{ws}$.

Definition 2.7.12 (β_l^m and the relation between $\mathcal{L}_{as}^{hs}$ and $\mathcal{L}_s^{ws}$, and between $\mathcal{L}_s^{hs}$ and $\mathcal{L}_{as}^{ws}$)**.** *Let us define β_l^m such that for functions $u, v \in \widetilde{H}^{1/2}(\mathbb{D})$, the bilinear form induced by $\mathcal{L}_{as}^{hs}$ can be written as*

$$\left\langle -\mathcal{L}_{as}^{hs} u, v \right\rangle_{\mathbb{D}} = \left\langle \mathcal{L}_s^{ws} \overrightarrow{curl}_{\mathbb{D}} u, \overrightarrow{curl}_{\mathbb{D}} v \right\rangle_{\mathbb{D}}, \tag{2.226}$$

and that for functions $u, v \in H^{1/2}(\mathbb{D})$ with zero mean, i.e. $\langle u, 1 \rangle_{\mathbb{D}} = 0$ and $\langle v, 1 \rangle_{\mathbb{D}} = 0$, the bilinear form induced by $\mathcal{L}_s^{hs}$ can be written as

$$\left\langle -\mathcal{L}_{s}^{hs} u, v \right\rangle_{\mathbb{D}} = \left\langle \mathcal{L}_{as}^{ws} \overrightarrow{curl}_{\mathbb{D}} u, \overrightarrow{curl}_{\mathbb{D}} v \right\rangle_{\mathbb{D}}. \tag{2.227}$$

Proposition 2.7.11 (Rewriting hypersingular operators)**.** *For real functions, Definition 2.7.12 can also be written as*

$$\mathcal{L}_{as}^{hs} = -\frac{1}{2} \left(\mathcal{L}_- \circ \mathcal{L}_s^{ws} \circ \mathcal{L}_+ + \mathcal{L}_+ \circ \mathcal{L}_s^{ws} \circ \mathcal{L}_- \right), \tag{2.228}$$

$$\mathcal{L}_{s}^{hs} = -\frac{1}{2} \left(\mathcal{L}_- \circ \mathcal{L}_{as}^{ws} \circ \mathcal{L}_+ + \mathcal{L}_+ \circ \mathcal{L}_{as}^{ws} \circ \mathcal{L}_- \right). \tag{2.229}$$

Proof Let us address the first identity. Let us rewrite the following variational expression:

$$\left\langle -\mathcal{L}_{as}^{hs} u\,,\, v \right\rangle_{\mathbb{D}} = -\int_{\mathbb{D}}\int_{\mathbb{D}} K_s^{ws}(\boldsymbol{x},\boldsymbol{y}) \left(\overrightarrow{\mathrm{curl}}_{\mathbb{D}} u(\boldsymbol{x}), \overrightarrow{\mathrm{curl}}_{\mathbb{D}} v(\boldsymbol{y}) \right) d\mathbb{D}(\boldsymbol{x}) d\mathbb{D}(\boldsymbol{y}). \tag{2.230}$$

Using Proposition 2.7.7 we can rewrite it as

$$\frac{1}{2}\int_{\mathbb{D}}\int_{\mathbb{D}} K_s^{ws}(\boldsymbol{x},\boldsymbol{y}) \left(\mathcal{L}_+^{\boldsymbol{x}} u(\boldsymbol{x}) \mathcal{L}_-^{\boldsymbol{y}} \overline{v(\boldsymbol{y})} + \mathcal{L}_-^{\boldsymbol{x}} u(\boldsymbol{x}) \mathcal{L}_+^{\boldsymbol{y}} \overline{v(\boldsymbol{y})} \right) d\mathbb{D}(\boldsymbol{x}) d\mathbb{D}(\boldsymbol{y}) \tag{2.231}$$

$$= \frac{1}{2}\int_{\mathbb{D}}\int_{\mathbb{D}} K_s^{ws}(\boldsymbol{x},\boldsymbol{y}) \left(-\mathcal{L}_+^{\boldsymbol{x}} u(\boldsymbol{x}) \overline{\mathcal{L}_+^{\boldsymbol{y}} v(\boldsymbol{y})} - \mathcal{L}_-^{\boldsymbol{x}} u(\boldsymbol{x}) \overline{\mathcal{L}_-^{\boldsymbol{y}} v(\boldsymbol{y})} \right) d\mathbb{D}(\boldsymbol{x}) d\mathbb{D}(\boldsymbol{y}) \tag{2.232}$$

$$= -\frac{1}{2}\left(\langle \mathcal{L}_s^{ws} \circ \mathcal{L}_+ u\,,\, \mathcal{L}_+ \overline{v} \rangle_{\mathbb{D}} + \langle \mathcal{L}_s^{ws} \circ \mathcal{L}_- \overline{u}\,,\, \mathcal{L}_- v \rangle_{\mathbb{D}} \right) \tag{2.233}$$

$$= -\frac{1}{2}\left(\langle \mathcal{L}_- \circ \mathcal{L}_s^{ws} \circ \mathcal{L}_+ u\,,\, \overline{v} \rangle_{\mathbb{D}} + \langle \mathcal{L}_+ \circ \mathcal{L}_s^{ws} \circ \mathcal{L}_- \overline{u}\,,\, v \rangle_{\mathbb{D}} \right) \tag{2.234}$$

$$= -\frac{1}{2}\left(\langle \mathcal{L}_- \circ \mathcal{L}_s^{ws} \circ \mathcal{L}_+ u\,,\, v \rangle_{\mathbb{D}} + \langle \mathcal{L}_+ \circ \mathcal{L}_s^{ws} \circ \mathcal{L}_- u\,,\, v \rangle_{\mathbb{D}} \right) \tag{2.235}$$

$$= -\frac{1}{2}\left\langle \left(\mathcal{L}_- \circ \mathcal{L}_s^{ws} \circ \mathcal{L}_+ + \mathcal{L}_+ \circ \mathcal{L}_s^{ws} \circ \mathcal{L}_- \right) u\,,\, v \right\rangle_{\mathbb{D}}, \tag{2.236}$$

which is the desired result. The second identity is obtained using a similar procedure. ∎

Using Definition 2.7.12, the goal is to prove that it implies that the value of β_l^m allows for the rewriting of $\mathcal{S}$ as $\mathcal{L}_s^{ws}$ for the disk. In what follows, we will examine the consequences of the definition of β_l^m given in Definition 2.7.12.

Proposition 2.7.12 (Recurrence relations for α_l^m and β_l^m)**.** *The values of α_l^m and β_l^m are linked by the recurrence relations*

$$\alpha_l^m = \frac{1}{2}\left(\frac{(l+m)(l-m+1)}{\beta_l^{m-1}} + \frac{(l-m)(l+m+1)}{\beta_l^{m+1}} \right), \tag{2.237}$$

for $l \geq 1$ and $l+m$ odd, and

$$\beta_l^m = \frac{1}{2}\left(\frac{(l+m)(l-m+1)}{\alpha_l^{m-1}} + \frac{(l-m)(l+m+1)}{\alpha_l^{m+1}} \right), \tag{2.238}$$

for $l \geq 1$ and $l+m$ even.

Proof From Corollary 2.7.2 we know the effect of angular momentum operators on disk basis functions y_l^m, thus we can easily compute, for $l+m$ odd,

$$\mathcal{L}_+ \circ \mathcal{L}_s^{ws} \circ \mathcal{L}_- y_l^m = \frac{(l-m+1)(l+m)}{\beta_l^{m-1}} y_l^m, \tag{2.239}$$

$$\mathcal{L}_- \circ \mathcal{L}_s^{ws} \circ \mathcal{L}_+ y_l^m = \frac{(l+m+1)(l-m)}{\beta_l^{m+1}} y_l^m, \tag{2.240}$$

which together with the action of $\mathcal{L}_{as}^{hs}$ over y_l^m gives the first recurrence relation. The second recurrence relation comes similarly from computing the effect of $\mathcal{L}_+ \circ \mathcal{L}_{as}^{ws} \circ \mathcal{L}_-$ and $\mathcal{L}_- \circ \mathcal{L}_{as}^{ws} \circ \mathcal{L}_+$ for $l+m$ even. ∎

Proposition 2.7.13 (Alternative expressions for α_l^m and β_l^m)**.** *The values of α_l^m and β_l^m can be rewritten without making use of recurrences as:*

$$\alpha_l^m = \frac{\pi}{4}\left(\prod_{i=1}^{(l+m-1)/2} \frac{2i+1}{2i} \right)\left(\prod_{i=1}^{(l-m-1)/2} \frac{2i+1}{2i} \right), \text{ for } l+m \text{ odd}, \tag{2.241}$$

$$\beta_l^m = \frac{4}{\pi}\left(\prod_{i=1}^{(l+m)/2}\frac{2i}{2i-1}\right)\left(\prod_{i=1}^{(l-m)/2}\frac{2i}{2i-1}\right),\ \textit{for } l+m \textit{ even.} \tag{2.242}$$

Proof Let us first recall the following property of the Gamma function [3, Eq. 6.1.12]:

$$\Gamma(n+1/2) = \frac{\sqrt{\pi}}{2^n}\prod_{i=1}^{n-1}(2i+1). \tag{2.243}$$

Let us now rewrite some factors making up α_l^m in (2.206) (for $l+m$ odd):

$$\Gamma\left(\frac{l+m+2}{2}\right) = \Gamma\left(\frac{l+m+1}{2}+\frac{1}{2}\right) = \frac{\sqrt{\pi}}{2^{\frac{l+m+1}{2}}}\prod_{i=1}^{\frac{l+m-1}{2}}(2i+1), \tag{2.244}$$

$$\Gamma\left(\frac{l-m+2}{2}\right) = \Gamma\left(\frac{l-m+1}{2}+\frac{1}{2}\right) = \frac{\sqrt{\pi}}{2^{\frac{l-m+1}{2}}}\prod_{i=1}^{\frac{l-m-1}{2}}(2i+1), \tag{2.245}$$

$$\left(\frac{l+m-1}{2}\right)! = 2^{-\frac{l+m-1}{2}}\prod_{i=1}^{\frac{l+m-1}{2}}(2i), \tag{2.246}$$

$$\left(\frac{l-m-1}{2}\right)! = 2^{-\frac{l-m-1}{2}}\prod_{i=1}^{\frac{l-m-1}{2}}(2i). \tag{2.247}$$

Replacing the four new expressions in (2.206) we get the desired formula for α_l^m.

Using recursion relation (2.237) from Proposition 2.7.12, a similar expression can be found for β_l^m when $l+m$ is even. Let us denote $f(i) = (2i+1)/2i$ and note that,

$$\alpha_l^{m-1} = \frac{\pi}{4}\prod_{i=1}^{\frac{l+m-2}{2}}f(i)\prod_{i=1}^{\frac{l-m}{2}}f(i) = \frac{1}{f\left(\frac{l+m}{2}\right)}\frac{\pi}{4}\prod_{i=1}^{\frac{l+m}{2}}f(i)\prod_{i=1}^{\frac{l-m}{2}}f(i), \tag{2.248}$$

$$\alpha_l^{m+1} = \frac{\pi}{4}\prod_{i=1}^{\frac{l+m}{2}}f(i)\prod_{i=1}^{\frac{l-m-2}{2}}f(i) = \frac{1}{f\left(\frac{l-m}{2}\right)}\frac{\pi}{4}\prod_{i=1}^{\frac{l+m}{2}}f(i)\prod_{i=1}^{\frac{l-m}{2}}f(i). \tag{2.249}$$

Let us also denote

$$A_l^m = \frac{\pi}{4}\prod_{i=1}^{\frac{l+m}{2}}f(i)\prod_{i=1}^{\frac{l-m}{2}}f(i). \tag{2.250}$$

Then β_l^m can be computed from the recursion as

$$\beta_l^m = \frac{1}{2A_l^m}\left(f\left(\frac{l+m}{2}\right)(l+m)(l-m+1) + f\left(\frac{l-m}{2}\right)(l-m)(l+m+1)\right) \tag{2.251}$$

$$= \frac{1}{2A_l^m}\left((l+m+1)(l-m+1) + (l-m+1)(l+m+1)\right) \tag{2.252}$$

$$= \frac{(l+m+1)(l-m+1)}{A_l^m} \tag{2.253}$$

$$\Rightarrow \beta_l^m = (l+m+1)(l-m+1)\frac{4}{\pi}\prod_{i=1}^{\frac{l+m}{2}}\frac{2i}{2i+1}\prod_{i=1}^{\frac{l-m}{2}}\frac{2i}{2i+1}. \tag{2.254}$$

Let us rewrite the following two products:

$$\prod_{i=1}^{\frac{l+m}{2}} \frac{1}{2i+1} = \frac{1}{(l+m+1)} \prod_{i=1}^{\frac{l+m}{2}} \frac{1}{2i-1}, \tag{2.255}$$

$$\prod_{i=1}^{\frac{l-m}{2}} \frac{1}{2i+1} = \frac{1}{(l-m+1)} \prod_{i=1}^{\frac{l-m}{2}} \frac{1}{2i-1}, \tag{2.256}$$

from which we finally write β_l^m as:

$$\beta_l^m = \frac{4}{\pi} \prod_{i=1}^{\frac{l+m}{2}} \frac{2i}{2i-1} \prod_{i=1}^{\frac{l-m}{2}} \frac{2i}{2i-1}. \tag{2.257}$$

■

Remark 2.7.7 (First values of β_l^m)**.** *The values of β_l^m are real for $l+m$, increasing with degree l, and decreasing with the absolute value of the order m. Table 2.6 shows, as an example, some of the first values of β_l^m.*

Table 2.6: Some of the first values of β_l^m, for degree $l \leq 4$, order $-4 \leq m \leq 4$ and $l+m$ even.

β_l^m	m=-4	m=-3	m=-2	m=-1	m=0	m=1	m=2	m=3	m=4
l=0					1.2732				
l=1				2.5465		2.5465			
l=2			3.3953		5.093		3.3953		
l=3		4.0744		6.7906		6.7906		4.0744	
l=4	4.6564		8.1487		9.0541		8.1487		4.6564

We will now show that the chosen value of β_l^m is such that it allows us to rewrite $\mathcal{S}$ as $\mathcal{L}_s^{ws}$ for the case of the symmetric Dirichlet Laplace problem for the disk screen.

Theorem 2.7.3 (K^{ws} is K_s^{ws})**.** *For $(\boldsymbol{x}, \boldsymbol{y}) \in \mathbb{D} \times \mathbb{D}$, the weakly singular integral kernel K^{ws}, associated with $\mathcal{S}$, is equal to the proposed weakly singular symmetric kernel K_s^{ws}.*

Proof It is easy to show that $\overrightarrow{\text{grad}}_{\mathbb{D}}^{\boldsymbol{x}} \|\boldsymbol{x}-\boldsymbol{y}\| = -\overrightarrow{\text{grad}}_{\mathbb{D}}^{\boldsymbol{y}} \|\boldsymbol{x}-\boldsymbol{y}\|$ and that $\overrightarrow{\text{grad}}_{\mathbb{D}}^{\boldsymbol{x}} K_s^{ws}(\boldsymbol{x}, \boldsymbol{y}) = -\overrightarrow{\text{grad}}_{\mathbb{D}}^{\boldsymbol{y}} K_s^{ws}(\boldsymbol{x}, \boldsymbol{y})$, and thus

$$\overrightarrow{\text{grad}}_{\mathbb{D}}^{\boldsymbol{x}} \left(\|\boldsymbol{x}-\boldsymbol{y}\| \, K_s^{ws}(\boldsymbol{x}, \boldsymbol{y}) \right) = -\overrightarrow{\text{grad}}_{\mathbb{D}}^{\boldsymbol{y}} \left(\|\boldsymbol{x}-\boldsymbol{y}\| \, K_s^{ws}(\boldsymbol{x}, \boldsymbol{y}) \right). \tag{2.258}$$

For a function f of $\boldsymbol{x}$ and $\boldsymbol{y}$ on the $\mathbb{D}$, we have that

$$\overrightarrow{\text{grad}}_{\mathbb{D}}^{\boldsymbol{x}} f(\boldsymbol{x}, \boldsymbol{y}) = 0 \Leftrightarrow \begin{cases} \cos\phi_{\boldsymbol{x}} \frac{\partial f}{\partial \rho_{\boldsymbol{x}}}(\boldsymbol{x}, \boldsymbol{y}) - \frac{\sin\phi_{\boldsymbol{x}}}{\rho_{\boldsymbol{x}}} \frac{\partial f}{\partial \phi_{\boldsymbol{x}}}(\boldsymbol{x}, \boldsymbol{y}) = 0 \\ \text{and} \\ \sin\phi_{\boldsymbol{x}} \frac{\partial f}{\partial \rho_{\boldsymbol{x}}}(\boldsymbol{x}, \boldsymbol{y}) + \frac{\cos\phi_{\boldsymbol{x}}}{\rho_{\boldsymbol{x}}} \frac{\partial f}{\partial \phi_{\boldsymbol{x}}}(\boldsymbol{x}, \boldsymbol{y}) = 0, \end{cases} \tag{2.259}$$

from where it is easy to conclude that

$$\overrightarrow{\text{grad}}_{\mathbb{D}}^{\boldsymbol{x}} \left(\|\boldsymbol{x}-\boldsymbol{y}\| \, K_s^{ws}(\boldsymbol{x}, \boldsymbol{y}) \right) = 0 \quad \Leftrightarrow \quad \mathcal{L}_+^{\boldsymbol{x}} \left(\|\boldsymbol{x}-\boldsymbol{y}\| \, K_s^{ws}(\boldsymbol{x}, \boldsymbol{y}) \right) = 0, \tag{2.260}$$

since both $\|\boldsymbol{x}-\boldsymbol{y}\|$ and $K_s^{ws}(\boldsymbol{x}, \boldsymbol{y})$ are real. Using the above identities, we have that

$$\mathcal{L}_+^{\boldsymbol{x}} \left(\|\boldsymbol{x}-\boldsymbol{y}\| \, K_s^{ws}(\boldsymbol{x}, \boldsymbol{y}) \right) = 0 \quad \Rightarrow \quad K_s^{ws}(\boldsymbol{x}, \boldsymbol{y}) = C K^{ws}(\boldsymbol{x}, \boldsymbol{y}), \tag{2.261}$$

for some constant C.

Let us then prove that $\mathcal{L}^{\boldsymbol{x}}_{+}\left(\|\boldsymbol{x}-\boldsymbol{y}\|\, K_s^{ws}(\boldsymbol{x},\boldsymbol{y})\right)=0$.

If we consider the Law of Cosines, or Generalized Pythagoras Theorem, i.e.

$$\|\boldsymbol{x}-\boldsymbol{y}\|^2=\rho_{\boldsymbol{x}}^2+\rho_{\boldsymbol{y}}^2-2\rho_{\boldsymbol{x}}\rho_{\boldsymbol{y}}\cos(\phi_{\boldsymbol{x}}-\phi_{\boldsymbol{y}}) \tag{2.262}$$

We can easily state the identities

$$\mathcal{L}^{\boldsymbol{x}}_{+}(\|\boldsymbol{x}-\boldsymbol{y}\|)=\frac{e^{\mathrm{i}\phi_{\boldsymbol{x}}}}{\|\boldsymbol{x}-\boldsymbol{y}\|}\left(\rho_{\boldsymbol{x}}-\rho_{\boldsymbol{y}}e^{-\mathrm{i}(\phi_{\boldsymbol{x}}-\phi_{\boldsymbol{y}})}\right) \tag{2.263}$$

and

$$\mathcal{L}^{\boldsymbol{x}}_{-}(\|\boldsymbol{x}-\boldsymbol{y}\|)=\frac{e^{-\mathrm{i}\phi_{\boldsymbol{x}}}}{\|\boldsymbol{x}-\boldsymbol{y}\|}\left(-\rho_{\boldsymbol{x}}+\rho_{\boldsymbol{y}}e^{\mathrm{i}(\phi_{\boldsymbol{x}}-\phi_{\boldsymbol{y}})}\right), \tag{2.264}$$

which allows us to write:

$$\mathcal{L}^{\boldsymbol{x}}_{+}(\|\boldsymbol{x}-\boldsymbol{y}\|)\mathcal{L}^{\boldsymbol{x}}_{-}(\|\boldsymbol{x}-\boldsymbol{y}\|)=-1, \tag{2.265}$$

$$\|\boldsymbol{x}-\boldsymbol{y}\|\mathcal{L}^{\boldsymbol{x}}_{+}(\|\boldsymbol{x}-\boldsymbol{y}\|)=\rho_{\boldsymbol{x}}e^{\mathrm{i}\phi_{\boldsymbol{x}}}-\rho_{\boldsymbol{y}}e^{-\mathrm{i}\phi_{\boldsymbol{y}}}, \tag{2.266}$$

$$\|\boldsymbol{x}-\boldsymbol{y}\|\mathcal{L}^{\boldsymbol{x}}_{-}(\|\boldsymbol{x}-\boldsymbol{y}\|)=-\rho_{\boldsymbol{x}}e^{-\mathrm{i}\phi_{\boldsymbol{x}}}+\rho_{\boldsymbol{y}}e^{-\mathrm{i}\phi_{\boldsymbol{y}}}. \tag{2.267}$$

Using (2.265) together with the product rule

$$\mathcal{L}^{\boldsymbol{x}}_{+}(\|\boldsymbol{x}-\boldsymbol{y}\|K_s^{ws}(\boldsymbol{x},\boldsymbol{y}))=\mathcal{L}^{\boldsymbol{x}}_{+}(\|\boldsymbol{x}-\boldsymbol{y}\|)K_s^{ws}(\boldsymbol{x},\boldsymbol{y})+\|\boldsymbol{x}-\boldsymbol{y}\|\mathcal{L}^{\boldsymbol{x}}_{+}(K_s^{ws}(\boldsymbol{x},\boldsymbol{y})), \tag{2.268}$$

we can write

$$\mathcal{L}^{\boldsymbol{x}}_{-}(\|\boldsymbol{x}-\boldsymbol{y}\|)\mathcal{L}^{\boldsymbol{x}}_{+}(\|\boldsymbol{x}-\boldsymbol{y}\|K_s^{ws}(\boldsymbol{x},\boldsymbol{y}))=-K_s^{ws}(\boldsymbol{x},\boldsymbol{y})+\|\boldsymbol{x}-\boldsymbol{y}\|\,\mathcal{L}^{\boldsymbol{x}}_{-}(\|\boldsymbol{x}-\boldsymbol{y}\|)\mathcal{L}^{\boldsymbol{x}}_{+}(K_s^{ws}(\boldsymbol{x},\boldsymbol{y})). \tag{2.269}$$

Since function $\mathcal{L}^{\boldsymbol{x}}_{-}(\|\boldsymbol{x}-\boldsymbol{y}\|)$ is not zero for all $\boldsymbol{x}$ and $\boldsymbol{y}$ on $\mathbb{D}$, we have

$$K_s^{ws}(\boldsymbol{x},\boldsymbol{y})=\|\boldsymbol{x}-\boldsymbol{y}\|\,\mathcal{L}^{\boldsymbol{x}}_{-}(\|\boldsymbol{x}-\boldsymbol{y}\|)\mathcal{L}^{\boldsymbol{x}}_{+}(K_s^{ws}(\boldsymbol{x},\boldsymbol{y})) \tag{2.270}$$

$$\iff \mathcal{L}^{\boldsymbol{x}}_{-}(\|\boldsymbol{x}-\boldsymbol{y}\|)\mathcal{L}^{\boldsymbol{x}}_{+}(\|\boldsymbol{x}-\boldsymbol{y}\|K_s^{ws}(\boldsymbol{x},\boldsymbol{y}))=0 \tag{2.271}$$

$$\iff \mathcal{L}^{\boldsymbol{x}}_{+}(\|\boldsymbol{x}-\boldsymbol{y}\|K_s^{ws}(\boldsymbol{x},\boldsymbol{y}))=0 \tag{2.272}$$

$$\iff \overrightarrow{\operatorname{grad}}^{\boldsymbol{x}}_{\mathbb{D}}(\|\boldsymbol{x}-\boldsymbol{y}\|K_s^{ws}(\boldsymbol{x},\boldsymbol{y}))=0 \tag{2.273}$$

As it has now become clearer, a way of proving the theorem is to demonstrate identity (2.270). In order to do so we will use the action of the angular momentum operators on the disk basis functions, contained in Corollary 2.7.2, and recurrence relations for β_l^m that we will conclude from the explicit expression for it given in Proposition 2.7.13.

Using (2.267) we can write

$$\|\boldsymbol{x}-\boldsymbol{y}\|\,\mathcal{L}^{\boldsymbol{x}}_{-}(\|\boldsymbol{x}-\boldsymbol{y}\|)\mathcal{L}^{\boldsymbol{x}}_{+}(K_s^{ws}(\boldsymbol{x},\boldsymbol{y}))=\left(-\rho_{\boldsymbol{x}}e^{-\mathrm{i}\phi_{\boldsymbol{x}}}+\rho_{\boldsymbol{y}}e^{-\mathrm{i}\phi_{\boldsymbol{y}}}\right)\mathcal{L}^{\boldsymbol{x}}_{+}(K_s^{ws}(\boldsymbol{x},\boldsymbol{y}). \tag{2.274}$$

We will use this to prove (2.270) in several steps:

1. Develop an expression for $-\rho_{\boldsymbol{x}}e^{-\mathrm{i}\phi_{\boldsymbol{x}}}\mathcal{L}^{\boldsymbol{x}}_{+}(K_s^{ws}(\boldsymbol{x},\boldsymbol{y}))$. This will be easy using (2.190) and (2.192) from Corollary 2.7.2.

2. Develop an expression for $\rho_{\boldsymbol{y}}e^{-\mathrm{i}\phi_{\boldsymbol{y}}}\mathcal{L}^{\boldsymbol{x}}_{+}(K_s^{ws}(\boldsymbol{x},\boldsymbol{y}))$. This will be a more difficult task because $\rho_{\boldsymbol{y}}e^{-\mathrm{i}\phi_{\boldsymbol{y}}}$, depending on $\boldsymbol{y}$, will have to be treated to match the terms in $\mathcal{L}^{\boldsymbol{x}}_{+}(K_s^{ws}(\boldsymbol{x},\boldsymbol{y}))$, whose exponential components depend on $\boldsymbol{x}$.

3. Finally we add both developed expressions to form $\|\boldsymbol{x}-\boldsymbol{y}\|\,\mathcal{L}^{\boldsymbol{x}}_{-}(\|\boldsymbol{x}-\boldsymbol{y}\|)\mathcal{L}^{\boldsymbol{x}}_{+}(K_s^{ws}(\boldsymbol{x},\boldsymbol{y}))$ and develop a suitable expression for K_s^{ws} to conclude that they are the same.

We will proceed in the same order.

1. Using (2.190) and (2.192) from Corollary 2.7.2 it is easy to see that

$$\mathcal{L}_+^{\boldsymbol{x}} K_s^{ws}(\boldsymbol{x},\boldsymbol{y}) = \frac{e^{i\phi_{\boldsymbol{x}}}}{2\rho_{\boldsymbol{x}}\sqrt{(1-\rho_{\boldsymbol{x}}^2)}} \sum_{l=0}^{\infty} \sum_{\substack{m=-l \\ l+m \text{ even}}}^{l} \frac{1}{\beta_l^m} \left[\left((l-m)\frac{\sqrt{(l+1)^2-m^2}}{\sqrt{(l+1)^2-1/4}} y_{l+1}^m(\boldsymbol{x}) - (l+m+1)\frac{\sqrt{l^2-m^2}}{\sqrt{l^2-1/4}} y_{l-1}^m(\boldsymbol{x}) \right) \overline{y_l^m(\boldsymbol{y})} \right.$$
$$\left. + \left((l+m)\frac{\sqrt{(l+1)^2-m^2}}{\sqrt{(l+1)^2-1/4}} \overline{y_{l+1}^m(\boldsymbol{x})} - (l-m+1)\frac{\sqrt{l^2-m^2}}{\sqrt{l^2-1/4}} \overline{y_{l-1}^m(\boldsymbol{x})} \right) y_l^m(\boldsymbol{y}) \right]. \tag{2.275}$$

Then, the desired term is:

$$-\rho_{\boldsymbol{x}} e^{-\mathrm{i}\phi_{\boldsymbol{x}}} \mathcal{L}_+^{\boldsymbol{x}} K_s^{ws}(\boldsymbol{x},\boldsymbol{y}) = \frac{-1}{2w(\rho_{\boldsymbol{x}})} \sum_{l=0}^{\infty} \sum_{\substack{m=-l \\ l+m \text{ even}}}^{l} \frac{1}{\beta_l^m} \left[\left((l-m)\frac{\sqrt{(l+1)^2-m^2}}{\sqrt{(l+1)^2-1/4}} y_{l+1}^m(\boldsymbol{x}) - (l+m+1)\frac{\sqrt{l^2-m^2}}{\sqrt{l^2-1/4}} y_{l-1}^m(\boldsymbol{x}) \right) \overline{y_l^m(\boldsymbol{y})} \right.$$
$$\left. + \left((l+m)\frac{\sqrt{(l+1)^2-m^2}}{\sqrt{(l+1)^2-1/4}} \overline{y_{l+1}^m(\boldsymbol{x})} - (l-m+1)\frac{\sqrt{l^2-m^2}}{\sqrt{l^2-1/4}} \overline{y_{l-1}^m(\boldsymbol{x})} \right) y_l^m(\boldsymbol{y}) \right]. \tag{2.276}$$

2. Now using (2.184) and (2.188) from Corollary 2.7.2 we write

$$\rho_{\boldsymbol{y}} e^{-\mathrm{i}\phi_{\boldsymbol{y}}} \mathcal{L}_+^{\boldsymbol{x}} K_s^{ws}(\boldsymbol{x},\boldsymbol{y}) = \frac{\rho_{\boldsymbol{y}} e^{-\mathrm{i}\phi_{\boldsymbol{y}}}}{w(\boldsymbol{x})} \sum_{l=0}^{\infty} \sum_{\substack{m=-l \\ l+m \text{ even}}}^{l} \frac{1}{\beta_l^m} \left(\sqrt{(l-m)(l+m+1)}\, y_l^{m+1}(\boldsymbol{x}) \overline{y_l^m}(\boldsymbol{y}) \right.$$
$$\left. - \sqrt{(l+m)(l-m+1)}\ \overline{y_l^{m-1}(\boldsymbol{x})}\ y_l^m(\boldsymbol{y}) \right). \tag{2.277}$$

Then, using (2.194) from Corollary 2.7.3:

$$\rho_{\boldsymbol{y}} e^{-i\phi_{\boldsymbol{y}}} \mathcal{L}_+(K_s^{ws}(\boldsymbol{x},\boldsymbol{y})) = \frac{\rho_{\boldsymbol{y}} e^{-i\phi(\boldsymbol{y})}}{w(\boldsymbol{x})} \sum_{l=0}^{\infty} \sum_{\substack{m=-l \\ l+m \text{ even}}}^{l} \frac{1}{\beta_l^m} \Bigg[$$
$$\sqrt{(l-m)(l+m+1)} y_l^{m+1}(\boldsymbol{x}) \left(\sqrt{\frac{(l-m)(l-m-1)}{(l^2-1/4)}}\ \overline{y_{l-1}^{m+1}(\boldsymbol{y})} - \sqrt{\frac{(l+m+1)(l+m+2)}{((l+1)^2-1/4)}} \overline{y_{l+1}^{m+1}(\boldsymbol{y})} \right)$$
$$+ \sqrt{(l+m)(l-m+1)}\ \overline{y_l^{m-1}(\boldsymbol{x})} \left(\sqrt{\frac{(l+m-1)(l+m)}{(l^2-1/4)}}\ y_{l-1}^{m-1}(\boldsymbol{y}) - \sqrt{\frac{(l-m+1)(l-m+2)}{((l+1)^2-1/4)}}\ y_{l+1}^{m-1}(\boldsymbol{y}) \right) \Bigg], \tag{2.278}$$

which can be ordered into

$$\rho_{\boldsymbol{y}} e^{-i\phi_{\boldsymbol{y}}} \mathcal{L}_+(K_s^{ws}(\boldsymbol{x},\boldsymbol{y})) = \frac{1}{2w(\boldsymbol{x})} \sum_{l=0}^{\infty} \sum_{\substack{m=-l \\ l+m \text{ even}}}^{l} \frac{1}{\beta_l^m} \Bigg[$$

$$(l-m)\sqrt{\frac{l^2-(m+1)^2}{l^2-1/4}}\, y_l^{m+1}(\boldsymbol{x})\overline{y_{l-1}^{m+1}(\boldsymbol{y})} \; - (l+m+1)\sqrt{\frac{(l+1)^2-(m+1)^2)}{(l+1)^2-1/4}} \; y_l^{m+1}(\boldsymbol{x})\overline{y_{l+1}^{m+1}(\boldsymbol{y})})$$

$$+(l+m)\,\sqrt{\frac{(l^2-(m-1)^2)}{(l^2-1/4)}}\overline{y_l^{m-1}(\boldsymbol{x})}\; y_{l-1}^{m-1}(\boldsymbol{y}) - (l-m+1)\sqrt{\frac{(l+v1)^2-(m-1)^2}{(l+1)^2-1/4}}\; \overline{y_l^{m-1}(\boldsymbol{x})}\; y_{l+1}^{m-1}(\boldsymbol{y})\Bigg]. \tag{2.279}$$

We will now treat each term of (2.279) as a different summation and we will change the summation indices to accommodate the whole expression so that it will only have terms on $y_l^m(\boldsymbol{y})$ and $\overline{y_l^m(\boldsymbol{y})}$, as the expression found for part 1. Let us consider the first separate summation:

$$\sum_{l=0}^{\infty} \sum_{\substack{m=-l \\ l+m \text{ even}}}^{l} \frac{1}{\beta_l^m}(l-m)\sqrt{\frac{l^2-(m+1)^2}{(l^2-1/4)}} y_l^{m+1}(\boldsymbol{x})\overline{y_{l-1}^{m+1}(\boldsymbol{y})}. \tag{2.280}$$

We need to sum the new indices $m-1$ and $l+1$ to get an expression that is a factor of $y_l^m(\boldsymbol{y})$. We use the properties of summations to get

$$\sum_{l=0}^{\infty} \sum_{\substack{m=-l \\ l+m \text{ even}}}^{l} \frac{(l-m)}{\beta_l^m}\sqrt{\frac{l^2-(m+1)^2}{(l^2-1/4}} y_l^{m+1}(\boldsymbol{x})\overline{y_{l-1}^{m+1}(\boldsymbol{y})} = \sum_{l=-1}^{\infty} \sum_{\substack{m=-l \\ l+m \text{ even}}}^{l+2} \frac{(l-m+2)}{\beta_{l+1}^{m-1}}\sqrt{\frac{(l+1)^2-m^2}{(l+1)^2-1/2}} y_{l+1}^m(\boldsymbol{x})\overline{y_l^m(\boldsymbol{y})}. \tag{2.281}$$

In comparison to the summation to which we would like to add it, summed only for $l>0$ and $-l<m<l$ with $l+m$ even, we are introducing additional terms for $(l,m)=(-1,1)$, $(l,m)=(0,2)$, $(l,m)=(1,3)$, etc. But, since (2.281) has a factor $(l-m+2)$, these additional terms are zero, providing us the desired transformation of the first term of the summation (2.279).

Transforming the summation of each one of the separate terms of (2.279) as indicated, it can be rewritten as

$$\rho_{\boldsymbol{y}} e^{-i\phi_{\boldsymbol{y}}} \mathcal{L}_+(K_s^{ws}(\boldsymbol{x},\boldsymbol{y})) = \frac{1}{2w(\boldsymbol{x})} \sum_{l=0}^{\infty} \sum_{\substack{m=-l \\ l+m \text{ even}}}^{l} \Bigg[$$

$$\frac{(l-m+2)}{\beta_{l+1}^{m-1}}\sqrt{\frac{((l+1)^2-m^2)}{((l+1)^2-1/4)}} y_{l+1}^m(\boldsymbol{x})\overline{y_l^m(\boldsymbol{y})} - \frac{(l+m-1)}{\beta_{l-1}^{m-1}}\sqrt{\frac{(l^2-m^2)}{(l^2-1/4)}} \; y_{l-1}^m(\boldsymbol{x})\overline{y_l^m(\boldsymbol{y})})$$

$$+\frac{(l+m+2)}{\beta_{l+1}^{m+1}}\; \sqrt{\frac{((l+1)^2-m^2)}{((l+1)^2-1/4)}}\overline{y_{l+1}^m(\boldsymbol{x})}\; y_l^m(\boldsymbol{y}) - \frac{(l-m-1)}{\beta_{l-1}^{m+1}}\sqrt{\frac{(l^2-m^2)}{(l^2-1/4)}}\; \overline{y_{l-1}^m(\boldsymbol{x})}\; y_l^m(\boldsymbol{y})\Bigg]. \tag{2.282}$$

3. Summing the terms developed in points 1. and 2. we get the following expression

$$\begin{aligned}
\|\boldsymbol{x}-\boldsymbol{y}\|\,\mathcal{L}_-(\|\boldsymbol{x}-\boldsymbol{y}\|)\mathcal{L}_+(K_s^{ws}(\boldsymbol{x},\boldsymbol{y}) &= \frac{1}{2w(\boldsymbol{x})}\sum_{l=0}^{\infty}\sum_{\substack{m=-l\\ l+m \text{ even}}}^{l}\Bigg[\\
&\left(\frac{l-m+2}{\beta_{l+1}^{m-1}}-\frac{l-m}{\beta_l^m}\right)\frac{\sqrt{(l+1)^2-m^2}}{\sqrt{(l+1)^2-1/4}}\; y_{l+1}^m(\boldsymbol{x})\overline{y_l^m(\boldsymbol{y})}\\
&+\left(\frac{l+m+1}{\beta_l^m}-\frac{l+m-1}{\beta_{l-1}^{m-1}}\right)\;\frac{\sqrt{l^2-m^2}}{\sqrt{l^2-1/4}}\; y_{l-1}^m(\boldsymbol{x})\overline{y_l^m(\boldsymbol{y})}\\
&+\left(\frac{l+m+2}{\beta_{l+1}^{m+1}}-\frac{l+m}{\beta_l^m}\right)\frac{\sqrt{(l+1)^2-m^2}}{\sqrt{(l+1)^2-1/4}}\;\overline{y_{l+1}^m(\boldsymbol{x})}y_l^m(\boldsymbol{y})\\
&+\left(\frac{l-m+1}{\beta_l^m}-\frac{l-m-1}{\beta_{l-1}^{m+1}}\right)\frac{\sqrt{l^2-m^2}}{\sqrt{l^2-1/4}}\;\overline{y_{l-1}^m(\boldsymbol{x})}y_l^m(\boldsymbol{y})\Bigg].
\end{aligned}\tag{2.283}$$

From Proposition 2.7.13 we can extract suitable relations for β_l^m that will further simplify the previous expression:

$$\begin{aligned}
&(l-m-1)\beta_l^m=(l-m)\beta_{l-1}^{m+1},\quad (l+m+2)\beta_l^m=(l+m+1)\beta_{l+1}^{m+1},\\
&(l-m+1)\beta_{l+1}^{m-1}=(l-m+2)\beta_l^m,\quad (l+m)\beta_{l-1}^{m-1}=(l+m-1)\beta_l^m.
\end{aligned}\tag{2.284}$$

Using these expressions we can rewrite (2.283) as

$$\begin{aligned}
\|\boldsymbol{x}-\boldsymbol{y}\|\,\mathcal{L}_-(\|\boldsymbol{x}-\boldsymbol{y}\|)\mathcal{L}_+(K_s^{ws}(\boldsymbol{x},\boldsymbol{y}) &= \frac{1}{2w(\boldsymbol{x})}\sum_{l=0}^{\infty}\sum_{\substack{m=-l\\ l+m \text{ even}}}^{l}\frac{1}{\beta_l^m}\Bigg[\\
&\frac{\sqrt{(l+1)^2-m^2}}{\sqrt{(l+1)^2-1/4}}\; y_{l+1}^m(\boldsymbol{x})\overline{y_l^m}(\boldsymbol{y})+\frac{\sqrt{l^2-m^2}}{\sqrt{l^2-1/4}}\;\; y_{l-1}^m(\boldsymbol{x}))\overline{y_l^m}(\boldsymbol{y})\\
&+(\frac{\sqrt{(l+1)^2-m^2}}{\sqrt{(l+1)^2-1/4}}\;\overline{y_{l+1}^m(\boldsymbol{x})}y_l^m(\boldsymbol{y})+\frac{\sqrt{l^2-m^2}}{\sqrt{l^2-1/4}}\;\;\overline{y_{l-1}^m(\boldsymbol{x})}\;y_l^m(\boldsymbol{y})\Bigg].
\end{aligned}\tag{2.285}$$

This last expression can be easily equated to K_s^{ws} applying identity (2.193) from Corollary 2.7.3 to y_l^m and $\overline{y_l^m}$:

$$\begin{aligned}
K^{ws}(\boldsymbol{x},\boldsymbol{y}) &= \sum_{l=0}^{\infty}\sum_{\substack{m=-l\\ l+m \text{ even}}}^{l}\frac{1}{\beta_l^m}\left(y_l^m(\boldsymbol{x})\overline{y_l^m}(\boldsymbol{y})+\overline{y_l^m}(\boldsymbol{x})y_l^m(\boldsymbol{y})\right) &(2.286)\\
&= \frac{1}{2w(\boldsymbol{x})}\sum_{l=0}^{\infty}\sum_{\substack{m=-l\\ l+m \text{ even}}}^{l}\frac{1}{\beta_l^m}\Bigg[\\
&\frac{\sqrt{(l+1)^2-m^2}}{\sqrt{(l+1)^2-1/4}}\; y_{l+1}^m(\boldsymbol{x})\overline{y_l^m}(\boldsymbol{y})+\frac{\sqrt{l^2-m^2}}{\sqrt{l^2-1/4}}\;\; y_{l-1}^m(\boldsymbol{x}))\overline{y_l^m}(\boldsymbol{y}) \quad .\\
&+\frac{\sqrt{(l+1)^2-m^2}}{\sqrt{(l+1)^2-1/4}}\;\overline{y_{l+1}^m(\boldsymbol{x})}y_l^m(\boldsymbol{y})+\frac{\sqrt{l^2-m^2}}{\sqrt{l^2-1/4}}\;\;\overline{y_{l-1}^m(\boldsymbol{x})}\;y_l^m(\boldsymbol{y})\Bigg].
\end{aligned}\tag{2.287}$$

This finishes part 3., allowing us to conclude that $K_s^{ws} = CK^{ws}$. We will now see that the constant C is equal to 1.

Using Proposition 2.7.10, Proposition 2.7.13, and Remark 2.7.2 (i.e. $y_0^0 = \gamma_0^0$, from (2.120)), it is easy to check that

$$\int_{\mathbb{D}} K_s^{ws}(\boldsymbol{x}, \boldsymbol{y}) \frac{y_0^0(\boldsymbol{x})}{w(\boldsymbol{x})} d\mathbb{D}(\boldsymbol{x}) = \frac{1}{\beta_0^0} y_0^0(\boldsymbol{x}) = \gamma_0^0 \frac{\pi}{4}. \tag{2.288}$$

On the other hand

$$\int_{\mathbb{D}} K^{ws}(\boldsymbol{x}, \boldsymbol{y}) \frac{y_0^0(\boldsymbol{x})}{w(\boldsymbol{x})} d\mathbb{D}(\boldsymbol{x}) = \gamma_0^0 \int_{\mathbb{D}} \frac{1}{4\pi \left\| \boldsymbol{x} - \boldsymbol{y} \right\| w(\boldsymbol{x})} d\mathbb{D}(\boldsymbol{x}). \tag{2.289}$$

It will suffice to show that the integral of $(4\pi \left\| \boldsymbol{x} - \boldsymbol{y} \right\| w(\boldsymbol{x}))^{-1}$ over $\mathbb{D}$ is $\pi/4$ to prove that $C = 1$. We know that $K_s^{ws} = CK^{ws}$, so we also know that the integral of $(4\pi \left\| \boldsymbol{x} - \boldsymbol{y} \right\| w(\boldsymbol{x}))^{-1}$ over $\mathbb{D}$ will be a constant for every $\boldsymbol{y}$. Let us choose the arbitrary point $\boldsymbol{y}_0 = (0, 0)$ to evaluate this integral.

We suppose that $\boldsymbol{y}$ has cylindrical coordinates $\boldsymbol{y} = (\rho_{\boldsymbol{y}}, 0)$ and express $\boldsymbol{x}$ in general cylindrical coordinates $\boldsymbol{x} = (\rho_{\boldsymbol{x}}, \phi_{\boldsymbol{x}})$. We will compute the integral over the sub-region of $\mathbb{D}$ such that $\rho_{\boldsymbol{x}} \geq \rho_{\boldsymbol{y}}$, and then compute the limit when $\rho_{\boldsymbol{y}} \to 0$. We will introduce the variable α such that,

$$\cos(\alpha) = \frac{\rho_{\boldsymbol{x}} \cos(\phi_{\boldsymbol{x}}) - \rho_{\boldsymbol{y}}}{\left\| \boldsymbol{x} - \boldsymbol{y} \right\|}, \quad \text{and} \quad \sin(\alpha) = \frac{\rho_{\boldsymbol{x}} \sin(\phi_{\boldsymbol{x}})}{\left\| \boldsymbol{x} - \boldsymbol{y} \right\|}, \tag{2.290}$$

which comply with $\cos^2(\alpha) + \sin^2(\alpha) = 1$ by the law of cosines for $\left\| \boldsymbol{x} - \boldsymbol{y} \right\|$. We will also use the standard change of variables $\rho_{\boldsymbol{x}} = \sin\theta_{\boldsymbol{x}}$ and $\rho_{\boldsymbol{y}} = \sin\theta_{\boldsymbol{y}}$.

Using variable α, for $\alpha \in [0, 2\pi]$, we can express the following terms:

$$\rho_{\boldsymbol{x}} \cos(\phi_{\boldsymbol{x}}) = \rho_{\boldsymbol{y}} \sin^2(\alpha) + \cos(\alpha) \sqrt{\rho_{\boldsymbol{x}}^2 - \rho_{\boldsymbol{y}}^2 \sin^2(\alpha)} \tag{2.291}$$

and

$$\left\| \boldsymbol{x} - \boldsymbol{y} \right\| = -\rho_{\boldsymbol{y}} + \sqrt{\rho_{\boldsymbol{x}}^2 - \rho_{\boldsymbol{y}}^2 \sin^2(\alpha)}. \tag{2.292}$$

This allows us express the following derivative that will permit us to compute the integral using the change of variables:

$$\frac{d\alpha}{d\phi_{\boldsymbol{x}}} = \frac{\rho_{\boldsymbol{x}}^2 - \rho_{\boldsymbol{y}} \rho_{\boldsymbol{x}} \cos(\phi_{\boldsymbol{x}})}{\left\| \boldsymbol{x} - \boldsymbol{y} \right\|^2} = \frac{\sqrt{\rho_{\boldsymbol{x}}^2 - \rho_{\boldsymbol{y}}^2 \sin^2(\alpha)}}{\left\| \boldsymbol{x} - \boldsymbol{y} \right\|}. \tag{2.293}$$

Using this change of variables, and making $\theta_{\boldsymbol{y}} = \arcsin(\rho_{\boldsymbol{x}})$, we can write the first integral for $\rho_{\boldsymbol{x}} \geq \rho_{\boldsymbol{y}}$ as

$$\frac{1}{4\pi} \int_0^{2\pi} \int_{\rho_{\boldsymbol{y}}}^1 \frac{\rho_{\boldsymbol{x}} d\rho_{\boldsymbol{x}} d\phi_{\boldsymbol{x}}}{\left\| \boldsymbol{x} - \boldsymbol{y} \right\| \sqrt{1 - \rho_{\boldsymbol{x}}^2}} = \frac{1}{4\pi} \int_0^{2\pi} \int_{\theta_{\boldsymbol{y}}}^{\pi/2} \frac{\sin(\theta_{\boldsymbol{x}})}{\sqrt{1 - \cos^2(\theta_{\boldsymbol{x}}) - \rho_{\boldsymbol{y}}^2 \sin^2(\alpha)}} d\theta_{\boldsymbol{x}} d\alpha. \tag{2.294}$$

Integrating first on $\theta_{\boldsymbol{x}}$ we have that

$$\int_{\theta_{\boldsymbol{y}}}^{\pi/2} \frac{\sin(\theta_{\boldsymbol{x}}) d\theta_{\boldsymbol{x}}}{\sqrt{1 - \cos^2(\theta_{\boldsymbol{x}}) - \rho_{\boldsymbol{y}}^2 \sin^2(\alpha)}} = \arcsin\left(\frac{\sqrt{1 - \rho_{\boldsymbol{y}}^2}}{\sqrt{1 - \rho_{\boldsymbol{y}}^2 \sin^2(\alpha)}} \right) \tag{2.295}$$

$$= \frac{\pi}{2} - \arccos\left(\frac{\sqrt{1 - \rho_{\boldsymbol{y}}^2}}{\sqrt{1 - \rho_{\boldsymbol{y}}^2 \sin^2(\alpha)}} \right), \tag{2.296}$$

so that

$$\frac{1}{4\pi}\int_0^{2\pi}\int_{\rho_{\boldsymbol{y}}}^{1}\frac{\rho_{\boldsymbol{x}}d\rho_{\boldsymbol{x}}d\phi_{\boldsymbol{x}}}{\|\boldsymbol{x}-\boldsymbol{y}\|\sqrt{1-\rho_{\boldsymbol{x}}^2}}=\frac{\pi}{4}-\frac{1}{4\pi}\int_0^{2\pi}\arccos\left(\frac{\sqrt{1-\rho_{\boldsymbol{y}}^2}}{\sqrt{1-\rho_{\boldsymbol{y}}^2\sin^2(\alpha)}}\right)d\alpha. \tag{2.297}$$

Summarizing, we have

$$\frac{1}{4\pi}\int_{\mathbb{D}}\frac{d\mathbb{D}(\boldsymbol{x})}{\|\boldsymbol{x}-\boldsymbol{y}_0\|\,w(\rho_{\boldsymbol{x}})}=\lim_{\rho_{\boldsymbol{y}}\to 0}\frac{1}{4\pi}\int_0^{2\pi}\int_{\rho_{\boldsymbol{y}}}^{1}\frac{\rho_{\boldsymbol{x}}d\rho_{\boldsymbol{x}}d\phi_{\boldsymbol{x}}}{\|\boldsymbol{x}-\boldsymbol{y}\|\sqrt{1-\rho_{\boldsymbol{x}}^2}} \tag{2.298}$$

$$=\frac{\pi}{4}-\lim_{\rho_{\boldsymbol{y}}\to 0}\frac{1}{4\pi}\int_0^{2\pi}\arccos\left(\frac{\sqrt{1-\rho_{\boldsymbol{y}}^2}}{\sqrt{1-\rho_{\boldsymbol{y}}^2\sin^2(\alpha)}}\right)d\alpha \tag{2.299}$$

$$=\frac{\pi}{4}, \tag{2.300}$$

which finishes the proof. ∎

Remark 2.7.8 ($\mathcal{S}$ is identified $\mathcal{L}_s^{ws}$)**.** *Being the integral kernels K^{ws} and K_s^{ws} equal for the case of the symmetric Dirichlet problem for the disk, the integral operators $\mathcal{S}$ and $\mathcal{L}_s^{ws}$ map the same functions from $\widetilde{H}^{-1/2}(\mathbb{D})$ to $H^{1/2}(\mathbb{D})$.*

Theorem 2.7.4 (Weakly singular operator on the disk basis functions)**.** *For $l+m$ even, the action of the weakly singular boundary integral operator $\mathcal{S}$ on a disk basis function y_l^m is*

$$\left(\mathcal{S}\frac{y_l^m}{w}\right)(\boldsymbol{x})=\frac{1}{\beta_l^m}y_l^m. \tag{2.301}$$

Proof This result comes straightforwardly from the Proposition 2.7.10, and the fact that $\mathcal{S}$ and $\mathcal{L}_s^{ws}$ produce the same mapping from $\widetilde{H}^{-1/2}(\mathbb{D})$ to $H^{1/2}(\mathbb{D})$. ∎

The result from Theorem 2.7.4 was later found to coincide with one from an article by Peter Wolfe [68]. It was achieved by a different method, taking the Fourier transform of the left-hand of (2.301) and inverting it. More recently, P. A. Martin has compared it to other expressions for the application of $\mathcal{S}$ in the case of the disk screen [47].

We will now develop the results that will lead to the proof of Theorem 2.7.1.

Proposition 2.7.14 (Relation between the symmetric weakly singular and the anti-symmetric hypersingular kernels on the disk)**.** *For $(\boldsymbol{x},\boldsymbol{y})\in\mathbb{D}\times\mathbb{D}$, the kernels K_s^{ws} and K_{as}^{hs} of the boundary integral operators $\mathcal{L}_s^{ws}$ and $\mathcal{L}_{as}^{hs}$ on disk $\mathbb{D}$ are linked by the Laplace-Beltrami operator:*

$$\Delta_{\mathbb{D}}K_s^{ws}=K_{as}^{hs}. \tag{2.302}$$

Proof In this proof we will develop two expressions for $\Delta_{\mathbb{D}}K_s^{ws}$ using the two expressions provided in Proposition 2.7.6 and then add them to recover the coefficients α_l^m needed for K_{as}^{hs} from the coefficients β_l^m using the recurrence relations from Proposition 2.7.12.

Let us proceed with the first expression for the Laplace-Beltrame operator. It is easy to show that $\mathcal{L}_{\pm}^{\boldsymbol{x}}K_s^{ws}(\boldsymbol{x},\boldsymbol{x})=-\mathcal{L}_{\pm}^{\boldsymbol{y}}K_s^{ws}(\boldsymbol{x},\boldsymbol{x})$, so we can write the first expression for the Laplace-Beltrami operator, as

$$\Delta_{\mathbb{D}}K_s^{ws}(\boldsymbol{x},\boldsymbol{y})=-\mathcal{L}_-^{\boldsymbol{x}}\circ\mathcal{L}_+^{\boldsymbol{x}}K_s^{ws}(\boldsymbol{x},\boldsymbol{y}) \tag{2.303}$$

$$=\mathcal{L}_-^{\boldsymbol{x}}\circ\mathcal{L}_+^{\boldsymbol{y}}K_s^{ws}(\boldsymbol{x},\boldsymbol{y}). \tag{2.304}$$

Using (2.184) and (2.187) we can obtain

$$\begin{aligned}\mathcal{L}_+^{\boldsymbol{y}} K_s^{ws}(\boldsymbol{x},\boldsymbol{y}) = \sum_{l=0}^{\infty} \sum_{\substack{m=-l \\ l+m \text{ even}}}^{l} \frac{1}{\beta_l^m} \Bigg[&-\sqrt{(l+m)(l-m+1)} \frac{y_l^m(\boldsymbol{x})}{w(\boldsymbol{x})} \frac{\overline{y_l^{m-1}(\boldsymbol{y})}}{w(\boldsymbol{y})} \\ &+\sqrt{(l-m)(l+m+1)} \frac{\overline{y_l^m(\boldsymbol{x})}}{w(\boldsymbol{x})} \frac{y_l^{m+1}(\boldsymbol{y})}{w(\boldsymbol{y})} \Bigg],\end{aligned} \tag{2.305}$$

and using (2.185) and (2.188)

$$\begin{aligned}\mathcal{L}_-^{\boldsymbol{x}} \circ \mathcal{L}_+^{\boldsymbol{y}} K_s^{ws}(\boldsymbol{x},\boldsymbol{y}) = -\sum_{l=0}^{\infty} \sum_{\substack{m=-l \\ l+m \text{ even}}}^{l} \frac{1}{\beta_l^m} \Bigg[&(l+m)(l-m+1) \frac{y_l^{m-1}(\boldsymbol{x})}{w(\boldsymbol{x})} \frac{\overline{y_l^{m-1}(\boldsymbol{y})}}{w(\boldsymbol{y})} \\ &+(l-m)(l+m+1) \frac{\overline{y_l^{m+1}(\boldsymbol{x})}}{w(\boldsymbol{x})} \frac{y_l^{m+1}(\boldsymbol{y})}{w(\boldsymbol{y})} \Bigg].\end{aligned} \tag{2.306}$$

As done in the proof of Theorem 2.7.3 we will analyze each term of the summand. Noting that the pairs $(l,m) = (0,0)$, $(l,m) = (1,-1)$, $(l,m) = (2,-2)$, etc. make $l+m = 0$ allows us to rewrite the first term as:

$$\sum_{l=0}^{\infty} \sum_{\substack{m=-l \\ l+m \text{ even}}}^{l} \frac{(l+m)(l-m+1)}{\beta_l^m} \frac{y_l^{m-1}(\boldsymbol{x})}{w(\boldsymbol{x})} \frac{\overline{y_l^{m-1}(\boldsymbol{y})}}{w(\boldsymbol{y})} = \sum_{l=0}^{\infty} \sum_{\substack{m=-l \\ l+m \text{ odd}}}^{l} \frac{(l-m)(l+m+1)}{\beta_l^{m+1}} \frac{y_l^m(\boldsymbol{x})}{w(\boldsymbol{x})} \frac{\overline{y_l^m(\boldsymbol{y})}}{w(\boldsymbol{y})}. \tag{2.307}$$

Noting that the pairs $(l,m) = (0,0)$, $(l,m) = (1,1)$, $(l,m) = (2,2)$, etc. make $l-m = 0$ allows us to rewrite the second term as:

$$\sum_{l=0}^{\infty} \sum_{\substack{m=-l \\ l+m \text{ even}}}^{l} \frac{(l-m)(l+m+1)}{\beta_l^m} \frac{\overline{y_l^{m+1}(\boldsymbol{x})}}{w(\boldsymbol{x})} \frac{y_l^{m+1}(\boldsymbol{y})}{w(\boldsymbol{y})} = \sum_{l=0}^{\infty} \sum_{\substack{m=-l \\ l+m \text{ odd}}}^{l} \frac{(l+m)(l-m+1)}{\beta_l^{m-1}} \frac{\overline{y_l^m(\boldsymbol{x})}}{w(\boldsymbol{x})} \frac{y_l^m(\boldsymbol{y})}{w(\boldsymbol{y})}. \tag{2.308}$$

Let us now obtain the second expression for the Laplace-Beltrami operator:

$$\Delta_{\mathbb{D}} K_s^{ws}(\boldsymbol{x},\boldsymbol{y}) = -\mathcal{L}_+^{\boldsymbol{x}} \circ \mathcal{L}_-^{\boldsymbol{x}} K_s^{ws}(\boldsymbol{x},\boldsymbol{y}) \tag{2.309}$$

$$= \mathcal{L}_+^{\boldsymbol{x}} \circ \mathcal{L}_-^{\boldsymbol{y}} K_s^{ws}(\boldsymbol{x},\boldsymbol{y}). \tag{2.310}$$

Using again (2.184), (2.185), (2.187), and (2.188), we can write

$$\begin{aligned}\mathcal{L}_+^{\boldsymbol{x}} \circ \mathcal{L}_-^{\boldsymbol{y}} K_s^{ws}(\boldsymbol{x},\boldsymbol{y}) = -\sum_{l=0}^{\infty} \sum_{\substack{m=-l \\ l+m \text{ even}}}^{l} \frac{1}{\beta_l^m} \Bigg[&(l-m)(l+m+1) \frac{y_l^{m+1}(\boldsymbol{x})}{w(\boldsymbol{x})} \frac{\overline{y_l^{m+1}(\boldsymbol{y})}}{w(\boldsymbol{y})} \\ &+(l+m)(l-m+1) \frac{\overline{y_l^{m-1}(\boldsymbol{x})}}{w(\boldsymbol{x})} \frac{y_l^{m-1}(\boldsymbol{y})}{w(\boldsymbol{y})} \Bigg].\end{aligned} \tag{2.311}$$

As with the first expression for the Laplace-Beltrame operator, noting that the pairs $(l,m) = (0,0)$, $(l,m) = (1,1)$, $(l,m) = (2,2)$, etc. make $l-m = 0$ allows us to rewrite the first term as:

$$\sum_{l=0}^{\infty} \sum_{\substack{m=-l \\ l+m \text{ even}}}^{l} \frac{(l-m)(l+m+1)}{\beta_l^m} \frac{y_l^{m+1}(\boldsymbol{x})}{w(\boldsymbol{x})} \frac{\overline{y_l^{m+1}(\boldsymbol{y})}}{w(\boldsymbol{y})} = \sum_{l=0}^{\infty} \sum_{\substack{m=-l \\ l+m \text{ odd}}}^{l} \frac{(l+m)(l-m+1)}{\beta_l^{m-1}} \frac{\overline{y_l^m(\boldsymbol{x})}}{w(\boldsymbol{x})} \frac{y_l^m(\boldsymbol{y})}{w(\boldsymbol{y})}. \tag{2.312}$$

Noting that the pairs $(l,m) = (0,0)$, $(l,m) = (1,-1)$, $(l,m) = (2,-2)$, etc. make $l+m = 0$ allows us to rewrite the second term as:

$$\sum_{l=0}^{\infty} \sum_{\substack{m=-l \\ l+m \text{ even}}}^{l} \frac{(l+m)(l-m+1)}{\beta_l^m} \frac{\overline{y_l^{m-1}(\boldsymbol{x})}}{w(\boldsymbol{x})} \frac{y_l^{m-1}(\boldsymbol{y})}{w(\boldsymbol{y})} = \sum_{l=0}^{\infty} \sum_{\substack{m=-l \\ l+m \text{ odd}}}^{l} \frac{(l-m)(l+m+1)}{\beta_l^{m+1}} \frac{\overline{y_l^m(\boldsymbol{x})}}{w(\boldsymbol{x})} \frac{y_l^m(\boldsymbol{y})}{w(\boldsymbol{y})}. \tag{2.313}$$

We can now add the two expressions for the Laplace-Beltrami operator to obtain

$$\Delta_{\mathbb{D}} K_s^{ws}(\boldsymbol{x},\boldsymbol{y}) = \frac{1}{2}(\mathcal{L}_-^{\boldsymbol{x}} \circ \mathcal{L}_+^{\boldsymbol{y}} + \mathcal{L}_+^{\boldsymbol{x}} \circ \mathcal{L}_-^{\boldsymbol{y}}) K_s^{ws}(\boldsymbol{x},\boldsymbol{y}) \tag{2.314}$$

$$= -\sum_{l=0}^{\infty} \sum_{\substack{m=-l \\ l+m \text{ odd}}}^{l} \left[\frac{1}{2} \left(\frac{(l+m)(l-m+1)}{\beta_l^{m-1}} + \frac{(l-m)(l+m+1)}{\beta_l^{m+1}} \right) \frac{y_l^m(\boldsymbol{x})}{w(\boldsymbol{x})} \frac{\overline{y_l^m(\boldsymbol{y})}}{w(\boldsymbol{y})} \right.$$

$$\left. + \frac{1}{2} \left(\frac{(l-m)(l+m+1)}{\beta_l^{m+1}} + \frac{(l+m)(l-m+1)}{\beta_l^{m-1}} \right) \frac{\overline{y_l^m(\boldsymbol{x})}}{w(\boldsymbol{x})} \frac{y_l^m(\boldsymbol{y})}{w(\boldsymbol{y})} \right]. \tag{2.315}$$

Using the recursion expression for α_l^m from Proposition 2.7.12 we can finally write

$$\Delta_{\mathbb{D}} K_s^{ws}(\boldsymbol{x},\boldsymbol{y}) = -\sum_{l=0}^{\infty} \sum_{\substack{m=-l \\ l+m \text{ odd}}}^{l} \alpha_l^m \left(\frac{y_l^m(\boldsymbol{x})}{w(\boldsymbol{x})} \frac{\overline{y_l^m(\boldsymbol{y})}}{w(\boldsymbol{y})} + \frac{\overline{y_l^m(\boldsymbol{x})}}{w(\boldsymbol{x})} \frac{y_l^m(\boldsymbol{y})}{w(\boldsymbol{y})} \right) \tag{2.316}$$

$$= K_{as}^{hs}(\boldsymbol{x},\boldsymbol{y}). \tag{2.317}$$

■

Theorem 2.7.5 (K^{hs} is K_{as}^{hs})**.** *For $(\boldsymbol{x},\boldsymbol{y}) \in \mathbb{D} \times \mathbb{D}$, the hypersingular kernel K^{hs}, associated with $\mathcal{N}$, is equal to the proposed hypersingular anti-symmetric kernel K_{as}^{hs}.*

Proof This result follows from the relation $\Delta_{\mathbb{D}} K^{ws}(\boldsymbol{x},\boldsymbol{y}) = K^{hs}(\boldsymbol{x},\boldsymbol{y})$ from Proposition 2.5.3, the identity $K^{ws}(\boldsymbol{x},\boldsymbol{y}) = K_s^{ws}(\boldsymbol{x},\boldsymbol{y})$ from Theorem 2.7.3, and the relation $\Delta_{\mathbb{D}} K_s^{ws}(\boldsymbol{x},\boldsymbol{y}) = K_{as}^{hs}(\boldsymbol{x},\boldsymbol{y})$ from Proposition 2.7.14. ■

It's now easy to prove Theorem 2.7.1.

Proof of Theorem 2.7.1 From Proposition 2.7.10, we know that

$$\left(\mathcal{L}_{as}^{hs} y_l^m\right)(\boldsymbol{y}) = -\alpha_l^m \frac{y_l^m(\boldsymbol{y})}{w(\boldsymbol{y})}, \quad \text{for } \boldsymbol{y} \in \mathbb{D}. \tag{2.318}$$

Integral operators $\mathcal{N}$ and $\mathcal{L}_{as}^{hs}$ have the same kernel for $\boldsymbol{x},\boldsymbol{y} \in \mathbb{D}$, from which we conclude the desired result:

$$\int_{\mathbb{D}} \frac{y^m(\boldsymbol{x}) d\mathbb{D}(\boldsymbol{x})}{4\pi \left\|\boldsymbol{x}-\boldsymbol{y}\right\|^3} = -\alpha_l^m \frac{y_l^m(\boldsymbol{y})}{w(\boldsymbol{y})}, \tag{2.319}$$

for $l+m$ odd and $\boldsymbol{y} \in \mathbb{D}$. ■

We will now use these new expressions of the boundary integral operators linked to the symmetric Dirichlet and anti-symmetric Neumann Laplace problems for the disk, and their inverses, to build variational formulations and Galerkin matrices usable in preconditioning methods. We will first summarize the previous results in a succinct and clear manner in the following table.

Remark 2.7.9. *The following table summarizes the situation so far:*

Table 2.7: Summary of the operators over $\mathbb{D}$ in their different forms.

BIO	Closed form kernel	DtN/NtD	Series Kernel	Series BIO	Mapping
$\mathcal{S}$	K^{ws}	NtD_s	K_s^{ws}	$\mathcal{L}_s^{ws}$	$\widetilde{H}^{-1/2}(\mathbb{D}) \to H^{1/2}(\mathbb{D})$
$\mathcal{N}$	K^{hs}	DtN_{as}	K_{as}^{hs}	$\mathcal{L}_{as}^{hs}$	$\widetilde{H}^{1/2}(\mathbb{D}) \to H^{-1/2}(\mathbb{D})$
$\mathcal{S}^{-1}$		DtN_s	$-K_s^{hs}$	$-\mathcal{L}_s^{hs}$	$H^{1/2}(\mathbb{D}) \to \widetilde{H}^{-1/2}(\mathbb{D})$
$\mathcal{N}^{-1}$		NtD_{as}	$-K_{as}^{ws}$	$-\mathcal{L}_{as}^{ws}$	$H^{-1/2}(\mathbb{D}) \to \widetilde{H}^{1/2}(\mathbb{D})$

2.7.6 Variational formulations and norms

We will now use the new defined integral operators to endow the Sobolev spaces with explicit inner products and norms.

Definition 2.7.13 (Induced bilinear forms)**.** *Let us define the following bilinear forms induced by the described boundary integral operators:*

$$a_s^{ws} \in L\left(\widetilde{H}^{-1/2}(\mathbb{D}) \times \widetilde{H}^{-1/2}(\mathbb{D}), \mathbb{C}\right) : a_s^{ws}(\lambda, \lambda^t) = \left\langle \mathcal{L}_s^{ws}\lambda, \lambda^t \right\rangle_{\mathbb{D}}, \tag{2.320}$$

$$b_s^{hs} \in L\left(H^{1/2}(\mathbb{D}) \times H^{1/2}(\mathbb{D}), \mathbb{C}\right) : b_s^{hs}(g, g^t) = \left\langle -\mathcal{L}_s^{hs} g, g^t \right\rangle_{\mathbb{D}}, \tag{2.321}$$

$$a_{as}^{hs} \in L\left(\widetilde{H}^{1/2}(\mathbb{D}) \times \widetilde{H}^{1/2}(\mathbb{D}), \mathbb{C}\right) : a_{as}^{hs}(\mu, \mu^t) = \left\langle -\mathcal{L}_{as}^{hs}\mu, \mu^t \right\rangle_{\mathbb{D}}, \tag{2.322}$$

$$b_{as}^{ws} \in L\left(H^{-1/2}(\mathbb{D}) \times H^{-1/2}(\mathbb{D}), \mathbb{C}\right) : b_{as}^{ws}(\varphi, \varphi^t) = \left\langle \mathcal{L}_{as}^{ws}\varphi, \varphi^t \right\rangle_{\mathbb{D}}. \tag{2.323}$$

Proposition 2.7.15 (Bilinear forms define inner products)**.** *The bilinear forms from Definition 2.7.13 define inner products in the following linear spaces: a_s^{ws} in $\widetilde{H}^{-1/2}(\mathbb{D})$, b_s^{hs} in $H^{1/2}(\mathbb{D})$, a_{as}^{hs} in $\widetilde{H}^{1/2}(\mathbb{D})$ and b_{as}^{ws} in $H^{-1/2}(\mathbb{D})$.*

Proof Let us focus on the first bilinear form, a_s^{ws} for the linear space $\mathcal{Y}_s^{1/w}$. Let us take two arbitrary functions $u, v \in \mathcal{Y}_s^{1/w}$ and show that conjugate symmetry, linearity, and positive-definitiveness are satisfied.

$$\langle \mathcal{L}_s^{ws} u\,,\, v\rangle_{\mathbb{D}} = \left\langle \mathcal{L}_s^{ws} \sum_{l=0}^{\infty} \sum_{\substack{m=-l \\ l+m \text{ even}}}^{l} u_l^m \frac{y_l^m}{w}\,,\, \sum_{l=0}^{\infty} \sum_{\substack{m=-l \\ l+m \text{ even}}}^{l} v_l^m \frac{y_l^m}{w} \right\rangle_{\mathbb{D}} \tag{2.324}$$

$$= \left\langle \sum_{l=0}^{\infty} \sum_{\substack{m=-l \\ l+m \text{ even}}}^{l} \frac{u_l^m}{\beta_l^m} y_l^m\,,\, \sum_{l=0}^{\infty} \sum_{\substack{m=-l \\ l+m \text{ even}}}^{l} v_l^m \frac{y_l^m}{w} \right\rangle_{\mathbb{D}} \tag{2.325}$$

$$= \sum_{l=0}^{\infty} \sum_{\substack{m=-l \\ l+m \text{ even}}}^{l} \frac{u_l^m \overline{v_l^m}}{2\beta_l^m} \tag{2.326}$$

$$= \overline{\sum_{l=0}^{\infty} \sum_{\substack{m=-l \\ l+m \text{ even}}}^{l} \frac{v_l^m \overline{u_l^m}}{2\beta_l^m}} \tag{2.327}$$

$$= \overline{\left\langle \mathcal{L}_s^{ws} \sum_{l=0}^{\infty} \sum_{\substack{m=-l \\ l+m \text{ even}}}^{l} v_l^m \frac{y_l^m}{w}\,,\, \sum_{l=0}^{\infty} \sum_{\substack{m=-l \\ l+m \text{ even}}}^{l} u_l^m \frac{y_l^m}{w} \right\rangle_{\mathbb{D}}} \tag{2.328}$$

$$= \overline{\langle \mathcal{L}_s^{ws} v\,,\, u\rangle_{\mathbb{D}}}. \tag{2.329}$$

Linearity on the first argument comes straightforwardly from the definition of the duality product. And finally,

$$\langle \mathcal{L}_s^{ws} u\,,\, u\rangle_{\mathbb{D}} = \sum_{l=0}^{\infty} \sum_{\substack{m=-l \\ l+m \text{ even}}}^{l} \frac{|u_l^m|^2}{2\beta_l^m} \tag{2.330}$$

shows that $a_s^{ws}(u, u)$ is always positive and that, only $u_l^m = 0$ for every l and m, and thus only for $u = 0$, makes $a_s^{ws}(u, u) = 0$, which shows the positive-definiteness property. The value (2.330) is finite by virtue of the bi-continuity of the bilinear form for its associated Neumann-to-Dirichlet operator, NtD_s from Section 2.6. Coercivity of the bilinear form induced by the corresponding operator NtD_s also guarantees that norm $\|\cdot\|_{a_s^{ws}}$ is equivalent to norm $\|\cdot\|_{\widetilde{H}^{-1/2}(\mathbb{D})}$. The same argument follows for the other three cases. ∎

Definition 2.7.14 (Norms for the trace spaces)**.** *Being inner products, the previous bilinear forms allow us to define the following norms in the Sobolev spaces:*

$$\|\lambda\|_{a_s^{ws}} = \sqrt{a_s^{ws}(\lambda,\lambda)}, \tag{2.331}$$

$$\|\mu\|_{a_{as}^{hs}} = \sqrt{a_{as}^{hs}(\mu,\mu)}, \tag{2.332}$$

$$\|g\|_{b_s^{hs}} = \sqrt{b_s^{hs}(g,g)}, \tag{2.333}$$

$$\|\varphi\|_{b_{as}^{ws}} = \sqrt{b_{as}^{ws}(\varphi,\varphi)}. \tag{2.334}$$

Proposition 2.7.16 (Computation of the norms associated with the new boundary integral operators)**.** *The norms from Definition 2.7.14 can be computed as follows:*

$$\|\lambda\|^2_{a_s^{ws}} = \sum_{l=0}^{\infty} \sum_{\substack{m=-l \\ l+m \ even}}^{l} \frac{1}{2\beta_l^m} \lambda_l^m \overline{\lambda_l^m}, \tag{2.335}$$

$$\|\mu\|^2_{a_{as}^{hs}} = \sum_{l=0}^{\infty} \sum_{\substack{m=-l \\ l+m \ odd}}^{l} \frac{\alpha_l^m}{2} \mu_l^m \overline{\mu_l^m}, \tag{2.336}$$

$$\|g\|^2_{b_s^{hs}} = \sum_{l=0}^{\infty} \sum_{\substack{m=-l \\ l+m \ even}}^{l} \frac{\beta_l^m}{2} g_l^m \overline{g_l^m}, \tag{2.337}$$

$$\|\varphi\|^2_{b_{as}^{ws}} = \sum_{l=0}^{\infty} \sum_{\substack{m=-l \\ l+m \ odd}}^{l} \frac{1}{2\alpha_l^m} \varphi_l^m \overline{\varphi_l^m}, \tag{2.338}$$

where

$$\lambda_l^m = (\lambda, y_l^m/w)_w, \tag{2.339}$$

$$\mu_l^m = (\mu, y_l^m)_{1/w}, \tag{2.340}$$

$$g_l^m = (g, y_l^m)_{1/w}, \tag{2.341}$$

$$\varphi_l^m = (\varphi, y_l^m/w)_w. \tag{2.342}$$

Proof These results follow straightforwardly from applying Corollary 2.7.4 together with the decomposition in bases described in Section 2.7.4. ∎

Proposition 2.7.17 (Variational formulations for the new integral operators)**.** *The previous bilinear forms are coercive in the appropriate spaces, and thus furnish appropriate variational formulations for the boundary integral equations. A variational formulation for the boundary integral equation associated with the boundary integral operator $\mathcal{L}_s^{ws}$ (identified with $\mathcal{S}$) is*

$$(\mathcal{L}_s^{ws}\text{–}VF) \begin{cases} \text{Given } g \in H^{1/2}(\mathbb{D}), \text{ find } \lambda \in \widetilde{H}^{-1/2}(\mathbb{D}), \text{ such that} \\ \\ \forall \lambda^t \in \widetilde{H}^{-1/2}(\mathbb{D}) \left(a_s^{ws}(\lambda, \lambda^t) = \left\langle g, \lambda^t \right\rangle_{\mathbb{D}} \right). \end{cases} \tag{2.343}$$

The boundary integral equation associated with the boundary integral operator $\mathcal{L}_s^{hs}$ (identified with $\mathcal{S}^{-1}$) admits the variational formulation

$$\left(\mathcal{L}_s^{hs}\text{–}VF\right) \begin{cases} \text{Given } \lambda \in \widetilde{H}^{-1/2}(\mathbb{D}), \text{ find } \lambda \in H^{1/2}(\mathbb{D}), \text{ such that} \\ \\ \forall g^t \in H^{1/2}(\mathbb{D}) \left(b_s^{hs}(g, g^t) = \left\langle \lambda, g^t \right\rangle_{\mathbb{D}} \right). \end{cases} \tag{2.344}$$

The boundary integral equation associated with the boundary integral operator $\mathcal{L}_{as}^{hs}$ (identified with $\mathcal{N}$) admits the variational formulation

$$\left(\mathcal{L}_{as}^{hs}\text{–}VF\right)\begin{cases} \text{Given } \varphi \in H^{-1/2}(\mathbb{D}), \text{ find } \mu \in \widetilde{H}^{1/2}(\mathbb{D}), \text{ such that} \\ \\ \forall \mu^t \in \widetilde{H}^{1/2}(\mathbb{D}) \left(a_{as}^{hs}(\mu, \mu^t) = \left\langle \varphi, \mu^t \right\rangle_{\mathbb{D}}\right). \end{cases} \tag{2.345}$$

The boundary integral equation associated with the boundary integral operator $\mathcal{L}_{as}^{ws}$ (identified with $\mathcal{N}^{-1}$) admits the variational formulation

$$(\mathcal{L}_{as}^{ws}\text{–}VF)\begin{cases} \text{Given } \mu \in \widetilde{H}^{1/2}(\mathbb{D}), \text{ find } \varphi \in H^{-1/2}(\mathbb{D}), \text{ such that} \\ \\ \forall \varphi^t \in H^{-1/2}(\mathbb{D}) \left(b_{as}^{ws}(\varphi, \varphi^t) = \left\langle \mu, \varphi^t \right\rangle_{\mathbb{D}}\right). \end{cases} \tag{2.346}$$

Proof Coercivity follows from the definitions of the norms for each space in Definition 2.7.14. Bi-continuity of the variational bilinear forms follows from the discrete Hölder's inequality. Let us consider the first case; the proof for the rest follows the same procedure.

$$a_s^{ws}(\lambda, \lambda^t) = \sum_{l=0}^{\infty} \sum_{\substack{m=-l \\ l+m \text{ even}}}^{l} \frac{\lambda_l^m \overline{(\lambda^t)_l^m}}{2\beta_l^m} \tag{2.347}$$

$$\leq \sum_{l=0}^{\infty} \sum_{\substack{m=-l \\ l+m \text{ even}}}^{l} \frac{|\lambda_l^m|}{\sqrt{2\beta_l^m}} \frac{\left|(\lambda^t)_l^m\right|}{\sqrt{2\beta_l^m}}. \tag{2.348}$$

Using the discrete Hölder's inequality we have

$$a_s^{ws}(\lambda, \lambda^t) \leq \sqrt{\sum_{l=0}^{\infty} \sum_{\substack{m=-l \\ l+m \text{ even}}}^{l} \frac{\left|\lambda_l^m\right|^2}{2\beta_l^m}} \sqrt{\sum_{l=0}^{\infty} \sum_{\substack{m=-l \\ l+m \text{ even}}}^{l} \frac{\left|(\lambda^t)_l^m\right|^2}{2\beta_l^m}} \tag{2.349}$$

$$\leq \|\lambda\|_{\widetilde{H}^{-1/2}(\mathbb{D})} \left\|\lambda^t\right\|_{\widetilde{H}^{-1/2}(\mathbb{D})}. \tag{2.350}$$

■

2.7.7 Spectral method and preconditioning of the Laplace problem for the disk screen

In this section we will use the developed theory to derive finite-dimensional variational formulations using the disk basis functions in order to solve the boundary integral equations linked with the four new integral operators. We will generate the Galerkin matrices associated with the finite-dimensional variational formulation and we will build the matrix preconditioners outlined by the optimal preconditioning strategy. In doing so, the preconditioning process will be clearly illustrated.

In order to consider N-dimensional finite subspaces of the involved Sobolev spaces, we will specify a way of counting the basis functions for each space, initially indexed by l and m.

Definition 2.7.15 (Counting the basis functions on the disk)**.** *For $l_{as}+m_{as}$ odd, we will count the basis functions sequentially with the index i_{as} as*

$$i_{as}(m_{as}, l_{as}) = \frac{1}{2}\left(l_{as}^2 + m_{as} + 1\right), \tag{2.351}$$

which in turn inversely gives

$$l_{as}(i_{as}) = 1 + \underset{\substack{l_{as} \geq 0 \\ l_{as}(l_{as}+1)/2 < i_{as}}}{\arg\max} \frac{l_{as}(l_{as}+1)}{2}, \quad \textit{and} \quad m_{as}(i_{as}) = 2i_{as} - l_{as}(i_{as})^2 - 1. \tag{2.352}$$

For $l_s + m_s$ even, we will count the basis functions sequentially with the index i_s as

$$i_s(m_s, l_s) = \frac{1}{2}\left(l_s^2 + 2l_s + m_s + 2\right), \tag{2.353}$$

which in turn inversely gives

$$l_s(i_s) = 1 + \underset{\substack{l_s \geq -1 \\ (l_s+1)(l_s+2)/2 < i_s}}{\arg\max} \frac{(l_s+1)(l_s+2)}{2}, \quad \textit{and} \quad m_s(i_s) = 2i_s - l_s(i_s)^2 - 2l_s(i_s) - 2. \tag{2.354}$$

Definition 2.7.16 (Finite subspaces of Sobolev trace spaces)**.** *Let us define the following N-dimensional subspaces to be used in the finite-dimensional variational formulations of the infinite-dimensional ones described above:*

$$V_N = span\left(\left\{y_{l_s(is)}^{m_s(i_s)}\right\}_{is=1}^{N}\right) \subset H^{1/2}(\mathbb{D}), \tag{2.355}$$

$$\tilde{V}_N = span\left(\left\{y_{l_{as}(i_{as})}^{m_{as}(i_{as})}\right\}_{i_{as}=1}^{N}\right) \subset \widetilde{H}^{1/2}(\mathbb{D}), \tag{2.356}$$

$$W_N = span\left(\left\{y_{l_{as}(i_{as})}^{m_{as}(i_{as})}/w\right\}_{i_{as}=1}^{N}\right) \subset H^{-1/2}(\mathbb{D}), \tag{2.357}$$

$$\tilde{W}_N = span\left(\left\{y_{l_s(i_s)}^{m_s(i_s)}/w\right\}_{i_s=1}^{N}\right) \subset \widetilde{H}^{-1/2}(\mathbb{D}). \tag{2.358}$$

Definition 2.7.17 (N-dimensional variational formulations)**.** *An N-dimensional discrete variational formulation for the boundary integral equation associated with the boundary integral operator $\mathcal{L}_s^{ws}$ (identified with $\mathcal{S}$) is*

$$(\mathcal{L}_s^{ws}\text{–}VF_N)\begin{cases} \textit{Given } g_N = \sum_{k=1}^{N} g_{l_s(k)}^{m_s(k)} y_{l_s(k)}^{m_s(k)} \in V_N, \textit{ find } \lambda_N = \sum_{i=1}^{N} \lambda_{l_s(i)}^{m_s(i)} \frac{y_{l_s(i)}^{m_s(i)}}{w} \in \widetilde{W}_N, \textit{ such that} \\ \sum_{i=1}^{N} \lambda_{l_s(i)}^{m_s(i)} a_s^{ws}\left(\frac{y_{l_s(i)}^{m_s(i)}}{w}, \frac{y_{l_s(j)}^{m_s(j)}}{w}\right) = \sum_{k=1}^{N} g_{l_s(k)}^{m_s(k)} \left\langle y_{l_s(k)}^{m_s(k)}, \frac{y_{l_s(j)}^{m_s(j)}}{w}\right\rangle_{\mathbb{D}}, \textit{ for } j = 1...N. \end{cases} \tag{2.359}$$

The boundary integral equation associated with the boundary integral operator $\mathcal{L}_s^{hs}$ (identified with $\mathcal{S}^{-1}$) admits the N-dimensional discrete variational formulation

$$\left(\mathcal{L}_s^{hs}\text{–}VF_N\right)\begin{cases} \textit{Given } \lambda_N = \sum_{k=1}^{N} \lambda_{l_s(k)}^{m_s(k)} \frac{y_{l_s(k)}^{m_s(k)}}{w} \in \widetilde{W}_N, \textit{ find } g_N = \sum_{i=1}^{N} g_{l_s(i)}^{m_s(i)} y_{l_s(i)}^{m_s(i)} \in V_N, \textit{ such that} \\ \sum_{i=1}^{N} g_{l_s(i)}^{m_s(i)} b_s^{hs}\left(y_{l_s(i)}^{m_s(i)}, y_{l_s(j)}^{m_s(j)}\right) = \sum_{k=1}^{N} \lambda_{l_s(k)}^{m_s(k)} \left\langle \frac{y_{l_s(k)}^{m_s(k)}}{w}, y_{l_s(j)}^{m_s(j)}\right\rangle_{\mathbb{D}}, \textit{ for } j = 1...N. \end{cases} \tag{2.360}$$

The boundary integral equation associated with the boundary integral operator $\mathcal{L}_{as}^{hs}$ (identified with $\mathcal{N}$) admits the N-dimensional discrete variational formulation

$$\left(\mathcal{L}_{as}^{hs}\text{–}VF_N\right)\begin{cases} \textit{Given } \varphi_N = \sum_{k=1}^{N} \varphi_{l_{as}(k)}^{m_{as}(k)} \frac{y_{l_{as}(k)}^{m_{as}(k)}}{w} \in W_N, \textit{ find } \mu_N = \sum_{i=1}^{N} \mu_{l_{as}(i)}^{m_{as}(i)} y_{l_{as}(i)}^{m_{as}(i)} \in \widetilde{V}_N, \textit{ such that} \\ \sum_{i=1}^{N} \mu_{l_{as}(i)}^{m_{as}(i)} a_{as}^{hs}\left(y_{l_{as}(i)}^{m_{as}(i)}, y_{l_{as}(j)}^{m_{as}(j)}\right) = \sum_{k=1}^{N} \varphi_{l_{as}(k)}^{m_{as}(k)} \left\langle \frac{y_{l_{as}(k)}^{m_{as}(k)}}{w}, y_{l_{as}(j)}^{m_{as}(j)}\right\rangle_{\mathbb{D}}, \textit{ for } j = 1...N. \end{cases} \tag{2.361}$$

The boundary integral equation associated with the boundary integral operator $\mathcal{L}_{as}^{ws}$ (identified with $\mathcal{N}^{-1}$) admits the N-dimensional discrete variational formulation

$$(\mathcal{L}_{as}^{ws}\text{–}VF_N)\begin{cases} \text{Given } \mu_N = \sum\limits_{k=1}^{N} \mu_{l_{as}(k)}^{m_{as}(k)} y_{l_{as}(k)}^{m_{as}(k)} \in \widetilde{V}_N, \text{ find } \varphi_N = \sum\limits_{i=1}^{N} \varphi_{l_{as}(i)}^{m_{as}(i)} \frac{y_{l_{as}(i)}^{m_{as}(i)}}{w} \in W_N, \text{ such that} \\ \sum\limits_{i=1}^{N} \varphi_{l_{as}(i)}^{m_{as}(i)} b_{as}^{ws}\left(\frac{y_{l_{as}(i)}^{m_{as}(i)}}{w}, \frac{y_{l_{as}(j)}^{m_{as}(j)}}{w}\right) = \sum\limits_{k=1}^{N} \mu_{l_{as}(k)}^{m_{as}(k)} \left\langle y_{l_{as}(k)}^{m_{as}(k)}, \frac{y_{l_{as}(j)}^{m_{as}(j)}}{w} \right\rangle_{\mathbb{D}}, \text{ for } j = 1...N. \end{cases} \tag{2.362}$$

Proposition 2.7.18 (Computation of bilinear forms)**.** *The computation of the bilinear forms from Definition 2.7.17 is performed as follows:*

$$a_s^{ws}\left(\frac{y_{l_s(i)}^{m_s(i)}}{w}, \frac{y_{l_s(j)}^{m_s(j)}}{w}\right) = \frac{1}{2\beta_{l_s(i)}^{m_s(i)}}\delta_j^i, \quad b_s^{hs}\left(y_{l_s(i)}^{m_s(i)}, y_{l_s(j)}^{m_s(j)}\right) = \frac{\beta_{l_s(i)}^{m_s(i)}}{2}\delta_j^i, \tag{2.363}$$

$$a_{as}^{hs}\left(y_{l_{as}(i)}^{m_{as}(i)}, y_{l_{as}(j)}^{m_{as}(j)}\right) = \frac{\alpha_{l_{as}(i)}^{m_{as}(i)}}{2}\delta_j^i, \quad b_{as}^{ws}\left(\frac{y_{l_{as}(i)}^{m_{as}(i)}}{w}, \frac{y_{l_{as}(j)}^{m_{as}(j)}}{w}\right) = \frac{1}{2\alpha_{l_{as}(i)}^{m_{as}(i)}}\delta_j^i. \tag{2.364}$$

Proof The values of the bilinear form follow directly from Corollary 2.7.4. ∎

Definition 2.7.18 (Galerkin matrices for the spectral discretization)**.** *The Galerkin matrices associated with the N-dimensional variational formulations from Definition 2.7.17 are defined as*

$$\boldsymbol{A}_s^{ws} = \frac{1}{2} diag\left(\frac{1}{\beta_{l_s(1)}^{m_s(1)}}, ..., \frac{1}{\beta_{l_s(N)}^{m_s(N)}}\right), \tag{2.365}$$

$$\boldsymbol{B}_s^{hs} = \frac{1}{2} diag\left(\beta_{l_s(1)}^{m_s(1)}, ..., \beta_{l_s(N)}^{m_s(N)}\right), \tag{2.366}$$

$$\boldsymbol{A}_{as}^{hs} = \frac{1}{2} diag\left(\alpha_{l_{as}(1)}^{m_{as}(1)}, ..., \alpha_{l_{as}(N)}^{m_{as}(N)}\right), \tag{2.367}$$

$$\boldsymbol{B}_{as}^{ws} = \frac{1}{2} diag\left(\frac{1}{\alpha_{l_{as}(1)}^{m_{as}(1)}}, ..., \frac{1}{\alpha_{l_{as}(N)}^{m_{as}(N)}}\right), \tag{2.368}$$

where diag defines a matrix by indicating the elements of its diagonal.

Proposition 2.7.19 (Computation of right-hand sides)**.** *The right-hand sides associated with the N-dimensional variational formulations from Definition 2.7.17 are computed as*

$$\left\langle y_{l_s(k)}^{m_s(k)}, \frac{y_{l_s(j)}^{m_s(j)}}{w} \right\rangle_{\mathbb{D}} = \frac{1}{2}\delta_j^k, \quad \left\langle \frac{y_{l_s(k)}^{m_s(k)}}{w}, y_{l_s(j)}^{m_s(j)} \right\rangle_{\mathbb{D}} = \frac{1}{2}\delta_j^k, \tag{2.369}$$

$$\left\langle \frac{y_{l_{as}(k)}^{m_{as}(k)}}{w}, y_{l_{as}(j)}^{m_{as}(j)} \right\rangle_{\mathbb{D}} = \frac{1}{2}\delta_j^k, \quad \left\langle y_{l_{as}(k)}^{m_{as}(k)}, \frac{y_{l_{as}(j)}^{m_{as}(j)}}{w} \right\rangle_{\mathbb{D}} = \frac{1}{2}\delta_j^k. \tag{2.370}$$

Proof Right-hand side values follow from the orthogonality properties for basis functions on the disk in Proposition 2.7.4. ∎

Proposition 2.7.20 (Spectral solution to the N-dimensional variational formulations)**.** *The coefficients of the solution to the discrete variational problem ($\mathcal{L}_s^{ws}$–VF_N) are*

$$\lambda_{l_s(i)}^{m_s(i)} = \beta_{l_s(i)}^{m_s(i)} g_{l_s(i)}^{m_s(i)}, \text{ for } i = 1, ..., N. \tag{2.371}$$

The coefficients of the solution to the discrete variational problem ($\mathcal{L}_s^{hs}-VF_N$) are

$$g_{l_s(i)}^{m_s(i)} = \frac{1}{\beta_{l_s(i)}^{m_s(i)}} \lambda_{l_s(i)}^{m_s(i)}, \ \textit{for } i = 1, ..., N. \tag{2.372}$$

The coefficients of the solution to the discrete variational problem ($\mathcal{L}_{as}^{hs}-VF_N$) are

$$\mu_{l_{as}(i)}^{m_{as}(i)} = \alpha_{l_{as}(i)}^{m_{as}(i)} \varphi_{l_{as}(i)}^{m_{as}(i)}, \ \textit{for } i = 1, ..., N. \tag{2.373}$$

The coefficients of the solution to the discrete variational problem ($\mathcal{L}_{as}^{ws}-VF_N$) are

$$\varphi_{l_{as}(i)}^{m_{as}(i)} = \frac{1}{\alpha_{l_{as}(i)}^{m_{as}(i)}} \mu_{l_{as}(i)}^{m_{as}(i)}, \ \textit{for } i = 1, ..., N. \tag{2.374}$$

Proof Let us consider the first N-dimensional variational formulation ($\mathcal{L}_s^{ws}-VF_N$). From Proposition 2.7.18 we know that the left-hand side is:

$$\sum_{i=1}^{N} \frac{\lambda_{l_s(i)}^{m_s(i)}}{2\beta_{l_s(i)}^{m_s(i)}} \delta_i^j, \qquad \text{for } j = 1...N. \tag{2.375}$$

We also know from Proposition 2.7.19 that the right-had side is

$$\sum_{k=1}^{N} \frac{1}{2} g_{l_s(k)}^{m_s(k)} \delta_k^j, \qquad \text{for } j = 1...N. \tag{2.376}$$

Then, we can compute each coefficient $\lambda_{l_s(j)}^{m_s(j)}$ determining solution λ_N as

$$\lambda_{l_s(j)}^{m_s(j)} = \beta_{l_s(j)}^{m_s(j)} g_{l_s(j)}^{m_s(j)}, \qquad \text{for } j = 1...N. \tag{2.377}$$

The same procedure, using Proposition 2.7.18 and Proposition 2.7.19 gives the desired results for the next three spectral formulations. ∎

The application of the preconditioning strategy into a preconditioning method for the Laplace problem using the described spectral discretization yields some interesting results. In the application of the optimal preconditioning theorem, Theorem 2.1.1, the Galerkin matrices and right-hand side vectors can be computed using the two previous propositions. Matrix $\boldsymbol{D}$, accounting for the duality pairing of the bases becomes $\frac{1}{2}\boldsymbol{I}$, with $\boldsymbol{I}$ being the identity matrix. Matrices $\boldsymbol{A}$ and $\boldsymbol{B}$ (for the symmetric Dirichlet and anti-symmetric Neumann cases) are diagonal, such that the application of the prescribed preconditions yields,

$$\boldsymbol{MA} = \boldsymbol{D}^{-1}\boldsymbol{B}\boldsymbol{D}^{-H}\boldsymbol{A} = \frac{1}{4}\boldsymbol{I}, \tag{2.378}$$

which has optimal condition number, i.e. $\text{cond}_2(\boldsymbol{MA}) = 1$, independently of the dimension N of the discretization. This shows the way in which optimal preconditioning works despite being a case where no preconditioning was required, since the linear systems arising from this discretization are diagonal and can be solved explicitly without recourse to linear solvers, as it was shown in Proposition 2.7.20.

In this present section we have found series forms for the operators $\mathcal{S}$ and $\mathcal{N}$ (identified with $\mathcal{L}_s^{ws}$ and $\mathcal{L}_{as}^{hs}$ respectively), and their inverses $\mathcal{S}^{-1}$ and $\mathcal{N}^{-1}$ (identified with $\mathcal{L}_s^{hs}$ and $\mathcal{L}_{as}^{ws}$ respectively). This allows us to build spectral discretizations to solve the associated problems, specially the ones of interest (symmetric Dirichlet and anti-symmetric Neumann), and to test the principles of operator preconditioning, although it is not practically needed when in a spectral method framework.

In the following section we will attempt to modify the integral kernels to obtain explicit and closed variational expressions that will be suited for boundary element method computations, attempting to escape the limitations of spectral methods and reach practical applications to screens other than the disk.

Chapter 3

Preconditioning for Screen Obstacles with Modified Integral Operators

The expressions found in the previous chapter for the inverses of the boundary integral operators involved in the solution of the symmetric Dirichlet and anti-symmetric Neumann are in the form of series. This makes their use inadequate for boundary element method computations and for the construction of associated Galerkin matrices capable of improving the preconditioning using the strategy outlined by Theorem 2.1.1 in a wider range of applications. In this chapter, roughly divisible in three parts, we will develop a strategy to overcome this problem.

In the first part, Section 3.1, using the previous two-dimensional case from Section 2.4 and the existing series representation for the disk from the previous chapter as hints, we will propose a modification to the series expressions for the inverse boundary integral operators. These modified operators, although not being the exact inverses, will be proven to have an explicit and closed variational expression, and thus be suited for use in boundary element method preconditioning methods while still preserving the behavior of the kernels' singularities from previously developed inverses.

In the second part, Section 3.2, we will define a special mesh partition suitable for the case of the screens and in particular for the disk. We will use this discretization to define boundary element spaces with which to formulate variational problems for the modified integral operators, and then we will use them to develop numerical methods to compute their respective Galerkin matrices. Using known solutions to the modified boundary integral operators, these methods will be tested numerically.

In the third part, Section 3.3, we will use the Galerkin matrices to build preconditioners that will be studied in numerical experiments. We will show that the preconditioners built with them are mutually optimal preconditioners, from which we will draw several conclusions about the variational problems associated with the modified integral operators, and about the mesh partition process. We will later show the preconditioning capabilities of these matrices when used as preconditioners to the matrices associated with operators $\mathcal{S}$ and $\mathcal{N}$. We will also show the preconditioning capabilities when applied to the matrices linked to the Helmholtz problem, i.e. $\mathcal{S}^k$ and $\mathcal{N}^k$. Finally, we will propose a technique to extend the exposed method to other screens.

3.1 Modified boundary integral operators with explicit closed variational form

In this section we will modify the kernel expressions in order to find closed forms of the integral operators suited for boundary element method computation. They will be suggested by the series expansion of the integral kernels of the weakly singular and hypersingular boundary integral equations when the domain of integration is the sphere in $\mathbb{R}^3$. In the case of the sphere, there are well-established results that allow us to change integral kernels from a series expression to a closed form expression. Theorem 1.5.3 will also allow us write the hypersingular integral operator using the weakly singular kernel. These two tools, as we shall see, will suggest the mentioned modifications.

3.1.1 Integral kernels for the weakly singular and hypersingular boundary integral operators on the sphere

Proposition 3.1.1 (Series for the weakly singular and hypersingular boundary integral operators on the sphere [51, Section 3.2.3])**.** *The application of the weakly singular operator $\mathcal{S}$ and hypersingular operator $\mathcal{N}$ on functions defined on $\mathbb{S}$ have the alternative series expressions:*

$$(\mathcal{S}\lambda)(\boldsymbol{y}) = \sum_{l=0}^{\infty}\sum_{m=-l}^{l}\frac{1}{2l+1}\lambda_l^m Y_l^m(\boldsymbol{y}), \tag{3.1}$$

$$(\mathcal{N}\mu)(\boldsymbol{y}) = -\sum_{l=0}^{\infty}\sum_{m=-l}^{l}\frac{l(l+1)}{2l+1}\mu_l^m Y_l^m(\boldsymbol{y}), \tag{3.2}$$

where

$$\lambda_l^m = \int_{\mathbb{S}}\lambda(\boldsymbol{x})\overline{Y_l^m(\boldsymbol{x})}d\mathbb{S}(\boldsymbol{x}) \quad \text{and} \quad \mu_l^m = \int_{\mathbb{S}}\mu(\boldsymbol{x})\overline{Y_l^m(\boldsymbol{x})}d\mathbb{S}(\boldsymbol{x}). \tag{3.3}$$

Proposition 3.1.2 (Series expression for the weakly singular kernel)**.** *The weakly singular kernel has the following series expression:*

$$K^{ws}(\boldsymbol{x},\boldsymbol{y}) = \sum_{l=0}^{\infty}\sum_{m=-l}^{l}\frac{1}{2l+1}Y_l^m(\boldsymbol{y})\overline{Y_l^m(\boldsymbol{x})}. \tag{3.4}$$

Proof

$$\begin{aligned}(\mathcal{S}\lambda)(\boldsymbol{y}) &= \sum_{l=0}^{\infty}\sum_{m=-l}^{l}\left(\frac{1}{2l+1}\right)\lambda_l^m Y_l^m(\boldsymbol{y})\\ &= \sum_{l=0}^{\infty}\sum_{m=-l}^{l}\left(\frac{1}{2l+1}\right)\int_{\mathbb{S}}\lambda(\boldsymbol{x})\overline{Y_l^m(\boldsymbol{x})}d\mathbb{S}(\boldsymbol{x})Y_l^m(\boldsymbol{y})\\ &= \int_{\mathbb{S}}\sum_{l=0}^{\infty}\sum_{m=-l}^{l}\left(\frac{1}{2l+1}\right)\overline{Y_l^m(\boldsymbol{x})}Y_l^m(\boldsymbol{y})\lambda(\boldsymbol{x})d\mathbb{S}(\boldsymbol{x}).\end{aligned} \tag{3.5}$$

$$\Rightarrow K^{ws}(\boldsymbol{x},\boldsymbol{y}) = \sum_{l=0}^{\infty}\sum_{m=-l}^{l}\frac{1}{2l+1}\overline{Y_l^m(\boldsymbol{x})}Y_l^m(\boldsymbol{y}) \tag{3.6}$$

$$\frac{1}{4\pi\|\boldsymbol{x}-\boldsymbol{y}\|} = \sum_{l=0}^{\infty}\sum_{m=-l}^{l}\frac{1}{2l+1}\overline{Y_l^m(\boldsymbol{x})}Y_l^m(\boldsymbol{y}). \tag{3.7}$$

■

The previous expression of the weakly singular kernel allows us to extract some conclusions that will further simplify the expression of the modified kernels proposed.

Corollary 3.1.1 (Realness of the series weakly singular kernel on the sphere)**.** *The series expression of the weakly singular integral kernel is real, i.e.*

$$\operatorname{Im}\left\{\sum_{l=0}^{\infty}\sum_{m=-l}^{l}\frac{1}{2l+1}\overline{Y_l^m(\boldsymbol{x})}Y_l^m(\boldsymbol{y})\right\}=0 \tag{3.8}$$

and thus can be written in either of the following two forms:

$$\sum_{l=0}^{\infty}\sum_{m=-l}^{l}\frac{1}{2l+1}\overline{Y_l^m(\boldsymbol{x})}Y_l^m(\boldsymbol{y})=\sum_{l=0}^{\infty}\sum_{m=-l}^{l}\frac{1}{2l+1}\overline{Y_l^m(\boldsymbol{y})}Y_l^m(\boldsymbol{x}). \tag{3.9}$$

3.1.2 Modified integral kernels and operators

The boundary integral operators on the disk, defined and studied in Section 2.7, have the desired mapping properties that induce bilinear forms that allow for preconditioning strategies in the sense defined by Theorem 2.1.1. However, having a series expression, they are not suited for use in boundary element method computations. In this section we will propose modified boundary integral operators, based on the previous ones, that will preserve the same behavior in ρ of the integral kernels on the edge of the disk, which is the key feature of their performance. This idea will be tested numerically in following sections.

The known relation between closed and series form for the kernels, in the case of the sphere, suggests a modification on the previously defined kernels. Let us define the following modified integral kernels in the form of series.

Definition 3.1.1 (Modified integral kernels for the disk)**.** *Let us define the following two weakly singular integral kernels for $(\boldsymbol{x},\boldsymbol{y})\in\mathbb{D}\times\mathbb{D}$, with $\boldsymbol{x}\neq\boldsymbol{y}$, as the formal series:*

$$\widetilde{K}_s^{ws}(\boldsymbol{x},\boldsymbol{y})=\sum_{l=0}^{\infty}\sum_{\substack{m=-l\\ l+m\ even}}^{l}\zeta_l y_l^m(\boldsymbol{y})\overline{y_l^m(\boldsymbol{x})}, \tag{3.10}$$

$$\widetilde{K}_{as}^{ws}(\boldsymbol{x},\boldsymbol{y})=\sum_{l=0}^{\infty}\sum_{\substack{m=-l\\ l+m\ odd}}^{l}\zeta_l y_l^m(\boldsymbol{y})\overline{y_l^m(\boldsymbol{x})}, \tag{3.11}$$

with

$$\zeta_l=\frac{2}{2l+1}. \tag{3.12}$$

Similarly, let us define the following two hypersingular integral kernels for $(\boldsymbol{x},\boldsymbol{y})\in\mathbb{D}\times\mathbb{D}$, with $\boldsymbol{x}\neq\boldsymbol{y}$, as the formal series:

$$\widetilde{K}_s^{hs}(\boldsymbol{x},\boldsymbol{y})=-\sum_{l=0}^{\infty}\sum_{\substack{m=-l\\ l+m\ even}}^{l}\eta_l\frac{y_l^m(\boldsymbol{y})}{w(\boldsymbol{y})}\frac{\overline{y_l^m(\boldsymbol{x})}}{w(\boldsymbol{x})}, \tag{3.13}$$

$$\widetilde{K}_{as}^{hs}(\boldsymbol{x},\boldsymbol{y})=-\sum_{l=0}^{\infty}\sum_{\substack{m=-l\\ l+m\ odd}}^{l}\eta_l\frac{y_l^m(\boldsymbol{y})}{w(\boldsymbol{y})}\frac{\overline{y_l^m(\boldsymbol{x})}}{w(\boldsymbol{x})}, \tag{3.14}$$

with

$$\eta_l=\frac{2l(l+1)}{2l+1}. \tag{3.15}$$

We will use these modified integral kernels to define modified boundary integral operators for which we will later find explicit and closed forms in variational contexts.

Definition 3.1.2 (Modified boundary integral operators on the disk)**.** *For $\boldsymbol{y} \in \mathbb{D}$ we define the following boundary integral operators:*

$$\left(\widetilde{\mathcal{L}}_s^{ws}\lambda\right)(\boldsymbol{y}) = \int_{\mathbb{D}} \widetilde{K}_s^{ws}(\boldsymbol{x},\boldsymbol{y})\lambda(\boldsymbol{x})d\mathbb{D}(\boldsymbol{x}), \tag{3.16}$$

$$\left(\widetilde{\mathcal{L}}_{as}^{ws}\varphi\right)(\boldsymbol{y}) = \int_{\mathbb{D}} \widetilde{K}_{as}^{ws}(\boldsymbol{x},\boldsymbol{y})\varphi(\boldsymbol{x})d\mathbb{D}(\boldsymbol{x}), \tag{3.17}$$

$$\left(\widetilde{\mathcal{L}}_s^{hs}g\right)(\boldsymbol{y}) = \int_{\mathbb{D}} \widetilde{K}_s^{hs}(\boldsymbol{x},\boldsymbol{y})g(\boldsymbol{x})d\mathbb{D}(\boldsymbol{x}), \tag{3.18}$$

$$\left(\widetilde{\mathcal{L}}_{as}^{hs}\mu\right)(\boldsymbol{y}) = \int_{\mathbb{D}} \widetilde{K}_{as}^{hs}(\boldsymbol{x},\boldsymbol{y})\mu(\boldsymbol{x})d\mathbb{D}(\boldsymbol{x}). \tag{3.19}$$

Up until this point, the modified integral operators ($\widetilde{\mathcal{L}}_s^{ws}$, $\widetilde{\mathcal{L}}_{as}^{ws}$, $\widetilde{\mathcal{L}}_s^{hs}$, and $\widetilde{\mathcal{L}}_{as}^{hs}$), modification of the ones known to be identified with $\mathcal{S}$ and $\mathcal{N}$ and their inverses ($\mathcal{L}_s^{ws}$, $\mathcal{L}_{as}^{ws}$, $\mathcal{L}_s^{hs}$, and $\mathcal{L}_{as}^{hs}$), present the same problem in their incorporation into a boundary element method: they are in series form. The next theorems, central to this section, will show that they can also be expressed in closed form, thus solving this problem while still preserving the same radial behavior in ρ that was present in the exact inverses in the $\mathbb{R}^2$ and $\mathbb{R}^3$ cases.

Theorem 3.1.1 (Closed variational form for the weakly singular integral kernels)**.** *The weakly singular integral operators from Definition 3.1.2 have the following closed form variational expressions:*

$$\left\langle \widetilde{\mathcal{L}}_s^{ws}\lambda\,,\,\lambda^t\right\rangle_{\mathbb{D}} = \int_{\mathbb{D}}\int_{\mathbb{D}} \frac{1}{4\pi}\left(\frac{1}{\|\boldsymbol{x}^+-\boldsymbol{y}^+\|}+\frac{1}{\|\boldsymbol{x}^--\boldsymbol{y}^+\|}\right)\lambda(\boldsymbol{x})\lambda^t(\boldsymbol{y})d\mathbb{D}(\boldsymbol{x})d\mathbb{D}(\boldsymbol{y}), \tag{3.20}$$

$$\left\langle \widetilde{\mathcal{L}}_{as}^{ws}\varphi\,,\,\varphi^t\right\rangle_{\mathbb{D}} = \int_{\mathbb{D}}\int_{\mathbb{D}} \frac{1}{4\pi}\left(\frac{1}{\|\boldsymbol{x}^+-\boldsymbol{y}^+\|}-\frac{1}{\|\boldsymbol{x}^--\boldsymbol{y}^+\|}\right)\varphi(\boldsymbol{x})\varphi^t(\boldsymbol{y})d\mathbb{D}(\boldsymbol{x})d\mathbb{D}(\boldsymbol{y}). \tag{3.21}$$

Proof Let us first consider the case of $\widetilde{K}_s^{ws}$. Let us consider a projection $T : \mathbb{S} \to \mathbb{D}$ taking points on the upper half-sphere to their vertical projections on the disk ($\boldsymbol{y} = T\boldsymbol{y}^+ = T\boldsymbol{y}^- \in \mathbb{D}$), to be used in integration by substitution. The application of $\widetilde{\mathcal{L}}_s^{ws}$ to a function λ defined on the disk yields, for $\boldsymbol{y} \in \mathbb{D}$:

$$\left(\widetilde{\mathcal{L}}_s^{ws}\lambda\right)(\boldsymbol{y}) = \int_{\mathbb{D}} \widetilde{K}_s^{ws}(\boldsymbol{x},\boldsymbol{y})\lambda(\boldsymbol{x})d\mathbb{D}(\boldsymbol{x}) \tag{3.22}$$

$$= \int_{\mathbb{S}^+} \sum_{l=0}^{\infty} \sum_{\substack{m=-l \\ l+m \text{ even}}}^{l} \zeta_l \overline{y_l^m(T\boldsymbol{x})} y_l^m(T\boldsymbol{y}^+)\lambda(T\boldsymbol{x})|\cos\theta_{\boldsymbol{x}}|d\mathbb{S}^+(\boldsymbol{x}). \tag{3.23}$$

Let us define $\lambda^+ = \lambda \circ T$ over $\mathbb{S}^+$, so that the application of $\widetilde{\mathcal{L}}_s^{ws}$ can be pulled to the upper half-sphere:

$$\left(\widetilde{\mathcal{L}}_s^{ws}\lambda\right)(\boldsymbol{y}) = \int_{\mathbb{S}^+} \sum_{l=0}^{\infty} \sum_{\substack{m=-l \\ l+m \text{ even}}}^{l} \zeta_l \overline{Y_l^m(\boldsymbol{x})} Y_l^m(\boldsymbol{y}^+)\lambda^+(\boldsymbol{x})|\cos\theta_{\boldsymbol{x}}|d\mathbb{S}^+(\boldsymbol{x}). \tag{3.24}$$

Let us now define $\widetilde{\lambda^+}$ as the mirror reflection over $\mathbb{S}^-$, so that it is an even function of x_3, i.e., $\widetilde{\lambda^+}(\boldsymbol{x}^+) = \widetilde{\lambda^+}(\boldsymbol{x}^-)$. Being $\overline{Y_l^m}(\boldsymbol{x})$ (for $l+m$ even), $|\cos\theta_{\boldsymbol{x}}|$, and $\widetilde{\lambda^+}(\boldsymbol{x})$ even functions of x_3,

the integration can be computed on the whole sphere as

$$\left(\widetilde{\mathcal{L}}_s^{ws}\lambda\right)(\boldsymbol{y}) = \frac{1}{2}\int_{\mathbb{S}} \sum_{l=0}^{\infty} \sum_{\substack{m=-l \\ l+m \text{ even}}}^{l} \zeta_l \overline{Y_l^m(\boldsymbol{x})} Y_l^m(\boldsymbol{y}^+) \widetilde{\lambda^+}(\boldsymbol{x}) |\cos\theta_{\boldsymbol{x}}| d\mathbb{S}(\boldsymbol{x}). \tag{3.25}$$

Also, for the rest of the (l,m) pairs, when $l+m$ is odd, Y_l^m will be odd, so that the integrand will also be odd, and thus,

$$l+m \text{ odd } \Rightarrow \int_{\mathbb{S}} \overline{Y_l^m(\boldsymbol{x})} Y_l^m(\boldsymbol{y}^+) \widetilde{\lambda^+}(\boldsymbol{x}) |\cos\theta_{\boldsymbol{x}}| d\mathbb{S}(\boldsymbol{x}) = 0. \tag{3.26}$$

Now these terms can be added to 3.25, so that the sum has all the (l,m) pairs:

$$\left(\widetilde{\mathcal{L}}_s^{ws}\lambda\right)(\boldsymbol{y}) = \frac{1}{2}\int_{\mathbb{S}} \sum_{0=l}^{\infty} \sum_{m=-l}^{l} \zeta_l \overline{Y_l^m(\boldsymbol{x})} Y_l^m(\boldsymbol{y}^+) \widetilde{\lambda^+}(\boldsymbol{x}) |\cos\theta_{\boldsymbol{x}}| d\mathbb{S}(\boldsymbol{x}). \tag{3.27}$$

By construction $\zeta_l/2 = 1/(2l+1)$, for which (3.4) from Proposition 3.1.2 allows us rewrite (3.27):

$$\begin{aligned}
\left(\widetilde{\mathcal{L}}_s^{ws}\lambda\right)(\boldsymbol{y}) &= \int_{\mathbb{S}} K^{ws}(\boldsymbol{x},\boldsymbol{y}^+) \widetilde{\lambda^+}(\boldsymbol{x}) |\cos\theta_{\boldsymbol{x}}| d\mathbb{S}(\boldsymbol{x}) && (3.28)\\
&= \int_{\mathbb{S}^+} K^{ws}(\boldsymbol{x},\boldsymbol{y}^+) \widetilde{\lambda^+}(\boldsymbol{x}) |\cos\theta_{\boldsymbol{x}}| d\mathbb{S}^+(\boldsymbol{x}) + \int_{\mathbb{S}^-} K^{ws}(\boldsymbol{x},\boldsymbol{y}^+) \widetilde{\lambda^+}(\boldsymbol{x}) |\cos\theta_{\boldsymbol{x}}| d\mathbb{S}^-(\boldsymbol{x}) && (3.29)\\
&= \int_{\mathbb{D}} K^{ws}(\boldsymbol{x}^+,\boldsymbol{y}^+) \lambda(\boldsymbol{x}) d\mathbb{D}(\boldsymbol{x}) + \int_{\mathbb{D}} K^{ws}(\boldsymbol{x}^-,\boldsymbol{y}^+) \lambda(\boldsymbol{x}) d\mathbb{D}(\boldsymbol{x}) && (3.30)\\
&= \int_{\mathbb{D}} \frac{1}{4\pi} \left(\frac{1}{\|\boldsymbol{x}^+ - \boldsymbol{y}^+\|} + \frac{1}{\|\boldsymbol{x}^- - \boldsymbol{y}^+\|} \right) \lambda(\boldsymbol{x}) d\mathbb{D}(\boldsymbol{x}), && (3.31)
\end{aligned}$$

which proves the identity (3.20) of the theorem.

The demonstration for $\widetilde{K}_{as}^{ws}$ can be deduced from the application of $\widetilde{\mathcal{L}}_{as}^{ws}$ to a function φ defined over $\mathbb{D}$, using the same argument with some modifications. Starting with the series definitions for $\widetilde{\mathcal{L}}_{as}^{ws}\varphi$, a function $\varphi^+ = \varphi \circ T$ is defined to pull the integral to $\mathbb{S}^+$. Defining $\widetilde{\varphi^+}$ now as the odd mirror reflection, i.e. $\widetilde{\varphi^+}(\boldsymbol{x}^+) = -\widetilde{\varphi^+}(\boldsymbol{x}^-)$, the same two key properties are achieved: 1) the integrand becomes even and thus it can be transformed into an integral over $\mathbb{S}$, and 2) the complementary (l,m) pairs (the even ones) integrate as zero and can be added to complete the series. Once the expression of the integral kernel for the sphere is recognizable from Proposition 3.1.2, it can be replaced and the integral later pulled back to the disk. Being $\widetilde{\varphi^+}$ odd, the minus sign appears naturally differentiating this case from the previous one.

■

These closed form expressions of two of the integral kernels, without resorting to series expressions, allow for the computation of boundary element calculations and the construction of Galerkin matrices as it will be shown later in this chapter. In the next theorem we use the closed form expressions of the weakly singular integral kernels to deliver closed form variational expressions for the modified hypersingular operators $\widetilde{\mathcal{L}}_s^{hs}$ and $\widetilde{\mathcal{L}}_{as}^{hs}$.

Theorem 3.1.2 (Closed variational form for the hypersingular integral kernels)**.** *The bilinear forms induced by the hypersingular boundary integral operator $\widetilde{\mathcal{L}}_{as}^{hs}$ admits the following two expressions of integration by parts:*

$$\left\langle -\widetilde{\mathcal{L}}_{as}^{hs}\mu\,,\,\mu^t \right\rangle_{\mathbb{D}} = \left\langle \widetilde{\mathcal{L}}_s^{ws} \overrightarrow{curl}_{\mathbb{D}}\mu, \overrightarrow{curl}_{\mathbb{D}}\mu^t \right\rangle_{\mathbb{D}} + \left\langle \widetilde{\mathcal{L}}_{as}^{ws} \left(\frac{1}{w}\frac{\partial \mu}{\partial \phi_{\boldsymbol{x}}} \right), \frac{1}{w}\frac{\partial \mu^t}{\partial \phi_{\boldsymbol{y}}} \right\rangle_{\mathbb{D}} \tag{3.32}$$

and

$$\left\langle -\widetilde{\mathcal{L}}_{as}^{hs}\mu\,,\,\mu^t\right\rangle_{\mathbb{D}}=\left\langle \widetilde{\mathcal{L}}_{as}^{ws}\frac{\mathcal{L}_3\mu}{w},\frac{\mathcal{L}_3\mu^t}{w}\right\rangle_{\mathbb{D}}-\frac{1}{2}\left\langle \widetilde{\mathcal{L}}_{s}^{ws}\mathcal{L}_+\mu,\mathcal{L}_-\mu^t\right\rangle_{\mathbb{D}}-\frac{1}{2}\left\langle \widetilde{\mathcal{L}}_{s}^{ws}\mathcal{L}_-\mu,\mathcal{L}_+\mu^t\right\rangle_{\mathbb{D}}. \tag{3.33}$$

Similarly, the bilinear forms induced by the hypersingular boundary integral operator $\widetilde{\mathcal{L}}_s^{hs}$ admits the following two expressions of integration by parts:

$$\left\langle -\widetilde{\mathcal{L}}_{s}^{hs}g\,,\,g^t\right\rangle_{\mathbb{D}}=\left\langle \widetilde{\mathcal{L}}_{as}^{ws}\overrightarrow{curl}_{\mathbb{D}}g,\overrightarrow{curl}_{\mathbb{D}}g^t\right\rangle_{\mathbb{D}}+\left\langle \widetilde{\mathcal{L}}_{s}^{ws}\left(\frac{1}{w}\frac{\partial g}{\partial\phi_{\boldsymbol{x}}}\right),\frac{1}{w}\frac{\partial g^t}{\partial\phi_{\boldsymbol{y}}}\right\rangle_{\mathbb{D}} \tag{3.34}$$

and

$$\left\langle -\widetilde{\mathcal{L}}_{s}^{hs}g\,,\,g^t\right\rangle_{\mathbb{D}}=\left\langle \widetilde{\mathcal{L}}_{s}^{ws}\frac{\mathcal{L}_3 g}{w},\frac{\mathcal{L}_3 g^t}{w}\right\rangle_{\mathbb{D}}-\frac{1}{2}\left\langle \widetilde{\mathcal{L}}_{as}^{ws}\mathcal{L}_+ g,\mathcal{L}_- g^t\right\rangle_{\mathbb{D}}-\frac{1}{2}\left\langle \widetilde{\mathcal{L}}_{as}^{ws}\mathcal{L}_- g,\mathcal{L}_+ g^t\right\rangle_{\mathbb{D}}. \tag{3.35}$$

Proof Let us demonstrate the expressions for $\widetilde{\mathcal{L}}_{as}^{hs}$; the ones for $\widetilde{\mathcal{L}}_{s}^{hs}$ can be deduced similarly. The bilinear form induced by $\widetilde{\mathcal{L}}_{as}^{hs}$ is written as:

$$\left\langle -\widetilde{\mathcal{L}}_{as}^{hs}\mu\,,\,\mu^t\right\rangle_{\mathbb{D}}=-\int_{\mathbb{D}}\int_{\mathbb{D}}\widetilde{K}_{as}^{hs}(\boldsymbol{x},\boldsymbol{y})\mu(\boldsymbol{x})\overline{\mu^t}(\boldsymbol{y})d\mathbb{D}(\boldsymbol{x})d\mathbb{D}(\boldsymbol{y}) \tag{3.36}$$

$$=\int_{\mathbb{D}}\int_{\mathbb{D}}\sum_{l=0}^{\infty}\sum_{\substack{m=-l\\ l+m\text{ odd}}}^{l}\eta_l\frac{\overline{y_l^m(\boldsymbol{x})}}{w(\boldsymbol{x})}\frac{y_l^m(\boldsymbol{y})}{w(\boldsymbol{y})}\mu(\boldsymbol{x})\overline{\mu^t}(\boldsymbol{y})d\mathbb{D}(\boldsymbol{x})d\mathbb{D}(\boldsymbol{y}). \tag{3.37}$$

Let us define $T:\mathbb{S}\to\mathbb{D}$ as the vertical projection of points from the sphere onto the disk, and let us define the following odd functions for points $\boldsymbol{x},\boldsymbol{y}$ on $\mathbb{S}$:

$$\tilde{\mu}(\boldsymbol{x})=\begin{cases}\mu(T\boldsymbol{x}) & \text{if } \boldsymbol{x}\in\mathbb{S}^+,\\ -\mu(T\boldsymbol{x}) & \text{if } \boldsymbol{x}\in\mathbb{S}^-,\end{cases}\quad\text{and }\tilde{\mu}^t(\boldsymbol{y})=\begin{cases}\mu^t(T\boldsymbol{y}) & \text{if } \boldsymbol{y}\in\mathbb{S}^+,\\ -\mu^t(T\boldsymbol{y}) & \text{if } \boldsymbol{y}\in\mathbb{S}^-.\end{cases} \tag{3.38}$$

Defined like this, we identify $\overline{Y_l^m(\boldsymbol{x})}\tilde{\mu}(\boldsymbol{x})$ and $Y_l^m(\boldsymbol{y})\overline{\tilde{\mu}^t}(\boldsymbol{y})$ as even functions for $l+m$ odd, and as odd functions for $l+m$ even. Thus, we can rewrite the bilinear form as:

$$\left\langle -\widetilde{\mathcal{L}}_{as}^{hs}\mu\,,\,\mu^t\right\rangle_{\mathbb{D}}=\frac{1}{2}\int_{\mathbb{S}}\int_{\mathbb{S}}\sum_{l=0}^{\infty}\sum_{m=-l}^{l}\frac{\eta_l}{2}\overline{Y_l^m(\boldsymbol{x})}Y_l^m(\boldsymbol{y})\tilde{\mu}(\boldsymbol{x})\overline{\tilde{\mu}^t}(\boldsymbol{y})d\mathbb{S}(\boldsymbol{x})d\mathbb{S}(\boldsymbol{y}). \tag{3.39}$$

Using Proposition 3.1.1 we can further write the expression as

$$\left\langle -\widetilde{\mathcal{L}}_{as}^{hs}\mu\,,\,\mu^t\right\rangle_{\mathbb{D}}=\frac{1}{2}\int_{\mathbb{S}}\int_{\mathbb{S}}K^{hs}(\boldsymbol{x},\boldsymbol{y})\tilde{\mu}(\boldsymbol{x})\overline{\tilde{\mu}^t}(\boldsymbol{y})d\mathbb{S}(\boldsymbol{x})d\mathbb{S}(\boldsymbol{y}). \tag{3.40}$$

Using Theorem 1.5.3, we can rewrite the previous expression as

$$\left\langle -\widetilde{\mathcal{L}}_{as}^{hs}\mu\,,\,\mu^t\right\rangle_{\mathbb{D}}=\frac{1}{2}\int_{\mathbb{S}}\int_{\mathbb{S}}K^{ws}(\boldsymbol{x},\boldsymbol{y})\left(\overrightarrow{\text{curl}}_{\mathbb{S}}\tilde{\mu}(\boldsymbol{x}),\overrightarrow{\text{curl}}_{\mathbb{S}}\tilde{\mu}^t(\boldsymbol{y})\right)d\mathbb{S}(\boldsymbol{x})d\mathbb{S}(\boldsymbol{y}). \tag{3.41}$$

Using now Remark 2.5.1, we can rewrite again the previous expression as

$$\left\langle -\widetilde{\mathcal{L}}_{as}^{hs}\mu\,,\,\mu^t\right\rangle_{\mathbb{D}}=$$

$$\frac{1}{2}\int_{\mathbb{S}}\int_{\mathbb{S}} K^{ws}(\boldsymbol{x},\boldsymbol{y})\frac{\partial\tilde{\mu}(\boldsymbol{x})}{\partial\phi_{\boldsymbol{x}}}\frac{\partial\overline{\tilde{\mu}^t}(\boldsymbol{y})}{\partial\phi_{\boldsymbol{y}}}d\mathbb{S}(\boldsymbol{x})d\mathbb{S}(\boldsymbol{y})$$
$$+\frac{1}{2}\int_{\mathbb{S}}\int_{\mathbb{S}} K^{ws}(\boldsymbol{x},\boldsymbol{y})\left[\cos\left(\phi_{\boldsymbol{x}}-\phi_{\boldsymbol{y}}\right)\left(\frac{\partial\tilde{\mu}(\boldsymbol{x})}{\partial\theta_{\boldsymbol{x}}}\frac{\partial\overline{\tilde{\mu}^t}(\boldsymbol{y})}{\partial\theta_{\boldsymbol{y}}}+\frac{\cos\theta_{\boldsymbol{x}}\cos\theta_{\boldsymbol{y}}}{\sin\theta_{\boldsymbol{x}}\sin\theta_{\boldsymbol{y}}}\frac{\partial\tilde{\mu}(\boldsymbol{x})}{\partial\phi_{\boldsymbol{x}}}\frac{\partial\overline{\tilde{\mu}^t}(\boldsymbol{y})}{\partial\phi_{\boldsymbol{y}}}\right)\right.$$
$$\left.+\sin\left(\phi_{\boldsymbol{x}}-\phi_{\boldsymbol{y}}\right)\left(\frac{\cos\theta_{\boldsymbol{y}}}{\sin\theta_{\boldsymbol{y}}}\frac{\partial\tilde{\mu}(\boldsymbol{x})}{\partial\theta_{\boldsymbol{x}}}\frac{\partial\overline{\tilde{\mu}^t}(\boldsymbol{y})}{\partial\phi_{\boldsymbol{y}}}-\frac{\cos\theta_{\boldsymbol{x}}}{\sin\theta_{\boldsymbol{x}}}\frac{\partial\tilde{\mu}(\boldsymbol{x})}{\partial\phi_{\boldsymbol{x}}}\frac{\partial\overline{\tilde{\mu}^t}(\boldsymbol{y})}{\partial\theta_{\boldsymbol{y}}}\right)\right]|\cos\theta_{\boldsymbol{x}}|\,|\cos\theta_{\boldsymbol{y}}|d\mathbb{S}(\boldsymbol{x})d\mathbb{S}(\boldsymbol{y}) \tag{3.42}$$

Let us focus on the first integral. Using Proposition 3.1.2, we can write:

$$\frac{1}{2}\int_{\mathbb{S}}\int_{\mathbb{S}} K^{ws}(\boldsymbol{x},\boldsymbol{y})\frac{\partial\tilde{\mu}(\boldsymbol{x})}{\partial\phi_{\boldsymbol{x}}}\frac{\partial\overline{\tilde{\mu}^t}(\boldsymbol{y})}{\partial\phi_{\boldsymbol{y}}}d\mathbb{S}(\boldsymbol{x})d\mathbb{S}(\boldsymbol{y})=\frac{1}{2}\int_{\mathbb{S}}\int_{\mathbb{S}}\sum_{l=0}^{\infty}\sum_{m=-l}^{l}\frac{\zeta_l}{2}\overline{Y_l^m(\boldsymbol{x})}Y_l^m(\boldsymbol{y})\frac{\partial\tilde{\mu}(\boldsymbol{x})}{\partial\phi_{\boldsymbol{x}}}\frac{\partial\overline{\tilde{\mu}^t}(\boldsymbol{y})}{\partial\phi_{\boldsymbol{y}}}d\mathbb{S}(\boldsymbol{x})d\mathbb{S}(\boldsymbol{y}), \tag{3.43}$$

and since $\tilde{\mu}$ and $\overline{\tilde{\mu}^t}$ are odd (and even (l,m) pairs vanish) functions we can write:

$$=\frac{1}{2}\int_{\mathbb{S}}\int_{\mathbb{S}}\sum_{l=0}^{\infty}\sum_{\substack{m=-l\\ l+m\text{ odd}}}^{l}\frac{\zeta_l}{2}\overline{Y_l^m(\boldsymbol{x})}Y_l^m(\boldsymbol{y})\frac{\partial\tilde{\mu}(\boldsymbol{x})}{\partial\phi_{\boldsymbol{x}}}\frac{\partial\overline{\tilde{\mu}^t}(\boldsymbol{y})}{\partial\phi_{\boldsymbol{y}}}d\mathbb{S}(\boldsymbol{x})d\mathbb{S}(\boldsymbol{y}) \tag{3.44}$$

$$=\int_{\mathbb{S}^+}\int_{\mathbb{S}}\sum_{l=0}^{\infty}\sum_{\substack{m=-l\\ l+m\text{ odd}}}^{l}\frac{\zeta_l}{2}\overline{Y_l^m(\boldsymbol{x})}Y_l^m(\boldsymbol{y})\frac{\partial\tilde{\mu}(\boldsymbol{x})}{\partial\phi_{\boldsymbol{x}}}\frac{\partial\overline{\tilde{\mu}^t}(\boldsymbol{y})}{\partial\phi_{\boldsymbol{y}}}d\mathbb{S}(\boldsymbol{x})d\mathbb{S}^+(\boldsymbol{y}) \tag{3.45}$$

$$=\int_{\mathbb{S}^+}\int_{\mathbb{S}^+}\sum_{l=0}^{\infty}\sum_{\substack{m=-l\\ l+m\text{ odd}}}^{l}\zeta_l\overline{Y_l^m(\boldsymbol{x})}Y_l^m(\boldsymbol{y})\frac{\partial\tilde{\mu}(\boldsymbol{x})}{\partial\phi_{\boldsymbol{x}}}\frac{\partial\overline{\tilde{\mu}^t}(\boldsymbol{y})}{\partial\phi_{\boldsymbol{y}}}d\mathbb{S}^+(\boldsymbol{x})d\mathbb{S}^+(\boldsymbol{y}) \tag{3.46}$$

$$=\int_{\mathbb{D}}\int_{\mathbb{D}}\sum_{l=0}^{\infty}\sum_{\substack{m=-l\\ l+m\text{ odd}}}^{l}\zeta_l\overline{y_l^m(\boldsymbol{x})}y_l^m(\boldsymbol{y})\frac{1}{w(\boldsymbol{x})}\frac{\partial\mu(\boldsymbol{x})}{\partial\phi_{\boldsymbol{x}}}\frac{1}{w(\boldsymbol{y})}\frac{\partial\overline{\mu^t}(\boldsymbol{y})}{\partial\phi_{\boldsymbol{y}}}d\mathbb{D}(\boldsymbol{x})d\mathbb{D}(\boldsymbol{y}) \tag{3.47}$$

$$=\left\langle\widetilde{\mathcal{L}}_{as}^{ws}\left(\frac{1}{w}\frac{\partial\mu}{\partial\phi_{\boldsymbol{x}}}\right),\frac{1}{w}\frac{\partial\mu^t}{\partial\phi_{\boldsymbol{y}}}\right\rangle_{\mathbb{D}}, \tag{3.48}$$

thus providing the desired result for the first integration in (3.42). Let us now address the second one. Let us first note that the following functions are even with respect to the plane $x_3=0$:

$$\frac{\partial\tilde{\mu}}{\partial\theta_{\boldsymbol{x}}}(\boldsymbol{x}),\quad \frac{\partial\tilde{\mu}^t}{\partial\theta_{\boldsymbol{y}}}(\boldsymbol{y}),\quad \frac{\cos\theta_{\boldsymbol{x}}}{\sin\theta_{\boldsymbol{x}}}\frac{\partial\tilde{\mu}}{\partial\phi_{\boldsymbol{x}}}(\boldsymbol{x})\quad\text{and}\quad \frac{\cos\theta_{\boldsymbol{y}}}{\sin\theta_{\boldsymbol{y}}}\frac{\partial\tilde{\mu}^t}{\partial\phi_{\boldsymbol{y}}}(\boldsymbol{y}). \tag{3.49}$$

Thus, we can rewrite the second integral in (3.42), eliminating the terms for $l+m$ odd, as:

$$\frac{1}{2}\int_{\mathbb{S}}\int_{\mathbb{S}}\sum_{l=0}^{\infty}\sum_{\substack{m=-l\\ l+m\text{ even}}}^{l}\frac{\zeta_l}{2}\overline{y_l^m(\boldsymbol{x})}y_l^m(\boldsymbol{y})\left[\cos\left(\phi_{\boldsymbol{x}}-\phi_{\boldsymbol{y}}\right)\left(\frac{\partial\tilde{\mu}(\boldsymbol{x})}{\partial\theta_{\boldsymbol{x}}}\frac{\partial\overline{\tilde{\mu}^t}(\boldsymbol{y})}{\partial\theta_{\boldsymbol{y}}}+\frac{\cos\theta_{\boldsymbol{x}}\cos\theta_{\boldsymbol{y}}}{\sin\theta_{\boldsymbol{x}}\sin\theta_{\boldsymbol{y}}}\frac{\partial\tilde{\mu}(\boldsymbol{x})}{\partial\phi_{\boldsymbol{x}}}\frac{\partial\overline{\tilde{\mu}^t}(\boldsymbol{y})}{\partial\phi_{\boldsymbol{y}}}\right)\right.$$
$$\left.+\sin\left(\phi_{\boldsymbol{x}}-\phi_{\boldsymbol{y}}\right)\left(\frac{\cos\theta_{\boldsymbol{y}}}{\sin\theta_{\boldsymbol{y}}}\frac{\partial\tilde{\mu}(\boldsymbol{x})}{\partial\theta_{\boldsymbol{x}}}\frac{\partial\overline{\tilde{\mu}^t}(\boldsymbol{y})}{\partial\phi_{\boldsymbol{y}}}-\frac{\cos\theta_{\boldsymbol{x}}}{\sin\theta_{\boldsymbol{x}}}\frac{\partial\tilde{\mu}(\boldsymbol{x})}{\partial\phi_{\boldsymbol{x}}}\frac{\partial\overline{\tilde{\mu}^t}(\boldsymbol{y})}{\partial\theta_{\boldsymbol{y}}}\right)\right]|\cos\theta_{\boldsymbol{x}}|\,|\cos\theta_{\boldsymbol{y}}|d\mathbb{S}(\boldsymbol{x})d\mathbb{S}(\boldsymbol{y}). \tag{3.50}$$

Using the same procedure as before for writing sphere integrals of even functions as integrals on $\mathbb{S}^+$ and on $\mathbb{D}$, and using (2.67) and (2.68) from Remark 2.5.1, we find the desired expression for the second integral.

For the second part regarding $\widetilde{a}_{as}^{hs}(\mu,\mu^t)$, using proposition 2.7.7, let us rewrite the first term of (3.32):

$$\left\langle \widetilde{\mathcal{L}}_s^{ws}\overrightarrow{\operatorname{curl}}_{\mathbb{D}}\mu, \overrightarrow{\operatorname{curl}}_{\mathbb{D}}\mu^t\right\rangle_{\mathbb{D}} = \int_{\mathbb{D}}\int_{\mathbb{D}} \widetilde{K}_s^{ws}(\boldsymbol{x},\boldsymbol{y})\left(\overrightarrow{\operatorname{curl}}_{\mathbb{D}}\mu, \overrightarrow{\operatorname{curl}}_{\mathbb{D}}\mu^t\right) d\mathbb{D}(\boldsymbol{x})d\mathbb{D}(\boldsymbol{y}) \tag{3.51}$$

$$= -\frac{1}{2}\int_{\mathbb{D}}\int_{\mathbb{D}} \widetilde{K}_s^{ws}(\boldsymbol{x},\boldsymbol{y})\left(\mathcal{L}_+\mu\mathcal{L}_-\mu^t + \mathcal{L}_+\overline{\mu}\mathcal{L}_-\overline{\mu^t}\right) d\mathbb{D}(\boldsymbol{x})d\mathbb{D}(\boldsymbol{y}) \tag{3.52}$$

$$= -\frac{1}{2}\left\langle \widetilde{\mathcal{L}}_{as}^{ws}\mathcal{L}_+\mu, \mathcal{L}_-\mu^t\right\rangle_{\mathbb{D}} - \frac{1}{2}\left\langle \widetilde{\mathcal{L}}_{as}^{ws}\mathcal{L}_-\mu, \mathcal{L}_+\mu^t\right\rangle_{\mathbb{D}}. \tag{3.53}$$

The second term of (3.32) can be easily rewritten, using the definition of operator $\mathcal{L}_3$ and its conjugate (Proposition 2.7.5), as:

$$\left\langle \widetilde{\mathcal{L}}_{as}^{ws}\left(\frac{1}{w}\frac{\partial\mu}{\partial\phi_{\boldsymbol{x}}}\right), \frac{1}{w}\frac{\partial\mu^t}{\partial\phi_{\boldsymbol{y}}}\right\rangle_{\mathbb{D}} = \int_{\mathbb{D}}\int_{\mathbb{D}} \widetilde{K}_{as}^{ws}(\boldsymbol{x},\boldsymbol{y})\frac{1}{w(\boldsymbol{x})}\frac{\partial\mu}{\partial\phi_{\boldsymbol{x}}}\frac{1}{w(\boldsymbol{y})}\frac{\partial\overline{\mu^t}}{\partial\phi_{\boldsymbol{y}}} d\mathbb{D}(\boldsymbol{x})d\mathbb{D}(\boldsymbol{y}) \tag{3.54}$$

$$= -\int_{\mathbb{D}}\int_{\mathbb{D}} \widetilde{K}_{as}^{ws}(\boldsymbol{x},\boldsymbol{y})\frac{1}{w(\boldsymbol{x})}\frac{1}{\mathrm{i}}\frac{\partial\mu}{\partial\phi_{\boldsymbol{x}}}\frac{1}{w(\boldsymbol{y})}\frac{1}{\mathrm{i}}\frac{\partial\overline{\mu^t}}{\partial\phi_{\boldsymbol{y}}} d\mathbb{D}(\boldsymbol{x})d\mathbb{D}(\boldsymbol{y}) \tag{3.55}$$

$$= -\int_{\mathbb{D}}\int_{\mathbb{D}} \widetilde{K}_{as}^{ws}(\boldsymbol{x},\boldsymbol{y})\frac{\mathcal{L}_3\mu(\boldsymbol{x})}{w(\boldsymbol{x})}\frac{\mathcal{L}_3\overline{\mu^t}(\boldsymbol{y})}{w(\boldsymbol{y})} d\mathbb{D}(\boldsymbol{x})d\mathbb{D}(\boldsymbol{y}) \tag{3.56}$$

$$= \int_{\mathbb{D}}\int_{\mathbb{D}} \widetilde{K}_{as}^{ws}(\boldsymbol{x},\boldsymbol{y})\frac{\mathcal{L}_3\mu(\boldsymbol{x})}{w(\boldsymbol{x})}\overline{\frac{\mathcal{L}_3\mu^t(\boldsymbol{y})}{w(\boldsymbol{y})}} d\mathbb{D}(\boldsymbol{x})d\mathbb{D}(\boldsymbol{y}) \tag{3.57}$$

$$= \left\langle \widetilde{\mathcal{L}}_{as}^{ws}\frac{\mathcal{L}_3\mu}{w(\boldsymbol{x})}, \frac{\mathcal{L}_3\mu^t}{w(\boldsymbol{y})}\right\rangle_{\mathbb{D}}. \tag{3.58}$$

This proves identities (3.32) and (3.33) from the theorem. Equations (3.34) and (3.35) regarding $\widetilde{\mathcal{L}}_s^{hs}$ can be obtained with the same procedure using complementary parity and symmetry. ∎

Proposition 3.1.3 (Modified integral operators' action over basis functions on the disk)**.** *The modified boundary integral operators from Definition 3.1.2 have the following mapping properties:*

$$\widetilde{\mathcal{L}}_s^{ws}\frac{y_l^m}{w} = \frac{\zeta_l}{2}y_l^m, \text{ for } l+m \text{ even}, \tag{3.59}$$

$$\widetilde{\mathcal{L}}_{as}^{ws}\frac{y_l^m}{w} = \frac{\zeta_l}{2}y_l^m, \text{ for } l+m \text{ odd}, \tag{3.60}$$

$$\widetilde{\mathcal{L}}_s^{hs}y_l^m = -\frac{\eta_l}{2}\frac{y_l^m}{w}, \text{ for } l+m \text{ even}, \tag{3.61}$$

$$\widetilde{\mathcal{L}}_{as}^{hs}y_l^m = -\frac{\eta_l}{2}\frac{y_l^m}{w}, \text{ for } l+m \text{ odd}. \tag{3.62}$$

Proof Let us analyze the first case.

$$\left(\widetilde{\mathcal{L}}_s^{ws}\frac{y_l^m}{w}\right)(\boldsymbol{y}) = \sum_{l'=0}^{\infty}\sum_{\substack{m'=-l'\\ l'+m' \text{ even}}}^{l'} \zeta_l \int_{\mathbb{D}} y_{l'}^{m'}(\boldsymbol{y})\overline{y_{l'}^{m'}}(\boldsymbol{x})\frac{y_l^m(\boldsymbol{x})}{w(\boldsymbol{x})}d\mathbb{D}(\boldsymbol{x}). \tag{3.63}$$

Using the orthogonality relations 2.7.4 and 2.7.1 it follows that

$$\left(\widetilde{\mathcal{L}}_s^{ws}\frac{y_l^m}{w}\right)(\boldsymbol{y}) = \sum_{l'=0}^{\infty}\sum_{\substack{m'=-l'\\ l'+m' \text{ even}}}^{l'} \zeta_l y_{l'}^{m'}(\boldsymbol{y})\frac{1}{2}\delta_l^{l'}\delta_m^{m'} \tag{3.64}$$

$$= \frac{\zeta_l}{2} y_l^m(\boldsymbol{y}). \tag{3.65}$$

The next three cases follow from similar procedures. ∎

Proposition 3.1.4 (Calderón-type identities for the modified boundary integral operators on the disk)**.** *The modified boundary integral operators from Definition 3.1.2 have the following Calderon-type identities:*

$$-\widetilde{\mathcal{L}}_s^{hs} \circ \widetilde{\mathcal{L}}_s^{ws} \lambda = \frac{1}{4}\left(\mathbb{I} + \frac{1}{w}\widetilde{\mathcal{L}}_s^{ws}\left(\frac{1}{w}\widetilde{\mathcal{L}}_s^{ws}\lambda\right)\right), \tag{3.66}$$

$$-\widetilde{\mathcal{L}}_{as}^{hs} \circ \widetilde{\mathcal{L}}_{as}^{ws} \varphi = \frac{1}{4}\left(\mathbb{I} + \frac{1}{w}\widetilde{\mathcal{L}}_{as}^{ws}\left(\frac{1}{w}\widetilde{\mathcal{L}}_{as}^{ws}\varphi\right)\right), \tag{3.67}$$

$$-\widetilde{\mathcal{L}}_s^{ws} \circ \widetilde{\mathcal{L}}_s^{hs} g = \frac{1}{4}\left(\mathbb{I} + \widetilde{\mathcal{L}}_s^{ws}\left(\frac{1}{w}\widetilde{\mathcal{L}}_s^{ws}\left(\frac{g}{w}\right)\right)\right), \tag{3.68}$$

$$-\widetilde{\mathcal{L}}_{as}^{ws} \circ \widetilde{\mathcal{L}}_{as}^{hs} \mu = \frac{1}{4}\left(\mathbb{I} + \widetilde{\mathcal{L}}_{as}^{ws}\left(\frac{1}{w}\widetilde{\mathcal{L}}_{as}^{ws}\left(\frac{\mu}{w}\right)\right)\right). \tag{3.69}$$

Proof Let us prove the first identity for $\widetilde{\mathcal{L}}_s^{hs} \circ \widetilde{\mathcal{L}}_s^{ws}$. Using Proposition 2.7.10 it is easy to see that, for $\lambda \in \widetilde{H}^{-1/2}(\mathbb{D})$

$$-\left(\widetilde{\mathcal{L}}_s^{hs} \circ \widetilde{\mathcal{L}}_s^{ws}\right)\lambda = \frac{1}{4}\sum_{l=0}^{\infty}\sum_{\substack{m=-l \\ l+m \text{ even}}}^{l} \zeta_l \eta_l \lambda_l^m \frac{y_l^m}{w} \tag{3.70}$$

$$= \sum_{l=0}^{\infty}\sum_{\substack{m=-l \\ l+m \text{ even}}}^{l} \frac{l(l+1)}{(2l+1)^2}\lambda_l^m \frac{y_l^m}{w}. \tag{3.71}$$

This expression can be separated as

$$\sum_{l=0}^{\infty}\sum_{\substack{m=-l \\ l+m \text{ even}}}^{l} \frac{l(l+1)}{(2l+1)^2}\lambda_l^m \frac{y_l^m}{w} = \sum_{l=0}^{\infty}\sum_{\substack{m=-l \\ l+m \text{ even}}}^{l} \lambda_l^m \frac{y_l^m}{w} - \sum_{l=0}^{\infty}\sum_{\substack{m=-l \\ l+m \text{ even}}}^{l} \frac{3l^2+3l+1}{(2l+1)^2}\lambda_l^m \frac{y_l^m}{w} \tag{3.72}$$

$$= \lambda - 3\sum_{l=0}^{\infty}\sum_{\substack{m=-l \\ l+m \text{ even}}}^{l} \frac{l(l+1)}{(2l+1)^2}\lambda_l^m \frac{y_l^m}{w} - \sum_{l=0}^{\infty}\sum_{\substack{m=-l \\ l+m \text{ even}}}^{l} \frac{1}{(2l+1)^2}\lambda_l^m \frac{y_l^m}{w}, \tag{3.73}$$

$$\Rightarrow -4\left(\widetilde{\mathcal{L}}_s^{hs} \circ \widetilde{\mathcal{L}}_s^{ws}\right)\lambda = \lambda - \sum_{l=0}^{\infty}\sum_{\substack{m=-l \\ l+m \text{ even}}}^{l} \frac{1}{(2l+1)^2}\lambda_l^m \frac{y_l^m}{w}. \tag{3.74}$$

The last term of the equation is easy to compose using operator $\widetilde{\mathcal{L}}_s^{ws}$. Using again Proposition 2.7.10 it's easy to see that

$$\frac{1}{w}\widetilde{\mathcal{L}}_s^{ws}\left(\frac{1}{w}\widetilde{\mathcal{L}}_s^{ws}\lambda\right) = \sum_{l=0}^{\infty}\sum_{\substack{m=-l \\ l+m \text{ even}}}^{l} \frac{1}{(2l+1)^2}\lambda_l^m \frac{y_l^m}{w}, \tag{3.75}$$

which proves the first case. The case for $\widetilde{\mathcal{L}}_{as}^{hs} \circ \widetilde{\mathcal{L}}_{as}^{ws}$ is done in the same way for $H^{-1/2}(\mathbb{D})$ but summing over $l+m$ odd pairs.

Let us now address the case $\widetilde{\mathcal{L}}_s^{ws} \circ \widetilde{\mathcal{L}}_s^{hs}$. In a way similar to the previous two cases, we have, for $g \in H^{1/2}(\mathbb{D})$,

$$-\left(\widetilde{\mathcal{L}}_s^{ws} \circ \widetilde{\mathcal{L}}_s^{hs}\right) g = \sum_{l=0}^{\infty}\sum_{\substack{m=-l \\ l+m \text{ even}}}^{l} \frac{l(l+1)}{(2l+1)^2} g_l^m y_l^m. \tag{3.76}$$

Using yet again Proposition 2.7.10 it's easy to see that

$$\widetilde{\mathcal{L}}_s^{ws}\left(\frac{1}{w}\widetilde{\mathcal{L}}_s^{ws}\left(\frac{g}{w}\right)\right)=\sum_{l=0}^{\infty}\sum_{\substack{m=-l\\ l+m \text{ even}}}^{l}\frac{1}{(2l+1)^2}g_l^m y_l^m, \tag{3.77}$$

which proves this case proceeding as in the previous two cases but replacing y_l^m/w with y_l^m. The case for $\widetilde{\mathcal{L}}_{as}^{ws}\circ\widetilde{\mathcal{L}}_{as}^{hs}$ is done in the same way for $\widetilde{H}^{1/2}(\mathbb{D})$ but summing over $l+m$ odd pairs. ■

3.1.3 Variational problems and norms

In this section we will use the modified boundary integral operators, for which we know their explicit variational expressions, to formulate variational problems that we will later use to build Galerkin matrices. The preconditioning capabilities of these matrices will be an important part of this chapter, and will be studied in subsequent sections.

Definition 3.1.3 (Induced bilinear forms)**.** *Let us define the following bilinear forms induced by the modified boundary integral operators from Definition 3.1.2:*

$$\widetilde{a}_s^{ws}\in L\left(\widetilde{H}^{-1/2}(\mathbb{D})\times\widetilde{H}^{-1/2}(\mathbb{D}),\mathbb{C}\right):\widetilde{a}_s^{ws}(\lambda,\lambda^t)=\left\langle\widetilde{\mathcal{L}}_s^{ws}\lambda,\lambda^t\right\rangle_{\mathbb{D}}, \tag{3.78}$$

$$\widetilde{b}_s^{hs}\in L\left(H^{1/2}(\mathbb{D})\times H^{1/2}(\mathbb{D}),\mathbb{C}\right):\widetilde{b}_s^{hs}(g,g^t)=\left\langle-\widetilde{\mathcal{L}}_s^{hs}g,g^t\right\rangle_{\mathbb{D}}, \tag{3.79}$$

$$\widetilde{a}_{as}^{hs}\in L\left(\widetilde{H}^{1/2}(\mathbb{D})\times\widetilde{H}^{1/2}(\mathbb{D}),\mathbb{C}\right):\widetilde{a}_{as}^{hs}(\mu,\mu^t)=\left\langle-\widetilde{\mathcal{L}}_{as}^{hs}\mu,\mu^t\right\rangle_{\mathbb{D}}, \tag{3.80}$$

$$\widetilde{b}_{as}^{ws}\in L\left(H^{-1/2}(\mathbb{D})\times H^{-1/2}(\mathbb{D}),\mathbb{C}\right):\widetilde{b}_{as}^{ws}(\varphi,\varphi^t)=\left\langle\widetilde{\mathcal{L}}_{as}^{ws}\varphi,\varphi^t\right\rangle_{\mathbb{D}}. \tag{3.81}$$

These bilinear forms define norms in the spaces spanned by the disk basis functions, as we will show in the next propositions.

Proposition 3.1.5 (The bilinear forms define inner products)**.** *The bilinear forms from Definition 3.1.3 define inner products in the linear spaces spanned by the set of disk basis functions: $\widetilde{a}_s^{ws}$ in $\mathcal{Y}_s^{1/w}$, $\widetilde{b}_s^{hs}$ in $\mathcal{Y}_s$, $\widetilde{a}_{as}^{hs}$ in $\mathcal{Y}_{as}$ and $\widetilde{b}_{as}^{ws}$ in $\mathcal{Y}_{as}^{1/w}$.*

Proof Let us focus on the first bilinear form, $\widetilde{a}_s^{ws}$ for the linear space spanned by $\mathcal{Y}_s^{1/w}$. Let us take two arbitrary functions $u,v\in\operatorname{span}\left(\mathcal{Y}_s^{1/w}\right)$ and show that conjugate symmetry, linearity, and positive definiteness are satisfied.

$$\left\langle\widetilde{\mathcal{L}}_s^{ws}u\,,\,v\right\rangle_{\mathbb{D}}=\left\langle\mathcal{L}_s^{ws}\sum_{l=0}^{\infty}\sum_{\substack{m=-l\\ l+m \text{ even}}}^{l}u_l^m\frac{y_l^m}{w}\,,\,\sum_{l=0}^{\infty}\sum_{\substack{m=-l\\ l+m \text{ even}}}^{l}v_l^m\frac{y_l^m}{w}\right\rangle_{\mathbb{D}} \tag{3.82}$$

$$=\left\langle\sum_{l=0}^{\infty}\sum_{\substack{m=-l\\ l+m \text{ even}}}^{l}\frac{\zeta_l}{2}u_l^m y_l^m\,,\,\sum_{l=0}^{\infty}\sum_{\substack{m=-l\\ l+m \text{ even}}}^{l}v_l^m\frac{y_l^m}{w}\right\rangle_{\mathbb{D}} \tag{3.83}$$

$$=\sum_{l=0}^{\infty}\sum_{\substack{m=-l\\ l+m \text{ even}}}^{l}\frac{\zeta_l u_l^m\overline{v_l^m}}{4} \tag{3.84}$$

$$=\overline{\sum_{l=0}^{\infty}\sum_{\substack{m=-l\\ l+m \text{ even}}}^{l}\frac{\zeta_l v_l^m\overline{u_l^m}}{4}} \tag{3.85}$$

$$=\overline{\left\langle\widetilde{\mathcal{L}}_s^{ws}v\,,\,u\right\rangle_{\mathbb{D}}}. \tag{3.86}$$

Linearity on the first argument comes straightforwardly from the definition of the duality product. And finally,

$$\left\langle \widetilde{\mathcal{L}}_s^{ws} u \, , \, u \right\rangle_{\mathbb{D}} = \sum_{l=0}^{\infty} \sum_{\substack{m=-l \\ l+m \text{ even}}}^{l} \zeta_l \frac{|u_l^m|^2}{4}, \tag{3.87}$$

shows that $\widetilde{a}_s^{ws}(u,u)$ is always positive and that, only $u_l^m = 0$ for every l and m, and thus only $u = 0$, makes $\widetilde{a}_s^{ws}(u,u) = 0$, which shows the positive-definiteness property. The same argument follows for the other three cases. ∎

Definition 3.1.4 (Norms associated with the modified operators)**.** *Being inner products, the previous bilinear forms from Definition 3.1.3 allow us to define the following norms for their respective spaces:*

$$\|\lambda\|_{\widetilde{a}_s^{ws}} = \sqrt{\widetilde{a}_s^{ws}(\lambda,\lambda)}, \tag{3.88}$$

$$\|\mu\|_{\widetilde{a}_{as}^{hs}} = \sqrt{\widetilde{a}_{as}^{hs}(\mu,\mu)}, \tag{3.89}$$

$$\|g\|_{\widetilde{b}_s^{hs}} = \sqrt{\widetilde{b}_s^{hs}(g,g)}, \tag{3.90}$$

$$\|\varphi\|_{\widetilde{b}_{as}^{ws}} = \sqrt{\widetilde{b}_{as}^{ws}(\varphi,\varphi)}. \tag{3.91}$$

Proposition 3.1.6 (Computation of the norms associated with the modified boundary integral operators)**.** *The norms from Definition 3.1.4 can be computed as follows:*

$$\|\lambda\|^2_{\widetilde{a}_s^{ws}} = \sum_{l=0}^{\infty} \sum_{\substack{m=-l \\ l+m \ even}}^{l} \frac{\zeta_l}{4} \lambda_l^m \overline{\lambda_l^m}, \ \textit{for } l+m \ \textit{even}, \tag{3.92}$$

$$\|\mu\|^2_{\widetilde{a}_{as}^{hs}} = \sum_{l=0}^{\infty} \sum_{\substack{m=-l \\ l+m \ odd}}^{l} \frac{\eta_l}{4} \mu_l^m \overline{\mu_l^m}, \ \textit{for } l+m \ \textit{odd}, \tag{3.93}$$

$$\|g\|^2_{\widetilde{b}_s^{hs}} = \sum_{l=0}^{\infty} \sum_{\substack{m=-l \\ l+m \ even}}^{l} \frac{\eta_l}{4} g_l^m \overline{g_l^m}, \ \textit{for } l+m \ \textit{even}, \tag{3.94}$$

$$\|\varphi\|^2_{\widetilde{b}_{as}^{ws}} = \sum_{l=0}^{\infty} \sum_{\substack{m=-l \\ l+m \ odd}}^{l} \frac{\zeta_l}{4} \varphi_l^m \overline{\varphi_l^m}, \ \textit{for } l+m \ \textit{odd}, \tag{3.95}$$

where

$$\lambda_l^m = (\lambda, y_l^m/w)_w, \tag{3.96}$$

$$\mu_l^m = (\mu, y_l^m)_{1/w}, \tag{3.97}$$

$$g_l^m = (g, y_l^m)_{1/w}, \tag{3.98}$$

$$\varphi_l^m = (\varphi, y_l^m/w)_w. \tag{3.99}$$

Proof The demonstration is done as the one for Proposition 2.7.16. ∎

We will use the bilinear forms induced by the modified boundary integral operators to pose variational problems. These variational problems will later give rise to the Galerkin matrices that will be the subject of study, especially in their preconditioning abilities.

Definition 3.1.5 (Variational problems for the modified boundary integral operators)**.** *Let us consider the following variational problems for the bilinear forms from Definition 3.1.3. A variation problem for the boundary integral equation associated with the boundary integral operator* $\widetilde{\mathcal{L}}_s^{ws}$ *is*

$$\left(\widetilde{\mathcal{L}}_s^{ws}\text{–}VF\right)\begin{cases} \text{Given } g \in H^{1/2}(\mathbb{D}), \text{ find } \lambda \in \widetilde{H}^{-1/2}(\mathbb{D}), \text{ such that} \\ \\ \forall \lambda^t \in \widetilde{H}^{-1/2}(\mathbb{D}) \left(\widetilde{a}_s^{ws}(\lambda, \lambda^t) = \left\langle g, \lambda^t \right\rangle_{\mathbb{D}}\right). \end{cases} \tag{3.100}$$

The boundary integral equation associated with the boundary integral operator $\widetilde{\mathcal{L}}_s^{hs}$ *admits the variational problem*

$$\left(\widetilde{\mathcal{L}}_s^{hs}\text{–}VF\right)\begin{cases} \text{Given } \lambda \in \widetilde{H}^{-1/2}(\mathbb{D}), \text{ find } \lambda \in H^{1/2}(\mathbb{D}), \text{ such that} \\ \\ \forall g^t \in H^{1/2}(\mathbb{D}) \left(\widetilde{b}_s^{hs}(g, g^t) = \left\langle \lambda, g^t \right\rangle_{\mathbb{D}}\right). \end{cases} \tag{3.101}$$

The boundary integral equation associated with the boundary integral operator $\widetilde{\mathcal{L}}_{as}^{hs}$ *admits the variational problem*

$$\left(\widetilde{\mathcal{L}}_{as}^{hs}\text{–}VF\right)\begin{cases} \text{Given } \varphi \in H^{-1/2}(\mathbb{D}), \text{ find } \mu \in \widetilde{H}^{1/2}(\mathbb{D}), \text{ such that} \\ \\ \forall \mu^t \in \widetilde{H}^{1/2}(\mathbb{D}) \left(\widetilde{a}_{as}^{hs}(\mu, \mu^t) = \left\langle \varphi, \mu^t \right\rangle_{\mathbb{D}}\right). \end{cases} \tag{3.102}$$

The boundary integral equation associated with the boundary integral operator $\widetilde{\mathcal{L}}_{as}^{ws}$ *admits the variational problem*

$$\left(\widetilde{\mathcal{L}}_{as}^{ws}\text{–}VF\right)\begin{cases} \text{Given } \mu \in \widetilde{H}^{1/2}(\mathbb{D}), \text{ find } \varphi \in H^{-1/2}(\mathbb{D}), \text{ such that} \\ \\ \forall \varphi^t \in H^{-1/2}(\mathbb{D}) \left(\widetilde{b}_{as}^{ws}(\varphi, \varphi^t) = \left\langle \mu, \varphi^t \right\rangle_{\mathbb{D}}\right). \end{cases} \tag{3.103}$$

Coercivity and bi-continuity in the Sobolev trace spaces must be proven for the associated Galerking matrices to be optimal preconditioners. These variational problems will provide the Galerkin matrices that are intended to produce the desired preconditioning effect on the Galerkin matrices associated with $\mathcal{S}$ and $\mathcal{N}$ by virtue of their kernels' behavior in the radial direction. This idea will be put to the test numerically in the next sections. These variational problems are not necessarily variational formulations for the modified integral operators in the relevant trace spaces on which these problems are posed, as their coercivity is not readily assured for the norms of the Sobolev trace spaces $\widetilde{H}^{-1/2}(\mathbb{D})$, $H^{1/2}(\mathbb{D})$, $\widetilde{H}^{1/2}(\mathbb{D})$ and $H^{-1/2}(\mathbb{D})$. In fact, following Propositions 2.7.16 and 3.1.6, the coercivity would need the existence of constants C_s^{ws}, C_s^{hs}, C_{as}^{ws} and C_{as}^{hs} such that

$$\frac{1}{\beta_l^m} \leq C_s^{ws}\zeta_l, \quad \beta_l^m \leq C_s^{hs}\eta_l, \quad \frac{1}{\alpha_l^m} \leq C_{as}^{ws}\zeta_l, \quad \text{and} \quad \alpha_l^m \leq C_{as}^{hs}\eta_l, \tag{3.104}$$

and the existence of constants $C_s'^{ws}$, $C_s'^{hs}$, $C_{as}'^{ws}$ and $C_{as}'^{hs}$ such that

$$\frac{1}{\beta_l^m} \geq C_s'^{ws}\zeta_l, \quad \beta_l^m \geq C_s'^{hs}\eta_l, \quad \frac{1}{\alpha_l^m} \geq C_{as}'^{ws}\zeta_l, \quad \text{and} \quad \alpha_l^m \geq C_{as}'^{hs}\eta_l. \tag{3.105}$$

This would amount to norm equivalency between the norms induced by the series operators presented in the previous section and the norms induced by modified series operators presented in this current section.

We will present the answer to some of this issues the following sections.

3.2 Boundary elements method implementation

Taking advantage of known series representation of the operators posed on the sphere, it was possible to consider in this present chapter slight modifications to the series form integral kernel from Definition 2.7.10, that had explicit and closed variational forms while preserving the singularity behavior properties of the integral kernels. These singularity behavior properties were signaled as a key feature of a previous achievement for a segment screen in $\mathbb{R}^2$ and in fact they were also shown for the series forms of the kernels of the inverse operators for the case of the disk. In the rest of this chapter we will describe a domain discretization suitable for the preconditioning strategy drawn from Theorem 2.1.1 and a boundary element method adapted to the case of the disk screen. With these tools we will build, in the subsequent sections, the Galerkin matrices for the new modified operators and we will test the numerical implementation with benchmark cases. Finally, once the implementation has been argued to be successful, we will explore the capacity for preconditioning of the new modified operators in various cases for the Laplace and Helmholtz screen problem for a disk obstacle. We will end this chapter showing an extension of the numerical method that can extend preconditioning capabilities into screens with other shapes.

3.2.1 Domain discretization

In this subsection we will address in further detail the triangular mesh partition of the surface of screens, particularly the disk. The main concepts about mesh partition were already described in Subsection 1.6.1. The details further developed in this present subsection will be related to the fulfillment of dimension matching conditions stipulated in Theorem 2.1.1 when the surface is not closed. Producing a mesh over which to specify supports for boundary element basis functions is more difficult for screens because the existence of a border of the surface ($\partial\mathbb{D} \neq \varnothing$), and because the fact that one of the Sobolev spaces has functions that are zero at this border (in fact, $\widetilde{H}^{1/2}(\mathbb{D}) \subseteq H_0^{1/2}(\mathbb{D})$).

Let us consider a triangular mesh $\mathcal{T}_h$ for the conformal triangular approximation $\mathbb{D}_h$ of $\mathbb{D}$ (Definition 1.6.1) and a triangular mesh $\mathcal{T}_h$ (Definition 1.6.2), made of N_T closed triangles (with t_i its i-th triangle), N_E edges and N_V vertices (with $\boldsymbol{v}_i$ its i-th vertex), of which N_V^0 are interior. The new domain of integration $\mathbb{D}_h$, an approximation of $\mathbb{D}$, is then $\mathbb{D}_h = \cup_{i=1}^{N_T} t_i$ (modulo a close-open topological operation).

Two dual meshes will be constructed starting from $\mathcal{T}_h$. The first dual mesh $\widetilde{\mathcal{T}}_h$ is constructed as it was indicated in Definition 1.6.10, but we will shortly refresh its main elements. We consider the six disjoint sub-triangles (of type $\hat{t}$ in Definition 1.6.3) resulting from dividing each triangle of $\mathcal{T}_h$ using its medians. We consider the set of piece-wise polygonal elements $\{L_i\}_{i=1}^{N_V}$, associated with the vertices of the primal mesh $\mathcal{T}_h$ such that piece-wise polygonal element L_i associated with $\boldsymbol{v}_i$ is the union of the collection of sub-triangles of type $\hat{t}$ that have vertex $\boldsymbol{v}_i$ of the mesh $\mathcal{T}_h$ as one of its own vertices. This construction also yields $\mathbb{D}_h = \cup_{i=1}^{N_V} L_i$ (modulo a close-open topological operation) and, when the discretized surface lies on a plane, elements L_i are not just piece-wise polygonal, but polygons themselves.

We will consider a second dual mesh in order to develop appropriate elements for a subspace of $H^{-1/2}(\mathbb{D})$, dual to $\widetilde{H}^{1/2}(\mathbb{D})$ of functions zero on the border, and to comply with the requirement that both finite subspaces have the same dimensions. The second dual mesh, denoted by $\widetilde{\mathcal{T}}_h^0$, will use a different subdivision of the triangles on the border of $\mathbb{D}_h$: triangles $t \in \mathcal{T}_h$ with two or three vertices on the edge $\partial\mathbb{D}_h$ will not be subdivided and will be considered proper sub-triangles, while the ones with one vertex over $\partial\mathbb{D}_h$ will be divided into two sub-triangles (of type $\tilde{t}$ in Definition 1.6.3) separated by the median associated with the vertex on the border $\partial\mathbb{D}_h$. Triangles without vertices on $\partial\mathbb{D}_h$ will be subdivided as in $\widetilde{\mathcal{T}}_h$. The dual mesh $\widetilde{\mathcal{T}}_h^0$ is then the set of piece-wise polygonal elements associated with the N_V^0 internal vertices of the mesh $\mathcal{T}_h$, $\{M_i\}_{i=0}^{N_V^0}$, such that the element M_i associated with the internal vertex $\boldsymbol{v}_i$ of $\mathcal{T}_h$ is the

collection of sub-triangles (now produced differently than for $\widetilde{\mathcal{T}}_h$) that have the internal vertex $\boldsymbol{v}_i$ of the $\mathcal{T}_h$ as one of their own vertices. Figure 3.1 illustrates the construction process for $\widetilde{\mathcal{T}}_h$ and $\widetilde{\mathcal{T}}_h^0$ showing the subdivision of triangles near edge $\partial\mathbb{D}_h$ on a sector the of $\mathbb{D}_h$. Figure 3.2 shows specimens of the three meshes for $\mathbb{D}_h$ for a given h.

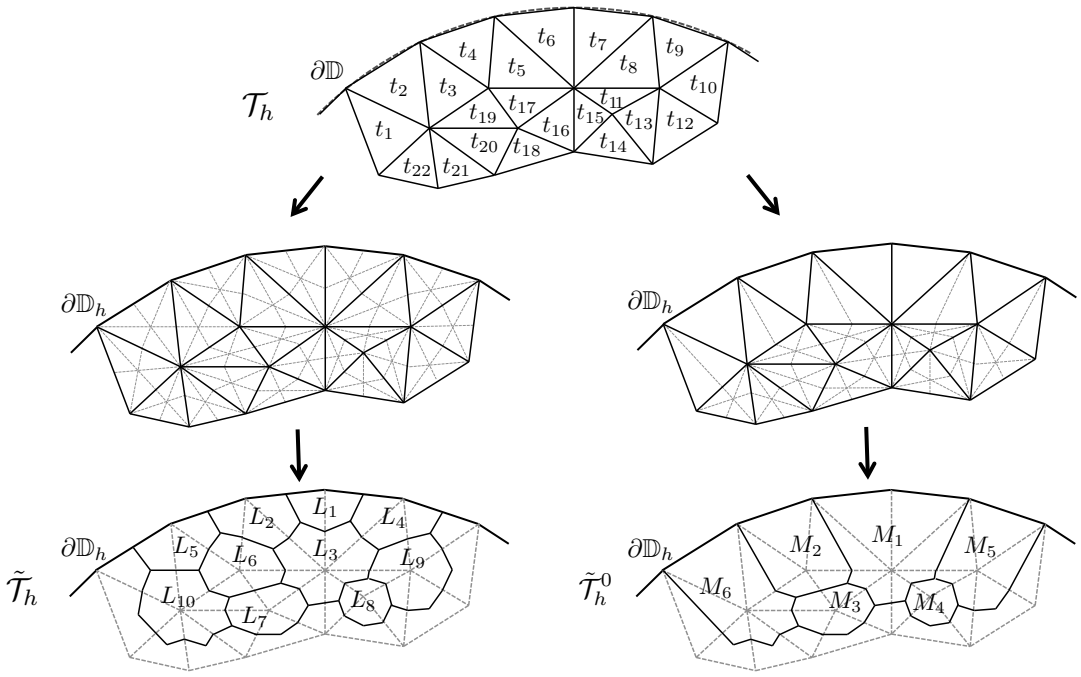

Figure 3.1: Detail of the subdivision of the triangles of a mesh $\mathcal{T}_h$ near the border of $\partial\mathbb{D}_h$, showing the subdivision border triangles for the construction of $\widetilde{\mathcal{T}}_h$ (left) and $\widetilde{\mathcal{T}}_h^0$ (right).

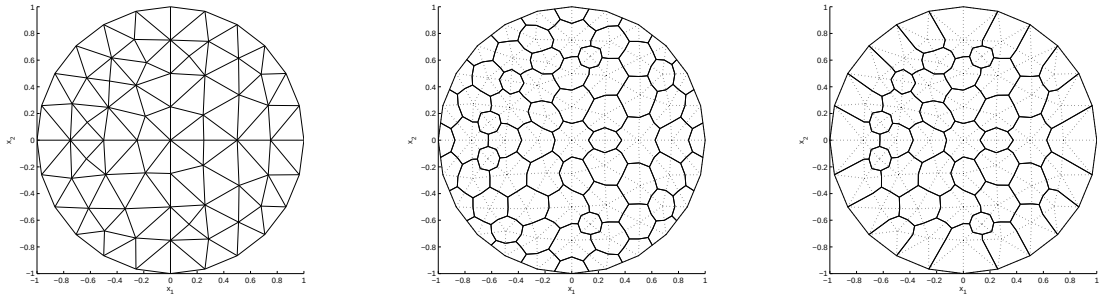

Figure 3.2: An example of triangular mesh partition $\mathcal{T}_h$ of $\mathbb{D}_h$ for a given mean edge size h exhibiting its triangles $\{t_i\}_{i=1}^{N_T}$ (left), with the resulting dual meshes $\widetilde{\mathcal{T}}_h$, exhibiting its components $\{L_i\}_{i=1}^{N_V}$ (center), and $\widetilde{\mathcal{T}}_h^0$ exhibiting its components $\{M_i\}_{i=1}^{N_V^0}$ (right).

A more formal definition will be given using the tools developed in Subsection 1.6.1.

Definition 3.2.1 (Secondary dual mesh $\widetilde{\mathcal{T}}_h^0$)**.** *We will call $\widetilde{\mathcal{T}}_h^0$ the secondary dual mesh of the triangular mesh $\mathcal{T}_h$ the set of piece-wise polygonal elements associated with the N_V^0 internal vertices of $\mathcal{T}_h$, $\{M_i\}_{i=1}^{N_V^0}$, where the element M_i associated with the internal vertex $\boldsymbol{v}_i$ is defined as:*

$$M_i = \left[\bigcup_{\substack{t \in T_{\boldsymbol{v} \to t}(\boldsymbol{v}_i) \\ |T_{t \to \boldsymbol{v}}(t) \cap \partial\mathbb{D}_h| = 2,3}} t \right] \bigcup \left[\bigcup_{\substack{t \in T_{\boldsymbol{v} \to t}(\boldsymbol{v}_i) \\ |T_{t \to \boldsymbol{v}}(t) \cap \partial\mathbb{D}_h| = 1}} \bigcup_{\tilde{t} \in T_{t \to \tilde{t}}(t)} \tilde{t} \right] \bigcup \left[\bigcup_{\substack{t \in T_{\boldsymbol{v} \to t}(\boldsymbol{v}_i) \\ |T_{t \to \boldsymbol{v}}(t) \cap \partial\mathbb{D}_h| = 0}} \bigcup_{\hat{t} \in T_{t \to \hat{t}}(t)} \hat{t} \right], \quad (3.106)$$

for $i = 1...N_V^0$ indexing the internal vertices of $\mathcal{T}_h$.

From its construction it is also clear that the dual mesh $\widetilde{\mathcal{T}}_h^0$ is also a partition of $\mathbb{D}_h$ in the sense that $\mathbb{D}_h = \cup_{i=1}^{N_V^0} M_i$ (modulo a close-open topological operation), and when the discretized surface lies in a plane elements M_i are not just piece-wise polygonal, but polygons themselves.

It is remarkable that the number of piece-wise polygonal elements of the first dual mesh $\widetilde{\mathcal{T}}_h$ is the same as the number of vertices of $\mathcal{T}_h$, and that the number of piece-wise polygonal elements of the secondary dual mesh $\widetilde{\mathcal{T}}_h^0$ is the same as the number of internal vertices of $\mathcal{T}_h$.

Notation 3.2.1 (Sub-triangles of piece-wise polygonal elements from $\widetilde{\mathcal{T}}_h$ and $\widetilde{\mathcal{T}}_h^0$)**.** *Given a piece-wise polygonal element L_i, associated with the vertex $\boldsymbol{v}_i$ of $\mathcal{T}_h$, the notation $k \in L_i$ will be used to mean that a triangle k is one of the sub-triangles of the element L_i (in this case, triangles of type $\hat{t}$ in Definition 1.6.3). Given a piece-wise polygonal element M_i, associated with the internal vertex $\boldsymbol{v}_i$ of $\mathcal{T}_h$, the notation $k \in M_i$ will be used to mean that a triangle k is one of the sub-triangles of the element M_i (in this case triangles of type $\hat{t}$ or type $\tilde{t}$ in Definition 1.6.3, or just triangles from $\mathcal{T}_h$).*

3.2.2 Mesh sets

In the presented modified boundary integral operators related to the Laplace equation for the disk, the kernels involved projections of points from disk $\mathbb{D}$ onto upper half-sphere $\mathbb{S}^+$ and onto lower half-sphere $\mathbb{S}^-$. When performing numerical integrations over $\mathbb{D}_h$, advantage can be taken performing them instead over projected conformal triangular approximations $\mathbb{S}_h^+$ and $\mathbb{S}_h^-$, which can be obtained from $\mathbb{D}_h$ or vice versa. A projected conformal triangular approximation is obtained using the weight function w, defined for the disk in (2.43) from Subsection 2.5.1. For the disk, function w provides the distance $\|\boldsymbol{x} - \boldsymbol{x}^{\pm}\|$ for $\boldsymbol{x} \in \mathbb{D}$. Thus, conformal triangular approximations $\mathbb{S}_h^{\pm}$ can be obtained from $\mathbb{D}_h$ taking the points of $\mathbb{S}_h^{\pm}$ to be the ones of $\mathbb{D}_h$ after projecting them vertically using function w. Likewise, any one of $\mathbb{S}_h^{\pm}$ can define $\mathbb{D}_h$ and the complementary half-sphere using a similar procedure. Using different weight functions for vertical projections will become a relevant tool when treating different screens, as it will be in the next section of this chapter.

The boundary element computations will use, as it will be seen later in this chapter, integration over triangles in the upper and lower half-spheres. The set of these three meshes, available for the computation of bilinear forms over $\mathbb{D}_h$, will be named mesh set.

Definition 3.2.2 (Mesh set)**.** *A mesh set for disk $\mathbb{D}$ is the set of conformal triangular approximations of $\mathbb{D}$, $\mathbb{S}^+$, and $\mathbb{S}^-$, i.e. $\{\mathbb{D}_h, \mathbb{S}_h^+, \mathbb{S}_h^-\}$ for a fixed discretization parameter h of $\mathbb{D}_h$, such that every vertex of $\mathbb{S}_h^+$ (and of $\mathbb{S}_h^-$) is the vertical projection of a vertex of $\mathbb{D}_h$ onto $\mathbb{S}^+$ (and onto $\mathbb{S}^-$).*

We will consider three different types of mesh sets. The interest in studying different meshes and mesh sets arises from: 1) the interest in providing mesh refinement near $\partial\mathbb{D}_h$ as some solutions to the relevant boundary integral equationes are expected to present singularities at the border of $\mathbb{D}$ (refer to Theorem 2.3.4), and 2) the interest in analyzing the effect of mesh uniformity (Definitions 1.6.8 and 1.6.9) on the numerical method to be proposed. Theorem 2.1.1 assures optimal preconditioning independently of the choice of the basis for the finite-dimentional subspaces of the relevant Sobolev trace spaces, provided that stability estimates are fulfilled by the chosen bases. The type of mesh sets to be considered are summarized and explained in Table 3.1. They are obtained fixing one of the three surfaces, taking it to be globally or locally quasi-uniform (Definitions 1.6.8 and 1.6.9) and generating the other two by projection.

Table 3.1: Description of the types of mesh sets considered for the numerical experiments and their construction processes for disk screen $\mathbb{D}$.

Type	$\mathbb{D}_h$	$\mathbb{S}_h^+$	$\mathbb{S}_h^-$
Mesh set #1	Projected from $\mathbb{S}_h^+$	Glob. q.-uniform triangular mesh of $\mathbb{S}^+$	Proj. from $\mathbb{S}_h^+$
Mesh set #1	Glob. q.-uniform mesh of $\mathbb{D}_h$	Projected from $\mathbb{D}_h$	Proj. from $\mathbb{D}_h$
Mesh set #3	Radially graded mesh of $\mathbb{D}_h$	Projected from $\mathbb{D}_h$	Proj. from $\mathbb{D}_h$

Specimens of the three types of mesh sets described in Table 3.1 are illustrated in Figures 3.3, 3.4 & 3.5 providing graphical representations of $\mathbb{D}_h$ and $\mathbb{S}_h^+$ for a given discretization parameter h.

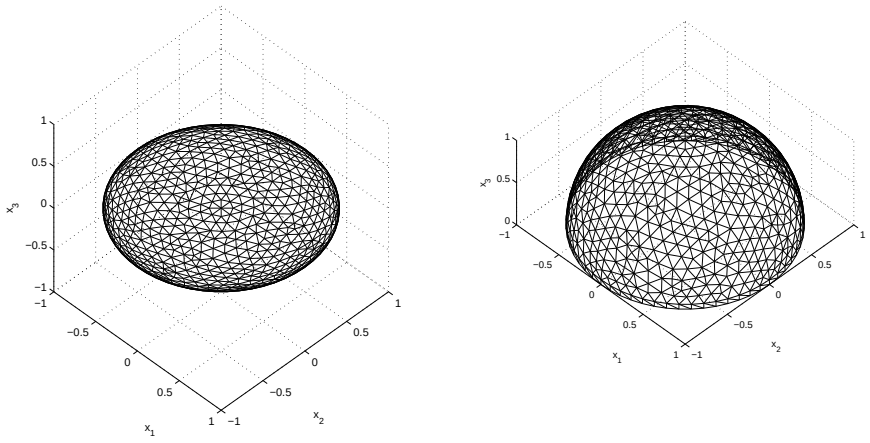

Figure 3.3: Example of discretized domains $\mathbb{D}_h$ (left) and $\mathbb{S}_h^+$ (right) in a mesh set of type Mesh set #1 for a given discretization parameter h.

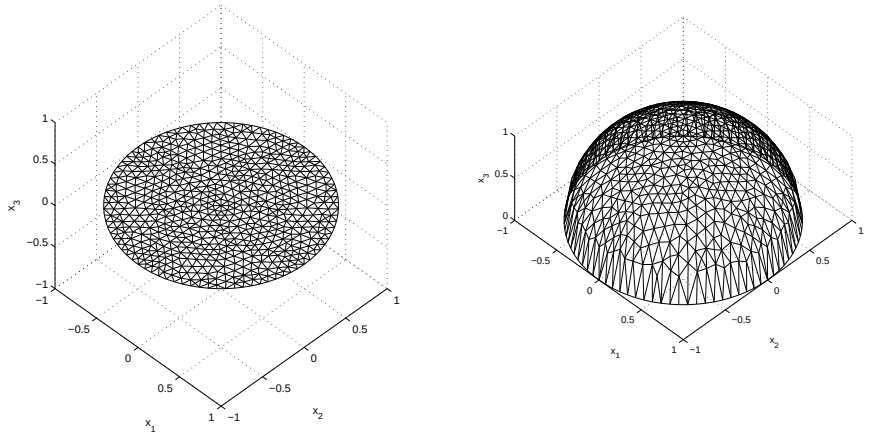

Figure 3.4: Example of discretized domains $\mathbb{D}_h$ (left) and $\mathbb{S}_h^+$ (right) in a mesh set of type Mesh set #2 for a given discretization parameter h.

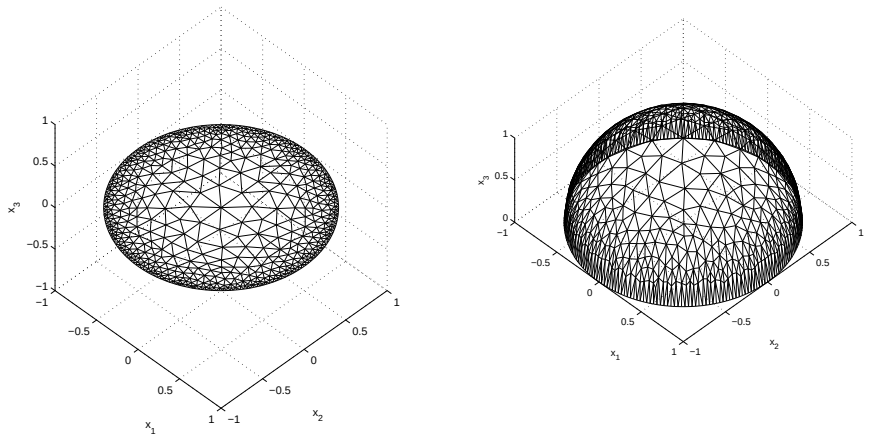

Figure 3.5: Example of discretized domains $\mathbb{D}_h$ (left) and $\mathbb{S}_h^+$ (right) in a mesh set of type Mesh set #3 for a given discretization parameter h.

3.2.3 Boundary element spaces and basis functions

We employ the described meshes and mesh sets to obtain zeroth and first order piecewise polynomial boundary element spaces, subspaces of the Sobolev trace spaces involved in the variational formulations for the new boundary integral operators on the disk. We call $\mathbb{P}^n$ the space of bi-variate polynomials of a degree less than or equal to n, and we then proceed to define the following boundary element spaces. The definitions that will be presented will resemble those of Subsection 1.6.2, but will differ in the treatment required for the finite-dimensional subspaces of the new spaces $\widetilde{H}^{1/2}(\mathbb{D})$ and $\widetilde{H}^{-1/2}(\mathbb{D})$, that were not considered in Chapter 1.

Definition 3.2.3 (Boundary element spaces)**.** *Let us define the following finite-dimensional boundary element spaces, piecewise polynomial on the triangles defined for the primal mesh $\mathcal{T}_h$ and on the piece-wise polygonal elements defined for its dual mesh $\widetilde{\mathcal{T}}_h$ and for its secondary dual mesh $\widetilde{\mathcal{T}}_h^0$:*

$$V_h\left(\mathbb{D}_h\right) = \left\{g_h \in C\left(\mathbb{D}_h\right) : \forall t \in \mathcal{T}_h \left(g_h|_t \in \mathbb{P}^1\right)\right\} \subset H^{1/2}\left(\mathbb{D}_h\right), \tag{3.107}$$

$$\widetilde{V}_h\left(\mathbb{D}_h\right) = \left\{\mu_h \in V_h\left(\mathbb{D}_h\right) : \mu_h|_{\partial\mathbb{D}_h} = 0\right\} \subset \widetilde{H}^{1/2}\left(\mathbb{D}_h\right), \tag{3.108}$$

$$\widetilde{W}_h\left(\mathbb{D}_h\right) = \left\{\lambda_h \in L^2\left(\mathbb{D}_h\right) : \forall L \in \widetilde{\mathcal{T}}_h \left(\lambda_h|_L \in \mathbb{P}^0\right)\right\} \subset \widetilde{H}^{-1/2}\left(\mathbb{D}_h\right), \tag{3.109}$$

$$W_h\left(\mathbb{D}_h\right) = \left\{\varphi_h \in L^2\left(\mathbb{D}_h\right) : \forall M \in \widetilde{\mathcal{T}}_h^0 \left(\varphi_h|_M \in \mathbb{P}^0\right)\right\} \subset H^{-1/2}\left(\mathbb{D}_h\right). \tag{3.110}$$

We will define precise basis functions that we will use in finite-dimensional versions of the variational problems for the modified boundary integral operators. These basis functions will be defined by slightly modifying those from Subsection 1.6.2.

Definition 3.2.4 (Basis functions for the boundary element spaces)**.** *We denote the standard zeroth and first order finite element basis functions for the previously defined finite dimensional spaces as follows.*

Let $i \in \{1...N_V\}$ index the vertices of mesh $\mathcal{T}_h$, and its associated piece-wise polygonal element $L_i \in \widetilde{\mathcal{T}}_h$.

$$\text{For } i \in \{1...N_V\}, \text{ we define } \kappa_i(\boldsymbol{x}) = \begin{cases} 1 \text{ if } \boldsymbol{x} \in L_i, \\ 0 \text{ if } \boldsymbol{x} \notin L_i. \end{cases} \tag{3.111}$$

Let $i \in \{1...N_V^0\}$ index the internal vertices of mesh $\mathcal{T}_h$, and its associated piece-wise polygonal element $M_i \in \widetilde{\mathcal{T}}_h^0$.

$$\text{For } i \in \{1...N_V^0\}, \text{ we define } \kappa_i^0(\boldsymbol{x}) = \begin{cases} 1 \text{ if } \boldsymbol{x} \in M_i, \\ 0 \text{ if } \boldsymbol{x} \notin M_i. \end{cases} \tag{3.112}$$

To define the first order finite element basis functions we will consider the set of vertices of a mesh $\mathcal{T}_h$, i.e. $\{\boldsymbol{v}_i\}_{i=1}^{N_V}$. Let $i \in \{1...N_V\}$ index the vertices of mesh $\mathcal{T}_h$.

$$\text{For } i \in \{1...N_V\}, \text{ we define } \chi_i \in V_h(\mathbb{D}_h) \text{ such that } \chi_i(\boldsymbol{v}_j) = \begin{cases} 1 \text{ if } i = j, \\ 0 \text{ if } i \neq j, \end{cases} \text{ for } j = 1...N_V. \tag{3.113}$$

We will use the superscript 0 in χ_i^0, to emphasize the case when a function χ_i cannot be associated with a vertex on the boundary of $\mathbb{D}_h$ in the case when $\chi_i \in \widetilde{V}_h(\mathbb{D}_h)$. This will facilitate the notation when referring to basis functions of the space $\widetilde{V}_h(\mathbb{D}_h)$, signaling when a basis function belongs to this space.

For piecewise affine functions χ_i or χ_i^0 we will denote their restriction to a triangle t_m as $\chi_i^{t_m}(\boldsymbol{x}) = a_i^m x_1 + b_i^m x_2 + c_i^m$. We will write $t_m \ni \boldsymbol{v}_i$ to mean that the triangle t_m has $\boldsymbol{v}_i$ as one of its vertices.

Remark 3.2.1 (Dimension matching of the boundary element spaces)**.** *Constructed like this, the defined finite-dimensional spaces are subspaces of the relevant Sobolev trace spaces associated with operators $\mathcal{S}$ and $\mathcal{N}$, and they also comply with the dimension matching requirement from Theorem 2.1.1:*

$$\dim\left(\widetilde{W}_h(\mathbb{D}_h)\right) = \dim\left(V_h(\mathbb{D}_h)\right) = N_V, \tag{3.114}$$

$$\dim\left(\widetilde{V}_h(\mathbb{D}_h)\right) = \dim\left(W_h(\mathbb{D}_h)\right) = N_V^0. \tag{3.115}$$

3.2.4 Finite-dimensional variational problems

Using the defined boundary element spaces, we will specify finite-dimensional versions to the variational problems from Definition 3.1.5 associated with the modified boundary integral operators. We will use these finite-variational problems in the construction of Galerkin matrices that will be used in solving boundary integral equations for the modified operators, and later in preconditioning methods.

Given a particular conformal triangular approximation $\mathbb{D}_h$ of $\mathbb{D}$, we will consider the following expressions for functions in the boundary element spaces.

Definition 3.2.5 (Representation of functions in the boundary element spaces)**.** *A function $\lambda_h \in \widetilde{W}_h(\mathbb{D}_h)$ will be expressed as*

$$\lambda_h(\boldsymbol{x}) = \sum_{i=1}^{N_V} \lambda_i^h \kappa_i(\boldsymbol{x}), \quad \text{for } \boldsymbol{x} \in \mathbb{D}_h. \tag{3.116}$$

A function $g_h \in V_h(\mathbb{D}_h)$ will be expressed as

$$g_h(\boldsymbol{x}) = \sum_{i=1}^{N_V} g_i^h \chi_i(\boldsymbol{x}), \quad \text{for } \boldsymbol{x} \in \mathbb{D}_h. \tag{3.117}$$

A function $\mu_h \in \widetilde{V}_h(\mathbb{D}_h)$ will be expressed as

$$\mu_h(\boldsymbol{x}) = \sum_{i=1}^{N_V^0} \mu_i^h \chi_i^0(\boldsymbol{x}), \quad \text{for } \boldsymbol{x} \in \mathbb{D}_h. \tag{3.118}$$

A function $\varphi_h \in W_h(\mathbb{D}_h)$ will be expressed as

$$\varphi_h(\boldsymbol{x}) = \sum_{i=1}^{N_V^0} \varphi_i^h \kappa_i^0(\boldsymbol{x}), \qquad \textit{for } \boldsymbol{x} \in \mathbb{D}_h. \tag{3.119}$$

Definition 3.2.6 (Finite-dimensional variational problems)**.** *We will adapt the variational problems from Definition 3.1.5 using finite-dimensional variational problems as follows. A variational problem for the boundary integral equation associated with the boundary integral operator $\widetilde{\mathcal{L}}_s^{ws}$ is*

$$\left(\widetilde{\mathcal{L}}_s^{ws}\text{–}VF_h\right) \begin{cases} \textit{Given } g_h \in V_h(\mathbb{D}_h), \textit{ find } \left\{\lambda_i^h\right\}_{i=1}^{N_V}, \textit{ such that} \\ \\ \sum\limits_{i=1}^{N_V} \lambda_i^h \, \widetilde{a}_s^{ws}(\kappa_i, \kappa_j) = \sum\limits_{k=1}^{N_V} g_k^h \left\langle \chi_k, \kappa_j \right\rangle_{\mathbb{D}_h}, \textit{ for } j = 1...N_V. \end{cases} \tag{3.120}$$

The boundary integral equation associated with the boundary integral operator $\widetilde{\mathcal{L}}_s^{hs}$ admits the variational problem

$$\left(\widetilde{\mathcal{L}}_s^{hs}\text{–}VF_h\right) \begin{cases} \textit{Given } \lambda_h \in \widetilde{W}_h(\mathbb{D}_h), \textit{ find } \left\{g_i^h\right\}_{i=1}^{N_V}, \textit{ such that} \\ \\ \sum\limits_{i=1}^{N_V} g_i^h \, \widetilde{b}_s^{hs}(\chi_i, \chi_j) = \sum\limits_{k=1}^{N_V} \lambda_k^h \left\langle \kappa_k, \chi_j \right\rangle_{\mathbb{D}_h}, \textit{ for } j = 1...N_V. \end{cases} \tag{3.121}$$

The boundary integral equation associated with the boundary integral operator $\widetilde{\mathcal{L}}_{as}^{hs}$ admits the variational problem

$$\left(\widetilde{\mathcal{L}}_{as}^{hs}\text{–}VF_h\right) \begin{cases} \textit{Given } \varphi_h \in W_h(\mathbb{D}_h), \textit{ find } \left\{\mu_i^h\right\}_{i=1}^{N_V^0}, \textit{ such that} \\ \\ \sum\limits_{i=1}^{N_V^0} \mu_i^h \, \widetilde{a}_{as}^{hs}(\chi_i^0, \chi_j^0) = \sum\limits_{k=1}^{N_V} \varphi_k^h \left\langle \kappa_k^0, \chi_j^0 \right\rangle_{\mathbb{D}_h}, \textit{ for } j = 1...N_V^0. \end{cases} \tag{3.122}$$

The boundary integral equation associated with the boundary integral operator $\widetilde{\mathcal{L}}_{as}^{ws}$ admits the variational problem

$$\left(\widetilde{\mathcal{L}}_{as}^{ws}\text{–}VF_h\right) \begin{cases} \textit{Given } \mu_h \in \widetilde{V}_h(\mathbb{D}_h), \textit{ find } \left\{\varphi_i^h\right\}_{i=1}^{N_V^0}, \textit{ such that} \\ \\ \sum\limits_{i=1}^{N_V^0} \varphi_i^h \, \widetilde{b}_{as}^{ws}(\kappa_i^0, \kappa_j^0) = \sum\limits_{k=1}^{N_V^0} \mu_k^h \left\langle \chi_k^0, \kappa_j^0 \right\rangle_{\mathbb{D}_h}, \textit{ for } j = 1...N_V^0. \end{cases} \tag{3.123}$$

In these variational problems we have kept the symbols of the bilinear forms from Definition 3.1.3, abusing the notation, but they represent here bilinear forms induced by the corresponding modified operators over the new domain on integration $\mathbb{D}_h$.

3.2.5 Boundary element computations

In this subsection we will describe how to compute numerically the bilinear forms associated with the previous finite-dimensional variational problems for the corresponding basis functions. Let us first establish the key numerical tool underlying all other boundary integral computations.

Remark 3.2.2 (Integrating K^{ws} over pairs of arbitrary triangles)**.** *The main tool behind the numerical computation of the bilinear forms associated with the four finite-dimensional variational problems from Definition 3.2.6 is the integration of the kernel K^{ws} over any two pairs of triangles, denoted here as k_1 and k_2, in $\mathbb{R}^3$:*

$$\int_{k_1}\int_{k_2} K^{ws}(\boldsymbol{x},\boldsymbol{y})dk_1(\boldsymbol{x})dk_2(\boldsymbol{y}) = \int_{k_1}\int_{k_2} \frac{dk_1(\boldsymbol{x})dk_2(\boldsymbol{y})}{4\pi\left\|\boldsymbol{x}-\boldsymbol{y}\right\|}. \tag{3.124}$$

This integral is computed using a 6 point Gauss-Lobatto quadrature scheme when triangles k_1 and k_2 are separated. If the triangles are adjacent (or if they are the same triangle) the integral is computed analytically as described in [34, Annex D.12] and [11]. Later in this subsection, triangles k_1 and/or k_2 from (3.124) will be triangles t in $\mathcal{T}_h$, sub-triangles of type $\hat{t}$, or sub-triangles of type $\tilde{t}$ (refer to Definition 1.6.3). This will be useful when integrating over pairs piece-wise polygonal elements in $\widetilde{\mathcal{T}}_h$ or $\widetilde{\mathcal{T}}_h^0$.

We will now proceed to specify the way in which the numerical computation of the bilinear forms will be performed. For integrations over piece-wise polygonal elements, we will follow Notation 3.2.1 and denote $k \in L_i$ the fact that a sub-triangle k is one of the sub-triangles that constitute a piece-wise polygonal element $L_i \in \widetilde{\mathcal{T}}_h$. In this case, sub-triangles k can only be of type $\hat{t}$. We will use the same notation, denoting by $k \in M_i$ the fact that a sub-triangle k is one the sub-triangles that constitute a piece-wise polygonal element $M_i \in \widetilde{\mathcal{T}}_h^0$. In this case, sub-triangles k can either be of type $\hat{t}$, $\tilde{t}$ or even t (refer to Definition 1.6.3). For couples of identified sub-triangles k_m and k_n, or their projections onto the upper or lower half-spheres, the integration of K^{ws} can be performed as indicated by the previous remark, i.e. Remark 3.2.2.

Notation 3.2.2 (Projected triangles)**.** *For any given triangle k with vertices on $\mathbb{D}_h$, we will denote by $k^{\pm}$ its projection into the upper o lower projected domains $\mathbb{S}_h^{\pm}$.*

Proposition 3.2.1 (Computation of bilinear variational forms associated with $\widetilde{\mathcal{L}}_s^{ws}$ and $\widetilde{\mathcal{L}}_{as}^{ws}$)**.** *The values of the bilinear forms associated with the weakly singular integral operators $\widetilde{\mathcal{L}}_s^{ws}$ and $\widetilde{\mathcal{L}}_{as}^{ws}$ for the piecewise constant basis functions are:*

$$\widetilde{a}_s^{ws}(\kappa_i,\kappa_j) = \int_{L_i}\int_{L_j} K^{ws}\left(\boldsymbol{x}^+,\boldsymbol{y}^+\right) dL_i(\boldsymbol{x})dL_j(\boldsymbol{y}) + \int_{L_i}\int_{L_j} K^{ws}\left(\boldsymbol{x}^-,\boldsymbol{y}^+\right) dL_i(\boldsymbol{x})dL_j(\boldsymbol{y}), \tag{3.125}$$

$$\widetilde{b}_{as}^{ws}(\kappa_i^0,\kappa_j^0) = \int_{M_i}\int_{M_j} K^{ws}\left(\boldsymbol{x}^+,\boldsymbol{y}^+\right) dM_i(\boldsymbol{x})dM_j(\boldsymbol{y}) - \int_{M_i}\int_{M_j} K^{ws}\left(\boldsymbol{x}^-,\boldsymbol{y}^+\right) dM_i(\boldsymbol{x})dM_j(\boldsymbol{y}). \tag{3.126}$$

Proof This comes easily from considering the bounded support of elements L_i and M_i and the definition of the bilinear forms in Definition 3.1.3. ∎

Notation 3.2.3 (Components of unit vector normal to a triangle)**.** *Given a triangle k in $\mathbb{R}^3$ we will denote by $\boldsymbol{n}^k$ its unit normal vector, and by $\boldsymbol{n}_i^k$, for $i = 1,2,3$, its coordinates.*

Definition 3.2.7 (Approximation of elementary integrals of K^{ws} over piece-wise polygonal elements)**.** *We will use the following approximations, signaled by $\approx$, for the integration of the weakly singular kernel with projected arguments:*

$$\int_{L_i}\int_{L_j} K^{ws}\left(\boldsymbol{x}^{\pm},\boldsymbol{y}^+\right) dL_i(\boldsymbol{x})dL_j(\boldsymbol{y}) \approx \sum_{k_m\subset L_i}\sum_{k_n\subset L_j} \left|\boldsymbol{n}_3^{k_m^{\pm}}\boldsymbol{n}_3^{k_n^+}\right| \int_{k_m^{\pm}}\int_{k_n^+} K^{ws}\left(\boldsymbol{x},\boldsymbol{y}\right) dk_m^{\pm}(\boldsymbol{x})dk_n^+(\boldsymbol{y}), \tag{3.127}$$

$$\int_{M_i}\int_{M_j} K^{ws}\left(\boldsymbol{x}^{\pm},\boldsymbol{y}^+\right) dM_i(\boldsymbol{x})dM_j(\boldsymbol{y}) \approx \sum_{k_m\subset M_i}\sum_{k_n\subset M_j} \left|\boldsymbol{n}_3^{k_m^{\pm}}\boldsymbol{n}_3^{k_n^+}\right| \int_{k_m^{\pm}}\int_{k_n^+} K^{ws}\left(\boldsymbol{x},\boldsymbol{y}\right) dk_m^{\pm}(\boldsymbol{x})dk_n^+(\boldsymbol{y}). \tag{3.128}$$

Proposition 3.2.2 (Computation of bilinear variational forms associated with $\widetilde{\mathcal{L}}_s^{hs}$ and $\widetilde{\mathcal{L}}_{as}^{hs}$)**.** *The values of the bilinear forms associated with the hypersingular integral operators $\widetilde{\mathcal{L}}_s^{hs}$ and $\widetilde{\mathcal{L}}_{as}^{hs}$ for the piecewise affine basis functions are:*

$$\widetilde{a}_{as}^{hs}(\chi_i^0,\chi_j^0) = \left\langle \widetilde{\mathcal{L}}_s^{ws}\overrightarrow{curl}_{\mathbb{D}_h}\chi_i^0, \overrightarrow{curl}\chi_j^0\right\rangle_{\mathbb{D}_h} + \left\langle \widetilde{\mathcal{L}}_{as}^{ws}\left(\frac{1}{w}\frac{\partial\chi_i^0}{\partial\phi_{\boldsymbol{x}}}\right), \frac{1}{w}\frac{\partial\chi_j^0}{\partial\phi_{\boldsymbol{y}}}\right\rangle_{\mathbb{D}_h}, \tag{3.129}$$

$$\widetilde{b}_s^{hs}(\chi_i,\chi_j)=\left\langle \widetilde{\mathcal{L}}_{as}^{ws}\overrightarrow{curl}_{\mathbb{D}_h}\chi_i,\overrightarrow{curl}_{\mathbb{D}_h}\chi_j\right\rangle_{\mathbb{D}_h}+\left\langle \widetilde{\mathcal{L}}_{s}^{ws}\left(\frac{1}{w}\frac{\partial\chi_i}{\partial\phi_{\boldsymbol{x}}}\right),\frac{1}{w}\frac{\partial\chi_j}{\partial\phi_{\boldsymbol{y}}}\right\rangle_{\mathbb{D}_h}. \tag{3.130}$$

Proof This follows straightforwardly from the definition of the bilinear forms. ∎

Definition 3.2.8 (Approximation of the elementary integrals for affine functions over triangles)**.** *We will approximate the integrals involved in the previous proposition. The first dual product of the bilinear forms (3.129) and (3.130) will be computed as:*

$$\left\langle \widetilde{\mathcal{L}}_{s/as}^{ws}\overrightarrow{curl}_{\mathbb{D}}\chi_i,\overrightarrow{curl}\chi_j\right\rangle_{\mathbb{D}_h}=\sum_{t_m\in T_{\boldsymbol{v}\to t}(\boldsymbol{v}_i)}\sum_{t_n\in T_{\boldsymbol{v}\to t}(\boldsymbol{v}_j)}\left\langle \widetilde{\mathcal{L}}_{s/as}^{ws}\overrightarrow{curl}_{\mathbb{D}_h}\chi_i^{t_m},\overrightarrow{curl}_{\mathbb{D}_h}\chi_j^{t_n}\right\rangle_{\mathbb{D}_h}, \tag{3.131}$$

with

$$\begin{aligned}\left\langle \widetilde{\mathcal{L}}_{s/as}^{ws}\overrightarrow{curl}_{\mathbb{D}_h}\chi_i^{t_m},\overrightarrow{curl}_{\mathbb{D}_h}\chi_j^{t_n}\right\rangle_{\mathbb{D}_h}&=\left(a_i^m a_j^n+b_i^m b_j^n\right)\int_{t_m}\int_{t_n}K^{ws}(\boldsymbol{x}^+,\boldsymbol{y}^+)dt_m(\boldsymbol{x})dt_n(\boldsymbol{y})\\&\pm\left(a_i^m a_j^n+b_i^m b_j^n\right)\int_{t_m}\int_{t_n}K^{ws}(\boldsymbol{x}^-,\boldsymbol{y}^+)dt_m(\boldsymbol{x})dt_n(\boldsymbol{y}),\end{aligned} \tag{3.132}$$

and

$$\int_{t_m}\int_{t_n}K^{ws}(\boldsymbol{x}^\pm,\boldsymbol{y}^+)dt_m(\boldsymbol{x})dt_n(\boldsymbol{y})\approx\left|\boldsymbol{n}_3^{t_m^\pm}\boldsymbol{n}_3^{t_n^+}\right|\int_{t_m^\pm}\int_{t_n^+}K^{ws}(\boldsymbol{x},\boldsymbol{y})dt_m^\pm(\boldsymbol{x})dt_n^+(\boldsymbol{y}). \tag{3.133}$$

Let us first define function F_w for points $\boldsymbol{x},\boldsymbol{y}\in\mathbb{D}_h$, triangles m and n, and vertices i and j of $\mathcal{T}_h$:

$$F_w(\boldsymbol{x},\boldsymbol{y},m,n,i,j)=\frac{1}{w(\boldsymbol{x})w(\boldsymbol{y})}\left[\boldsymbol{x}\cdot\begin{pmatrix}b_i^m\\-a_i^m\end{pmatrix}\right]\left[\boldsymbol{y}\cdot\begin{pmatrix}b_j^n\\-a_j^n\end{pmatrix}\right], \tag{3.134}$$

where a_i^m, b_i^m, a_j^n, and b_j^n are defined in Definition 3.2.4.

The second dual product of the bilinear forms (3.129) and (3.130) will be computed as:

$$\left\langle \widetilde{\mathcal{L}}_{s/as}^{ws}\left(\frac{1}{w}\frac{\partial\chi_i}{\partial\phi_{\boldsymbol{x}}}\right),\frac{1}{w}\frac{\partial\chi_j}{\partial\phi_{\boldsymbol{y}}}\right\rangle_{\mathbb{D}_h}=\sum_{t_m\in T_{\boldsymbol{v}\to t}(\boldsymbol{v}_i)}\sum_{t_n\in T_{\boldsymbol{v}\to t}(\boldsymbol{v}_j)}\left\langle \widetilde{\mathcal{L}}_{s/as}^{ws}\left(\frac{1}{w}\frac{\partial\chi_i^{t_m}}{\partial\phi_{\boldsymbol{x}}}\right),\frac{1}{w}\frac{\partial\chi_j^{t_n}}{\partial\phi_{\boldsymbol{y}}}\right\rangle_{\mathbb{D}_h}, \tag{3.135}$$

with

$$\begin{aligned}\left\langle \widetilde{\mathcal{L}}_{s/as}^{ws}\left(\frac{1}{w}\frac{\partial\chi_i^{t_m}}{\partial\phi_{\boldsymbol{x}}}\right),\frac{1}{w}\frac{\partial\chi_j^{t_n}}{\partial\phi_{\boldsymbol{y}}}\right\rangle_{\mathbb{D}_h}&=\int_{t_m}\int_{t_n}K^{ws}(\boldsymbol{x}^+,\boldsymbol{y}^+)F_w(\boldsymbol{x},\boldsymbol{y},m,n)dt_m(\boldsymbol{x})dt_n(\boldsymbol{y})\\&\pm\int_{t_m}\int_{t_n}K^{ws}(\boldsymbol{x}^-,\boldsymbol{y}^+)F_w(\boldsymbol{x},\boldsymbol{y},m,n)dt_m(\boldsymbol{x})dt_n(\boldsymbol{y}),\end{aligned} \tag{3.136}$$

and

$$\int_{t_m}\int_{t_n}K^{ws}(\boldsymbol{x}^\pm,\boldsymbol{y}^+)F_w(\boldsymbol{x},\boldsymbol{y},m,n)dt_m(\boldsymbol{x})dt_n(\boldsymbol{y})\approx F(\boldsymbol{r}_c^m,\boldsymbol{r}_c^n,m,n,i,j)\int_{t_m}\int_{t_n}K^{ws}(\boldsymbol{x}^\pm,\boldsymbol{y}^+)dt_m(\boldsymbol{x})dt_n(\boldsymbol{y}), \tag{3.137}$$

where $\boldsymbol{r}_c^m$ and $\boldsymbol{r}_c^n$ are the centroids of triangles t_m and t_n.

3.2.6 Galerkin matrices

Using the previously defined boundary element computations we will proceed to define the construction of the Galerkin matrices associated with the new modified boundary integral equations.

Definition 3.2.9 (Galerkin matrices associated with the new modified operators)**.** *We will define the Galerkin matrices associated with the bilinear forms described in this section. These matrices will be used in the resolution of boundary integral equations associated with the proposed operators for testing purposes and later in preconditioning methods. We define* $\boldsymbol{S}_s^h \in \mathbb{C}^{N_V \times N_V}$ *as*

$$\boldsymbol{S}_s^h[i,j] = \widetilde{a}_s^{ws}(\kappa_i, \kappa_j), \quad \text{for } i,j = 1...N_V. \tag{3.138}$$

We define $\boldsymbol{S}_{as}^h \in \mathbb{C}^{N_V^0 \times N_V^0}$ *as*

$$\boldsymbol{S}_{as}^h[i,j] = \widetilde{a}_{as}^{ws}(\kappa_i^0, \kappa_j^0), \quad \text{for } i,j = 1...N_V^0. \tag{3.139}$$

We define $\boldsymbol{N}_s^h \in \mathbb{C}^{N_V \times N_V}$ *as*

$$\boldsymbol{N}_s^h[i,j] = \widetilde{a}_s^{hs}(\chi_i, \chi_j) + \alpha \left\langle \chi_i \, , \, \chi_j \right\rangle_{\mathbb{D}_h}, \quad \text{for } i,j = 1...N_V. \tag{3.140}$$

We define $\boldsymbol{N}_{as}^h \in \mathbb{C}^{N_V^0 \times N_V^0}$ *as*

$$\boldsymbol{N}_{as}^h[i,j] = \widetilde{a}_{as}^{hs}(\chi_i^0, \chi_j^0), \quad \text{for } i,j = 1...N_V^0. \tag{3.141}$$

The variational problem associated with $\widetilde{\mathcal{L}}_s^{hs}$ *is being modified in (3.140), augmented with a parameter* $\alpha \in \mathbb{R}^+$ *to eliminate the kernel space. It becomes evident from (3.61) in Proposition 3.1.3 that the modified integral operator* $\widetilde{\mathcal{L}}_s^{hs}$ *has the constant functions on* $\mathbb{D}_h$ *as kernel space (since they can be spanned by function* y_0^0*, and* $l = 0 \Rightarrow \eta_l = 0$*).*

Remark 3.2.3 (Computational implementation)**.** *The variational problems, as well as all the following computational experiments regarding preconditioning, have been implemented using several computational languages and libraries. The main programs were implemented using* C++ *along the style of [17]. Core routines for the integration of* K^{ws} *for any two triangles in* $\mathbb{R}^3$ *have been coded in FORTRAN, though accessed from* C++*, from slight modifications of the code explained in [34]. Scientific computing libraries such as LAPACK [6] and EIGEN [27] were used to perform matrix operations and condition number computations. BOOST scientific library for* C++ *was used for the computation of values of special functions (*Γ *function and Spherical Harmonics) [1]. Conformal mesh approximation of the surfaces* $\mathbb{D}$*,* $\mathbb{S}$ *and* $\mathbb{S}^+$ *(and other geometries to be exhibited in the nest subsections) were done using Gmsh [21].*

3.2.7 Benchmarks

In this subsection we will test the numerical implementation of the Galerkin matrices arising from the variational problem using the described discretization and boundary element computations. By solving boundary integral equations associated with the new modified boundary integral operators for given data we can compare the computed results with the known solutions. Using Proposition 3.1.3, boundary integral equations with known exact solutions can be considered for each one of the four modified boundary integral operators on the disk. Approximations λ^h, μ^h, g^h and φ^h can then be computed with the finite-dimensional variational problem from Definition 3.2.6 using the described boundary element computations. Table 3.2 shows four boundary integral equations for given data, each one associated with one of the new modified boundary integral operators on the disk, and their known exact solutions (as given by Proposition 3.1.3). We will exhibit the of error of the computed solutions for the boundary integral equations on Table 3.2, in order to show that the proposed numerical method is valid, despite not having *a priori* error estimations.

Table 3.2: Boundary integral equations for the modified integral operators to be used as benchmark cases.

Variational Problem	Integral Equation	Exact Solution	Computed Solution
$\widetilde{\mathcal{L}}_s^{ws}$–$VF_h$	$\widetilde{\mathcal{L}}_s^{ws}\lambda = \frac{y_1^1}{3}$	$\lambda = \frac{y_1^1}{w}$	λ_h
$\widetilde{\mathcal{L}}_{as}^{ws}$–$VF_h$	$\widetilde{\mathcal{L}}_{as}^{ws}\varphi = \frac{y_2^1}{5}$	$\varphi = \frac{y_2^1}{w}$	φ_h
$\widetilde{\mathcal{L}}_s^{hs}$–$VF_h$	$\widetilde{\mathcal{L}}_s^{hs} g = -\frac{2y_1^1}{3w}$	$g = y_1^1$	g_h
$\widetilde{\mathcal{L}}_{as}^{hs}$–$VF_h$	$\widetilde{\mathcal{L}}_{as}^{hs}\mu = -\frac{6y_1^1}{7w}$	$\mu = y_2^1$	μ_h

We will be interested in the convergence of the relative error by which the computed solutions approximate the exact ones. In what follows, we will show this relative error convergence using the Sobolev norms, for which an expression was established in Proposition 2.7.16, and using the norms induced by the modified boundary integral operators in Definition 3.1.4.

Relative error convergence in Sobolev norms

Let us consider the four boundary integral equations and their variational problems from Table 3.2. We will be interested in the convergence of the associated relative error in Sobolev norms, as it will be summarized in Table 3.3

Table 3.3: Sobolev norms relative errors for the boundary integral equations for the modified integral operators.

Variational Problem	Exact Solution	Computed Solution	Relative Error
$\widetilde{\mathcal{L}}_s^{ws}$–$VF_h$	λ	λ_h	$\frac{\|\lambda - \lambda_h\|_{a_s^{ws}}}{\|\lambda\|_{a_s^{ws}}}$
$\widetilde{\mathcal{L}}_{as}^{ws}$–$VF_h$	φ	φ_h	$\frac{\|\varphi - \varphi_h\|_{b_{as}^{ws}}}{\|\varphi\|_{b_{as}^{ws}}}$
$\widetilde{\mathcal{L}}_s^{hs}$–$VF_h$	g	g_h	$\frac{\|g - g_g\|_{b_s^{hs}}}{\|g\|_{b_s^{hs}}}$
$\widetilde{\mathcal{L}}_{as}^{hs}$–$VF_h$	μ	μ_h	$\frac{\|\mu - \mu_h\|_{a_{as}^{hs}}}{\|\mu\|_{a_{as}^{hs}}}$

In the following figures, Figure 3.6, 3.7 & 3.8 (for the three types of mesh sets described in Table 3.1), we will show the convergence of the relative error of the computed solutions from Table 3.2 & 3.3 for the different variational problems for different mesh refinements measured by the discretization parameter h of $\mathbb{D}_h$.

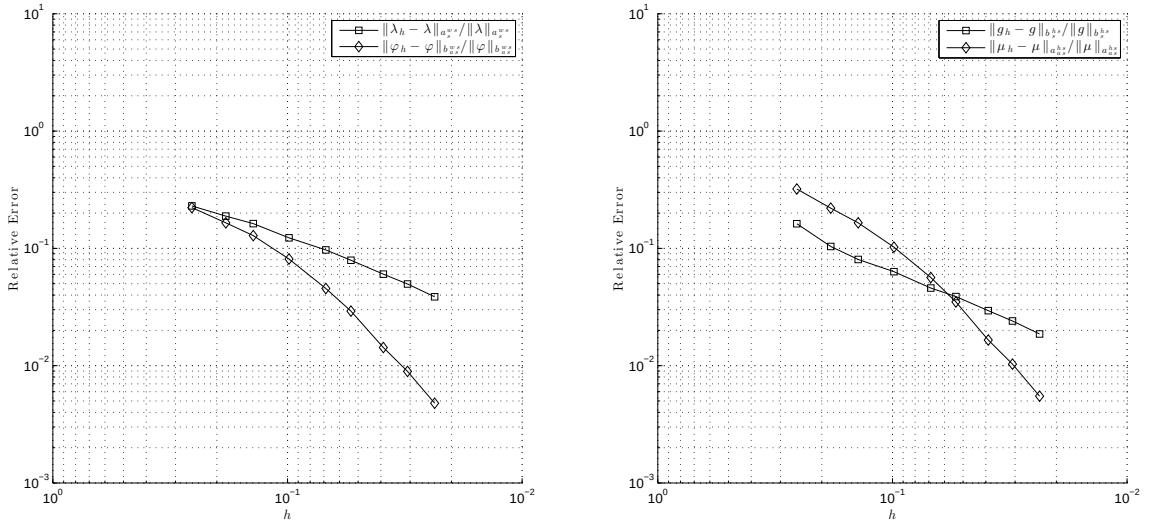

Figure 3.6: Convergence of the relative error in Sobolev norms between the exact solutions and the computed solutions described in Table 3.2 using a mesh set of type **Mesh set** #1 with mesh refinement parameter h of $\mathbb{D}_h$

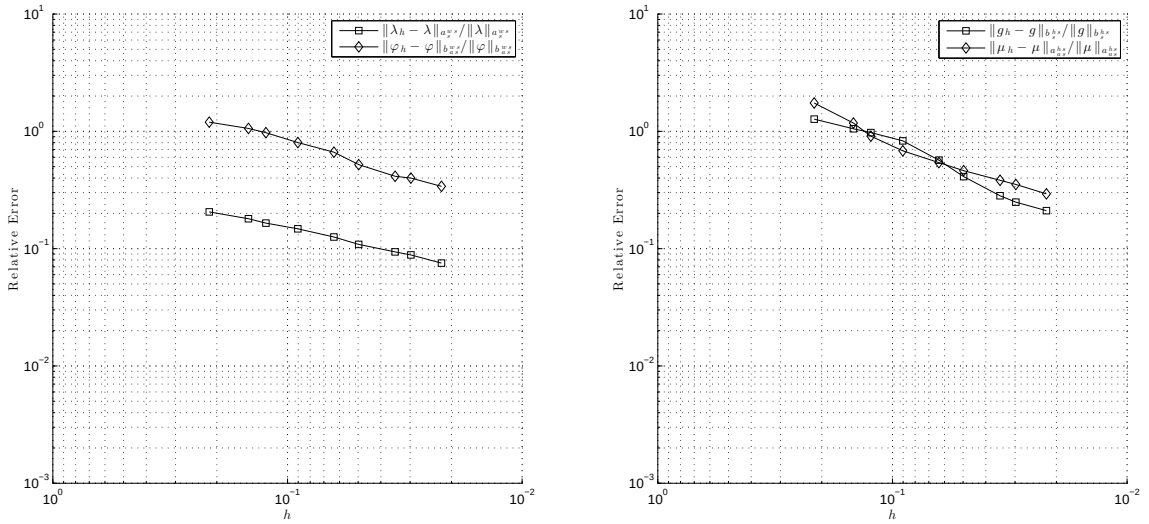

Figure 3.7: Convergence of the relative error in Sobolev norms between the exact solutions and the computed solutions described in Table 3.2 using a mesh set of type **Mesh set** #2 with mesh refinement parameter h of $\mathbb{D}_h$

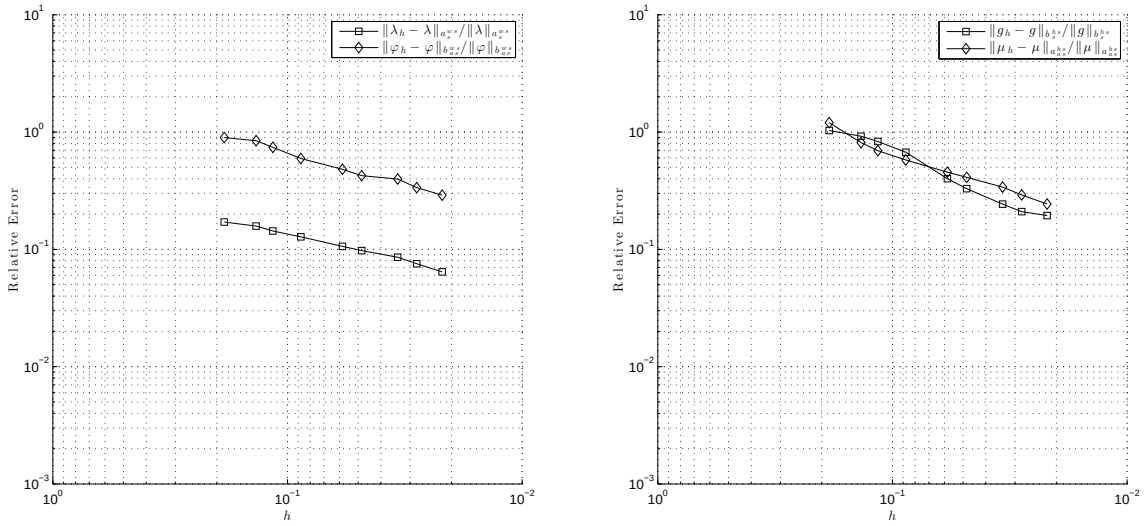

Figure 3.8: Convergence of the relative error in Sobolev norms between the exact solutions and the computed solutions described in Table 3.2 using a mesh set of type **Mesh set** #3 with mesh refinement parameter h of $\mathbb{D}_h$

Relative error convergence in modified norms

Let us consider the four boundary integral equations and their variational problems from Table 3.2. We will be interested in the convergence of the associated relative error in the norms induced be the modified integral operators, as it will be summarized in Table 3.4

Table 3.4: Modified norms relative errors for the boundary integral equations for the modified integral operators..

Variational Problem	Exact Solution	Computed Solution	Relative Error
$\widetilde{\mathcal{L}}_s^{ws}$–$VF_h$	λ	λ_h	$\frac{\|\lambda-\lambda_h\|_{\widetilde{a}_s^{ws}}}{\|\lambda\|_{\widetilde{a}_s^{ws}}}$
$\widetilde{\mathcal{L}}_{as}^{ws}$–$VF_h$	φ	φ_h	$\frac{\|\varphi-\varphi_h\|_{\widetilde{b}_{as}^{ws}}}{\|\varphi\|_{\widetilde{b}_{as}^{ws}}}$
$\widetilde{\mathcal{L}}_s^{hs}$–$VF_h$	g	g_h	$\frac{\|g-g_g\|_{\widetilde{b}_s^{hs}}}{\|g\|_{\widetilde{b}_s^{hs}}}$
$\widetilde{\mathcal{L}}_{as}^{hs}$–$VF_h$	μ	μ_h	$\frac{\|\mu-\mu_h\|_{\widetilde{a}_{as}^{hs}}}{\|\mu\|_{\widetilde{a}_s^{hs}}}$

In the following figures, Figure 3.9, 3.10 & 3.11 (for the three types of mesh sets described in Table 3.1) , we will show the convergence of the relative error of the computed solutions from Table 3.2 & 3.4 for the different variational problems for different mesh refinements measured by the discretization parameters h of $\mathbb{D}_h$.

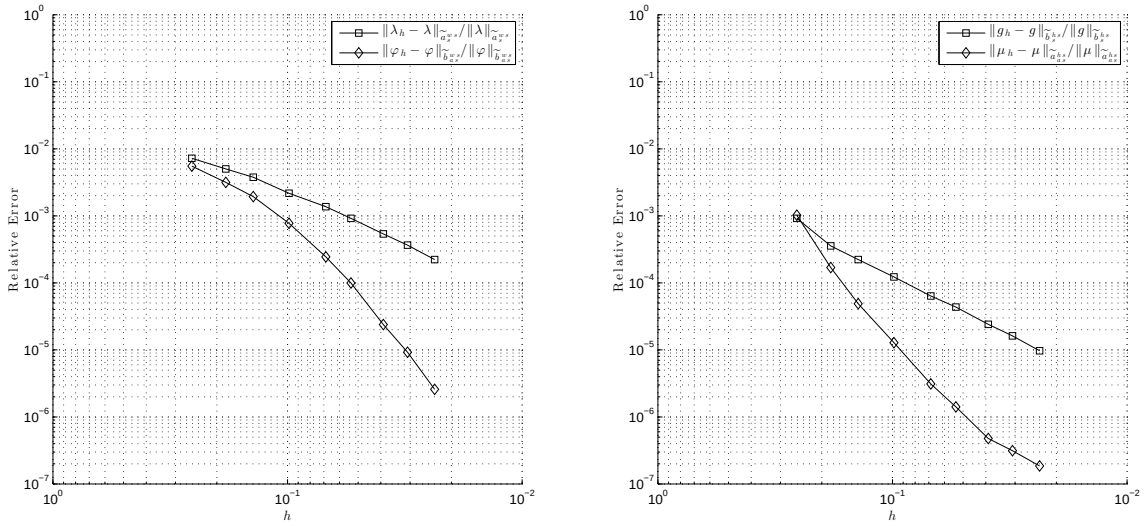

Figure 3.9: Convergence of the relative error in modified norms between the exact solutions and the computed solutions described in Table 3.2 using a mesh set of type **Mesh set** #1 with mesh refinement parameter h of $\mathbb{D}_h$

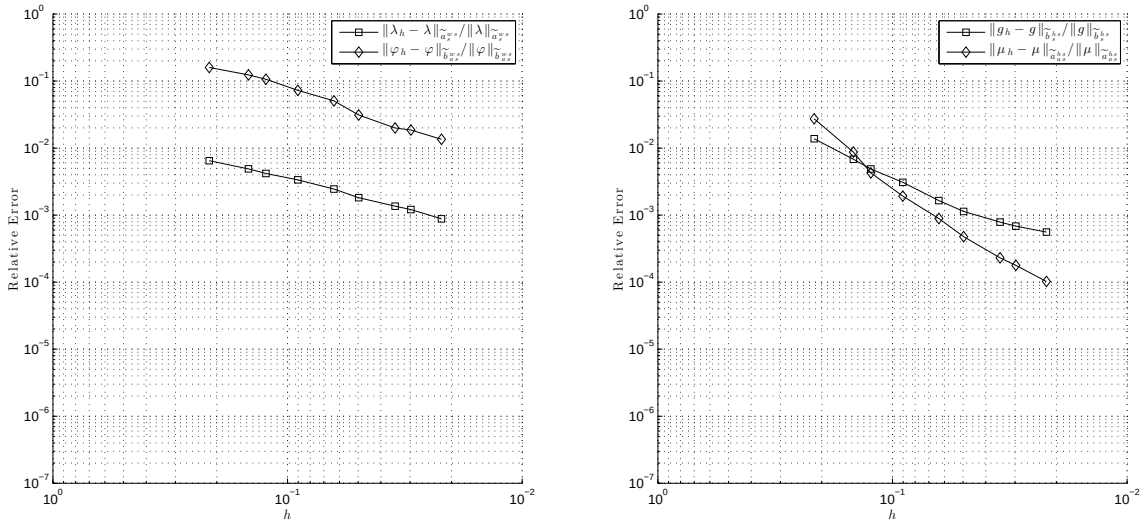

Figure 3.10: Convergence of the relative error in modified norms between the exact solutions and the computed solutions described in Table 3.2 using a mesh set of type **Mesh set** #2 with mesh refinement parameter h of $\mathbb{D}_h$

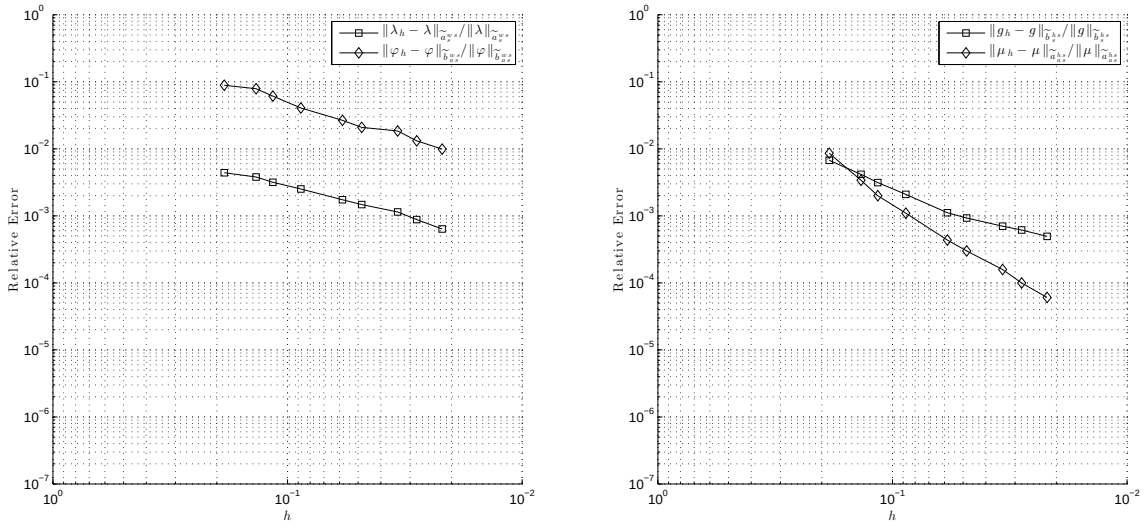

Figure 3.11: Convergence of the relative error in modified norms between the exact solutions and the computed solutions described in Table 3.2 using a mesh set of type **Mesh set** #3 with mesh refinement parameter h of $\mathbb{D}_h$

Validation of the numerical method

Remark 3.2.4 (*A posteriori* validation of the numerical implementation)**.** *Figures 3.6, 3.7 & 3.8, and Figures 3.9, 3.10 & 3.11 show the a posteriori error convergence, strongly suggesting the validity of the mesh partition process and the boundary element computations.*

Remark 3.2.5 (Variational problems allow for the resolution of boundary integral equations for disk basis function data)**.** *These results also suggest that the variational problems from Definition 3.1.5 are adequate in that, even if the bilinear forms are not assured to be coercive for the relevant trace spaces indicated for them (relevant for the symmetric Dirichlet and anti-symmetric Neumann problems, i.e., $\widetilde{H}^{1/2}(\mathbb{D})$, $H^{-1/2}(\mathbb{D})$, $\widetilde{H}^{-1/2}(\mathbb{D})$, and $H^{1/2}(\mathbb{D})$). They are coercive in some spaces spanned by the disk basis functions and where the bilinear forms can induce coercive bilinear forms (Definition 3.1.4), and where boundary integral equations for the modified operators can be correctly posed using right-hand side data from the set of basis functions.*

3.3 Preconditioning

In the previous section it was argued that the boundary element implementation for the bilinear forms induced by the modified boundary integral operators was correct in the sense that their Galerkin matrices correctly represent their associated variational problems, providing solutions of diminishing relative error to the associated boundary integral equations of known solutions. In this section we will study these Galerkin matrices in their use as preconditioners. We will first describe the construction of the preconditioning matrices following the strategy from Definition 2.1.1 outlined by Theorem 2.1.1, but using the modified boundary integral operators.

In a first part of this section we will study the mutual preconditioning effect of the Galerkin matrices from Definition 3.2.9. In order to do so, we will build the bases' duality pairing matrix $\boldsymbol{D}$ from Theorem 2.1.1. The Galerkin matrices associated with the modified integral operators will prove to be mutual optimal preconditioners. This will provide us with relevant information on the stability of the duality pairing of the basis from the sub-spaces of the dual spaces involved in the boundary integral equations for the disk screen. It will also allow us to extract some conclusions about the variational problems from Definition 3.1.5. In the second part of this section we will use these Galerkin matrices to precondition the matrices associated with operators $\mathcal{S}$ and $\mathcal{N}$, related to the boundary integral equations for the symmetric Dirichlet and anti-symmetric Neumann problems. In a third and fourth part we will extend the use of these preconditioners to the case of the Helmholtz equation and to other screens, modifying the weight function w.

3.3.1 Mutual preconditioning of the Galerkin matrices for the modified boundary integral operators

In order to build preconditioning matrices as outlined in the optimal preconditioning strategy from Definition 2.1.1, we will take bilinear operator d from Theorem 2.1.1 to be the duality pairing, with which we will build the bases' duality pairing matrices.

Definition 3.3.1 (Bases' duality pairing matrices)**.** *Let us consider the following matrices for a triangular mesh $\mathcal{T}_h$ for the conformal triangular approximation $\mathbb{D}_h$ of $\mathbb{D}$, with N_V vertices, of which N_V^0 are internal.*

We define $\boldsymbol{D}_D^h \in \mathbb{R}^{N_V \times N_V}$ as:

$$\boldsymbol{D}_D^h[i,j] = \langle \kappa_i \, , \, \chi_j \rangle_{\mathbb{D}_h} \, , \qquad \text{for } i,j = 1...N_V . \tag{3.142}$$

We define $\boldsymbol{D}_N^h \in \mathbb{R}^{N_V^0 \times N_V^0}$ as:

$$\boldsymbol{D}_N^h[i,j] = \left\langle \kappa_i^0 \, , \, \chi_j^0 \right\rangle_{\mathbb{D}_h} \, , \qquad \text{for } i,j = 1...N_V^0 . \tag{3.143}$$

Remark 3.3.1 (Bases duality pairing matrices are sparse)**.** *Because the chosen bases for the boundary element spaces have local support, matrices $\boldsymbol{D}_D^h$ and $\boldsymbol{D}_N^h$ will be sparse. This will result in a lower inversion complexity, when required in building preconditioning matrices, as stated in Remark 2.1.3*

We now have all the necessary elements to build the preconditioning matrices, following the optimal preconditioning strategy from Definition 2.1.1 taking the preconditioning operator to be not the exact inverses, for which we do not have an explicit variational formulation, but the modified integral operators ($\widetilde{\mathcal{L}}_s^{hs}$ and $\widetilde{\mathcal{L}}_{as}^{ws}$), for which we do.

Definition 3.3.2 (Preconditioning matrices)**.** *Let as consider matrices $\boldsymbol{N}_s^h$ and $\boldsymbol{S}_{as}^h$ from Definition 3.2.9, associated with the modified integral operators $\widetilde{\mathcal{L}}_s^{hs}$ and $\widetilde{\mathcal{L}}_{as}^{ws}$, and matrices $\boldsymbol{D}_S^h$*

and $\boldsymbol{D}_N^h$ *from Definition 3.3.1, to define the following preconditioning matrices as in Theorem 2.1.1. We define* $\boldsymbol{M}_D^h \in \mathbb{C}^{N_V \times N_V}$ *as*

$$\boldsymbol{M}_D^h = \left(\boldsymbol{D}_D^h\right)^{-1} \boldsymbol{N}_s^h \left(\boldsymbol{D}_D^h\right)^{-H}. \tag{3.144}$$

We define $\boldsymbol{M}_N^h \in \mathbb{C}^{N_V^0 \times N_V^0}$ *as*

$$\boldsymbol{M}_N^h = \left(\boldsymbol{D}_N^h\right)^{-1} \boldsymbol{S}_{as}^h \left(\boldsymbol{D}_N^h\right)^{-H}. \tag{3.145}$$

We will now consider using matrix $\boldsymbol{M}_D^h$ to precondition matrix $\boldsymbol{S}_s^h$ and matrix $\boldsymbol{M}_N^h$ to precondition matrix $\boldsymbol{N}_{as}^h$. These two matrices on which to apply the preconditioners come from the variational problems from Definition 3.1.5 and do not correspond to the variational problems from Proposition 2.7.17, which are linked to operators $\mathcal{S}$ and $\mathcal{N}$. In doing this, however, will we show some interesting properties of the variational problems stated in Definition 3.1.5, and we will extract conclusions regarding the discretization and the boundary element method proposed.

Figures 3.12, 3.13 and 3.14 will show, for the three different types of mesh sets considered, the evolution of the condition number for matrices $\boldsymbol{S}_s^h$, $\boldsymbol{S}_{as}^h$, $\boldsymbol{N}_s^h$ and $\boldsymbol{N}_{as}^h$, and that of the preconditioned matrices $\boldsymbol{M}_D^h \boldsymbol{S}_s^h$ and $\boldsymbol{M}_N^h \boldsymbol{N}_{as}^h$.

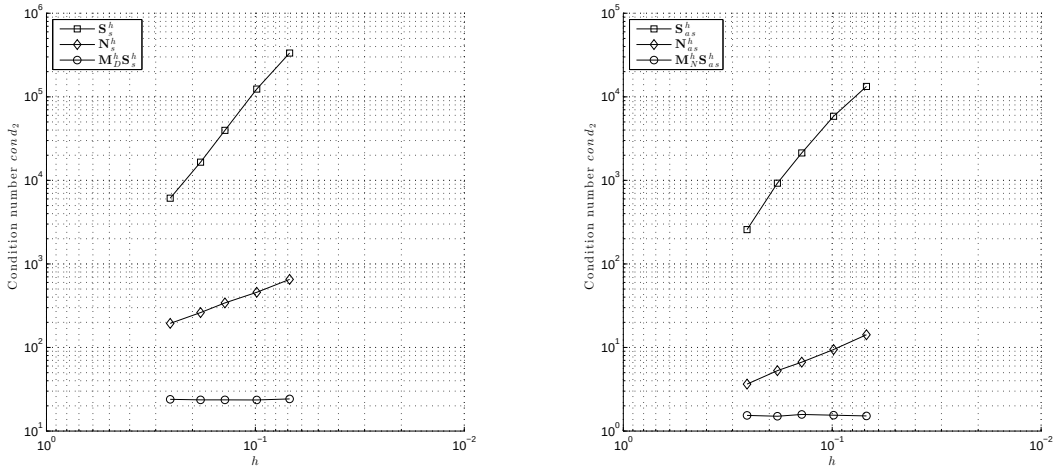

Figure 3.12: Preconditioning of matrix $\boldsymbol{S}_s^h$ by matrix $\boldsymbol{M}_D^h$ (left) and matrix $\boldsymbol{N}_{as}^h$ by matrix $\boldsymbol{M}_N^h$ for the mesh set of type **Mesh set** #1.

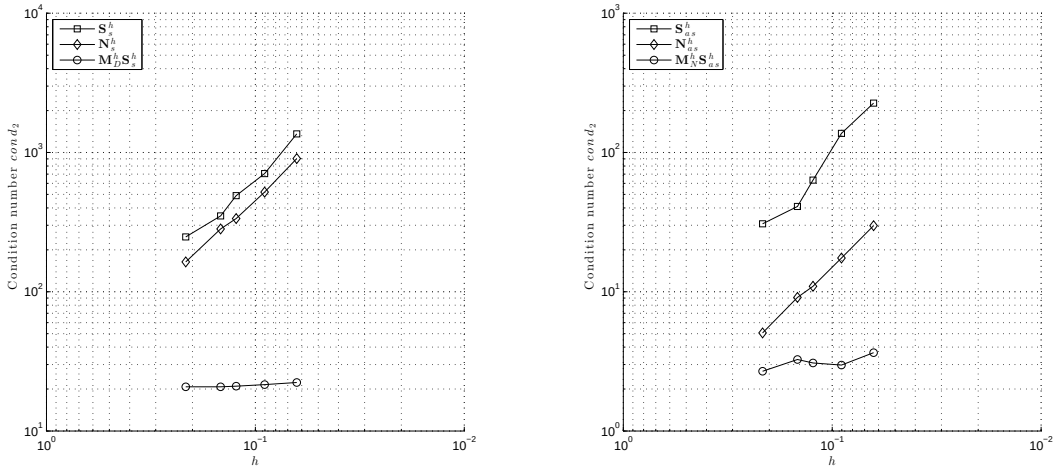

Figure 3.13: Preconditioning of matrix $\boldsymbol{S}_s^h$ by matrix $\boldsymbol{M}_D^h$ (left) and matrix $\boldsymbol{N}_{as}^h$ by matrix $\boldsymbol{M}_N^h$ for the mesh set of type **Mesh set** #2.

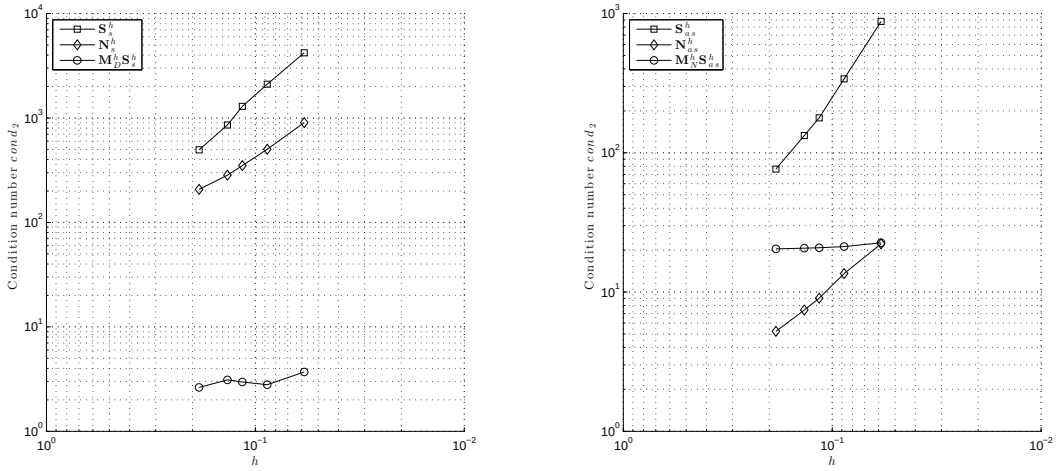

Figure 3.14: Preconditioning of matrix $\boldsymbol{S}_s^h$ by matrix $\boldsymbol{M}_D^h$ (left) and matrix $\boldsymbol{N}_{as}^h$ by matrix $\boldsymbol{M}_N^h$ for the mesh set of type **Mesh set** #3.

As appreciated from the previous figures, matrices $\boldsymbol{S}_s^h$, $\boldsymbol{S}_{as}^h$, $\boldsymbol{N}_s^h$, and $\boldsymbol{N}_{as}^h$ are naturally ill-conditioned, but they act as optimal mutual pre-conditioners.

Remark 3.3.2 (Spaces of the variational problem for the modified integral operators)**.** *Even if the bilinear forms induced by the modified boundary integral operators are not coercive in the relevant Sobolev trace spaces specified for the variational problem from Definition 3.1.5 (as it was stated in the final comments to Section 3.1), the fact that they provide optimal mutual preconditioning suggests that the modified boundary integral operators do induce coercive bilinear forms in the spaces spanned by the disk basis functions, and that these are pair-wise mutual duals.*

Remark 3.3.3 (Stability of the bases duality pairing for the boundary element spaces)**.** *As an extension to the previous remark, the fact that modified boundary integral operators provide optimal mutual preconditioning suggests that the bases' duality pairing for basis of the spaces*

$\widetilde{V}_h(\mathbb{D}_h)$ *and* $W_h(\mathbb{D}_h)$ *is also stable, as it was shown to be the case for* $\widetilde{W}_h(\mathbb{D}_h)$ *and* $V_h(\mathbb{D}_h)$ *in Proposition 2.2.1, where, for a closed surface* Γ*, it's evident that* $\widetilde{W}_h(\Gamma_h) = W_h(\Gamma_h)$*.*

In the next subsection, we will use the preconditioning matrices from Definition 3.3.2 on the matrices associated with the boundary integral operators $\mathcal{S}$ and $\mathcal{N}$, associated with the symmetric Dirichlet and the anti-symmetric Neumann problems.

3.3.2 Preconditioning the matrices for the symmetric Dirichlet and anti-symmetric Neumann problems on the disk

We will now specify the construction of the Galerkin matrices for the symmetric Dirichlet and the anti-symmetric Neumann problems for the disk screen. This matrices will be defined as in Definition 1.6.17 and as in Subsection 2.2.1, but now explicitely for open surfaces using the tools and definitions developed in this chapter.

Definition 3.3.3 (Galerkin matrices associated with $\mathcal{S}$ and $\mathcal{N}$)**.** *Let us define the Galerkin matrices associated with boundary integral operators* $\mathcal{S}$ *and* $\mathcal{N}$ *on the conformal triangular approximation* $\mathbb{D}_h$ *for the disk. As usual, we denote by* N_V *the number of vertices of the mesh* $\mathcal{T}_h$ *for* $\mathbb{D}_h$*, of which* N_V^0 *are internal.*

We define $\boldsymbol{S}^h \in \mathbb{C}^{N_V \times N_V}$ *as*

$$\boldsymbol{S}^h[i,j] = \langle \mathcal{S}\kappa_i \, , \, \kappa_j \rangle_{\mathbb{D}_h} \, , \qquad \text{for } i,j = 1...N_V. \tag{3.146}$$

We define $\boldsymbol{S}^h \in \mathbb{C}^{N_V^0 \times N_V^0}$ *as*

$$\boldsymbol{N}^h[i,j] = \left\langle -\mathcal{N}\chi_i^0 \, , \, \chi_j^0 \right\rangle_{\mathbb{D}_h} + \alpha \left\langle \chi_i^0 \, , \, 1 \right\rangle_{\mathbb{D}_h} \left\langle 1 \, , \, \chi_j^0 \right\rangle_{\mathbb{D}_h} \, , \qquad \text{for } i,j = 1...N_V^0, \tag{3.147}$$

with a parameter $\alpha \in \mathbb{R}^+$ *to suppress the kernel space of operator* $\mathcal{N}$ *(refer to Theorem 1.5.3), as it was done for the Galerkin matrix associated with operator* $\widetilde{\mathcal{L}}_s^{hs}$ *from Definition 3.2.9.*

We will now consider the preconditioning effect of matrix $\boldsymbol{M}_D^h$ on matrix $\boldsymbol{S}^h$, and of matrix $\boldsymbol{M}_N^h$ on matrix $\boldsymbol{N}^h$. Figures 3.15, 3.16 & 3.17 will show the evolution of the condition number of matrices $\boldsymbol{S}^h$ and $\boldsymbol{N}^h$, and the preconditioned matrices $\boldsymbol{M}_D^h\boldsymbol{S}^h$ and $\boldsymbol{M}_N^h\boldsymbol{N}^h$ using the different types of mesh sets defined.

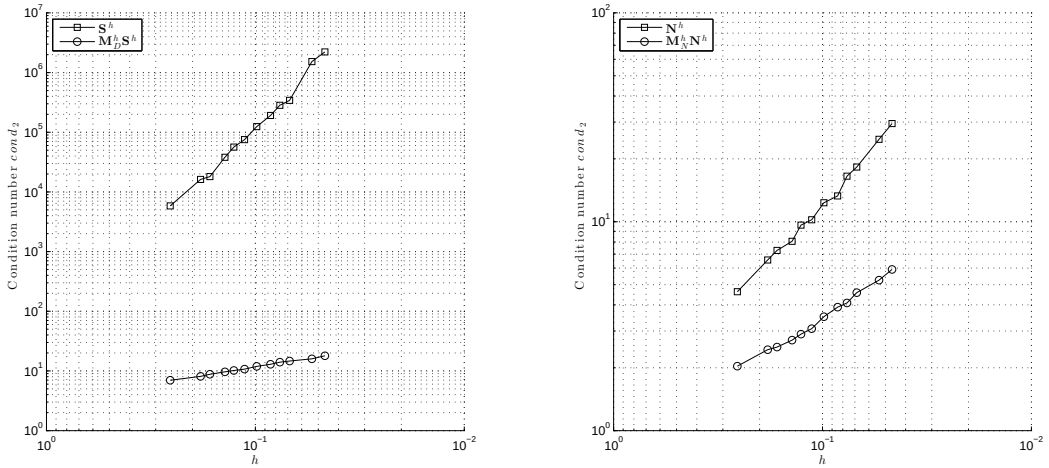

Figure 3.15: Preconditioning of matrix $\boldsymbol{S}^h$ by matrix $\boldsymbol{M}_D^h$ (left) and of matrix $\boldsymbol{N}^h$ by matrix $\boldsymbol{M}_D^h$ for a mesh set of type **Mesh set** #1.

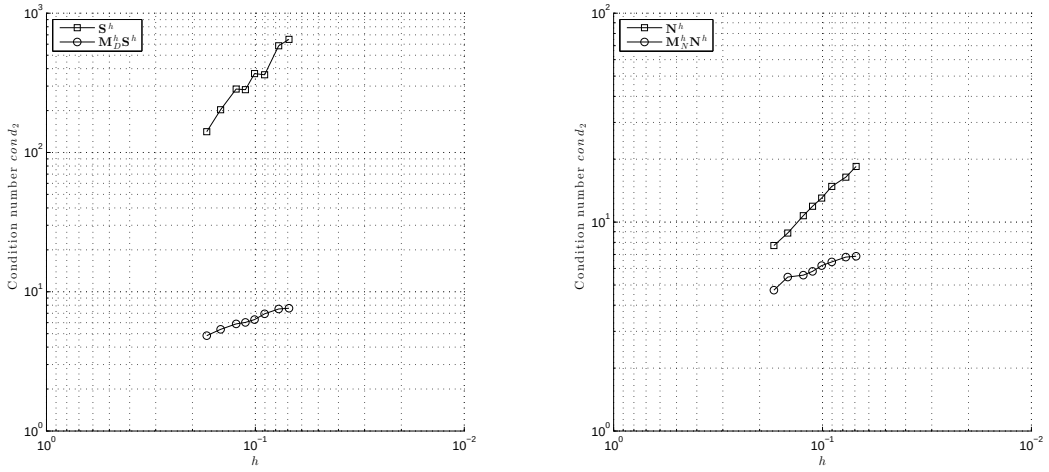

Figure 3.16: Preconditioning of matrix $\boldsymbol{S}^h$ by matrix $\boldsymbol{M}_D^h$ (left) and of matrix $\boldsymbol{N}^h$ by matrix $\boldsymbol{M}_D^h$ for a mesh set of type **Mesh set** #2.

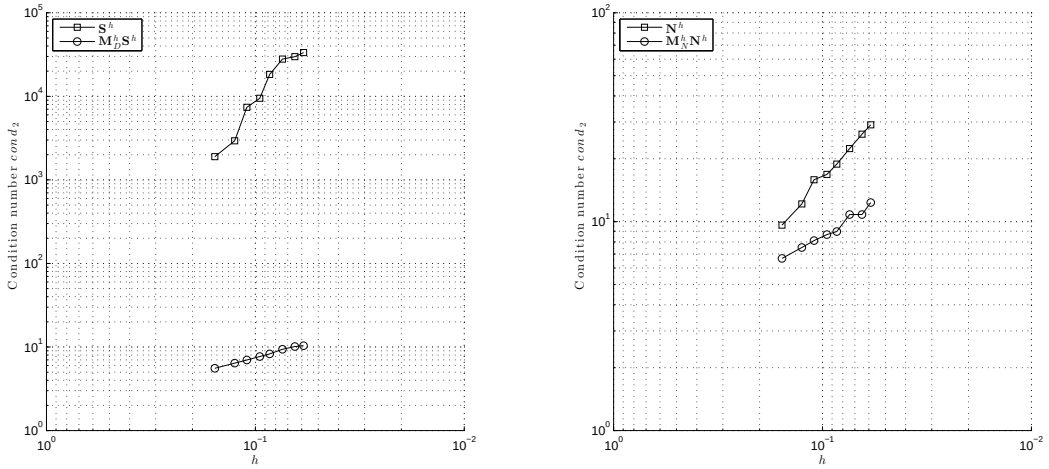

Figure 3.17: Preconditioning of matrix $\boldsymbol{S}^h$ by matrix $\boldsymbol{M}_D^h$ (left) and of matrix $\boldsymbol{N}^h$ by matrix $\boldsymbol{M}_D^h$ for a mesh set of type **Mesh set** #3.

In stark difference with the cases from Subsection 3.3.1, matrix $\boldsymbol{M}_D^h$ is not an optimal preconditioner for $\boldsymbol{S}^h$ as it was for $\boldsymbol{S}_s^h$, and matrix $\boldsymbol{M}_N^h$ is not an optimal preconditioner for $\boldsymbol{N}^h$ as it was for $\boldsymbol{N}_{as}^h$. As suggested in Remark 3.3.3, the dual pairing of bases for the finite-dimensional spaces is stable in the sense of (2.3) as required by Theorem 2.1.1, and as it was proven for the closed surfaces in Proposition 2.2.1. Also, as suggested by Remark 3.3.2, the bilinear forms induced by the modified boundary integral operators are coercive and continuous in some spaces, but their coercivity and continuity was not assured on the relevant Sobolev trace spaces for the symmetric Dirichlet and anti-symmetric Neumann problems for the disk (as warned in the closing remarks for Section 3.1).

The fact that matrix $\boldsymbol{M}_D^h$ is not an optimal preconditioner for $\boldsymbol{S}^h$ as it was for $\boldsymbol{S}_s^h$, and matrix $\boldsymbol{M}_N^h$ is not an optimal preconditioner for $\boldsymbol{N}^h$ as it was for $\boldsymbol{N}_{as}^h$, strongly suggests that it is the case that the bilinear forms induced by the modified boundary integral operators are not coercive and continuous in the relevant Sobolev trace spaces for the symmetric Dirichlet

and anti-symmetric Neumann. However, there is a significant improvement in the condition number of the preconditioned matrices, which is due to the radial behavior of the kernels of the modified boundary integral operators. This was the guiding principle in devising operator preconditioning techniques from the modifications of the exact inverses developed in Chapter 2.

When preconditioning, the bilinear forms $\widetilde{b}_s^{hs}$ and $\widetilde{b}_{as}^{ws}$ used to precondition the matrices associated to the boundary integral operators $\mathcal{S}$ and $\mathcal{N}$ respectively, can be shown to fail to be continuous and coercive in the relevant spaces: $H^{1/2}(\mathbb{D})$ and $H^{-1/2}(\mathbb{D})$. We will analyze this carefully in what follows, picking up the discussion at the end of Section 3.1

$\widetilde{b}_s^{hs}$ is not continuous in $H^{1/2}(\mathbb{D})$

In order for $\widetilde{b}_s^{hs}$ to be continuous in $H^{1/2}(\mathbb{D})$ there would have to be a constant $C > 0$ such that

$$\eta_l \leq C\beta_l^m, \tag{3.148}$$

for all $l \geq 0$ and $l + m$ even. However, the opposite can be shown: there is no constant $C > 0$ such that inequality hold. Given the fact that $\beta_l^l \leq \beta_l^m$ for all $l \geq 0$ and $l + m$ even, it suffices to show that there is no constant $C > 0$ such that

$$\eta_l \leq C\beta_l^l, \tag{3.149}$$

or equivalently, that the series η_l/β_l^l does not has an upper bound for all $l \geq 0$. The following figure shows that this is the case.

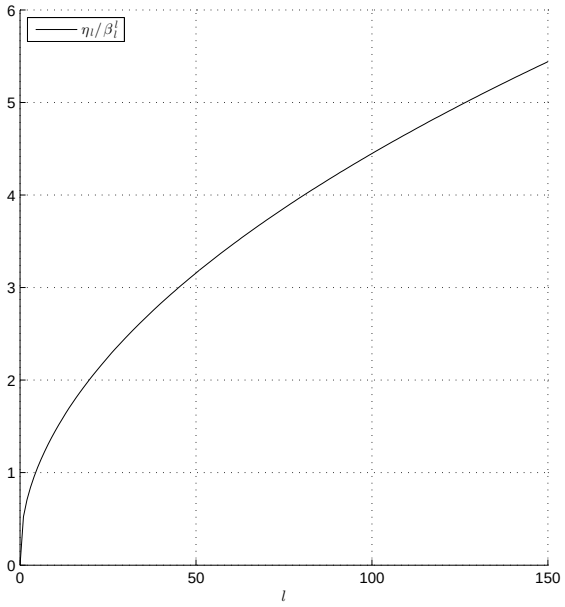

Figure 3.18: No-continuity of $\widetilde{b}_s^{hs}$ in $H^{1/2}(\mathbb{D})$ shown by the unboundness of η_l/β_l^l.

$\widetilde{b}_s^{hs}$ is not coercive in $H^{1/2}(\mathbb{D})$

In order for $\widetilde{b}_s^{hs}$ to be coercive in $H^{1/2}(\mathbb{D})$ there would have to be a constant $C > 0$ such that

$$\eta_l \geq C\beta_l^m, \tag{3.150}$$

for all $l \geq 0$ and $l+m$ even. The existence of such a constant is impossible, since $\eta_0 = 0$. However, it's worth noting that in the subspace of functions from $H^{1/2}(\mathbb{D})$ with zero mean, $\widetilde{b}_s^{hs}$ would be coercive. Noting that $\beta_l^0 \geq \beta_l^m$, the existence of $C > 0$ for $l \geq 1$ such that (3.150) holds can be assured by the existence of a constant $C' > 0$ such that

$$\eta_l \geq C' \beta_l^0, \tag{3.151}$$

or equivalently, that the series η_l / β_l^0 has a lower bound for all $l \geq 1$. The following figure shows that this is the case.

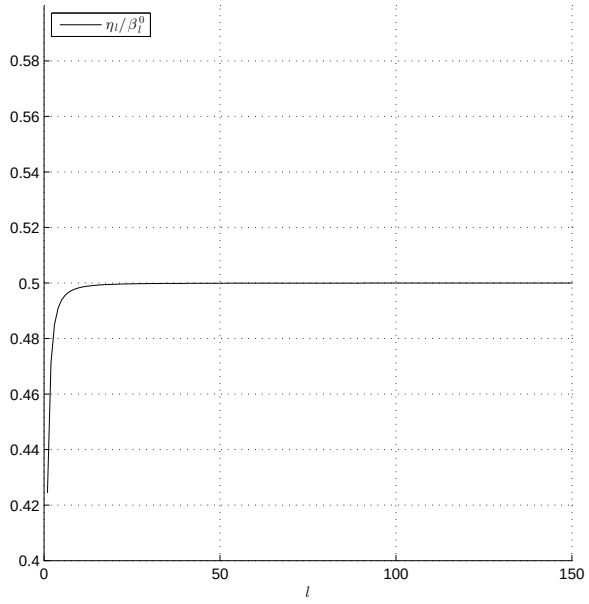

Figure 3.19: Coercivity of $\widetilde{b}_s^{hs}$ for zero-mean functions of $H^{1/2}(\mathbb{D})$ shown by the lower boundness of η_l / β_l^0.

$\widetilde{b}_{as}^{ws}$ is continuous in $H^{-1/2}(\mathbb{D})$

In order for $\widetilde{b}_{as}^{ws}$ to be continuous in $H^{-1/2}(\mathbb{D})$ there would have to be a constant $C > 0$ such that

$$\zeta_l \leq \frac{C}{\alpha_l^m}, \tag{3.152}$$

for all $l \geq 1$ and $l+m$ odd. Given the fact that $\alpha_l^0 \geq \alpha_l^m$ for all $l \geq 1$ and $l+m$ odd, it suffices to show that there is a constant $C' > 0$ such that

$$\zeta_l \leq \frac{C'}{\alpha_l^0}; \tag{3.153}$$

or equivalently, that the series $\zeta_l \alpha_l^0$ has an upper bound for all $l \geq 1$. The following figure shows that this is the case.

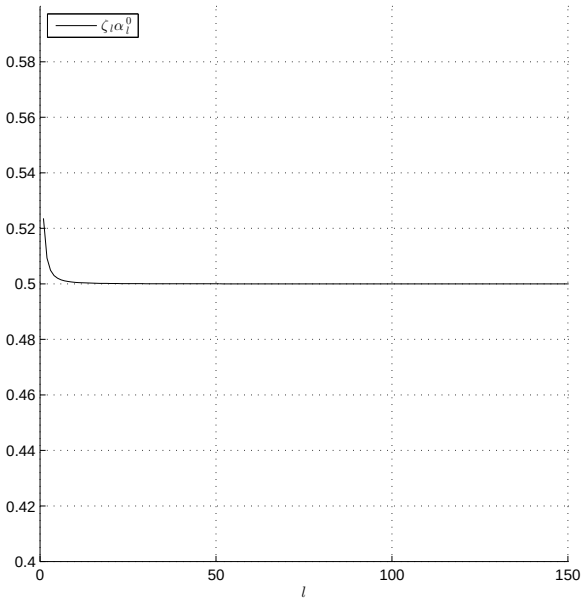

Figure 3.20: Continuity of $\widetilde{b}_{as}^{ws}$ in $H^{-1/2}(\mathbb{D})$ shown by the boundness of $\zeta_l \alpha_l^0$.

$\widetilde{b}_{as}^{ws}$ is not coercive in $H^{-1/2}(\mathbb{D})$

In order for $\widetilde{b}_{as}^{ws}$ to be coercive in $H^{-1/2}(\mathbb{D})$ there would have to be a constant $C > 0$ such that

$$\zeta_l \geq \frac{C}{\alpha_l^m}, \tag{3.154}$$

for all $l \geq 1$ and $l + m$ odd. Noting that $\alpha_l^{l-1} \leq \alpha_l^m$, the existence of $C > 0$ for $l \geq 1$ such that (3.154) holds can be assured by the existence of a constant $C' > 0$ such that

$$\zeta_l \geq \frac{C'}{\alpha_l^{l-1}}, \tag{3.155}$$

or equivalently, that the series $\zeta_l \alpha_l^{l-1}$ has a lower bound for all $l \geq 1$. This is not the case, and the non-existence of such a constant would be assured by the impossibility of the existence of a lower bound for the series $\zeta_l \alpha_l^{l-1}$ for $l \geq 1$. However, a simple numerical experiment does not provide a convincing argument, as the following figure illustrates.

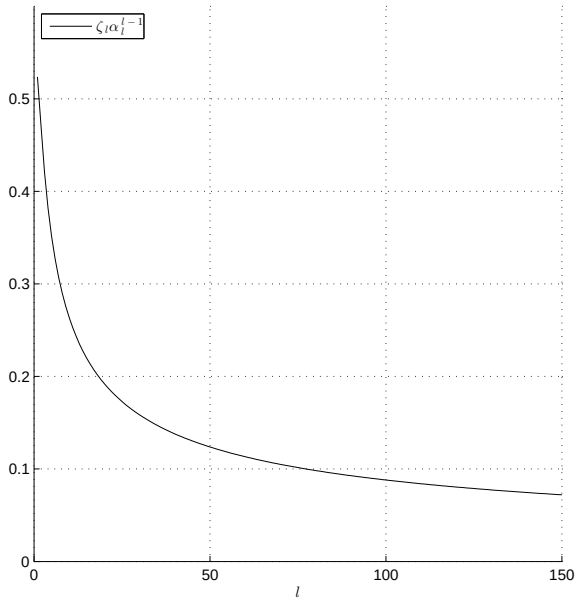

Figure 3.21: No-coercivity of $\widetilde{b}_{as}^{ws}$ in $H^{-1/2}(\mathbb{D})$ shown by the lower unboundness of $\zeta_l \alpha_l^{l-1}$.

An explicit determination of the limit of the sequence provides the argument required to assure that $\widetilde{b}_{as}^{ws}$ is not coercive in $H^{-1/2}(\mathbb{D})$.

Lemma 3.3.1 (Limits of the sequence associated with the coerciveness of $\widetilde{b}_{as}^{ws}$ in $H^{-1/2}(\mathbb{D})$)**.** *The limits value of the sequence $\zeta_l \alpha_l^{l-1}$ is:*

$$\lim_{l \to \infty} \zeta_l \alpha_l^{l-1} = 0. \tag{3.156}$$

Proof Using the definition of α_l^m we can write

$$\alpha_l^{l-1} = \frac{\Gamma\left(l + 1/2\right) \Gamma\left(3/2\right)}{\Gamma\left(l\right) \Gamma\left(1\right)}, \tag{3.157}$$

where Γ stands for the special function Gamma.

Using the properties of the Gamma function, we can rewrite

$$\alpha_l^{l-1} = \frac{\pi}{2^{2l+1}} \frac{(2l)!}{l!(l-1)!}. \tag{3.158}$$

We now consider the sequence

$$\zeta_l \alpha_l^{l-1} = \frac{\pi}{2^{2l}(2l+1)} \frac{(2l)!}{l!(l-1)!}. \tag{3.159}$$

We recall that Stirling's approximations provide us with the following bounds for the factorial of numbers $n > 0$:

$$\sqrt{2\pi} n^{n+1/2} e^{-n} \leq n! \leq e n^{n+1/2} e^{-n}. \tag{3.160}$$

Using Stirling's approximations from (3.160) we can produce bounds for the factorial factors in the expression of the sequence (3.159):

$$(2l)! \leq e(2l)^{2l+1/2} e^{-2l}, \tag{3.161}$$

$$\frac{1}{l!} \leq \frac{e^l}{\sqrt{2\pi}} \frac{1}{l^{l+1/2}}, \tag{3.162}$$

$$\frac{1}{(l-1)!} \leq \frac{e^{l-1}}{\sqrt{2\pi}} \frac{1}{(l-1)^{l-1/2}}. \tag{3.163}$$

Using these bounds we can now establish a bound for the sequence (3.159) as

$$\zeta_l \alpha_l^{l-1} \leq 2^{2/3} \frac{l^l}{(2l-1)(l-1)^{l-1/2}}. \tag{3.164}$$

A rearrangement of terms,

$$\zeta_l \alpha_l^{l-1} \leq 2^{2/3} \left(\frac{l}{l-1}\right)^l \frac{\sqrt{l-1}}{l-1}, \tag{3.165}$$

shows that

$$\lim_{l\to\infty} \zeta_l \alpha_l^{l-1} = 0. \tag{3.166}$$

■

In the next subsections we will extend the principle explored in the present one to confirm that the Laplace preconditioners preserve their preconditioning capabilities when applied to the Helmholtz case when the surface is a screen (open), and we will further extend it to adapt this preconditioning method to cover screens other than the disk by modifying the weight function w.

3.3.3 The Helmholtz problem for the unit disk in three dimensions as a compact perturbation

In Section 2.2 it was shown that the boundary integral operators for the Laplace problems provided equally good preconditioners for the integral operators for the Helmholtz problems when the surface on which they were posed were Lipschitz-regular. That is, the Galerkin matrix associated with the bilinear form induced by $\mathcal{S}$, provides an optimal preconditioner for the Galerkin matrix associated with the bilinear form induced by $\mathcal{N}^k$, and that the Galerkin matrix associated with the bilinear form induced by $\mathcal{N}$ provided an optimal preconditioner for the Galerkin matrix associated with the bilinear form induced by $\mathcal{S}^k$ (following Notation 2.2.1). In what follows we will apply the same reasoning to the case of screen obstacles using the disk as an example. For that, we will define the Helmholtz Galerkin matrices for operators $\mathcal{S}^k$ and $\mathcal{N}^k$, now explicitly for the disk screen.

Definition 3.3.4 (Galerkin matrices associated with $\mathcal{S}^k$ and $\mathcal{N}^k$)**.** *Let us define the Galerkin matrices associated with boundary integral operators $\mathcal{S}^k$ and $\mathcal{N}^k$ on the conformal triangular approximation $\mathbb{D}_h$ for the disk. As usual, we denote by N_V the number of vertices of the mesh $\mathcal{T}_h$ for $\mathbb{D}_h$, of which N_V^0 are internal.*

We define $\boldsymbol{S}_k^h \in \mathbb{C}^{N_V \times N_V}$ as

$$\boldsymbol{S}_k^h[i,j] = \left\langle \mathcal{S}^k \kappa_i \, , \, \kappa_j \right\rangle_{\mathbb{D}_h}, \quad \text{for } i,j = 1...N_V. \tag{3.167}$$

We define $\boldsymbol{N}_k^h \in \mathbb{C}^{N_V^0 \times N_V^0}$ as

$$\boldsymbol{N}_k^h[i,j] = \left\langle -\mathcal{N}^k \chi_i^0 \, , \, \chi_j^0 \right\rangle_{\mathbb{D}_h}, \quad \text{for } i,j = 1...N_V^0. \tag{3.168}$$

Remark 3.3.4 (The bilinear forms for the Helmholtz case are compact perturbations of the ones for the Laplace case)**.** *By the same reasoning as that exposed in Subsection 2.2.2, the bilinear forms for the Helmholtz case for the disk, i.e. $\left\langle \mathcal{S}^k \lambda \, , \, \lambda^t \right\rangle_{\mathbb{D}_h}$ and $\left\langle -\mathcal{N}^k \mu \, , \, \mu^t \right\rangle_{\mathbb{D}_h}$, are compact perturbations of the ones used for the Laplace case and defined in Definition 3.3.3.*

Figure 3.22 will show the evolution of the condition number of matrices $\boldsymbol{S}_k^h$ and $\boldsymbol{N}_k^h$, defined in Definition 3.3.4, and the evolution of the condition number of the preconditioned matrices $\boldsymbol{M}_D^h\boldsymbol{S}_k^h$ and $\boldsymbol{M}_N^h\boldsymbol{N}_k^h$ using the pre-conditioners defined in Definition 3.3.2, for diminishing discretization parameter h.

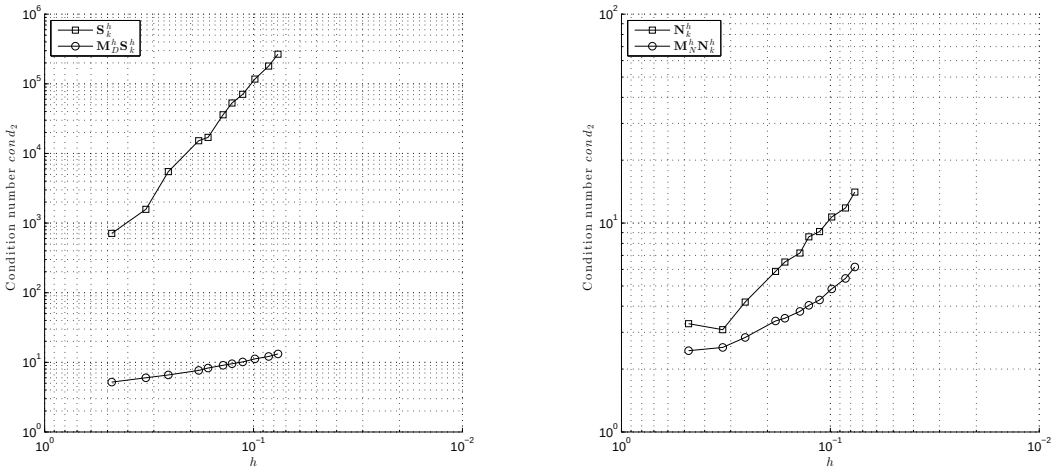

Figure 3.22: Preconditioning of matrix $\boldsymbol{S}_k^h$ by matrix $\boldsymbol{M}_D^h$ (left) and of matrix $\boldsymbol{N}_k^h$ by matrix $\boldsymbol{M}_D^h$ for a mesh set of type **Mesh set** #1.

The same preconditioning effect is observed when preconditioning the symmetric Dirichlet and the anti-symmetric Neumann Helmholtz problem for the unit disk using the Laplace pre-condifioners. Figure 3.23 exemplifies the scenario of a wave propagation numerical simulation where the disk screen is the obstacle for an incoming wave.

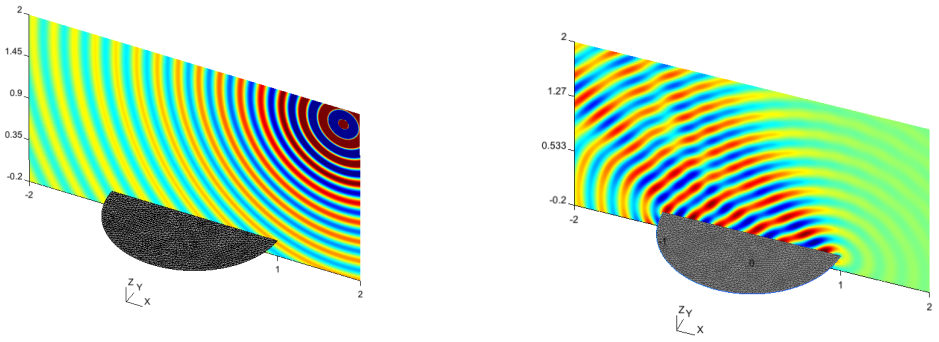

Figure 3.23: Example of a numerical simulation of wave propagation where a disk screen is the obstacle for an incoming wave, showing the incoming wave (left) and the scattered wave (right).

3.3.4 Generalization to planar polygonal screens

The preconditioning effect of matrices $\boldsymbol{M}_D^h$ and $\boldsymbol{M}_N^h$ is achieved by selecting kernels $\widetilde{K}_s^{hs}$ and $\widetilde{K}_{as}^{ws}$ that induce integral operators that, while not providing exact inverses for $\mathcal{S}$ and $\mathcal{N}$, have kernels that behave similarly to those of the known inverses. This was related to the known behavior of the jump of traces of the solutions of the Laplace problems, as stated in Remark 2.7.3, related to $w(\rho)$ and $1/w(\rho)$. The weight function w was also intimately linked to the relation between the sphere and the disk. This role manifests itself in the subsequent proposed

method in the fact that vertical projection of point $\boldsymbol{x}$ on the disk onto the half-spheres, i.e. $\boldsymbol{x}^{\pm}$, was separated by a quantity $w(\boldsymbol{x})$. This effect was included in the numerical method in two different ways: 1) considering the upper and lower conformal triangular approximations $\mathbb{S}_h^{\pm}$ that were produced with weight function w to perform the integrations involved in the boundary element computations in Subsection 3.2.5, and 2) in the explicit use of the weight function w in the proposed numerical scheme in (3.134).

In this section we will extend the action of the defined preconditioners to some planar polygonal screens Γ, by preserving the behavior of the modified integral operators' kernels near the edges of the screen. To do so, we will propose a different weight function for each screen Γ, that will be related to the distance of a given point $\boldsymbol{x} \in \Gamma$ to edge $\partial\Gamma$ when in the vicinity of this edge. We will begin by dividing the planar polygonal screen Γ into zones, and defining for each one of them a distance function with which we will later define a global modified weight function w_Γ for screen Γ.

Let us state formally the definition of division by zones of a planar polygonal screen Γ.

Definition 3.3.5 (Zone division of a planar polygonal screen)**.** *Let us consider a planar and polygonal screen Γ divided in N_Z disjoint zones $\{Z_i\}_{i=1}^{N_Z}$ such that each one of them reaches the edge $\partial\Gamma$, i.e., for $i = 1...N_Z$ we have $\overline{Z_i} \cap \partial\Gamma \neq \varnothing$, and such that the set $\overline{Z_i} \cap \partial\Gamma \neq \varnothing$ belongs to a line in $\mathbb{R}^3$. The set $\{Z_i\}_{i=1}^{N_Z}$ is called a zone division for the planar polygonal screen Γ.*

Let us consider the case of a square-shaped and an L-shaped screen to illustrate this extended method. We will divide the square-shaped screen into four zones, and the L-shaped screen into six zones as indicated in Figure 3.24 and in compliance with Definition 3.3.5.

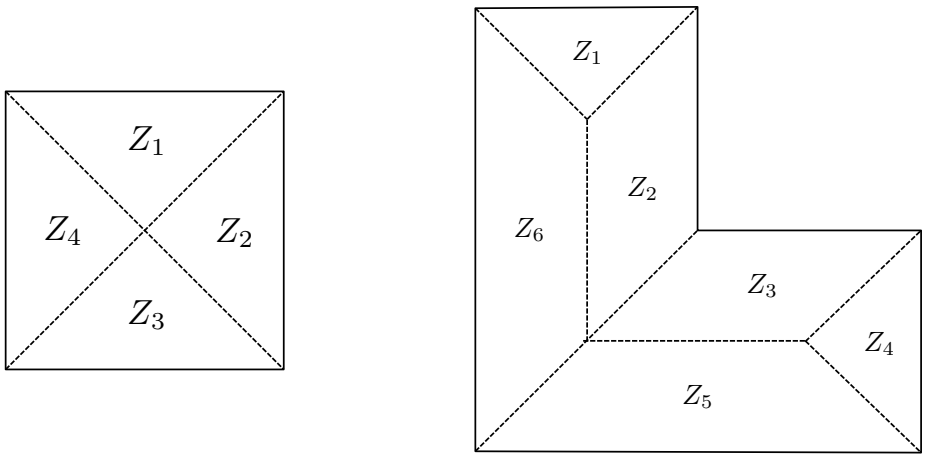

Figure 3.24: Zone division of a square-shaped screen (left) and an L-shaped screen (right).

Let consider the following geometrical definition that will be useful in defining the mentioned zone-wise distance functions.

Definition 3.3.6 (External edge line of a zone)**.** *For each zone Z_i of a zone division $\{Z_i\}_{i=1}^{N_Z}$ for a planar polygonal screen Γ, we will define the external edge line ℓ_i as the only straight line in $\mathbb{R}^3$ containing the segment $\overline{Z_i} \cap \partial\Gamma \neq \varnothing$.*

We can now formally define the zone-wise distance-to-edge function.

Definition 3.3.7 (Zone-wise distance-to-edge function)**.** *For each zone Z_i of a zone division $\{Z_i\}_{i=1}^{N_Z}$ for a planar polygonal screen Γ, we will define the zone-wise distance-to-edge function*

$dist_{Z_i}(\boldsymbol{x})$ for a point $\boldsymbol{x} \in Z_i$ as

$$dist_{Z_i}(\boldsymbol{x}) = dist\,(\boldsymbol{x}, \ell_i)\,, \tag{3.169}$$

where function $dist\,(\cdot,\cdot)$ is defined in Definition 1.2.2.

Finally, using the zone-wise distance-to-edge function we can define the global modified weight function w_Γ for a planar polygonal screen Γ.

Definition 3.3.8 (Global modified weight function w_Γ for a planar polygonal screen Γ)**.** *Given a planar polygonal screen Γ divided in N_Z disjoint zones $\{Z_i\}_{i=1}^{N_Z}$, we define the global modified weight function w_Γ for $\boldsymbol{x} \in \Gamma$ as*

$$w_\Gamma(\boldsymbol{x}) = \begin{cases} \sqrt{dist_{Z_1}(\boldsymbol{x})}, & \text{if } \boldsymbol{x} \in Z_1, \\ \vdots & \vdots \\ \sqrt{dist_{Z_{N_Z}}(\boldsymbol{x})}, & \text{if } \boldsymbol{x} \in Z_{N_Z}. \end{cases} \tag{3.170}$$

Although this global modified weight function could be discontinuous at the intersection of zones in which a screen is subdivided, it is easy to produce continuous ones for a considerably wide range of screen geometries, such as the ones depicted in Figure 3.24. We will focus on these examples, using this global modified weight function w_Γ to generate the mesh set $\{\Gamma_h, \Gamma_h^+, \Gamma_h^-\}$ by means of vertical projections, where $\Gamma_h^\pm$ are the upper and lower conformal triangular approximation determined by vertical projections using function w_Γ to project form Γ_h. Figures 3.25 & 3.26 illustrate the achieved mesh set for a square-shaped and an L-shaped screen by showing Γ_h and Γ_h^+.

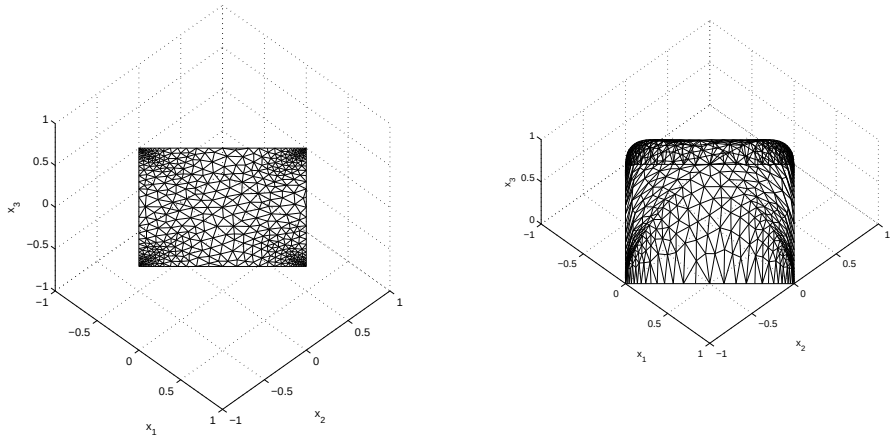

Figure 3.25: Discretized square-shaped screen Γ_h (left) with its upper projection Γ_h^+ (right) generated using the global modified weight function w_Γ.

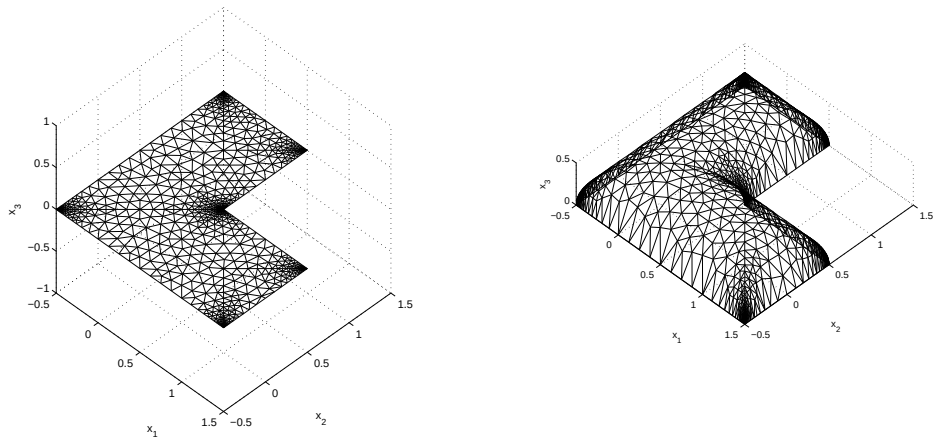

Figure 3.26: Discretized L-shaped screen Γ_h (left) with its upper projection Γ_h^+ (right) generated using the global modified weight function w_Γ.

Given a planar polygonal screen Γ and given a chosen zone division for it, we use the global modified weight function w_Γ over a conformal triangular approximation Γ_h to generate the mesh set $\{\Gamma_h, \Gamma_h^+, \Gamma_h^-\}$. Together with replacing function w by w_Γ in (3.134) this allows to redefine the boundary element computations to generate the Galerkin matrices for the particular case of a planar polygonal screen Γ. Using these matrices, we will test again the preconditioning capabilities of matrices $\boldsymbol{M}_D^h$ and $\boldsymbol{M}_D^h$ computed with these prescribed modifications.

Figure 3.27 shows the evolution of the condition number of matrix $\boldsymbol{S}^h$ and the condition number of the preconditioned matrix $\boldsymbol{M}_D^h\boldsymbol{S}^h$, and also the evolution $\boldsymbol{N}^h$ and the condition number of the preconditioned matrix $\boldsymbol{M}_N^h\boldsymbol{N}^h$, for diminishing minimum edge lengths h, all while using a square-shaped screen. Figure 3.28 shows the evolution of the condition number of matrix $\boldsymbol{S}^h$ and the condition number of the preconditioned matrix $\boldsymbol{M}_D^h\boldsymbol{S}^h$, and the evolution $\boldsymbol{N}^h$ and the condition number of the preconditioned matrix $\boldsymbol{M}_N^h\boldsymbol{N}^h$ for diminishing discretization parameter h.

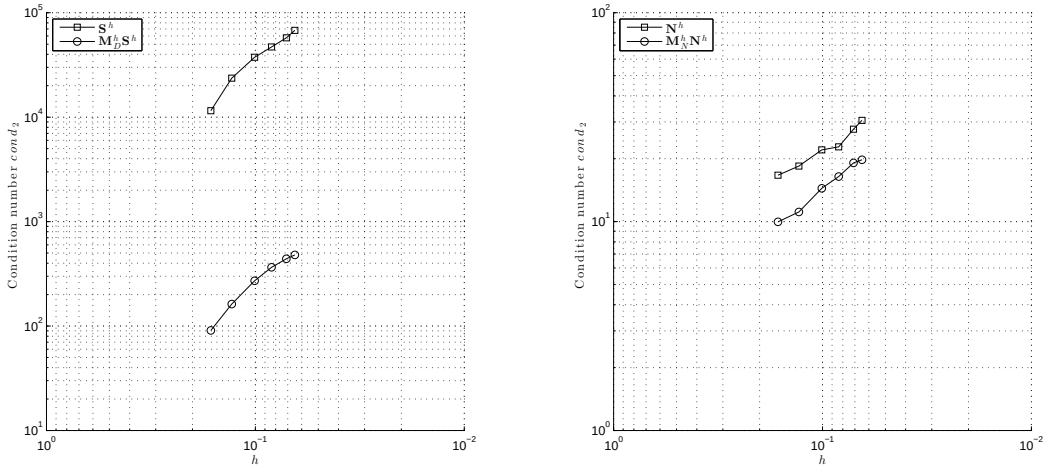

Figure 3.27: Evolution of the condition numbers for $\boldsymbol{S}^h$ and $\boldsymbol{M}_D^h\boldsymbol{S}^h$ (left) and $\boldsymbol{N}^h$ and $\boldsymbol{M}_N^h\boldsymbol{N}^h$ (right) for a squared-shaped screen Γ with diminishing discretization parameter h.

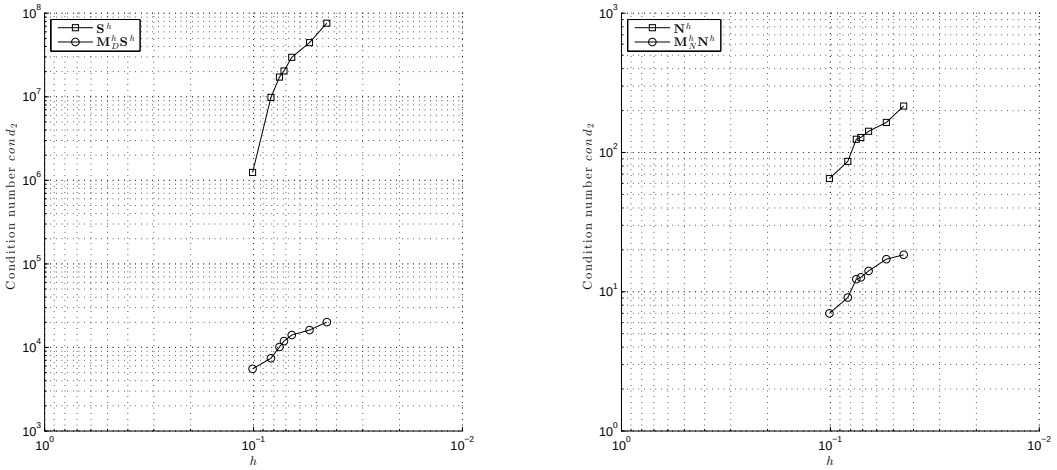

Figure 3.28: Evolution of the condition numbers for $\boldsymbol{S}^h$ and $\boldsymbol{M}_D^h\boldsymbol{S}^h$, (left) and $\boldsymbol{N}^h$ and $\boldsymbol{M}_N^h\boldsymbol{N}^h$ (right) for an L-shaped screen Γ with diminishing discretization parameter h.

Remarkably, the condition number has greatly improved, especially for the symmetric Dirichlet problem, although it presents anomalies in its evolution as the discretization parameter diminishes. This is due to the fact that the broken angles on the edge of the screen introduce other singularities on the jump of the traces, not described so far, and fall out of the scope of the functional framework given by the available theorems provided in Section 2.3. These anomalies are sensitive to the values α chosen to eliminate kernel spaces for the operator $\widetilde{\mathcal{L}}_s^{hs}$, which explains why they only occur in the use of its associated matrix $\boldsymbol{M}_D^h$.

Chapter 4

Applications to the Design and Testing of Remote Perception Technologies

In this chapter we will present some results related to the use of numerical simulations in the assessment of remote sensing technologies such as the ground-penetrating radar. This application example will highlight the need for robust and efficient numerical simulation of physical phenomena, such as the one outlined in Chapter 1, to which Chapters 2 & 3 suggest ways of improving it.

As discussed in Section 1.7, computational complexity and numerical inaccuracy can severely limit the usefulness of the application of numerical methods to solve partial differential equations modeling physical phenomena. This becomes especially true when the solution to a partial differential equation has to be computed in numerous repetitions for different parameters, or when its solution has to be fed into a process that has a feedback loop that might amplify the error. A wide variety of relevant applications that involve the evolution of some physical system make these situations unavoidable, such as automated design, optimization, automatic control, or the solution of some inverse problems. The ground-penetrating radar technology is an example where multiple and numerous transmitting and receiving spatial positions are used to determine some physical property of the underground. The assessment of a given type of radar can thus be performed by computing the direct problems associated with each of the numerous emitting-receiving positions to simulate physical wave propagation. Then, these results to feed an inverse problem solver that will determine some parameter of the physical system that was involved in the evolution of the direct physical problems. This procedure allows for the assessment of the performance of a system before it is built, which in turn allows for a more efficient, and sometimes even a possible, development process.

In this chapter we will give a description of ground-penetrating radar systems, emphasizing the ones that rely on time-harmonic radar signals. We will present a type of ground-penetrating radar called holographic radar and a special variant. Next, we will discuss how to simulate the propagation of radio waves using the Helmholtz equation for this chosen type of radar. This will be a simplification of the more precise but costly simulations using the Maxwell equations for the electromagnetic phenomena. This simplification is, however, a useful and standard practice in the framework of the development of many remote perception technologies. This discussion will include the modeling of reflective radar targets, the treatment of the interface between the air above-ground and the subsurface, the cost of solving a large number of wave propagation problems (as required by this setting), and how the approach developed in the previous chapter can help reduce this burden. Finally, the simulations will be used as examples in the assessment of a radar imaging principle that, because it relies on many assumptions that usually go unverified, provides a case of study suited for the use of numerical simulations.

4.1 Ground-penetrating radars

A ground-penetrating radar is a device that uses radio signals to gather physical information from the underground of a given portion of land. More generally, they are considered to be part of the subsurface radars, that include devices that use radio signals to gather physical information that is otherwise inaccessible behind a wall, clothes, skin tissue, canopy, or other material hiding a target of interest. The ground-penetrating radar often emits a radio signal (unless it is a passive radar) that travels across the surface, reaches an underground area of interest, and then is scattered back to the radar's antennas. The most common use for a ground-penetrating radar is the location and identification of underground objects that can scatter an incoming radio wave depending on their reflectivity, which is determined by different physical parameters. These objects can be, according to the application of the technology, structures of archeological interest, pipes, bodies of water, cavities, undesired remnants from previous industrial activities, and even unexploded ordnance or landmines. Using the backscattered radio waves, a ground-penetrating radar can locate the reflectivity, position, depth, and possibly the shape of a reflective target depending on its design. These physical parameters that determine the reflectivity of an underground target are of great importance in the description a physical scenario in which a ground-penetrating radar is to be used. Radio waves are reflected by interfaces between media with different electromagnetic characteristics, which can be modeled by the point-wise values of complex electrical permittivity and magnetic permeability when time-harmonic radio waves are considered (cf. [63, Section 2.1]). A common scenario is that of a bounded target buried within a sufficiently homogeneous underground material. In this scenario, the contrast in the electromagnetic properties of the underground and those of the target determine its reflectivity. A relevant type of target is the totally reflective target, often called a hard boundary object. This type of target is such that all incoming waves are reflected and no carried energy penetrates into its interior. In what follows, we will consider homogeneous above-ground and underground domains where homogeneous totally reflective targets can be buried. We will detail in the next sections the framework to be considered.

Ground-penetrating radar systems can be classified according to numerous criteria. We will provide some of them in the next subsection in order to precisely describe a given type. This type will allow us to show the advantages attainable by more efficient numerical simulations, such as the ones achievable using the numerical method proposed in Chapter 3, and how this can help in the testing and design of radar imaging methods.

4.1.1 Types of ground-penetrating radars

Ground-penetrating radar systems can be classified according to different and numerous criteria. We will mention the ones that will become relevant to the description of the system on which we will focus our attention.

Proximity to the ground surface

In the framework of the ground-penetrating radars, the proximity of the antennas of a radar system to the surface hiding the relevant propagation domain where a target of interest is possibly hidden, is one of the distinguishing characteristics. We will differentiate two types of proximities that are relevant for practical reasons: 1) single domain, or contact ground-penetrating radars, and 2) double domain or interface ground-penetrating radars.

Single domain, or contact ground-penetrating radars have their emitting and receiving antennas in contact with the ground's surface or very close to it, thus generating relevant wave propagation only in the underground domain; hence its name. These radars normally require ground support to be put in position, and rely on ground transportation and mobility. This has two major consequences: 1) there is interaction between the ground under analysis and

radar equipment and/or even its operators, which can be problematic in the case of landmines, unexploded ordnance or archeological sites, and 2) the effect of the geometry and reflectivity of the surface can be better controlled.

Double domain, or interface ground-penetrating radars have their emitting and receiving antennas considerably above the surface of the ground under analysis, making the distance that the wave travels above ground of importance, often introducing distorting effects depending on the geometry and reflectivity of the interface surface between the above-ground and underground. This is the case of airborne ground-penetrating radars, and has the advantage of removing the possible mechanical interaction between the radar equipment and the ground, and avoiding dependence on ground mobility which is often less agile, allowing less ground coverage in a given amount of operation time.

Configuration of transmitting and receiving positions

Radars in general, and ground-penetrating radars in particular, have antennas that emit and receive the radio signals used to scan the surroundings or the underground. These antennas can be the same or different (for emission and reception), and a radar system can have one or multiple antennas. One distinguishing characteristic is the spatial and temporal sequentiation, and the type configuration of the radar measurements. If the antennas of a radar system move above the ground, their movement will be often much slower than the propagation speed of the radio wave, so that a radar measurement can be considered as a still photograph. Variations from this setting for high speed radar systems or targets can be taken into account considering the doppler effect, but often fall outside the scope of ground-penetrating radars. Each one of these measurements will be recorded by a number of antennas from the echoes produced by the radio signal emitted by the same or possibly other antennas. According to this, we will differentiate: 1) multi-bistatic ground-penetrating radars and 2) multi-monostatic ground-penetrating radars.

A multi-bistatic (MBS) ground-penetrating radar records radar measurements from different antennas as they receive the backscattered radio signal emitted from other antennas. A common configuration is recording on all the antennas while only one is transmitting separately.

A multi-monostatic (MMS) ground-penetrating radar records in numerous positions the backscattered radio signal using the same antenna that produced it. The relevant feature is that emission and reception are produced in the same spatial position, and can in fact be separate but close-by antennas depending on the application.

Time-domain or frequency-domain radars

One of the most relevant and distinguishing aspects of the different types of ground-penetrating radar, is the kind signal that they transmit and then receive back. The signal that a radar system transmits through its antenna is generated internally in its electronic components. This signal can be [40]: 1) a time-domain impulse signal, or 2) a frequency-domain signal.

Time-domain impulse signals are characterized by short bursts of energy compacted into a short duration of time that create a propagating wave that travels into the underground generating echoes in its contact with the boundaries of reflective buried targets when present. The relative compactness in time of the signals allows for the echoes to arrive separately so that they are distinguishable when their arrival time is determined. This information, together with the speed of propagation of radio waves in the different domains involved, provides relevant spatial information about the targets that gave origin to the received reflections. This kind of wave phenomenon lies out of the scope of the modeling described in Chapter 1 and adopted throughout this document, unless it is used with Fourier analysis decomposition techniques for transient signals.

Frequency-domain signals are characterized by continuous emission of a single-frequency, time-harmonic radio wave, so that at a given time, the antenna receives the sum of all backscattered reflections, with different amplitudes and phases according to the traveled distances and possible attenuations. This radar type is also known as continuous-wave radar, and can be further classified in: 1) continuos-wave frequency-modulated and 2) holographic radars. The first ones, not often used in ground-penetrating radars, introduce slight changes in the frequency of the radio signal, and are suited to detect the presence of targets, and their range and speed though doppler analysis. The second ones emit a phase-coherent single-frequency radio wave and record at each receiving antenna the amplitude and the phase of the incoming backscattered wave. They are called holographic radars because the principle used in taking radar measurements is analogous to the optical recording of an holographic image using coherent light illumination and interference on a photographic plate [2, Section 1.2] [54].

In what remains of this chapter we will consider a specific type of ground-penetrating radar. According to our exhibited classification characteristics, it falls under the interface, multi-monostatic, holographic, ground-penetrating radar type. The motivation is closely linked to the rise of airborne instrumentation using drones and the improvements on data storage and treatment.

4.1.2 Airborne ground-penetrating radars

The ground-penetrating radar to be considered as an example in this chapter is intended to be fit for use on board of a flight platform such a drone. This has determined some of its characteristics, as the ones that have been specified in the previous subsection. A line array of multi-monostatic antennas, taking holographic radar measurement, is positioned in a drone or other flying platform aligned perpendicular to the flight path. The different antennas on the line array are switched to take monostatic, time-harmonic, holographic radar measurements, i.e., emitting a single-frequency, continuous-wave, and measuring the amplitude and the phase of the sum of all incoming reflected backscattered signals from the ground and the underground. As this switching provides measurements of the different antennas along the array, and as this array travels over a portion of ground due to the movement along a flight path, the result is a collection of N_{MMS} amplitude and phase backscattered sample measurements taken at points $\{\boldsymbol{r}_i^H\}_{i=1}^{N_{MMS}}$ contained in a surface above ground described by the movement of the array on the air. This surface, which we will denote by Γ^H contains the recorded hologram of the double domain for the wave propagation scenario. This scenario consists of an above-ground propagation domain Ω^+ and an underground propagation domain Ω^-, separated by the ground's surface, which we will denote as the interface surface Γ^I. A target possibly buried in Ω^-, of boundary Γ^T, is considered. Figure 4.1 illustrates the proposed scenario. In the case of a single under domain radar, the hologram recording surface Γ^H is just placed at the surface of the ground.

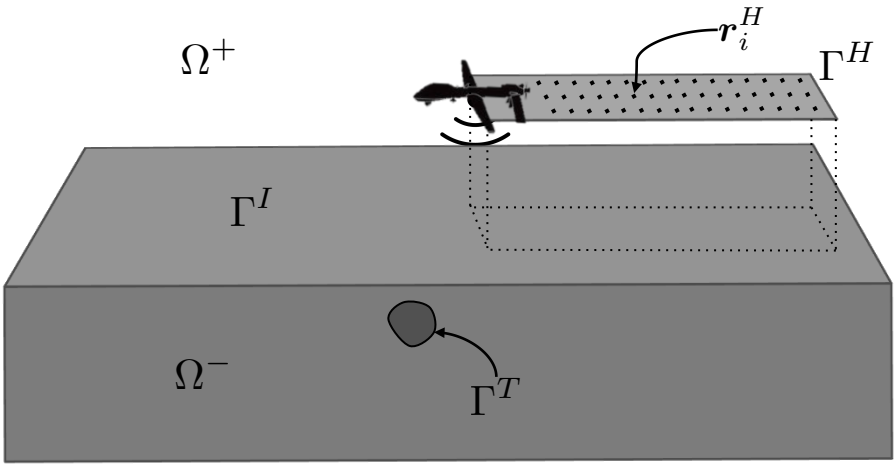

Figure 4.1: Illustration of an airborne line-array of antennas taking multi-monostatic radar measurements over a given portion of land.

The interest on this configuration lies in that it allows for recording of underground data for large portions of terrains in short periods of time. This relies, however, on complementary technologies such as precise flight positioning and navigation, laser telemetry of the determination of the shape of Γ^I, and the storage and treatment of large volumes of data. Despite the disadvantages of the stress put on the need for robust complementary technologies, and the narrower range of ground-penetrating radar configurations usable in this setting, it offers several advantages. Analyzing the underground of large portions of terrain can provide a critical cost- and time-effective first assessment of a terrain when scouting for targets. This can become critical when, for example, the intended radar targets are landmines and the assessment is set to provide quick clearance of suspicious terrains or clear safe ground paths on it.

This particular radar type and sampling setting have many different variants, but we have focused on radar systems consistent with the developments achieved in [18] and [13]. This two documents describe a precise procedure to take multi-monostatic holographic radar samples. The second, particularly, is suited to produce the kind of sampling data described in this subsection using airborne platforms.

4.2 Simulating time-harmonic radio signals

In this section we will show how to take advantage of some of the proposed techniques developed in the previous chapters to perform simulations of the wave propagation problem involved in ground-penetrating radar techniques. There are different ways of modeling these phenomena, and while the Maxwell's equations provide a more comprehensive modeling that takes into account physical characteristics particular to the electromagnetic behavior such as polarization, the use of scalar wave equations is a standard recourse in the radar community (cf. [2,23,58]). Doing this still yields useful conclusions, insight, and methods while simplifying the theoretical framework to be used and the numerical complexity of the simulations involved. In this chapter we will describe how to use different models and assumptions to take advantage of the preconditioning tools developed in the previous chapters to evaluate a given ground-penetrating radar system.

We will begin by setting the precise assumptions and tools that will be used to treat scalar wave propagation and scattering produced by the boundaries present in a simulation scenario, be it a single underground domain, or double domain or interface scenario as described in the classification provided in Subsection 4.1.1. We will specify the notation to be used in each one of these two scenarios, and the treatment that will be given to the reflective underground targets and to the air-ground interfaces. Next, we will address the cost of simulating a wave propagation in these scenarios. It is in this part where the previous results will be shown to be significant by increasing time-efficiency even for simplistic implementations. Finally, we will state the precise problem definition for the computation of the holographic recording for a single underground domain ground-penetrating radar scenario, and for an interface ground-penetrating scenario. We will also provide examples of how these solutions look for relatively complex radar targets such as the L-shaped screen presented in Subsection 3.3.4 from the previous chapter. This screen target will be used throughout the chapter as it presents less symmetries than other described screens such as the disk or the square-shaped screen. It will also provide us with the chance to study the consequences of the preconditioning methods described in Subsection 3.3.4.

4.2.1 General setting and assumptions

In the modeling of the behavior of wave propagation across surfaces, the Helmholtz equation will use some assumptions that will give rise to a set o boundary conditions. Let us consider the Helmholtz equation for acoustics governing the behavior of a scalar wave field u. Let us focus a on given oriented interface surface Γ^I with unit normal $\boldsymbol{n}$ with upper side $+$ and lower side $-$. We will call $u^{\pm}$ the upper/lower restriction of u. The interface separates two propagating homogeneous domains, Ω^+ and Ω^-, having wave velocities c^+ and c^-, wavelengths λ^+ and λ^-, and wavenumbers k^+ and k^- respectively. Enforcing continuity conditions across the surface Γ^I, we have the following continuity conditions:

$$\begin{cases} u^-(\boldsymbol{x}) = u^+(\boldsymbol{x}), & \text{for } \boldsymbol{x} \in \Gamma^I, \\ \\ \dfrac{\partial u^-}{\partial \boldsymbol{n}}(\boldsymbol{x}) = n^2 \dfrac{\partial u^+}{\partial \boldsymbol{n}}(\boldsymbol{x}), & \text{for } \boldsymbol{x} \in \Gamma^I. \end{cases} \tag{4.1}$$

where $n = c^+/c^- = \lambda^+/\lambda^- = k^-/k^+$ is the refraction index between the two media. The second condition in (4.1) comes from applying the time-harmonic conservation of momentum across the interface Γ^I from (1.9). Figure 4.2 shows in detail the elements to be considered and defined at the interface surface.

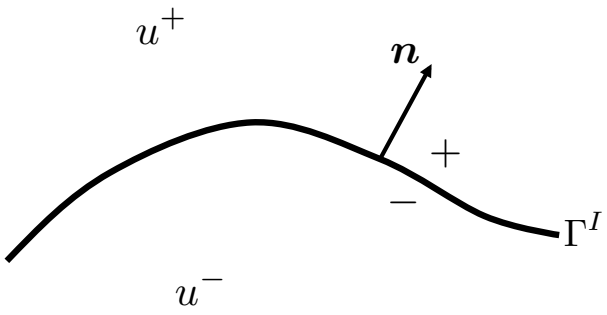

Figure 4.2: Composition of the scalar wave fields at both sides of an interface Γ^I.

Let us shortly define the geometrical settings for the two operation scenarios to be considered hereinafter: a single underground propagation domain and a double domain divided by an interface. In the first one the antennas contained in the hologram plane Γ^H are in contact with the ground's surface and the only propagation domain is the underground Ω^-. In the second one, the antennas contained in the hologram recording surface Γ^H are above-ground and there are two propagation domains: the above-ground and the underground. We will call the above-ground domain Ω^+, the underground domain Ω^-, we recall that the surface containing the multi-monosstatic radar measurement is Γ^H, and the air-ground interface is Γ^I. In both cases we will denote by Γ^T the surface of an underground radar target. Let us denote the above ground (underground) wave velocity c^+ (c^-), the wavelength λ^+ (λ^-), and the wavenumber k^+ (k^-). Figure 4.3 shows both scenarios: the described single domain, and the interface scenario for the holographic ground-penetrating radar simulations that will be specified in this section.

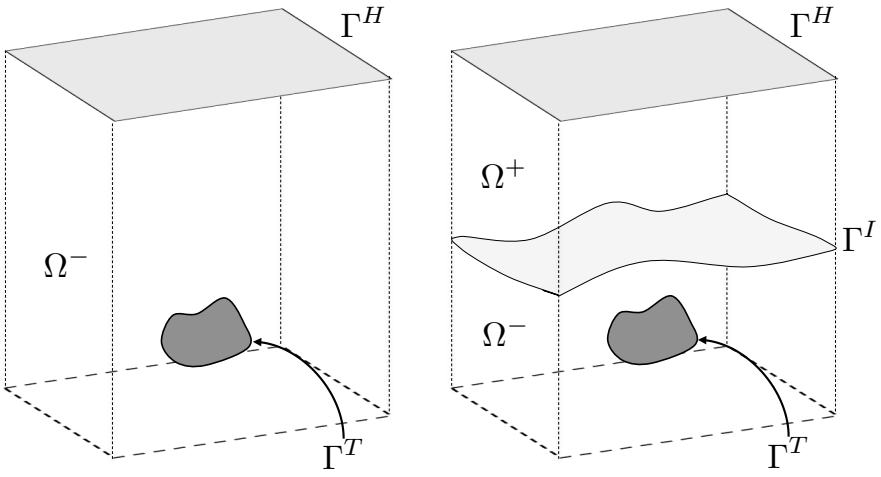

Figure 4.3: General setting for a holographic ground-penetrating simulation for a single domain (left) and a double domain scenario (right).

We will now adopt further specifications. We will consider a set of emitting-receiving (monostatic) samples recording amplitude and phase values $\{c_i^H\}_{i=1}^{N_{MMS}}$, with $c_i^H \in \mathbb{C}$, each associated with one of the sampling points $\{\boldsymbol{r}_i^H\}_{i=1}^{N_{MMS}} \subset \Gamma^H$. A position $\boldsymbol{r}_i^H$ is a position where an antenna has emitted a time-harmonic radio signal, which will be modeled by a point source represented by a Diract delta function. The scalar wave field u will be decomposed

in u_{inc} and u_{scat}. Let u_{inc} be each scalar field caused by the radiation of each antenna at point $\boldsymbol{r}_i^H \in \Gamma^H$, propagating towards the radar target, be it in in a single domain or through an interface. Let u_{scat} be the corresponding scalar field scattered back by the surface of the reflective radar target Γ^T. When the scenario to be considered consists of a double domain or interface problem, their restrictions to the above-ground domain Ω^+ will be called u_{inc}^+ and u_{scat}^+, and their restrictions to the underground domain Ω^- will be called u_{inc}^- and u_{scat}^-. Figure 4.5 illustrates the situation for a single domain scenario, and Figure 4.5 for a double domain or interface scenario.

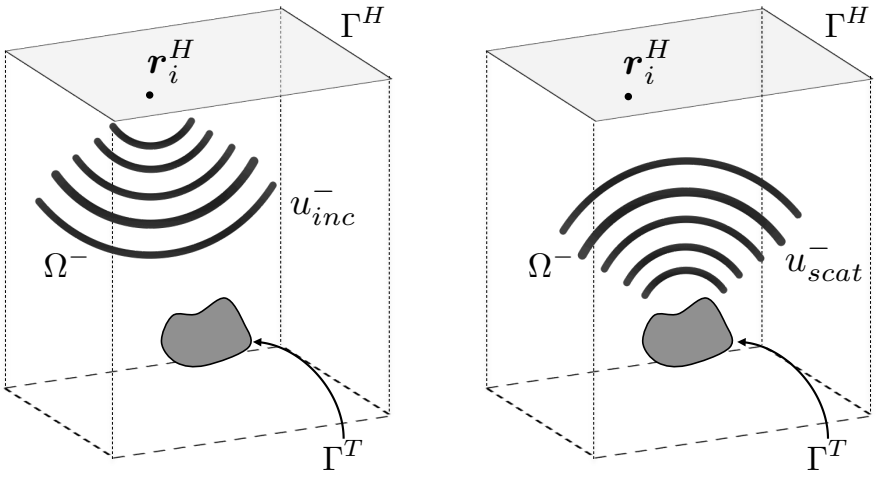

Figure 4.4: General setting for a holographic ground-penetrating simulation for a single underground domain scenario showing the incident (left) and the scattered (right) wave.

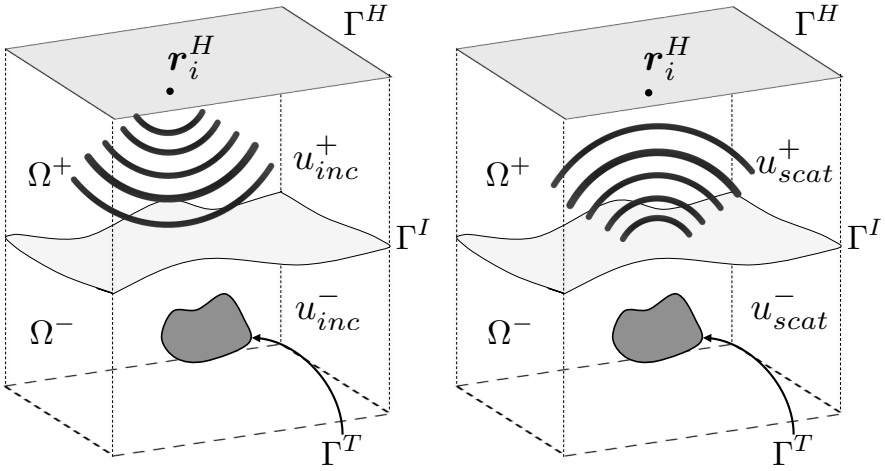

Figure 4.5: General setting for a holographic ground-penetrating simulation for a double domain or interface scenario showing the incident (left) and the scattered (right) wave.

4.2.2 Radar targets

For the examples to come in this chapter we will use totally reflecting screen radar targets with boundaries denoted by Γ^T. This will impose the following Neumann boundary condition on the exterior of the screen surface:

$$\frac{\partial u^-_{scat}}{\partial \boldsymbol{n}}(\boldsymbol{x}) = -\frac{\partial u^-_{inc}}{\partial \boldsymbol{n}}(\boldsymbol{x}), \text{ for } \boldsymbol{x} \in \Gamma^T. \tag{4.2}$$

This is in accordance with the more general conditions (4.1) when taken to be for a surface Γ^T considered totally reflective. In this case the transmitted scalar wave field is zero and that the exterior field is decomposed as $u^- = u^-_{inc} + u^-_{scat}$, yielding the stated boundary condition on Γ^T.

For the examples that follow we will consider an L-shaped screen radar target to provide a complex geometry that will allow us to test the resoling capacities of the ground-penetrating radar to be simulated. Let us consider the following parametric square-shaped horizontal screen:

$$\square^{a\times b}_{\boldsymbol{r}} = \left\{(x_1,x_2,x_3) : r_1 - \frac{a}{2} \leq x_1 \leq r_1 + \frac{a}{2},\ r_2 - \frac{b}{2} \leq x_2 \leq r_2 + \frac{b}{2},\ x_3 = r_3\right\}. \tag{4.3}$$

This parametric screen will prove useful in the definition of several surfaces in this chapter. We will use this parametric squared-shaped screen to define the radar target screen Γ^T as:

$$\Gamma^T = \left(\square^{0.2\times 0.1}_{(0.05,0,0)}\right) \bigcup \left(\square^{0.1\times 0.2}_{(0,0.05,0)}\right), \tag{4.4}$$

which is a 20cm wide and 20cm long L-shaped flat screen on the plane $x_3 = 0$. We will consider a conformal triangular approximation Γ^T_h for $h \approx 5$ millimeters. According to the requirements for the relation between h and the wavelength λ^- from Section 1.7, this should safely allow us to simulate up to frequencies resulting in $\lambda^- = 5$cm. Figure 4.6 shows the conformal triangular approximation Γ^T_h of Γ^T for $h \approx 5$ milimeters and 2872 triangles.

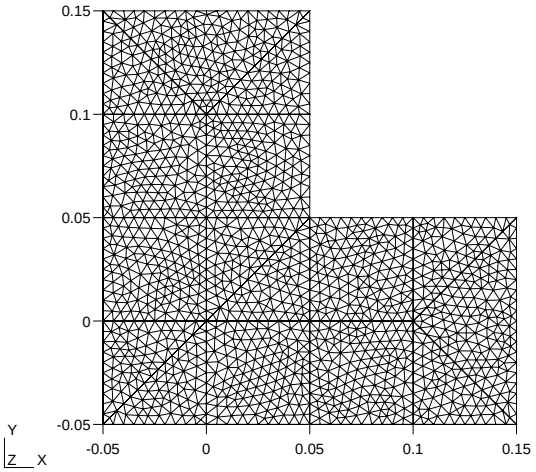

Figure 4.6: Conformal triangular approximation Γ^T_h of the radar target Γ^T for $h = 4.9$ milimeters resulting in 2872 triangles.

4.2.3 Computational cost and conditioning

In this subsection we will analyze the cost of computing the wave scattered by the underground screen target Γ^T described in (4.4) using conformal triangular meshes, the boundary element method, and the Galerkin matrix $\boldsymbol{N}_k^h$ from (3.168) in Definition 3.3.4 to solve the anti-symmetric Neumann Helmholtz problem for the screen Γ^T (Problem 1.3.12 for Neumann data (4.2)). We will consider and compare two ways of solving this problem: 1) directly solving the linear system for matrix $\boldsymbol{N}_k^h$ for screen as computed in Definition 3.3.4, and 2) preconditioning the matrix $\boldsymbol{N}_k^h$ using a preconditioner $\boldsymbol{M}_N^h$ computed as indicated in Subsection 3.3.4 before solving the linear system now for the preconditioned matrix $\boldsymbol{M}_N^h \cdot \boldsymbol{N}_k^h$. This second way of solving a linear system will be indexed by the superscript PC, meaning *preconditioned*, in the several variables we will define.

Let us consider different conformal triangular approximations Γ_h^T of the screen target Γ^T from (4.4) for different discretization parameters h. With each discretization parameters h we will associate the admissible shortest wavelength $\lambda^- = 10 \cdot h$, a highest admissible wavenumber $k_{=}2\pi/\lambda^-$ or a highest admissible simulation frequency $f = c^-/\lambda^-$, for an underground wave velocity c^-. For each progressively finer mesh approximation, indexed by h, we will compute the matrix $\boldsymbol{N}_{k^-}^h$ and solve the associated linear system using the GMRES iterative method, taking N_{iter} iterations to be solved. Likewise, we will also considered the preconditioned linear system for matrix $\boldsymbol{M}_N^h \cdot \boldsymbol{N}_{k^-}^h$ and solve it also using the GMRES iterative method, now taking N_{iter}^{PC} iterations. Table 4.1 shows the number of triangles N_T, and the admissible wavelength λ^- in the underground for the target Γ^T approximated by progressively finer triangular approximations Γ_h^T indexed by h. It also show the condition number of the associated preconditioned and unpreconditioned matrix, and the number of iterations required in each case.

Table 4.1: Condition number and number of iterations required to solve the linear system associated with unpreconditioned matrix $\boldsymbol{N}_k^h$ and with the preconditioned matrix $\boldsymbol{M}_N^h \cdot \boldsymbol{N}_k^h$ for progressively finer meshes for the L-shaped screen Γ^T using the GMRES iterative solver. The row for the radar target chosen in Subsection 4.2.2 has been highlighted.

N_T	h	λ^-	k^-	$\text{cond}_2(\boldsymbol{N}_{k^-}^h)$	N_{iter}	$\text{cond}_2(\boldsymbol{M}_N^h \boldsymbol{N}_{k^-}^h)$	N_{iter}^{PC}
176	0.019936	0.1993	31.5174	5.697	23	1.714	17
204	0.018175	0.1817	34.5792	6.758	25	1.777	18
388	0.013331	0.1333	47.1314	7.694	28	2.052	17
668	0.010116	0.1011	62.1132	8.381	63	2.495	18
1214	0.007398	0.0739	84.9305	11.486	82	3.047	22
2872	0.004969	0.0496	126.4352	12.984	122	6.730	29

It could be hastily concluded from Table 4.1 that applying matrix preconditioning might increase efficiency when solving a single direct problem, i.e., solving the backscattered wave when the target has been reached by the incoming wave coming from a single emitter at $\boldsymbol{r}_i^H$ in the hologram recording surface Γ^H. A closer look into the time-efficiency of the processes involved in preconditioning will indicate otherwise.

Let us consider the following definition of time lapses associated with different parts of the matrix computation and linear system solving in the context of the matrix preconditioning methods described in Chapter 3.

Definition 4.2.1 (Time lapses associated with linear systems solving and preconditioning)**.** *Let us consider the different conformal triangular approximations Γ_h^T (of the radar target Γ^T from (4.4)) referred to in Table 4.1 and indexed by the discretization parameter h. For the unpreconditioned linear system, let us define the following time lapses in seconds:*

- *$T_{setup}(h)$: Time required to compute the matrix $\boldsymbol{N}_{k^-}^h$ for Γ_h^T.*
- *$T_{GMRES}(h)$: Time required to compute the solution of the linear system using the GMRES iterative method once the linear system has been assembled.*

- $T_{LS}(h)$: *Time required to assemble and solve the linear associated with* $\boldsymbol{N}_{k^-}^h$ *given Neumann data* (4.2) *for a single direct problem for single emitter/receiver in* $\boldsymbol{r}_i^H \in \Gamma^H$, *i.e.,* $T_{setup}(h) + T_{GMRES}(h)$.

For the preconditioned linear system, let us define the following time lapses in seconds:

- $T_{PC}(h)$: *Time required to precondition matrix* $\boldsymbol{N}_{k^-}^h$ *for* Γ_h^T. *This includes the time required to compute matrix* $\boldsymbol{S}_{as}^h$ *from* (3.139) *in Definition 3.2.9, the time required to compute matrix* $\boldsymbol{D}_N^h$ *from* (3.142) *in Definition 3.3.1, the time required to invert it, the time required to compute matrix* $\boldsymbol{M}_N^h$ *from* (3.145) *in Definition 3.3.2 and the time multiply it by* $\boldsymbol{N}_{k^-}^h$.
- $T_{setup}^{PC}(h)$: *Time required to compute the matrix* $\boldsymbol{M}_N^h \cdot \boldsymbol{N}_{k^-}^h$ *for* Γ_h^T, *i.e.,* $T_{setup}(h) + T_{PC}(h)$.
- $T_{GMRES}^{PC}(h)$: *Time required to compute the solution of the preconditioned linear system using the GMRES iterative method once the linear system has been assembled.*
- $T_{LS}^{PC}(h)$: *Time required to assemble and solve the linear system associated with* $\boldsymbol{M}_N^h \cdot \boldsymbol{N}_{k^-}^h$ *given Neumann data* (4.2) *for a single direct problem for single emitter receiver in* $\boldsymbol{r}_i^H \in \Gamma^H$, *i.e.,* $T_{setup}^{PC}(h) + T_{GMRES}^{PC}(h)$.
- $T_{saved}(h)$: *Total time saved when solving a linear system for the anti-symmetric Neumann Helmholtz problem due to preconditioning, i.e.* $T_{LS}(h) - T_{LS}^{PC}(h)$.

Remark 4.2.1 (The time required to assemble right-hand sides is neglected)**.** *In the time lapses from Definition 4.2.1 the time required to assemble the right-hand side of the linear system has been intentionally neglected as its algorithmic complexity involved in doing so is significantly lower than the complexity involved in the other processes.*

Remark 4.2.2 (Times are dependent on the machine used)**.** *The time needed to assemble and solve a linear system also depends on the computer and the algorithms used. The matrix inversion algorithm was chosen from the Eigen library as stated in Remark 3.2.3 (not optimized for sparse matrices), and the machine used had a dual 3GHz Intel i7 core and 16GBytes of RAM memory. Both parameters could be optimized to improve the required processing times, but this wouldn't affect the argument made throughout this subsection.*

We will see that while preconditioned linear systems can be solved faster, the over time-efficiency is not always poised to improve. Table 4.2 shows, for the same progressively finer triangular approximations Γ_h^T of Γ^T indexed by h, some of the time durations from Definition 4.2.1.

Table 4.2: Time duration in seconds of the different processes involved in matrix assembling, preconditining and solving for progressively finer triangular approximation Γ_h^T of the screen radar target Γ^T.

N_T	h	T_{setup}	T_{GMRES}	T_{LS}	T_{setup}^{PC}	T_{GMRES}^{PC}	T_{LS}^{PC}	T_{saved}
176	0.019936	0.7288	0.0259	0.7548	4.2468	0.0169	4.2637	-3.5089
204	0.018175	0.9531	0.0311	0.9842	5.3685	0.0221	5.3907	-4.4064
388	0.013331	3.9945	0.0812	4.0758	18.2498	0.0357	18.2856	-14.2098
668	0.010116	11.199	0.4115	11.6111	47.4604	0.0974	47.5578	-35.9467
1214	0.007398	36.804	1.9721	38.7763	131.8325	0.7201	132.5525	-93.7762
2872	0.004969	236.57	10.3864	246.9604	652.3295	2.3754	654.7049	-407.7445

As anticipated, the last column of Table 4.2 shows that despite the fact that the proposed preconditioning strategy from Subsection 3.3.4 allows for faster solving of the associated linear system in less iterations, the overall time required for the assembly and solving of the linear systems can grow with mesh refinement and be less time-efficient. Although these particular

time lapses presented in Table 4.2 could be improved in view of Remark 4.2.2, the following exposition will make use of this chosen application example to show the relevance of improved algorithmic complexity as a motivation for the development preconditioning methods and acceleration/compression methods. This will be the case regardless of observations about the particular machine used and inversion algorithm chosen and commented in Remark 4.2.2. The other advantage of matrix preconditioning, i.e., improved accuracy, will not be tested.

Let us reconsider the global problem of simulating the radar acquisition process for a holographic ground-penetrating such as it described in Subsection 4.2.1, and let us analyze the time-cost of computing the scattering produced by the radar target Γ^T when illuminated by radio waves coming from N_{MMS} different sources placed in the hologram recording surface Γ^H. This is the so-called multi-monostatic scattering problem for positions $\{\boldsymbol{r}_i^H\}_{i=1}^{N_{MMS}}$.

Definition 4.2.2 (Time lapses associated with the multi-monostatic scattering problem for the radar target)**.** *Let us consider the different conformal triangular approximations Γ_h^T (of the radar target Γ^T from (4.4)) referred to in Table 4.1 and indexed by the discretization parameters h, the time lapses defined from Definition 4.2.1 and let N_{MMS} be a number of multi-monostatic scattering problems to be solved. Let us define the time in seconds needed to assemble and solve the linear system for the anti-symmetric Neumann Helmholtz problem:*

$$T_{MMS}(h, N_{MMS}) = T_{setup}(h) + N_{MMS} T_{GMRES}(h). \tag{4.5}$$

Likewise, let us define the time in seconds needed to assemble, precondition and solve the linear system for the anti-symmetric Neumann Helmholtz problem:

$$T_{MMS}^{PC}(h, N_{MMS}) = T_{setup}^{PC}(h) + N_{MMS} T_{GMRES}^{PC}(h). \tag{4.6}$$

Since the assembling and preconditioning of a matrix is only performed once for many Neumann data, i.e., different positions $\boldsymbol{r}_i^H$, the gain in time when solving the system will outweigh the time lost in preconditioning after a certain value of N_{MMS}. Let us consider the radar target from Subsection 4.2.2 and its discretization Γ_h^T highlighted on Tables 4.1 & 4.2, with 2872 triangles and $h \approx 5$mm, allowing for simulation frequencies resulting in wavelength down to $\lambda^- \approx 5$cm. Let us define the percent time gain for a given number N_{MMS} of emitting/receiving points in Γ^H:

$$T_{MMS}^{\%}(h, N_{MMS}) = 100 \cdot \frac{T_{MMS}(h, N_{MMS}) - T_{MMS}^{PC}(h, N_{MMS})}{T_{MMS}(h, N_{MMS})}, \tag{4.7}$$

which can be easily shown to be equal to

$$T_{MMS}^{\%}(h, N_{MMS}) = 100 \cdot \frac{N_{MMS}\left(T_{GMRES}(h) - T_{GMRES}^{PC}(h)\right) - T_{PC}(h)}{N_{MMS}\, T_{GMRES}(h) + T_{setup}(h)}. \tag{4.8}$$

The limit value, also directly obtainable, exemplifies the usefulness of the improvements leading to increased time-efficiency of linear system solving in problems requiring the solution for a massive number of different right-hand side data:

$$T_{MMS}^{\%}(h, N_{MMS}) \xrightarrow[N_{MMS}\to\infty]{} 100 \cdot \frac{T_{GMRES}(h) - T_{GMRES}^{PC}(h)}{T_{GMRES}(h)}. \tag{4.9}$$

Figure 4.7 shows the evolution of $T_{MMS}^{\%}(h, N_{MMS})$ for the chosen radar target approximation Γ^T from Subsection 4.2.2, for $h = 0.0049695$ and $N_T = 2872$ and to be used in the subsequent simulations, for an increasing number N_{MMS} of multi-monostatic radar measuring points in the hologram recording surface Γ^H.

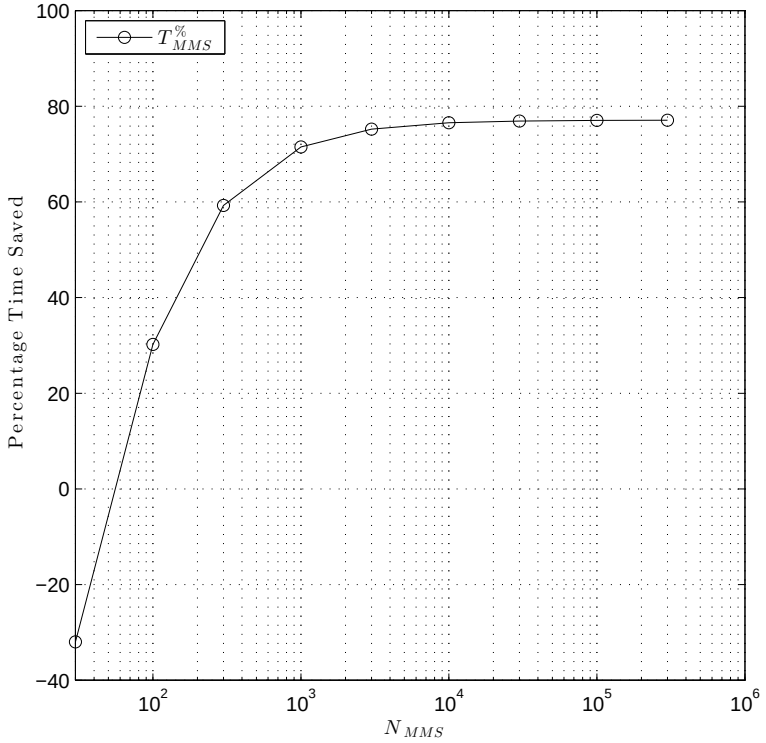

Figure 4.7: Evolution of $T^{\%}_{MMS}(h, N_{MMS})$ for the chosen radar target approximation Γ^T_h, for $h = 0.0049695$ and $N_T = 2872$ for an increasing number N_{MMS} of multi-monostatic radar measuring points in the hologram recording surface Γ^H

4.2.4 Air-ground interface, hologram recording surfaces, and imaging surfaces

In this subsection we will describe three surfaces of importance to the modeling of the radar system: the air-ground interface surface Γ^I, the hologram recording surface Γ^H, and the imaging surface Γ^R.

For the cases presented in this chapter we will consider the air-ground interface surface Γ^I to be an aperture surface from where the radio waves will enter and then exit the underground. For the purposes of the following exposition, we will describe it parametrically in $\mathbb{R}^3$, fixing a given range in x_1 and x_2, where it will be inscribed, and describing the height of the interface surface with a function f_I of these two variables:

$$\Gamma^I = \{(x_1, x_2, x_3) : -0.5 \leq x_1, x_2 \leq 0.5,\, x_3 = f_I(x_1, x_2)\}\,. \tag{4.10}$$

When specifying an interface surface, a range for x_1 and x_2 will be provided along with a given resolution δ^I determining the number N_I of area elements to be used in computations. These area elements are arranged in a rectangular grid.

Figure 4.8 shows a discretized approximation of surface Γ^I for the function f_I the function, e.g.,

$$f_I(x_1, x_2) = \frac{7}{20} - \frac{1}{2}(x_1^2 + x_2^2). \tag{4.11}$$

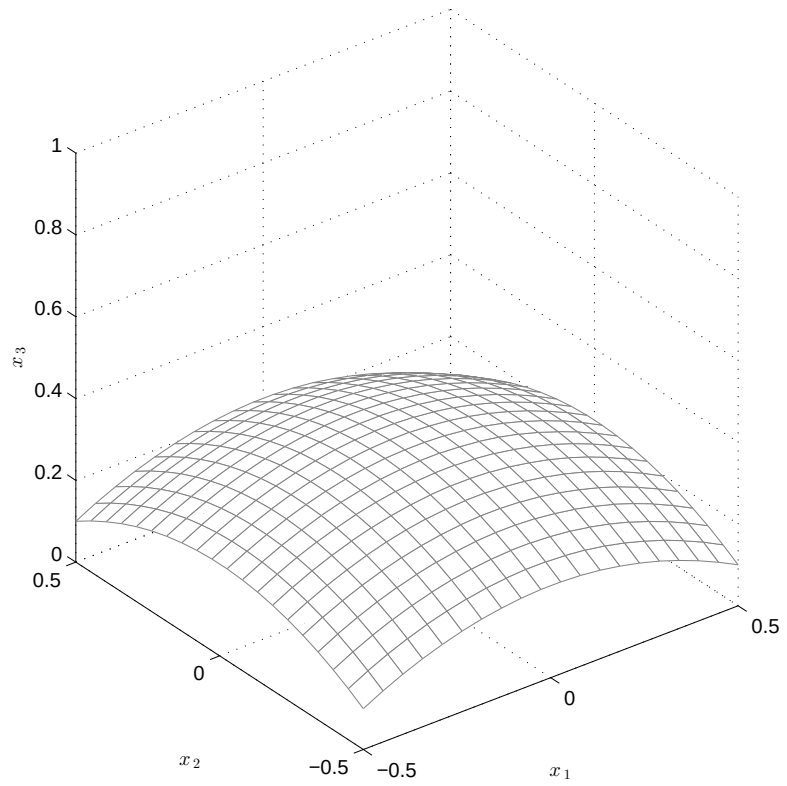

Figure 4.8: Rectangular grid approximation of Γ_h^I of surface Γ^I, made of 400 elements (for illustrative purposes) for the function f_I from (4.11)

The hologram recording surface Γ^H is the surface that contains all sample points where the monostatic holographic radar measurement are taken. In the case of a switching line array of antennas moving at a height above the ground, as described in Subsection 4.1.2, the result is most often a plane in three-dimensional space. In our examples, we will consider in fact a plane which we will describe using the parametric square-shaped screen from (4.3) as:

$$\Gamma^H = \square_{\boldsymbol{r}_H}^{a\times b}. \tag{4.12}$$

When specifying a hologram recording surface, a, b, and $\boldsymbol{r}_H$ will be provided along with a given resolution δ^H determining sampling points $\{\boldsymbol{r}_i^H\}_{i=1}^{N_{MMS}} \subset \Gamma^H$ for the multi-monostatic configuration using a rectangular grid such that

$$N_{MMS} = \frac{ab}{(\delta^H)^2}. \tag{4.13}$$

The recorded hologram is $\mathcal{H}\left(\Gamma^H\right) \to \mathbb{C}$, so that for a sampling point $\boldsymbol{r}_i^H \in \Gamma^H$ the value $\mathcal{H}\left(\boldsymbol{r}_i^H\right)$ is the complex value of the backscattered radio wave: $u_{scat}^-(\boldsymbol{r}_i^H)$ (in the context of a single underground domain) or $u_{scat}^+(\boldsymbol{r}_i^H)$ (in the context of a double domain of interface problem). The complex value of a backscattered radio wave will provide us with the amplitude and phase information needed for a holographic ground-penetrating radar image reconstruction. Given a fixed hologram recording surface Γ^H, taking enough sample points $\{\boldsymbol{r}_i^H\}_{i=1}^{N_{MMS}}$ (choosing a sufficiently small δ^H) allows for the determination of the map $\mathcal{H}$ through interpolation, and the magnitude of the values $\mathcal{H}(\boldsymbol{r}_i^H)$ for $i = 1...N_{MMS}$ can be regarded as the pixel values of the holographic image recorded on Γ^H.

Finally, we will describe the imagining surface where the reflectivity values of the underground will be computed using the holographic ground-penetrating radar and the imaging principle to be described. Similarly to the description of Γ^H, we will define the reflectivity imaging surface using the parametric square-shaped screen surface (4.3) as:

$$\Gamma^R = \square^{c\times d}_{\boldsymbol{r}_R}. \tag{4.14}$$

Unlike for the hologram recording surface, for all the examples presented we will consider $c = d = 1$m, a resolution of $\delta^R = 1$cm, and we will put the imaging surface at the center of the target Γ^T, setting $\boldsymbol{r}_R = (0, 0, 0)$.

Using the reflective imaging surface Γ^R, the recorded reflectivity image will be $\mathcal{R}\left(\Gamma^R\right) \to \mathbb{C}$, so that for a sampling point $\boldsymbol{r}_i^R \in \Gamma^R$ the value $\mathcal{R}\left(\boldsymbol{r}_i^R\right)$ is the complex reflectivity reconstructed using the imaging principle to be described in the next section. Given a fixed image recording surface Γ^R, taking enough sample points $\{\boldsymbol{r}_i^R\}_{i=1}^{N_R}$ (choosing a sufficiently small δ^R, with $N_R = cd/(\delta^R)^2$) allows for the determination of the map $\mathcal{R}$ through interpolation, and the magnitude of the values $\mathcal{R}(\boldsymbol{r}_i^R)$ for $i = 1...N_R$ can be regarded as the pixel values of the reconstructed reflectivity image recorded on Γ^R.

4.2.5 Simulating single domain and interface problems

In this subsection we will show the results of example simulations of wave propagation in the prescribed scenarios, i.e., for a single underground domain scenario and for a double domain or interface scenario. In both cases we will use the radar target Γ^T described in Subsection 4.2.2. We will position a single emitter in an arbitrary position and we will compute the incident scalar wave field u_{inc} and the scattered scalar wave field created by the L-shaped screen radar target Γ^T contained in the plane $x_3 = 0$. In providing these examples we will show how to compute incident wave scattering and backscattered waves, especially when they travel across an interface surface Γ^I separating the above ground and the underground domains using an aperture model. These simulations will be explained and performed for a single monostatic holographic radar acquisition from a single sampling point $\boldsymbol{r}_i^H$.

For the results described and exemplified in this subsection, we will consider the single emitter to be in $\boldsymbol{r}_i^H = (0.5, 0, 1.1)$, and we will plot the values of the real part of the incident wave field u_{inc} and the backscattered field u_{scat} on a plane $\Pi_{x_2=0}$ given by:

$$\Pi_{x_2=0} = \{(x_1, x_2, x_3) : x_2 = 0,\, -0.5 \leq x_1 \leq 0.5,\, -0.1 \leq x_3 \leq 0.7\}. \tag{4.15}$$

The description exhibited here for the computation of the scattered fields will be applied in the next section to compute recorded holograms $\mathcal{H}$ to be used in imaging algorithms that will provide reflectivity images of the underground.

Single underground domains

The following definition will state the procedure for computing a single direct problem for a single emitter/receiver in a single underground domain scenario. This will then be used in the next section to compute recorded hologram data $\mathcal{H}$ using this procedure for each emitting/receiving point.

Definition 4.2.3 (Single underground domain wave computation)**.** *For a single monostatic direct problem computation the procedure is as follows:*

1. *Select an emitting/receiving point* $\boldsymbol{r}_i^H$.
2. *Compute* u^-_{inc} *in* Ω^- *as* $u^-_{inc}(\boldsymbol{y}) = G^{k^-}(\boldsymbol{r}_i^H, \boldsymbol{y})$ *for* $\boldsymbol{y} \in \Omega^-$.

3. *Compute the Neumann data of the scattered field on the surface of* Γ^T *as*

$$\frac{\partial u^-_{scat}}{\partial \boldsymbol{n_y}}(\boldsymbol{y}) = -\frac{\partial u^-_{inc}}{\partial \boldsymbol{n_y}}(\boldsymbol{y}), \quad \text{for } \boldsymbol{y} \in \Gamma^T. \tag{4.16}$$

4. *Assemble and compute the linear system for the discrete variational formulation of*

$$-\mathcal{N}^{k^-}\mu = \frac{\partial u^-_{scat}}{\partial \boldsymbol{n_y}}(\boldsymbol{y}). \tag{4.17}$$

5. *Solve the jump of the Dirichlet traces* μ.

6. *Compute the scattered scalar wave field* u^-_{scat} *as* $u^-_{scat}(\boldsymbol{y}) = -\mathcal{D}^{k^-}\mu(\boldsymbol{y})$ *for* $\boldsymbol{y} \in \Omega^-$.

7. *Compute the value of the recorded hologram at* $\boldsymbol{r}_i^H$ *as* $u^-_{scat}(\boldsymbol{r}_i^H)$.

In the following example, there is only one unbounded propagation domain Ω^-, with propagation parameters described in Table 4.3.

Table 4.3: Parameters for the single underground domain example simulations

	Parameter	Value	Units
Domain Ω^-	λ^-	5	cm
	k^-	125.66	cm^{-1}
Target	Γ^T_h	(4.4)	
	h	5	mm

Figure 4.9 shows an example computation of radio wave propagation in a single underground domain scenario using the radar target Γ^T described in Subsection 4.2.2 using parameters from Table 4.3 and the procedure from Definition 4.2.3.

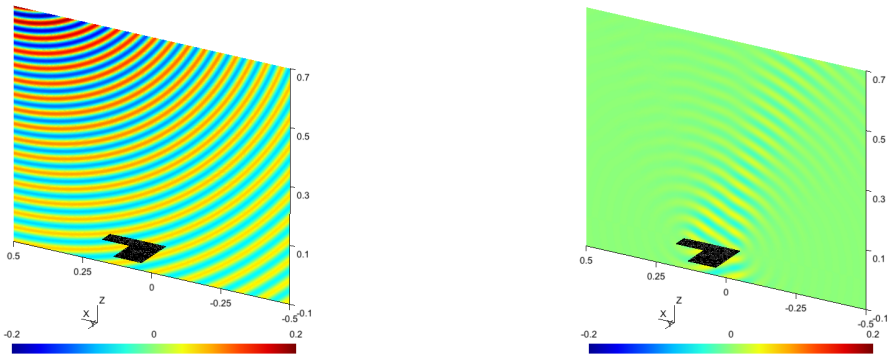

Figure 4.9: Example computation of radio wave propagation in a single underground domain scenario using the radar target Γ^T described in Subsection 4.2.2 using parameters from Table 4.3 and the procedure from Definition 4.2.3. The real values of the scalar wave fields u_{inc} (left) and u_{scat} (right) are plotted on the plane $\Pi_{x_2=0}$.

Double domain or interface problems

In order to compute incident and scalar fields across an aperture interface surface Γ^I we will consider the Kirchhoff's diffraction formula [12, Section 8.3.2]. For known traces of u^-_{inc} and $\frac{\partial u^-_{inc}}{\partial \boldsymbol{n}}$ on Γ^I from Ω^-, we compute

$$u^-_{inc}(\boldsymbol{y}) = \int_{\Gamma^I} \left[u^-_{inc}(\boldsymbol{x}) \frac{\partial}{\partial \boldsymbol{n_x}} G^{k^-}(\boldsymbol{x}, \boldsymbol{y}) - G^{k^-}(\boldsymbol{x}, \boldsymbol{y}) \frac{\partial u^-_{inc}}{\partial \boldsymbol{n_x}}(\boldsymbol{x}) \right] d\Gamma^I(\boldsymbol{x}), \quad \text{for } \boldsymbol{y} \in \Omega^-. \tag{4.18}$$

For known traces of u^+_{scat} and $\frac{\partial u^+_{scat}}{\partial \boldsymbol{n}}$ on Γ^I from Ω^+, we compute

$$u^+_{scat}(\boldsymbol{y}) = -\int_{\Gamma^I} \left[u^+_{scat}(\boldsymbol{x}) \frac{\partial}{\partial \boldsymbol{n}_{\boldsymbol{x}}} G^{k^+}(\boldsymbol{x},\boldsymbol{y}) - G^{k^+}(\boldsymbol{x},\boldsymbol{y}) \frac{\partial u^+_{scat}}{\partial \boldsymbol{n}_{\boldsymbol{x}}}(\boldsymbol{x}) \right] d\Gamma^I(\boldsymbol{x}), \quad \text{for } \boldsymbol{y} \in \Omega^+. \tag{4.19}$$

The successful modeling of the propagation across surface Γ^I using the previously enunciated Kirchhoff's diffraction formula for the to cases of interest assumes that dist $\left(\Gamma^I, \boldsymbol{y}\right) \gg \lambda_{\pm}$.

Definition 4.2.4 (Double domain interface wave computation)**.** *For a single monostatic direct problem computation the procedure is as follows:*

1. *Select an emitting/receiving point* $\boldsymbol{r}^H_i$.
2. *Compute* u^+_{inc} *in* Ω^+ *as* $u^+_{inc}(\boldsymbol{y}) = G^{k^+}(\boldsymbol{r}^H_i, \boldsymbol{y})$ *for* $\boldsymbol{y} \in \Omega^+$.
3. *Compute the values of* u^+_{inc} *and* $\frac{\partial u^+_{inc}}{\partial \boldsymbol{n}}$ *at* Γ^I *as*

$$u^+_{inc}(\boldsymbol{y}) = G^{k^+}(\boldsymbol{r}^H_i, \boldsymbol{y}) \quad \text{and} \quad \frac{\partial u^+_{inc}}{\partial \boldsymbol{n}_{\boldsymbol{y}}} = \frac{\partial}{\partial \boldsymbol{n}_{\boldsymbol{y}}} G^{k^+}(\boldsymbol{r}^H_i, \boldsymbol{y}) \quad \text{for } \boldsymbol{y} \in \Gamma^I. \tag{4.20}$$

4. *Compute the values of* u^-_{inc} *and* $\frac{\partial u^-_{inc}}{\partial \boldsymbol{n}}$ *at* Γ^I *as*

$$u^-_{inc}(\boldsymbol{y}) = u^-_{inc}(\boldsymbol{y}) \quad \text{and} \quad \frac{\partial u^-_{inc}}{\partial \boldsymbol{n}_{\boldsymbol{y}}} = n^2 \frac{\partial u^+_{inc}}{\partial \boldsymbol{n}_{\boldsymbol{y}}} \quad \text{for } \boldsymbol{y} \in \Gamma^I, \tag{4.21}$$

   with $n = \lambda^+/\lambda^-$.

5. *Compute* u^-_{inc} *in* Ω^- *as*

$$u^-_{inc}(\boldsymbol{y}) = \int_{\Gamma^I} \left[u^-_{inc}(\boldsymbol{x}) \frac{\partial G^{k^-}}{\partial \boldsymbol{n}_{\boldsymbol{x}}}(\boldsymbol{x},\boldsymbol{y}) - G^{k^-}(\boldsymbol{x},\boldsymbol{y}) \frac{\partial u^-_{inc}}{\partial \boldsymbol{n}_{\boldsymbol{x}}}(\boldsymbol{x}) \right] d\Gamma^I(\boldsymbol{x}), \quad \text{for } \boldsymbol{y} \in \Omega^-. \tag{4.22}$$

6. *Compute the normal derivative of* u^-_{inc} *on* Γ^T *as*

$$\frac{\partial u^-_{inc}}{\partial \boldsymbol{n}_{\boldsymbol{y}}}(\boldsymbol{y}) = \int_{\Gamma^I} \left[u^-_{inc}(\boldsymbol{x}) \frac{\partial^2 G^{k^-}}{\partial \boldsymbol{n}_{\boldsymbol{x}} \partial \boldsymbol{n}_{\boldsymbol{y}}}(\boldsymbol{x},\boldsymbol{y}) - \frac{\partial G^{k^-}}{\partial \boldsymbol{n}_{\boldsymbol{y}}}(\boldsymbol{x},\boldsymbol{y}) \frac{\partial u^-_{inc}}{\partial \boldsymbol{n}_{\boldsymbol{x}}}(\boldsymbol{x}) \right] d\Gamma^I(\boldsymbol{x}), \quad \text{for } \boldsymbol{y} \in \Gamma^T. \tag{4.23}$$

7. *Compute the Neumann data of the scattered field on the surface of* Γ^T *as*

$$\frac{\partial u^-_{scat}}{\partial \boldsymbol{n}_{\boldsymbol{y}}}(\boldsymbol{y}) = -\frac{\partial u^-_{inc}}{\partial \boldsymbol{n}_{\boldsymbol{y}}}(\boldsymbol{y}), \quad \text{for } \boldsymbol{y} \in \Gamma^T. \tag{4.24}$$

8. *Assemble the linear system for the discrete variational formulation of*

$$-\mathcal{N}^{k^-}\mu = \frac{\partial u^-_{scat}}{\partial \boldsymbol{n}_{\boldsymbol{y}}}(\boldsymbol{y}). \tag{4.25}$$

9. *Solve the jump of the Dirichlet traces* μ.
10. *Compute the scattered scalar wave field* u^-_{scat} *as* $u^-_{scat}(\boldsymbol{y}) = -\mathcal{D}^{k^-}\mu(\boldsymbol{y})$ *for* $\boldsymbol{y} \in \Omega^-$.

11. *Compute the values of* u^-_{scat} *and* $\frac{\partial u^-_{scat}}{\partial \boldsymbol{n}}$ *at* Γ^I *as*

$$u^-_{scat}(\boldsymbol{y}) = -\mathcal{D}^{k^-}\mu(\boldsymbol{y}) \quad \text{and} \quad \frac{\partial u^-_{scat}}{\partial \boldsymbol{n_y}} = -\frac{\partial}{\partial \boldsymbol{n_y}}\mathcal{D}^{k^-}\mu(\boldsymbol{y}) \quad \text{for } \boldsymbol{y} \in \Gamma^I. \tag{4.26}$$

12. *Compute the values of* u^+_{scat} *and* $\frac{\partial u^+_{scat}}{\partial \boldsymbol{n}}$ *at* Γ^I *as*

$$u^+_{scat}(\boldsymbol{y}) = u^-_{scat}(\boldsymbol{y}) \quad \text{and} \quad \frac{\partial u^+_{scat}}{\partial \boldsymbol{n_y}} = \frac{1}{n^2}\frac{\partial u^-_{scat}}{\partial \boldsymbol{n_y}} \quad \text{for } \boldsymbol{y} \in \Gamma^I, \tag{4.27}$$

with $n = \lambda^+/\lambda^-$.

13. *Compute* u^+_{scat} *in* Ω^+ *as*

$$u^+_{scat}(\boldsymbol{y}) = -\int_{\Gamma^I}\left[u^+_{scat}(\boldsymbol{x})\frac{\partial G^{k^+}}{\partial \boldsymbol{n_x}}(\boldsymbol{x},\boldsymbol{y}) - G^{k^+}(\boldsymbol{x},\boldsymbol{y})\frac{\partial u^+_{scat}}{\partial \boldsymbol{n_x}}(\boldsymbol{x})\right]d\Gamma^I(\boldsymbol{x}), \quad \text{for } \boldsymbol{y} \in \Omega^+. \tag{4.28}$$

14. *Compute the value of the recorded hologram at* $\boldsymbol{r}^H_i$ *as* $u^+_{scat}(\boldsymbol{r}^H_i)$.

In the following example, there are two unbounded propagation domains, the underground $\Omega-$, and the above-ground Ω^+, with propagation parameters described in Table 4.4.

Table 4.4: Parameters for double domain example simulations

	Parameter	Value	Units
Domain Ω^-	λ^-	5	cm
	k^-	125.66	cm^{-1}
Domain Ω^+	λ^+	10	cm
	k^+	62.83	cm^{-1}
	$n = \lambda^+/\lambda^-$	2	dimensionless
Interface Γ^I	f_I	(4.11)	m
Target	Γ^T	(4.4)	m
	h	5	mm

Figures 4.10 & 4.11 shows an example computation of radio wave propagation in a double domain scenario using the radar target Γ^T described in Subsection 4.2.2 using parameters from Table 4.4, using the interface surface from Subsection 4.2.4 and the procedure from Definition 4.2.4.

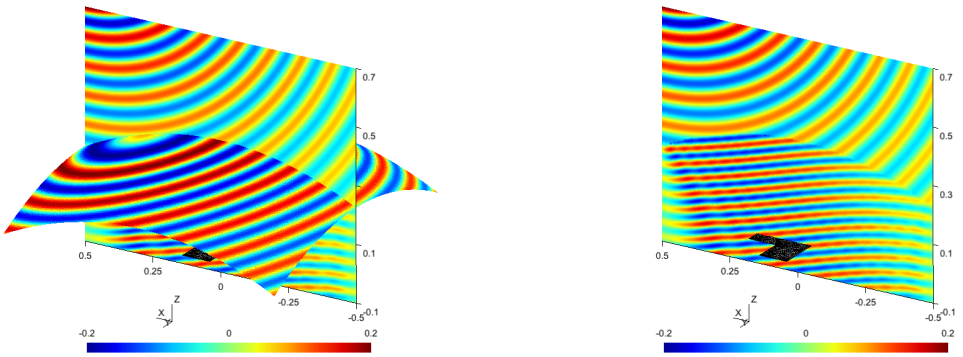

Figure 4.10: Incident wave field example computation of radio wave propagation in a double domain scenario using the radar target Γ^T described in Subsection 4.2.2 using parameters from Table 4.4 and the procedure from Definition 4.2.4. The real part of the incident scalar wave field u_{inc} is shown with its values on Γ^I (left) and on the plane $\Pi_{x_2=0}$ (right).

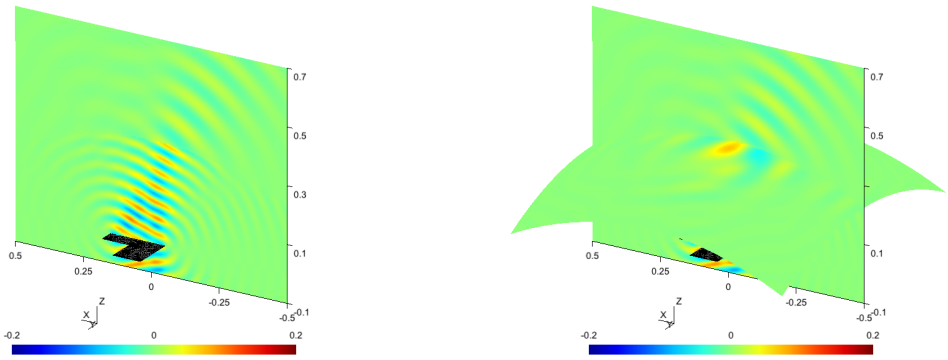

Figure 4.11: Scattered wave field example computation of radio wave propagation in a double domain scenario using the radar target Γ^T described in Subsection 4.2.2 using parameters from Table 4.4 and the procedure from Definition 4.2.4. The real part of the scattered scalar wave field u_{scat} is shown with its values on the plane $\Pi_{x_2=0}$ (left) and on Γ^I (right).

4.3 A type of subsurface holographic radar

Given a configuration for radar acquisition in a scenario in which radar target Γ^T is buried in the underground Ω^-, and there is possibly a surface Γ^I separating it from an above-ground domain Ω^+, multi-monostatic holographic radar measurements can be taken on a recording hologram surface Γ^H to determine the map $\mathcal{H}$, as described in Subsection 4.2.4. An imaging method uses an imaging principle, the holographic data measurement represented by the map $\mathcal{H}$, possibly the knowledge of a known interface Γ^I, and the physical parameters of the media to compute a reflectivity complex map $\mathcal{R}$ on a reflectivity image surface Γ^R. The magnitude of the values of this map on the surface Γ^R is the reflectivity image that signals the possible presence of a reflective radar target buried at the position where that reflectivity image surface has been computed.

In this section we will describe a type of imaging principle and method for the holographic ground-penetrating radar. We will explain the motivations and assumptions behind it, and we will propose simplifications leading to new methods. These motivations are not the improvement of the quality or robustness of the capacities to identify a reflective target, but the reduction of the cost and an increase of the speed in doing so. In fact, we will present principles and methods that will progressively rely on more stringent assumptions that will allow for faster image computations at the expense of robustness and quality. This provides, on the other hand, the motivation for efficient simulation tools capable of predicting the performance of such imaging methods and thus assessing their usefulness despite the lack of robustness in many scenarios of interest. It is precisely the point that, through efficient simulation, the spectrum of scenarios on which these methods can be relied upon may be correctly delimited.

We will begin by explaining the imaging principle used by the radar type chosen as motivation, as explained in Section 4.1 and especially, in Subsection 4.1.2. We will also provide a general framework for holographic radar imaging. We will present an imaging method based on that principle for single underground domain scenarios and subsequent adaptations for double domains or interface scenarios. We will provide image reconstructions for several cases of interest giving some insight into the capabilities of the studied radar system while showing the usefulness of the proposed simulation methods in such endeavor.

4.3.1 Holographic radar imaging and principles

Given a scenario for ground-penetrating radar analysis such as those given in Subsection 4.2.1, the result of performing multi-monostatic radar acquisition provides the following available data:

- A hologram recording surface Γ^H.
- A set of multi-monostatic holographic radar measurements $\{c_i^H\}_{i=1}^{N_{MMS}}$ taken at sample points $\{\boldsymbol{r}_i^H\}_{i=1}^{N_{MMS}} \subset \Gamma^H$. Through interpolation this provides the mapping $\mathcal{H} : \Gamma^H \to \mathbb{C}$.
- A chosen reflective image surface Γ^R on which to compute the complex reflectivity map $\mathcal{R} : \Gamma^T \to \mathbb{C}$.
- Knowledge of the physical parameters of the underground. In our case λ^-, (k^-).
- If the scenario has an interface surface, it's geometry is also assumed to be known, so that the geometrical object Γ^I is defined, as well as the physical parameters of the above-ground domain. In our case λ^+, (k^+).

The position and the shape of the radar target is not know. But, a reflectivity image surface has been chosen on which to compute the reflectivity of the underground on that area.

A general holographic imaging method can be expressed as a family of filter functions $\mathcal{F} : \Gamma^H \times \Gamma^R \to \mathbb{C}$ such that the complex reflectivity image is computed as

$$\mathcal{R}(\boldsymbol{y}) = \int_{\Gamma^H} \mathcal{F}(\boldsymbol{x}, \boldsymbol{y}) \mathcal{H}(\boldsymbol{x}) d\Gamma^H(\boldsymbol{x}), \quad \text{for } \boldsymbol{y} \in \Gamma^R. \tag{4.29}$$

In the case of a double domain or interface scenario, where the above-ground is separated from the underground by a surface Γ^I, the filter function depends on the interface surface and is denoted as $\mathcal{F}_I : \Gamma^H \times \Gamma^R \to \mathbb{C}$, resulting in a complex reflectivity image

$$\mathcal{R}(\boldsymbol{y}) = \int_{\Gamma^H} \mathcal{F}_I(\boldsymbol{x}, \boldsymbol{y}) \mathcal{H}(\boldsymbol{x}) d\Gamma^H(\boldsymbol{x}), \quad \text{for } \boldsymbol{y} \in \Gamma^R. \tag{4.30}$$

The principles and methods used in what follows come from geometrical optics, especially in it's use of Snell's law for radio waves. Other techniques have used geometrical optics and Snell's law in ground-penetrating technologies, but mostly for time-domain radars [7,53,59,67]. Under this approach, radio waves are being treated under the assumption that wavelengths are considerably smaller than all other geometrical distances and magnitudes in consideration. The imaging principle on which the methods here considered are base on, is the so-called conjugate-phase matching (CPM) principle [23, 50], and it is based on the principle of minimum optical path length. In this context, the optical path length, or optical distance, is the product of the geometric length of a wave path through an optical system, and the refraction index of the medium where the wave propagates. The minimum optical path length between two points is then the shortest between all possible wave paths joining the two points. The stated assumption in which the wavelength of a time-harmonic radio wave is much smaller than all other geometrical distances in consideration is crucial to the meaningfulness of the optical path length. This assumption will soon prove to be excessive for ground-penetrating radars, and it is one of the elements that compromise the robustness of these imaging methods in exchange for speed and simplicity.

The conjugate-phase matching principle uses a conjugate phase propagation function G_c^k and the minimum optical path length, under geometrical optics' assumptions, to provide a measure of phase coherence between the observed holographic data contained in the map $\mathcal{H}$, and a possible reflective target at a given position in Γ^R. Given the fundamental solution governing wave propagation in the framework described in Section 1.4, the conjugate phase propagation function uses the minimum optical path length, hereinafter called ℓ, as:

$$G_c^k(\ell) = e^{-\mathrm{i}k\ell}. \tag{4.31}$$

In the next subsection we will provide an explicit expression for $\mathcal{F}$ for the case of a single underground domain that will illustrate how the minimum optical path length is used by the conjugate-phase matching holographic imaging method. This method was described and tested by Giubbolini and Sambuelli in [23] for single underground domains.

4.3.2 Imaging method for single underground domain scenarios

Given $\boldsymbol{x} \in \Gamma^H$ and $\boldsymbol{y} \in \Gamma^R$, the minimum optical path length of the round-trip path is the geometrical distance between the two points, i.e. $2\left\|\boldsymbol{x} - \boldsymbol{y}\right\|$, times the refraction index n_- for the underground domain:

$$\ell(\boldsymbol{x}, \boldsymbol{y}) = 2n_- \left\|\boldsymbol{x} - \boldsymbol{y}\right\|. \tag{4.32}$$

Being Ω^- the only domain under consideration, the refraction index can be set to $n_- = 1$ setting Ω^- as the reference propagation domain. The filter function for the single underground domain scenario in the conjugate-phase matching method is then given by

$$\mathcal{F}(\boldsymbol{x}, \boldsymbol{y}) = G_c^{k^-}(\ell(\boldsymbol{x}, \boldsymbol{y})) = e^{-\mathrm{i}k^- 2\|\boldsymbol{x}-\boldsymbol{y}\|}. \tag{4.33}$$

The complex reflectivity image can be then computed as:

$$\mathcal{R}(\boldsymbol{y}) = \int_{\Gamma^H} e^{-\mathrm{i}k^- 2\|\boldsymbol{x}-\boldsymbol{y}\|} \mathcal{H}(\boldsymbol{x}) d\Gamma^H(\boldsymbol{x}), \quad \text{for } \boldsymbol{y} \in \Gamma^R, \tag{4.34}$$

or in its discrete version, using the points from the rectangular grid defined in Subsection 4.2.4 for Γ^H and Γ^R, as:

$$\mathcal{R}(\boldsymbol{r}_i^R) = (\delta^H)^2 \sum_{j=1}^{N_{MMS}} e^{-\mathrm{i}k^- 2\|\boldsymbol{r}_j^H - \boldsymbol{r}_i^R\|} \mathcal{H}(\boldsymbol{r}_j^H), \quad \text{for } i = 1...N_R. \tag{4.35}$$

In what follows we will provide an example of complex image reconstruction using the algorithm described in this subsection and synthesized in (4.35). As for the rest of the reconstruction examples of complex reflectivity images given in this chapter, we will present a table summarizing the main parameters for the considered scenario, for the multi-monostatic holographic radar acquisition, and for the image reconstruction.

Table 4.5 shows the parameters used for a multi-monostatic simulation and image reconstruction using a single underground scenario.

Table 4.5: Parameters used for a multi-monostatic simulation and image reconstruction using a single underground scenario

	Parameter	Value	Units
Domain Ω^-	λ^-	5	cm
	k^-	125.66	m^{-1}
Hologram $\mathcal{H}$	Γ^H	$\square^{1\times1}_{(0,0,1)}$	meters
	δ^H	2.5	cm
Image $\mathcal{R}$	Γ^R	$\square^{1\times1}_{(0,0,0)}$	meters
	δ^R	1	cm
	Method	(4.35)	
Target	Γ^T	(4.4)	m
	h	5	mm

The following figures show the scenario for the simulated multi-monostatic holographic radar acquisition and the magnitude of the maps $\mathcal{H}$ on Γ^H, and $\mathcal{R}$ on Γ^R. The values of $\mathcal{R}$ are represented on an arbitrary reflectivity scale.

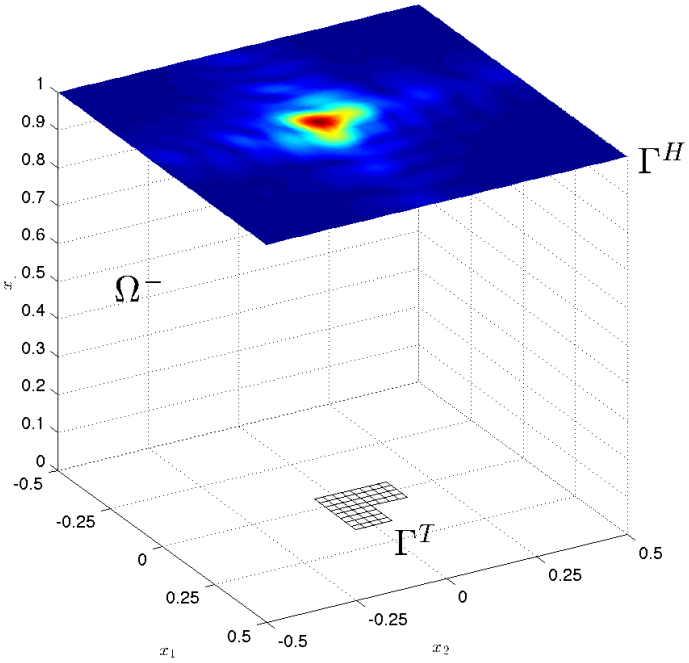

Figure 4.12: Scenario for the simulated multi-monostatic holographic radar acquisition using parameters of Table 4.5, showing the underground propagation domain, the radar target, and Γ^H with the magnitude of the values of $\mathcal{H}$ painted on.

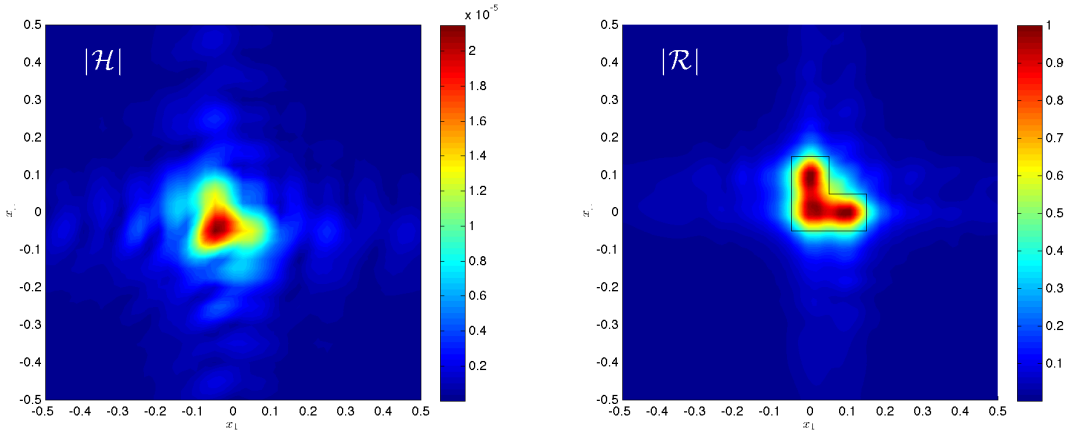

Figure 4.13: Magnitude of the values of the map $\mathcal{H}$ painted on Γ^H (left), and magnitude of the values of the map $\mathcal{R}$ painted on Γ^R (right) using parameters of Table 4.5. The known shape of the radar target Γ^T has been drawn on the reflectivity image on the right as a reference.

As seen in Figure 4.13, the method proposed in [23], synthesized in (4.35) for our framework, is capable of generating a reflectivity image $\mathcal{R}$ where the radar target Γ^T can be resolved using the parameters given in Table 4.5. In the next subsection, we will extend the principles used to the case of a radar scenario with an above-ground and an underground domain separated by a non-flat interface. We will draw inspiration from geometrical optics techniques mentioned in Subsection 4.3.1 and in particular from [14] for the treatment of the interface as a lens.

4.3.3 Imaging method for double domains scenarios

When the scenario consists of an above-ground domain Ω^+, and an underground domain Ω^- separated by an interface surface Γ^I, the application of the same method using the principle of minimum path length becomes a more difficult task. This is because now the determination of the minimum path length for the round-trip from a point on the hologram recording surface and a point in the imaging surface is not trivial as it was in (4.32). We will consider all possible round-trips between $\boldsymbol{x}$ and $\boldsymbol{y}$, then we will consider the subset of those complying with Snell's law for the paths' entrance and exit across Γ^I, and finally we will choose the one with the minimum optical path length.

A given (possibly non-physical) round-trip between points $\boldsymbol{x} \in \Gamma^H$ and $\boldsymbol{y} \in \Gamma^R$, can be decomposed in the incident go trip from $\boldsymbol{x}$ to $\boldsymbol{y}$, crossing Γ^I at $\boldsymbol{r}^I_{inc}$, and the scattered return trip from $\boldsymbol{y}$ to $\boldsymbol{x}$, crossing Γ^I at $\boldsymbol{r}^I_{scat}$. We will consider the following geometrical distances:

$$l^+_{inc} = \left\|\boldsymbol{x} - \boldsymbol{r}^I_{inc}\right\|, \quad l^-_{inc} = \left\|\boldsymbol{y} - \boldsymbol{r}^I_{inc}\right\|, \quad l^+_{scat} = \left\|\boldsymbol{x} - \boldsymbol{r}^I_{scat}\right\|, \quad \text{and} \quad l^-_{scat} = \left\|\boldsymbol{y} - \boldsymbol{r}^I_{scat}\right\|. \tag{4.36}$$

We will also define the following directions given by unit vectors:

$$\boldsymbol{v}^+_{inc} = \frac{\boldsymbol{r}^I_{inc} - \boldsymbol{x}}{l^+_{inc}}, \quad \boldsymbol{v}^-_{inc} = \frac{\boldsymbol{y} - \boldsymbol{r}^I_{inc}}{l^-_{inc}}, \quad \boldsymbol{v}^+_{scat} = \frac{\boldsymbol{x} - \boldsymbol{r}^I_{scat}}{l^+_{scat}}, \quad \text{and } \boldsymbol{v}^-_{scat} = \frac{\boldsymbol{r}^I_{scat} - \boldsymbol{y}}{l^-_{scat}}. \tag{4.37}$$

When $\lambda_\pm$ ($k_\pm$) are known, and we fix Ω^+ as the reference media for refraction, i.e. $n = \lambda^+/\lambda^-$, only a subset of all the possible round-trips between the two points comply with Snell's law of angles. A round-trip will be called admissible or physical if both its incident go trip wave path and its scattered return trip wave path comply with Snell's law of angles.

Using Snell's law we can compute the direction of the transmitted wave paths across the interface surfaces for the incident wave and for the scattered wave. For the incident wave path joining $\boldsymbol{x}$ and $\boldsymbol{r}^I_{inc}$ we have that the transmitted direction $\hat{\boldsymbol{v}}^-_{inc}$ should be

$$\hat{\boldsymbol{v}}^-_{inc} = \frac{1}{n}\left(\boldsymbol{v}^+_{inc} - \left(\left(\boldsymbol{v}^+_{inc}\cdot\boldsymbol{n}_{\boldsymbol{r}^I_{inc}}\right) + \sqrt{n^2 - 1 + \left(\boldsymbol{v}^+_{inc}\cdot\boldsymbol{n}_{\boldsymbol{r}^I_{inc}}\right)^2}\right)\boldsymbol{n}_{\boldsymbol{r}^I_{inc}}\right). \tag{4.38}$$

so that the error in the transmitted angle for the incident wave is

$$\theta^e_{inc} = \arccos(\hat{\boldsymbol{r}}^-_{inc} \cdot \boldsymbol{v}^-_{inc}). \tag{4.39}$$

A given incident path will be called admissible or physical if $\theta^e_{inc} = 0$.

Likewise for the scattering wave, for the scattered wave path joining $\boldsymbol{y}$ and $\boldsymbol{r}^I_{scat}$ we can compute the direction $\hat{\boldsymbol{v}}^+_{scat}$ that the outgoing wave path should have as

$$\hat{\boldsymbol{v}}^+_{scat} = n\left(\boldsymbol{v}^-_{scat} - \left(\left(\boldsymbol{v}^-_{scat}\cdot\boldsymbol{n}_{\boldsymbol{r}^I_{scat}}\right) - \sqrt{\frac{1}{n^2} - 1 + \left(\boldsymbol{v}^-_{scat}\cdot\boldsymbol{n}_{\boldsymbol{r}^I_{scat}}\right)^2}\right)\boldsymbol{n}_{\boldsymbol{r}^I_{scat}}\right). \tag{4.40}$$

and determine the error in the angle with the actual direction for that given return path as

$$\theta^e_{scat} = \arccos(\hat{\boldsymbol{v}}^+_{scat} \cdot \boldsymbol{v}^+_{scat}). \tag{4.41}$$

A given scattered path will be called admissible or physical if $\theta^e_{scat} = 0$.

Figure 4.14 illustrates the defined values and vector for a given round-trip between points $\boldsymbol{x} \in \Gamma^H$ and $\boldsymbol{y} \in \Gamma^R$.

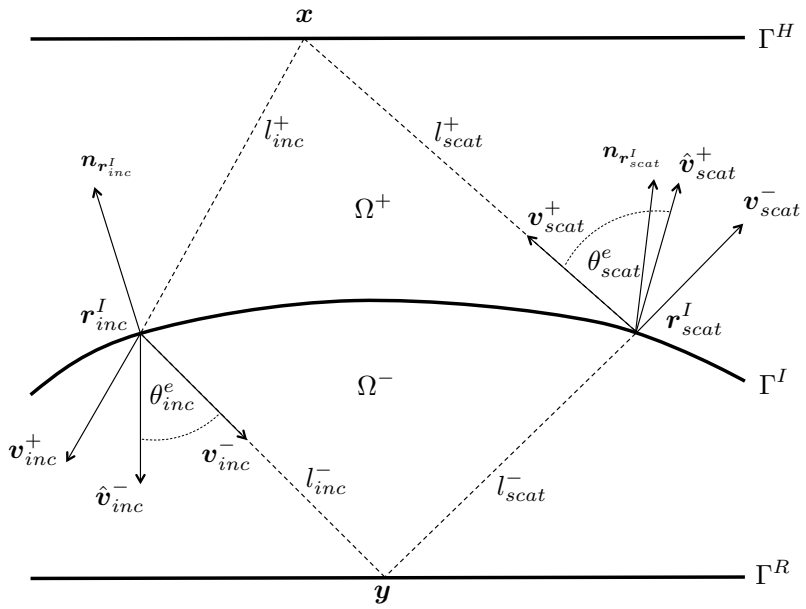

Figure 4.14: Geometrical lengths and vectors for an arbitrary round-trip between points $\boldsymbol{x} \in \Gamma^H$ and $\boldsymbol{y} \in \Gamma^R$.

A given round-trip will be called admissible if both the incident and the scattered wave paths are admissible. For every admissible trip, let us define the optical path length as

$$\ell_I(\boldsymbol{x}, \boldsymbol{y}) = l^+_{inc} + l^+_{scat} + n\left(l^-_{inc} + l^-_{scat}\right). \tag{4.42}$$

From all the admissible round-trips, let $\ell^*_I(\boldsymbol{x}, \boldsymbol{y})$ be the minimum optical path length, with associated geometrical distances l^{+*}_{inc}, l^{-*}_{inc}, l^{+*}_{scat}, and l^{-*}_{scat}. Then the new filter function $\mathcal{F}_I$ is

$$\mathcal{F}_I(\boldsymbol{x}, \boldsymbol{y}) = G^{k^+}_c(\ell^*_I(\boldsymbol{x}, \boldsymbol{y})) = e^{-\mathrm{i}k^+\ell^*_I(\boldsymbol{x},\boldsymbol{y})} = e^{-\mathrm{i}2\pi\left(\frac{l^{+*}_{inc}}{\lambda^+} + \frac{l^{-*}_{inc}}{\lambda^-} + \frac{l^{-*}_{scat}}{\lambda^-} + \frac{l^{+*}_{scat}}{\lambda^+}\right)}. \tag{4.43}$$

The imaging method is then

$$\mathcal{R}(\boldsymbol{y}) = \int_{\Gamma^H} \mathcal{F}_I(\boldsymbol{x}, \boldsymbol{y})\mathcal{H}(\boldsymbol{x}) d\Gamma^H(\boldsymbol{x}), \quad \text{for } \boldsymbol{y} \in \Gamma^H. \tag{4.44}$$

In practice, in a discrete version, for every sample taken at $\boldsymbol{r}^H_j \Gamma^H$, and every reconstruction point $\boldsymbol{r}^R_i \in \Gamma^R$, we explore a finite number of points on a rectangular grid on Γ^I and consider admissible the paths that comply with a tolerance θ_{tol}, i.e., $\theta^e_{inc} \leq \theta_{tol}$ and $\theta^e_{scat} \leq \theta_{tol}$. Then, the optical path length is computed for all the admissible paths and the shortest one is selected as $\ell^*_I(\boldsymbol{r}^H_j, \boldsymbol{r}^R_i)$. We then compute the complex reflectivity image at points $\{\boldsymbol{r}^R_i\}_{i=1}^{N_R}$ as:

$$\mathcal{R}(\boldsymbol{r}^R_i) = (\delta^H)^2 \sum_{j=1}^{N_{MMS}} e^{-\mathrm{i}k^+\ell^*_I(\boldsymbol{r}^H_j, \boldsymbol{r}^R_i)} \mathcal{H}(\boldsymbol{r}^H_j), \quad \text{for } i = 1...N_R. \tag{4.45}$$

The proposed method, synthesized in (4.45) an called hereinafter Across-Interface Conjugate-Phase Matching (AI-CPM), is capable of generating a reflectivity image $\mathcal{R}$ where the radar target Γ^T can be resolved, as it will be seen in subsequent subsections. This comes at a cost, since the complexity algorithm (4.45) is $\mathcal{O}\left(N_R \cdot N_{MMS} \cdot N_I\right)$. In the next subsection, we will further extend the principles for the case of a radar scenario with an above-ground and an underground domain using additional assumptions that will distance us further from correct physical representation and will achieve lower algorithmic complexities at the expense of robustness. We propose a new simplified imaging method based on the one presented in this subsection and we will test it under different circumstances using numerical simulations.

4.3.4 A simplified imaging method for double domain scenarios

In a further simplification of the imaging method from Subsection 4.3.3 we will adopt the assumption that the incident incoming wave path and the scattered outgoing wave path between points $\boldsymbol{x} \in \Gamma^H$ and $\boldsymbol{y} \in \Gamma^R$ are not siginificantly different in magnitude, i.e., we will assume that

$$l^+_{inc} + l^-_{inc} \approx l^+_{scat} + l^-_{scat} \tag{4.46}$$

Under assumption (4.46), the task of computing the minimum wave path lengths is simplified because we can compute only one of them. In a new simplified algorithm, and under this new assumption, we will consider the entry and exit wave paths that pass through points $\boldsymbol{x} \in \Gamma^I$ and $\boldsymbol{y} \in \Gamma^R$ and we will determine the corresponding point $\tilde{\boldsymbol{r}}^H \in \Gamma^H$ that complies with Snell's law, for which we will consider the exit wave path. The direction $\boldsymbol{v}^-_{scat}$ of the wave path exiting the domain Ω^- is computed as before using the new points:

$$\boldsymbol{v}^-_{scat} = \frac{\boldsymbol{x} - \boldsymbol{y}}{\|\boldsymbol{x} - \boldsymbol{y}\|}. \tag{4.47}$$

Then, the direction $\boldsymbol{v}^+_{scat}$ of the exit wave path in the domain Ω^+ can be computed similarly as in (4.40):

$$\hat{\boldsymbol{v}}^+_{scat} = n\left(\boldsymbol{v}^-_{scat} - \left(\left(\boldsymbol{v}^-_{scat}\cdot\boldsymbol{n}_{\boldsymbol{x}}\right) - \sqrt{\frac{1}{n^2} - 1 + \left(\boldsymbol{v}^-_{scat}\cdot\boldsymbol{n}_{\boldsymbol{x}}\right)}\right)\boldsymbol{n}_{\boldsymbol{x}}\right). \tag{4.48}$$

Using the exit direction $\hat{\boldsymbol{v}}^+_{scat}$, and if the holographic recording surface Γ^H is contained in a plane at a given height r^H_3, then the corresponding the point $\tilde{\boldsymbol{r}}^H \in \Gamma^H$ on Γ^H can be found using $\boldsymbol{x} = (x_1, x_2, x_3) \in \Gamma^I$ as

$$\tilde{\boldsymbol{r}}^H(\boldsymbol{x}, \boldsymbol{y}) = \boldsymbol{x} + \frac{r^H_3 - x_3}{\hat{\boldsymbol{e}}_3 \cdot \hat{\boldsymbol{v}}^+_{scat}}\hat{\boldsymbol{v}}^+_{scat}. \tag{4.49}$$

Figure 4.15 illustrates the described geometrical process.

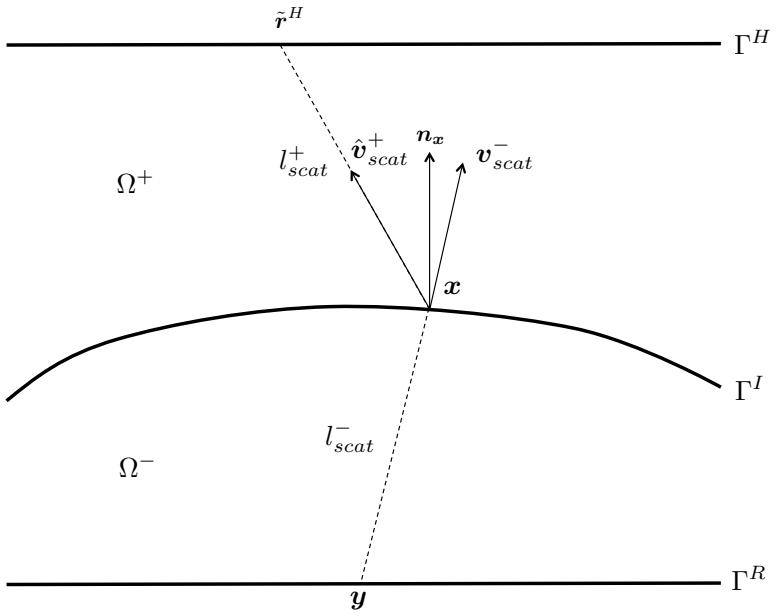

Figure 4.15: Geometrical lengths and vectors for the simplified round-trip passing through between points $\boldsymbol{x} \in \Gamma^I$ and $\boldsymbol{y} \in \Gamma^R$.

Taking Ω^+ as reference medium and $n = \lambda^+/\lambda^-$, the corresponding round-trip optical path length is

$$\ell_I(\tilde{\boldsymbol{r}}^H(\boldsymbol{x},\boldsymbol{y}),\boldsymbol{y}) = 2\left(\left\|\tilde{\boldsymbol{r}}^H(\boldsymbol{x},\boldsymbol{y}) - \boldsymbol{x}\right\| + n\left\|\boldsymbol{x}-\boldsymbol{y}\right\|\right), \tag{4.50}$$

and the new filter function $\mathcal{F}_I$ is

$$\mathcal{F}_I(\tilde{\boldsymbol{r}}^H(\boldsymbol{x},\boldsymbol{y}),\boldsymbol{y}) = G_c^{k^+}(\ell_I(\tilde{\boldsymbol{r}}^H(\boldsymbol{x},\boldsymbol{y}),\boldsymbol{y})) = e^{-\mathrm{i}k^+\ell_I(\tilde{\boldsymbol{r}}^H(\boldsymbol{x},\boldsymbol{y}),\boldsymbol{y})}. \tag{4.51}$$

Using this new filter function, now defined for points on Γ^T and Γ^I, the imaging method is expressed as

$$\mathcal{R}(\boldsymbol{y}) = \int\limits_{\Gamma^I} \mathcal{F}_I(\tilde{\boldsymbol{r}}^H(\boldsymbol{x},\boldsymbol{y}),\boldsymbol{y})\mathcal{H}(\tilde{\boldsymbol{r}}^H(\boldsymbol{x},\boldsymbol{y}))d\Gamma^I(\boldsymbol{x}), \text{ for } \boldsymbol{y}\in\Gamma^I. \tag{4.52}$$

Given a rectangular grid of points $\{\boldsymbol{r}_i^I\}_{i=1}^{N_I}$ with resolution δ^I, the new simplified imaging algorithm is

$$\mathcal{R}(\boldsymbol{r}_i^R) = \sum_{j=1}^{N_I} \mathcal{F}_I(\tilde{\boldsymbol{r}}^H(\boldsymbol{r}_j^I,\boldsymbol{r}_i^R),\boldsymbol{r}_i^R)\mathcal{H}(\tilde{\boldsymbol{r}}^H(\boldsymbol{r}_j^I,\boldsymbol{r}_i^R))\delta\Gamma^I(\boldsymbol{r}_j^I), \quad \text{for } i = 1...N_R, \tag{4.53}$$

where the area element is

$$\delta\Gamma^I(\boldsymbol{r}_j^I) = (\delta^I)^2\sqrt{1+\left(\frac{\partial f_I}{\partial x_1}(\boldsymbol{r}_j^I)\right)^2+\left(\frac{\partial f_I}{\partial x_2}(\boldsymbol{r}_j^I)\right)^2}. \tag{4.54}$$

The value $\mathcal{H}(\tilde{\boldsymbol{r}}^H)$ is available through interpolation whenever the resolution δ^H of the recorded hologram is small enough, and whenever $\widetilde{r}^H \in \Gamma^H$ and the there is a physical return-trip ray. It is remarkable that the complexity of the new imaging method (4.53) is now $\mathcal{O}(N_R \cdot N_I)$. This new and simplified method, synthesized in (4.53) and called hereinafter Single-Path Across-Interface Conjugate-Phase Matching (SPAI-CPM), is capable of producing reflectivity images of the underground as it will be seen in the next subsection. Its resolving capabilities and robustness will be, as expected, worse than those of the previously described method, AS-CPM from Subsection 4.3.4. This less performant method, relying on additional assumptions, will be able to produce reflectivity images but it will also show greater image degradation as the scenarios on which it's used deviate from conditions less challenging to those assumptions.

In what follows we will provide examples of complex image reconstruction using the algorithm described in this subsection, synthesized in (4.53), and in the previous subsection, synthesized in (4.45).

4.3.5 Simulated examples

In this subsection we will present simulated examples of the two proposed imaging methods for underground reflectivity in double domain scenarios. The aim of these simulations is to exemplify how numerical simulations of the global direct problem, i.e. solving a direct backscattering wave problem for each monostatic radar sampling position, can help predict the performance of a ground penetrating radar as the one considered. The two particular underground imaging schemes proposed pose a case of interest because they are based on assumptions that are commonly violated in realistic scenarios, and their performance must be assessed via numerical simulations.

The different scenarios under which the imaging schemes will be evaluated, and the simulations of wave propagation and backscattering in them, will share many parameters. Those parameters particular to each scenario will be specified explicitly, while those shared will be presented in the following table.

Table 4.6: Parameters used for example cases of a multi-monostatic simulation and image reconstruction in double domain scenarios

	Parameter	Value	Units
Domain Ω^+	λ^+	10	cm
	k^+	62.83	m^{-1}
Domain Ω^-	λ^-	5	cm
	k^-	125.66	m^{-1}
	$n = \lambda^+/\lambda^-$	2	dimensionless
Interface Γ^I	x_1, x_2	$-0.5 \leq x_1, x_2 \leq 0.5$	m
	δ^I	5	mm
	$f_I(x_1, x_2)$	$h_I - a(x_1^2 + x_2^2) + b\sin\left(\frac{2\pi x_1}{l}\right)$	m
Hologram $\mathcal{H}$	Γ^H	$\square^{L^H \times L^H}_{(0,0,x_3^H)}$	m
	δ^H	5	cm
Image $\mathcal{R}$	Γ^R	$\square^{1\times 1}_{(0,0,0)}$	m
	δ^H	1	cm
	Methods	AI-CPM (4.45), and SPAI-CPM (4.53)	
Target	Γ^T	(4.4)	m
	h	5	mm

The parameters specified in Table 4.6 show settings similar to those used for simulations in Subsection 4.2.5 and image reconstruction in Subsection 4.3.2. We will use the target defined in Subsection 4.2.2. The main difference between the scenarios that will be presented, as anticipated in Table 4.6, will be the interface surface Γ^I, parametrized by the values h_I, a, b, and l, and the surface Γ^H of holographic recording, parametrized by its height x_3^H and its size L^H. The following table summarized the scenarios that will be presented and the values for the mentioned parameters that will define them.

Table 4.7: Summary of the scenarios presented under which the two underground imaging methods will be evaluated using numerical simulations with common parameters from Table 4.6 and particular parameters for each case in meters.

Scenario	h_I	a	b	l	x_3^H	L^H
A	0.35	0.00	0.000	0.0	1.0	1.0
B	0.35	0.50	0.000	0.0	1.0	1.0
C	0.35	0.00	0.000	0.0	3.0	1.5
D	0.35	0.00	0.025	0.8	1.0	1.0
E	0.35	0.00	0.025	0.4	1.0	1.0
F	0.35	0.00	0.025	0.2	1.0	1.0
G	0.35	0.00	0.070	0.1	1.0	1.0

The scenarios considered are divided in two main groups. In the first group we consider a flat surface, a parabolic surface, and a radio sampling performed from a greater distance from the surface and on a wider area, in a setting more similar to airborne acquisition. In a second group we explore the effect of the presence of ripple on the interface surface, ranging from moderate to acute in comparison to the wavelength used.

For each scenario four figures will be presented. The first one will show a three-dimensional scenario showing the position and shape of the radar target Γ^T, the interface surface Γ^I, and the surface of holographic recording Γ^H with the magnitude of the recorded hologram, i.e. $\mathcal{H}|$, painted on it. The second one will show the magnitude of the complex values of the map $\mathcal{H}$ for the N_{MMS} points sampled in Γ^H. The third and fourth figures will show the magnitude of the complex values of the maps $\mathcal{R}$ painted on the reconstruction points on Γ^R for the AI-CPM

and SPAI-CPM methods.

The reconstructed reflectivity maps $\mathcal{R}$ are represented using an arbitrary and normalized scale across the examples presented. The edge of the original radar target it drawn over every map to provide as reference of the accuracy of the reconstruction.

Scenario A

Scenario	h_I	a	b	l	x_3^H	L^H
A	0.35	0.00	0.000	0.0	1.0	1.0

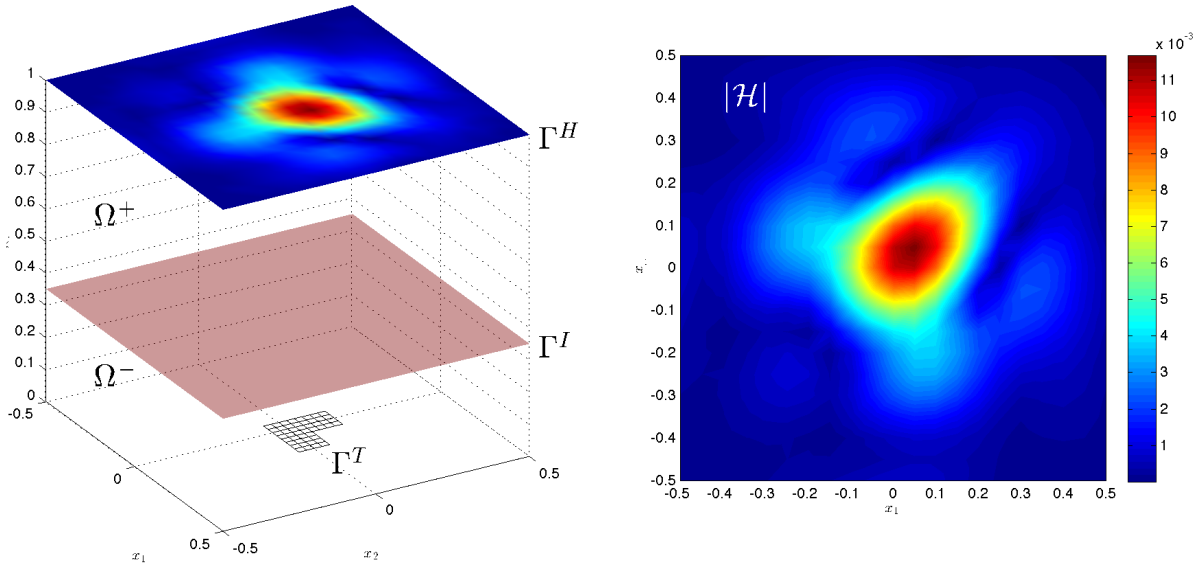

Figure 4.16: Three-dimensional depiction of Scenario A showing the radar target Γ^T, the interface surface Γ^I, the surface of holographic recording Γ^H and the absolute value of $\mathcal{H}$ painted on it (**left**), and the absolute values of the map $\mathcal{H}$ painted on Γ^H (**right**).

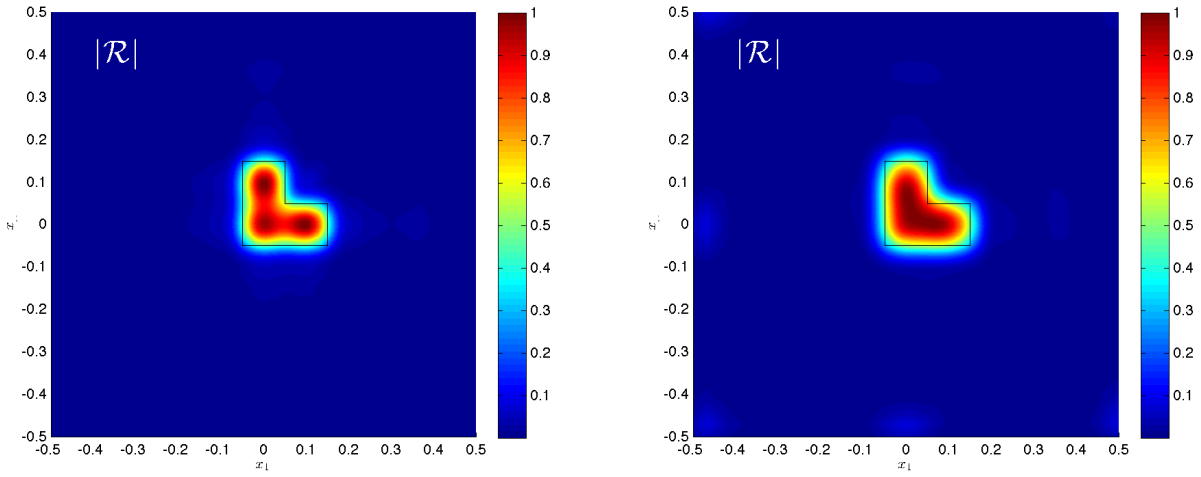

Figure 4.17: Absolute values of map $\mathcal{R}$ reconstructed for Scenario A using AI-CPM (**left**) and SPAI-CPM (**right**), painted on Γ^R.

Scenario B

Scenario	h_I	a	b	l	x_3^H	L^H
B	0.35	0.50	0.000	0.0	1.0	1.0

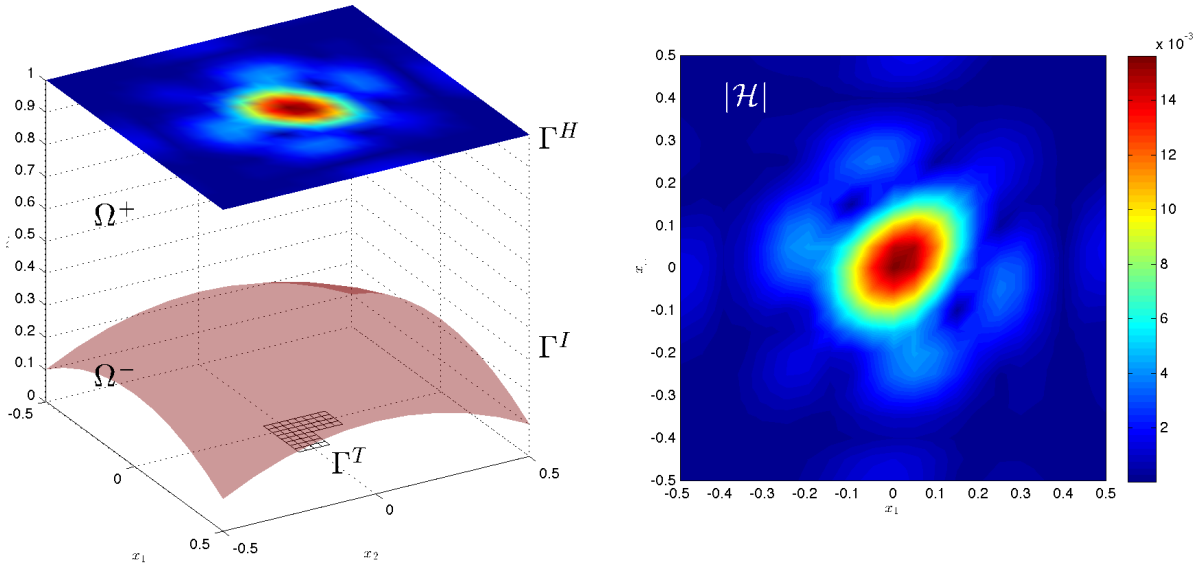

Figure 4.18: Three-dimensional depiction of Scenario B showing the radar target Γ^T, the interface surface Γ^I, the surface of holographic recording Γ^H and the absolute value of $\mathcal{H}$ painted on it (**left**), and the absolute values of the map $\mathcal{H}$ painted on Γ^H (**right**).

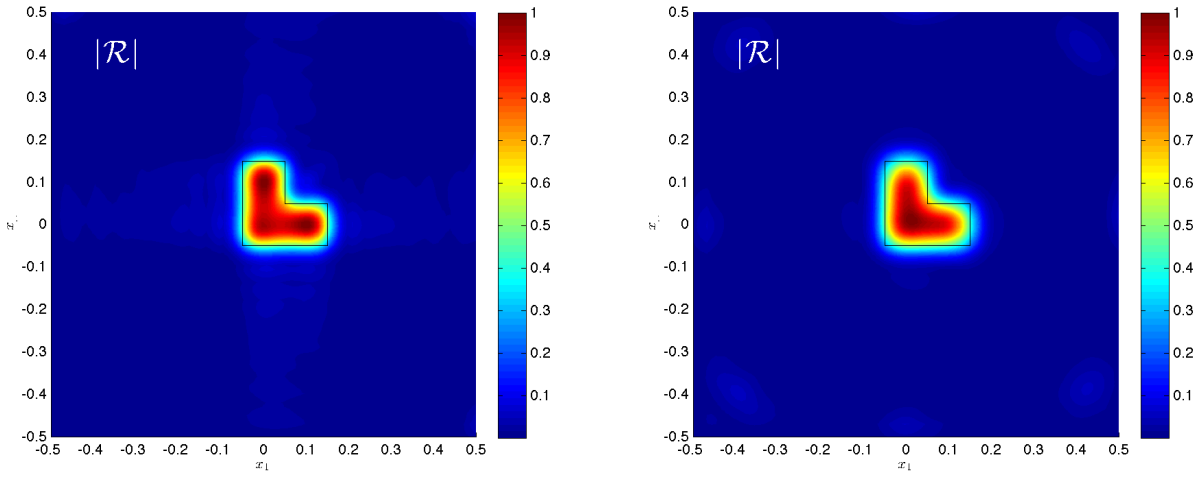

Figure 4.19: Absolute values of map $\mathcal{R}$ reconstructed for Scenario B using AI-CPM (**left**) and SPAI-CPM (**right**), painted on Γ^R.

Scenario C

Scenario	h_I	a	b	l	x_3^H	L^H
C	0.35	0.00	0.000	0.0	3.0	1.5

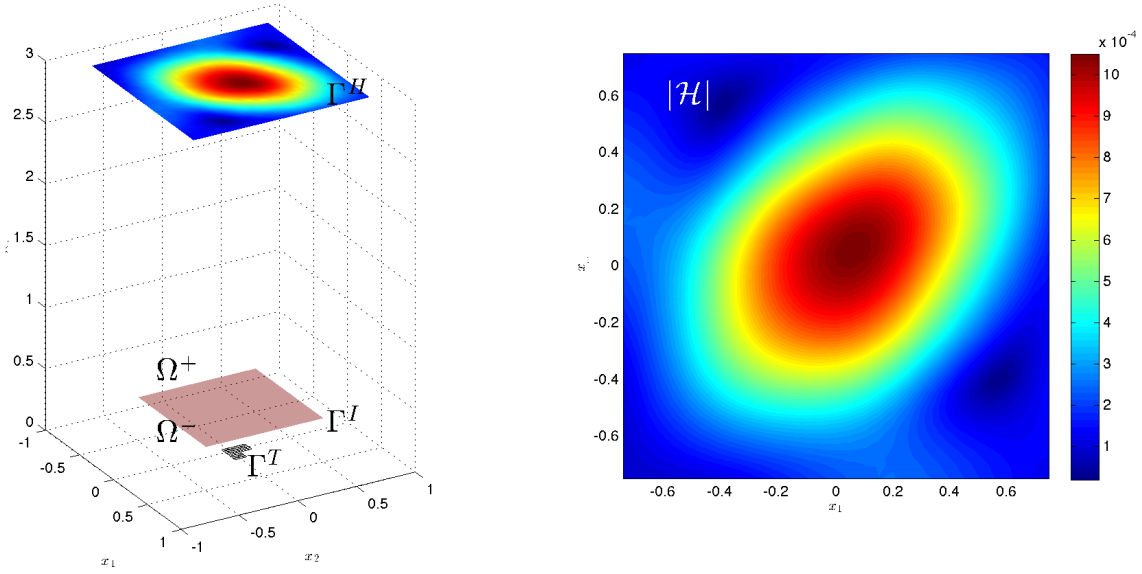

Figure 4.20: Three-dimensional depiction of Scenario C showing the radar target Γ^T, the interface surface Γ^I, the surface of holographic recording Γ^H and the absolute value of $\mathcal{H}$ painted on it (**left**), and the absolute values of the map $\mathcal{H}$ painted on Γ^H (**right**).

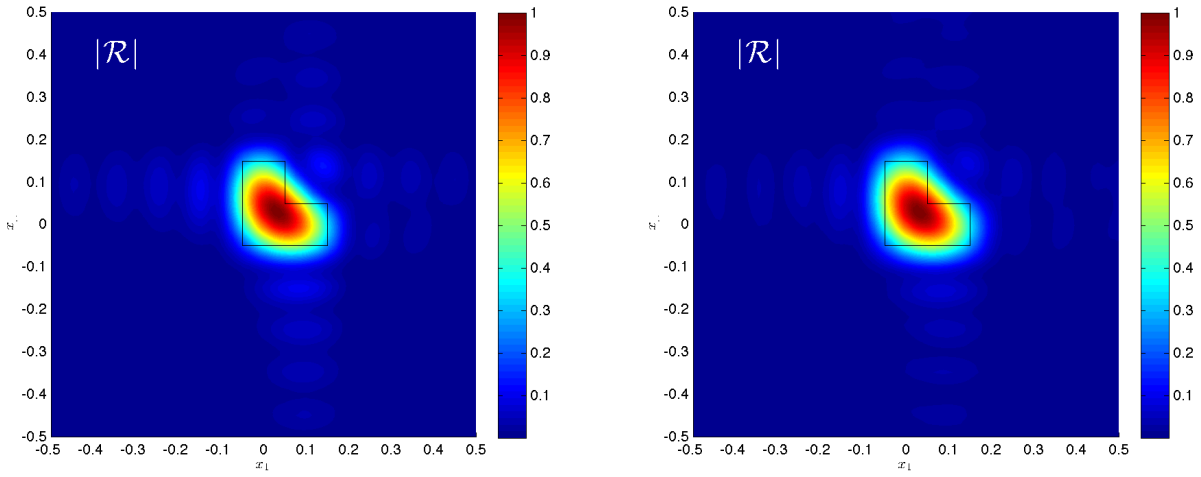

Figure 4.21: Absolute values of map $\mathcal{R}$ reconstructed for Scenario C using AI-CPM (**left**) and SPAI-CPM (**right**), painted on Γ^R.

Scenario D

Scenario	h_I	a	b	l	x_3^H	L^H
D	0.35	0.00	0.025	0.8	1.0	1.0

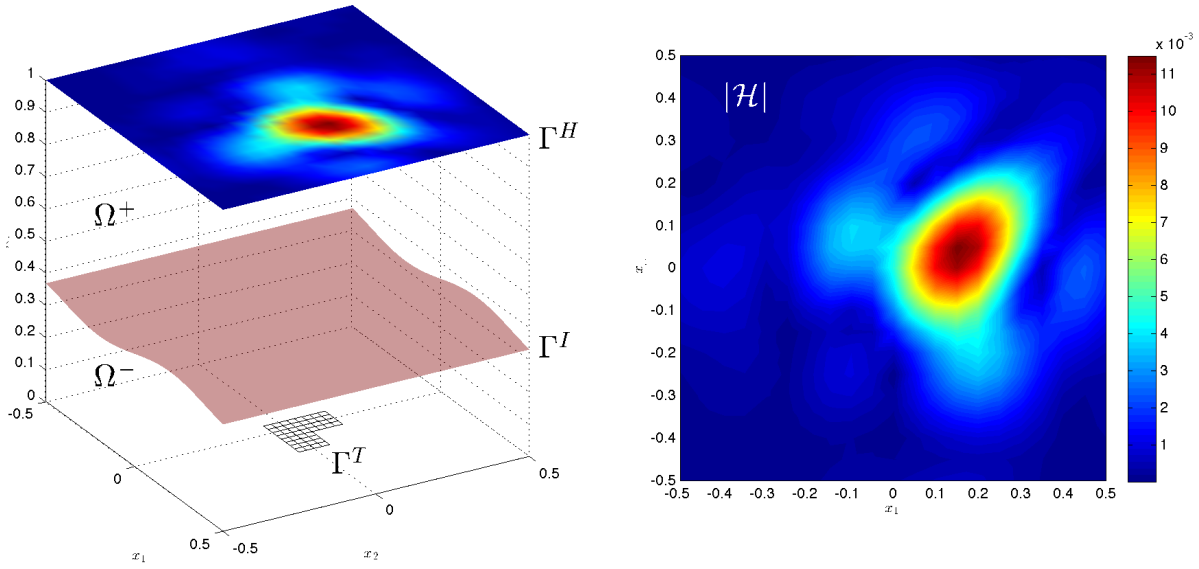

Figure 4.22: Three-dimensional depiction of Scenario D showing the radar target Γ^T, the interface surface Γ^I, the surface of holographic recording Γ^H and the absolute value of $\mathcal{H}$ painted on it (**left**), and the absolute values of the map $\mathcal{H}$ painted on Γ^H (**right**).

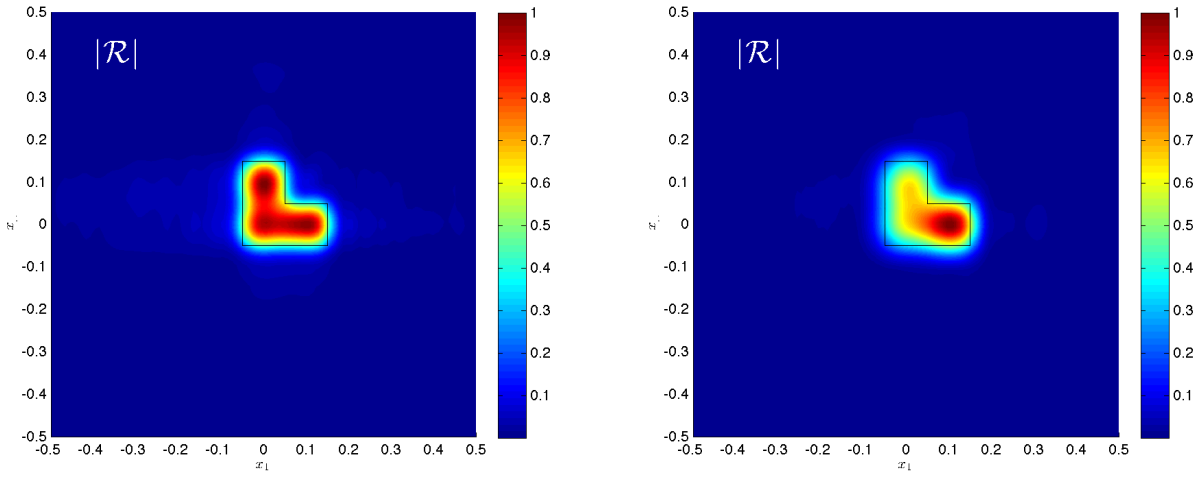

Figure 4.23: Absolute values of map $\mathcal{R}$ reconstructed for Scenario D using AI-CPM (**left**) and SPAI-CPM (**right**), painted on Γ^R.

Scenario E

Scenario	h_I	a	b	l	x_3^H	L^H
E	0.35	0.00	0.025	0.4	1.0	1.0

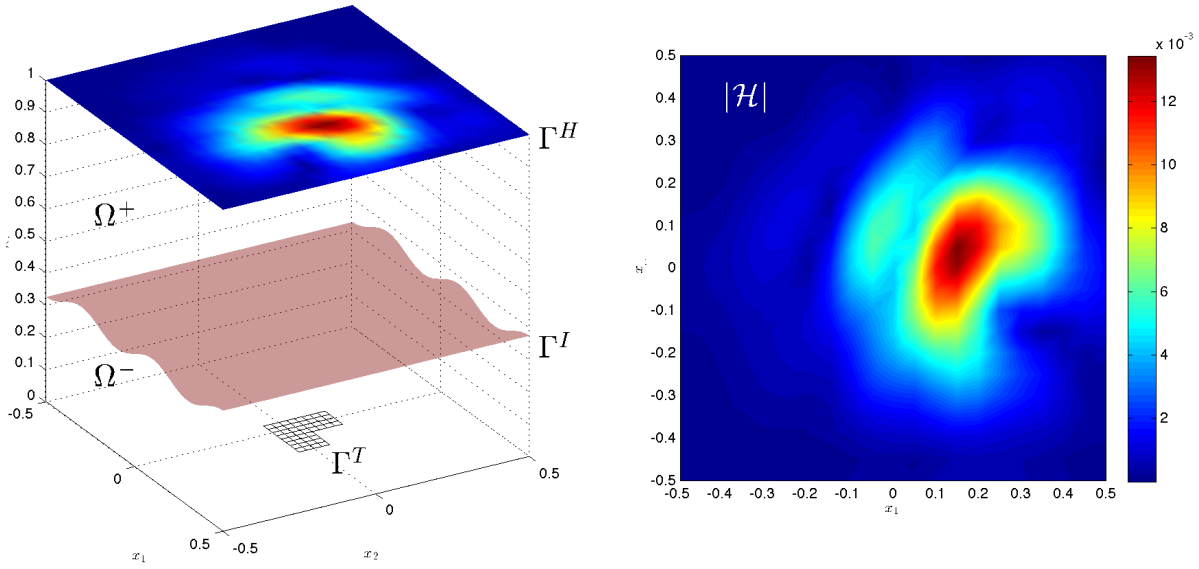

Figure 4.24: Three-dimensional depiction of Scenario E showing the radar target Γ^T, the interface surface Γ^I, the surface of holographic recording Γ^H and the absolute value of $\mathcal{H}$ painted on it (**left**), and the absolute values of the map $\mathcal{H}$ painted on Γ^H (**right**).

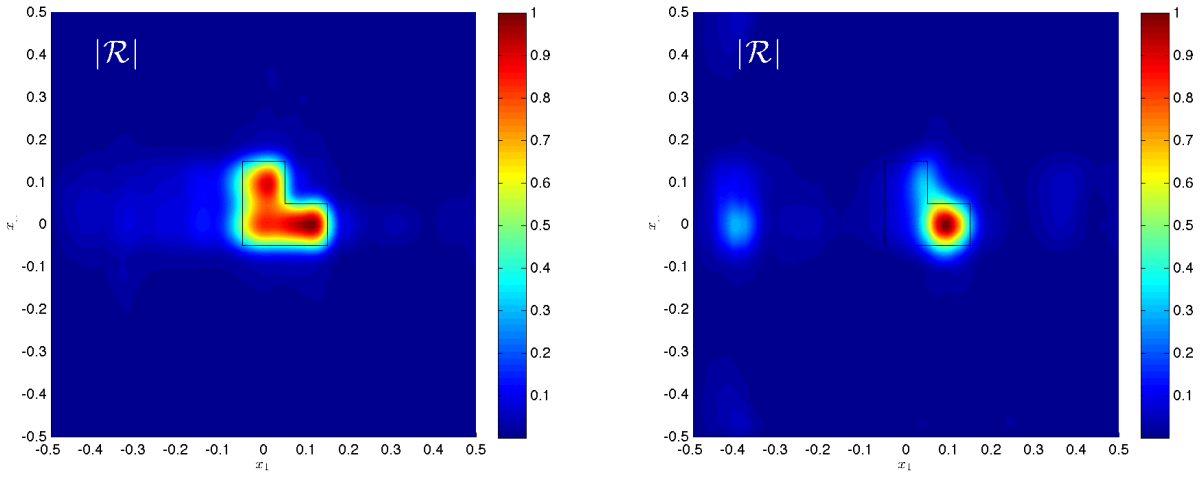

Figure 4.25: Absolute values of map $\mathcal{R}$ reconstructed for Scenario E using AI-CPM (**left**) and SPAI-CPM (**right**), painted on Γ^R.

Scenario F

Scenario	h_I	a	b	l	x_3^H	L^H
F	0.35	0.00	0.025	0.2	1.0	1.0

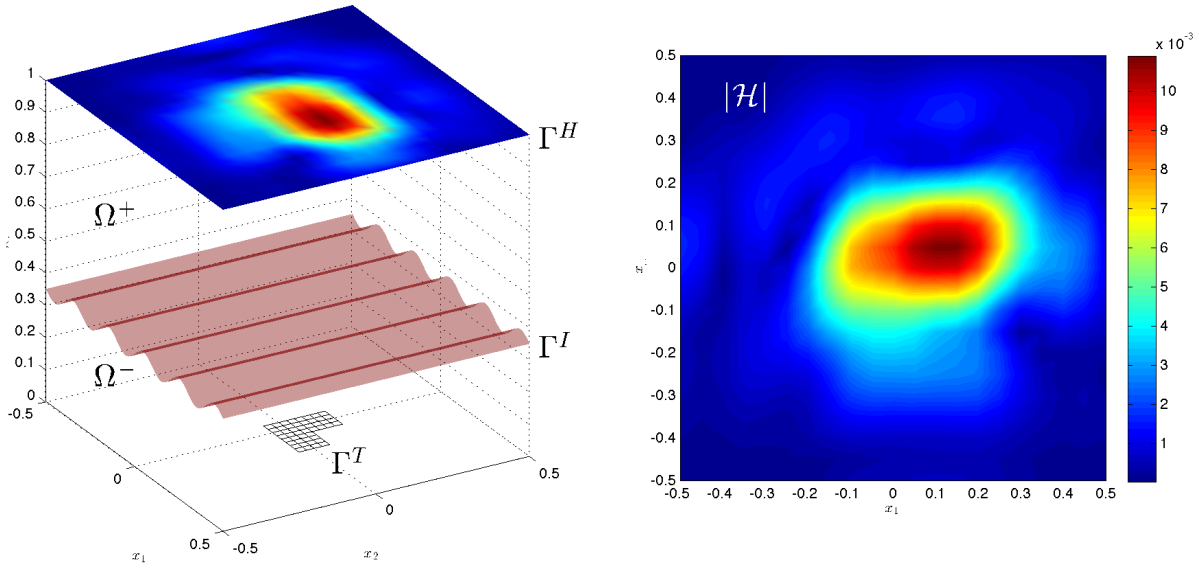

Figure 4.26: Three-dimensional depiction of Scenario F showing the radar target Γ^T, the interface surface Γ^I, the surface of holographic recording Γ^H and the absolute value of $\mathcal{H}$ painted on it (**left**), and the absolute values of the map $\mathcal{H}$ painted on Γ^H (**right**).

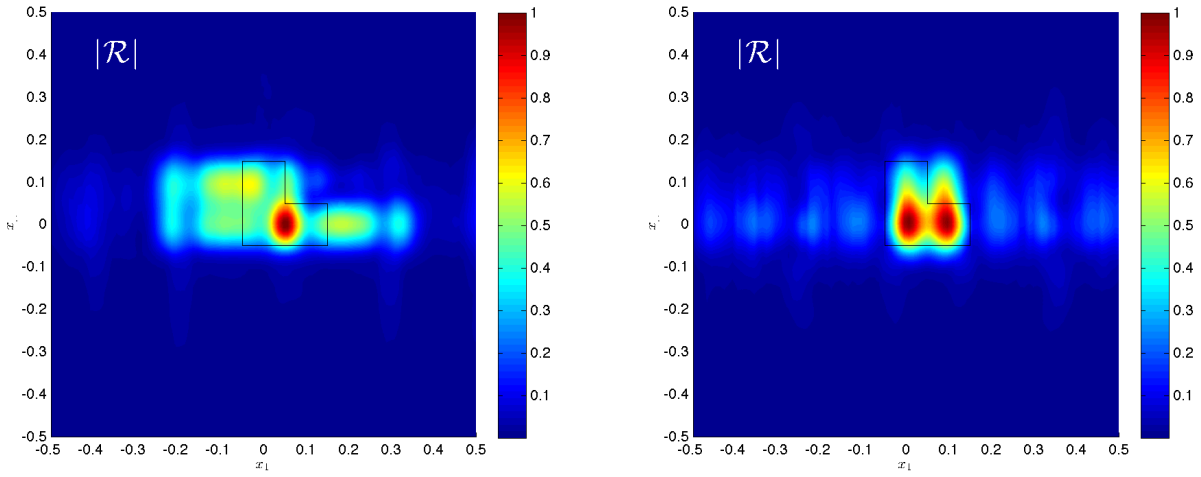

Figure 4.27: Absolute values of map $\mathcal{R}$ reconstructed for Scenario F using AI-CPM (**left**) and SPAI-CPM (**right**), painted on Γ^R.

Scenario G

Scenario	h_I	a	b	l	x_3^H	L^H
G	0.35	0.00	0.070	0.1	1.0	1.0

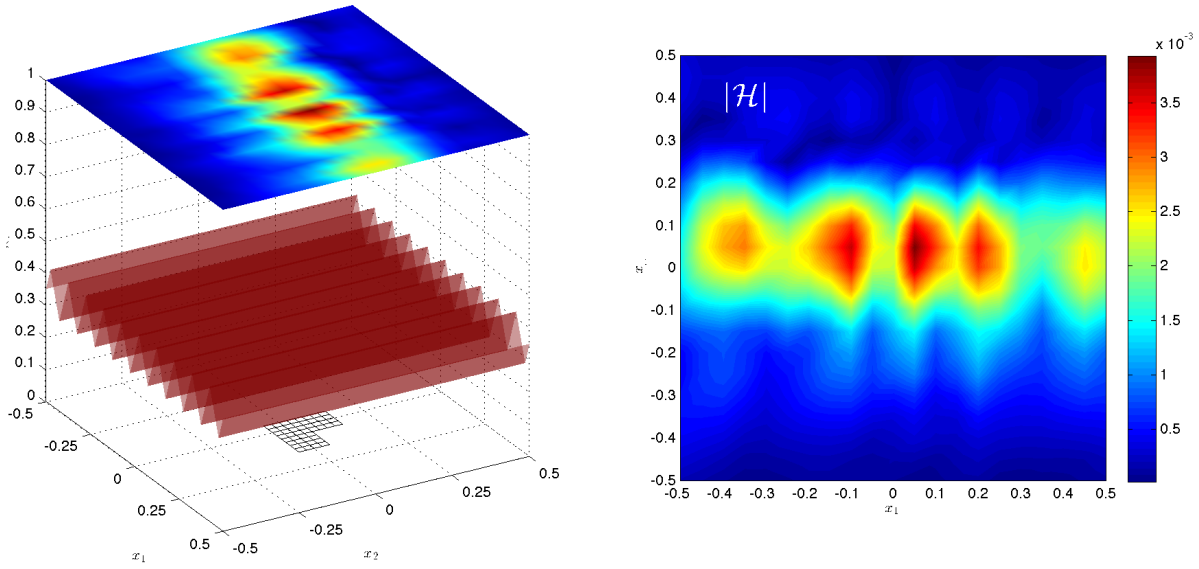

Figure 4.28: Three-dimensional depiction of Scenario G showing the radar target Γ^T, the interface surface Γ^I, the surface of holographic recording Γ^H and the absolute value of $\mathcal{H}$ painted on it (**left**), and the absolute values of the map $\mathcal{H}$ painted on Γ^H (**right**).

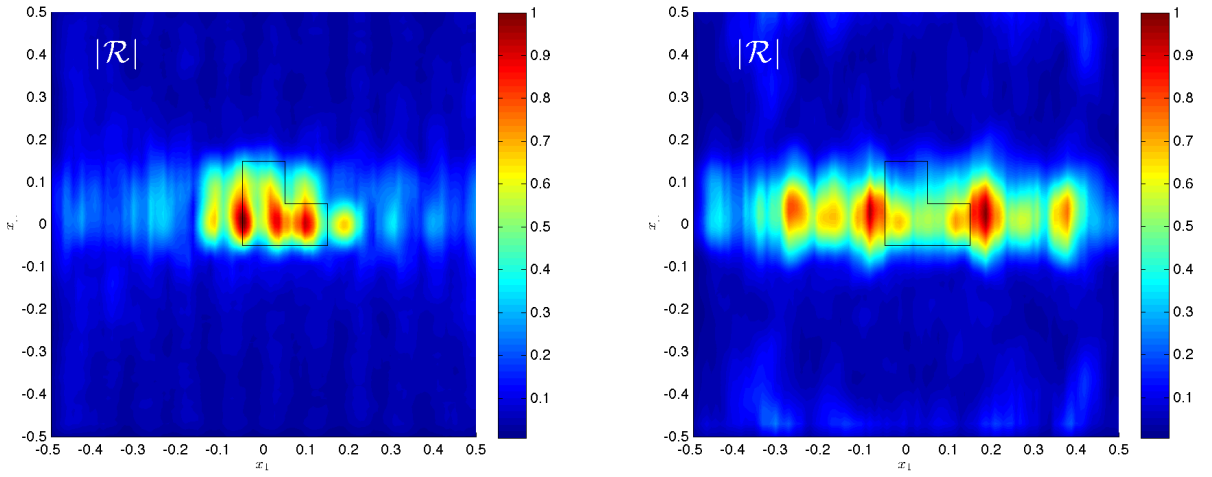

Figure 4.29: Absolute values of map $\mathcal{R}$ reconstructed for Scenario G using AI-CPM (**left**) and SPAI-CPM (**right**), painted on Γ^R.

The results provided for the cases A through G, described in Subsection 4.3.5 and with parameters summarized in Table 4.6, show an overall satisfactory performance. Even if many cases violate the assumption underlying the imagining principles of both methods, i.e., that the wavelength is very small in comparison to the geometrical features of the scenario, the algorithms produce reflectivity maps $\mathcal{R}$ whose absolute values allow for the location and (in many cases) the identification of the shape of the radar target. From the somewhat restricted set of simulated examples, some conclusions can be extracted about the imaging methods. Besides the performance of the imaging methods, their simulations proves the proposed simulation method appropriate to measure it, and highlights the improvements leading to more efficient numerical simulations.

The first method, called AI-CPM, a proposed extension of the method described and tested for single domain scenarios in [23], is able to resolve the obstacle even when the geometrical features of the interface surface violate the assumptions of geometrical optics on which it is based. It does however provide poorer results the further this violation goes. Depending on the actual refraction index and on the used wavelength in a real scenario, this method stands as promising for use with airborne ground-penetrating radars when the underground is assumed to be sufficiently homogeneous and the geometrical features of the interface surface are larger than the wave used length. The second method, SPAI-CPM, relying on additional and most often unrealistic assumptions, stands out by its lower algorithmic complexity while its resolving performance remains useful for a range of cases that could prove useful for some applications.

References

[1] *The boost C++ libraries*. Schäling, Boris, 2011.

[2] P. A. and Z. Y. *Radar imaging and holography*, volume 19 of *Radar, Sonar, and Navigation Series*. IET, 2005.

[3] M. Abramowitz and I. A. Stegun. *Handbook of Mathematical Functions*. Dover, 1964.

[4] G. Allaire. *Numerical Analysis and Optimization: An Introduction to Mathematical Modelling and Numerical Simulation*. Oxford University Press, 2007.

[5] B. O. Almroth, P. Stern, and F. A. Brogan. Automatic choice of global shape functions in structural analysis. *AIAA Journal*, 16:525–528, May 1978.

[6] E. Anderson, Z. Bai, C. Bischof, S. Blackford, J. Demmel, J. Dongarra, J. Du Croz, A. Greenbaum, S. Hammarling, A. McKenney, and D. Sorensen. *LAPACK Users' Guide*. Society for Industrial and Applied Mathematics, Philadelphia, PA, third edition, 1999.

[7] G. S. Baker. Applying avo analysis to gpr data. *Geophysical Research Letters*, 25(3):397–400, 1998.

[8] M. Bebendorf. Approximation of boundary element matrices. *Numerical Mathematics*, 86(4):565–589, 2000.

[9] M. Bebendorf. Hierarchical lu decomposition based on preconditioners for bem. *Computing*, 74:225–247, 2005.

[10] M. Bebendorf and S. Rjasanow. Adaptive low-rank approximation of collocation matrices. *Computing*, 70(1):1–24, 2003.

[11] A. Bendali and C. Devys. Calcul numérique du rayonnement de cornets électromagnétiques dont l'ouverture est partiellement remplie par un diélectrique. *Onde électrique*, 66(1):77–81, 1986.

[12] M. Born and E. Wolf. *Principles of optics: electromagnetic theory of propagation, interference and diffraction of light*. Pergamon, 6th edition, 1986.

[13] C. Chekroun, M. Duran, O. Bohbot, and R. Seneor. Device for detecting objects such as mines. US20140121969A1, CA2840848A1, DE112012002840T5, WO2013004924A1, WO2013004924A9, July 2011.

[14] C. Chekroun, R. SENEOR, and M. DURAN. Device for detecting at least one object buried in a pile and method implemented in such a device. WO2013004978A1, EP2729832A1, July 2011.

[15] K. Chen. *Matrix preconditioning techniques and applications*, volume 19. Cambridge University Press, 2005.

[16] S. H. Christiansen and J.-C. Nédélec. Des préconditionneurs pour la résolution numérique des équations intégrales de frontière de l'acoustique. *Comptes Redus de l'Académie des Sciences, Series I, Mathématiques*, 330(7):617–622, 2000.

[17] I. Danaila, F. Hecht, and O. Pironneau. *Simulation numérique en C++*. DUNOD, 2003.

[18] M. Durán and M. Guarini. System and method for detecting, locating and identifying objects located above ground or below ground in a pre-referenced area of interest. US8508402, EP2244101A1, EP2244101A4, US20110037639, WO2009087260A1, January 2008.

[19] M. Duràn, R. Hein, and J.-C. Nédélec. *Mathematical Methods for Wave Propagation in Science and Engineering*, volume 1. Ediciones UC, 2012.

[20] V. J. Ervin and E. Stephan. Collocation with chebyshev polynomials for a hypersingular integral equation on an interval. *Journal of computational and applied mathematics*, 43(1):221–229, 1992.

[21] C. Geuzaine and J.-F. Remacle. Gmsh: A 3-d finite element mesh generator with built-in pre-and post-processing facilities. *International Journal for Numerical Methods in Engineering*, 79(11):1309–1331, 2009.

[22] D. Gilbarg and N. S. Trudinger. *Elliptic partial differential equations of second order*. Springer, Berlin, 1983.

[23] L. Giubbolini and L. Sambuelli. New developments in ground probing radar: the possibility of reconstructing a holographic image of underground reflectivity. *Annals of Geophysics*, 43(6), December 2000.

[24] G. H. Golub and C. F. V. Loan. *Matrix Computations*. John Hopkins Studies in the Mathematicas Sciences. John Hopkins University Press, 4th edition, 2013.

[25] L. Greengard. The rapid evaluation of potential fields in particle systems. *Frontiers in Applied Mathematics*, 1988.

[26] L. Greengard and V. Rokhlin. A fast algorithm for particle simulations. *Journal of Computational Physics*, 73(2):325–348, 1987.

[27] G. Guennebaud, B. Jacob, et al. Eigen v3. http://eigen.tuxfamily.org, 2010.

[28] W. Hackbusch. A sparse arithmetic based on $\mathcal{H}$-matrices. part i: Introduction to $\mathcal{H}$-matrices. *Computing*, 62(2):89–108, 1999.

[29] W. Hackbusch. A sparse arithmetic based on $\mathcal{H}$-matrices. part ii: Application to multi-dimensional problems. *Computing*, 64(1):21–47, 2000.

[30] W. Hackbusch, B. N. Khoromskij, and S. Sauter. *Lectures on Applied Mathematics*, chapter On $\mathcal{H}^2$-matrices, pages 9–29. Springer-Verlag, 2000.

[31] W. Hackbusch and Z. P. Nowak. On the complexity of the panel method. In *International Conference on Modern Problems in Numerical Analysis*, 1986.

[32] W. Hackbusch and Z. P. Nowak. On the fast matrix multiplication in the boundary element method by panel clustering. *Numerical Mathematics*, 54(4):463–491, 1989.

[33] T. Hartmann and E. Stephan. Rates of convergence for collocation with jacobi polynomials for the airfoil equation. *Journal of computational and applied mathematics*, 51(2):179–191, 1994.

[34] R. Hein. *Green's functions and integral equations for the Laplace and Helmholtz operators in impedance half-spaces*. PhD thesis, Ecole Polytechnique, 2010.

[35] R. Hiptmair. Operator preconditioning. *Computers and methematics with Applications*, 52(5):699–706, 2006.

[36] R. Hiptmair, C. Jerez-Hanckes, and C. Urzua. Mesh-independent operator preconditioning for boundary elements on open curves. *SIAM Journal on Numerical Analysis*, 52(5):2295–2314, 2014.

[37] R. Hiptmair, C. Jerez-Hanckes, and C. Urzúa-Torres. Optimal operator preconditioning for hypersingular operator over 3d screens. Technical Report 2016-9, Seminar for Applied Mathematics, ETH Zürich, 2016.

[38] G. C. Hsiao and W. L. Wendland. *Boundary integral equations*. Springer, 2008.

[39] F. Ihlenburg. *Finite Element Analysis of Acoustic Scattering*. Springer, 1998.

[40] S. I. Ivashov, V. V. Razevig, I. A. Vasiliev, A. V. Zhuravlev, T. D. Bechtel, and L. Capineri. Holographic subsurface radar of rascan type: Development and applications. *IEEE Journal of Selected Topics in Applied Earth Observations and Remote Sensing*, 4(4):765–778, 2011.

[41] C. Jerez-Hanckes and J.-C. Nédélec. Explicit variational forms for the inverses of integral logarithmic operators over an interval. *SIAM Journal on Mathematical Analysis*, 44(4):2666–2694, 2012.

[42] S. Krenk. A circular crack under asymmetric loads and some related integral equation. *Journal of Applied Mechanics*, 46(4):821–826, 1979.

[43] C. Leung and S. Walker. Iterative solution of large three-dimensional bem elastostatic analyses using the gmres technique. *International Journal for numerical methods in engineering*, 40(12):2227–2236, 1997.

[44] S. Lintner and O. Bruno. A generalized calderón formula for open-arc diffraction problems: theoretical considerations. *ArXiv Preprint. arXiv:1204.3699v2 [math.AP] . ArXiv.*, 2012.

[45] W. Mansur, F. Araujo, and J. Malaghini. Solution of bem systems of equations via iterative techniques. *International Journal for Numerical Methods in Engineering*, 33(9):1823–1841, 1992.

[46] P. A. Martin. Orthogonal polynomial solutions for pressurized elliptical cracks. *The Quarterly Journal of Mechanics and Applied Mathematics*, 39(2):269–287, 1986.

[47] P. A. Martin. Exact solution of some integral equations over a circular disc. *Journal of Integral Equations and Applications*, 18:39–58, 2006.

[48] W. McLean. *Strongly Elliptic Systems and Boundary Integral Equations*. Cambridge University Press, 2000.

[49] W. McLean and O. Steinbach. Boundary element preconditioners for a hypersingular integral equation on an interval. *Advances in Computational Mathematics*, 11(4):271–286, 1999.

[50] D. L. Mensa. High resolution radar cross-section imaging. *Boston, MA, Artech House, 1991, 280 p.*, 1, 1991.

[51] J.-C. Nédélec. *Acoustic and Electromagnetic Equations: Integral Representations for Harmonic Problems*. Number 144 in Applied Mathematical Sciences. Springer, 2001.

[52] N. Nishimura. Fast multipole accelerated boundary integral equation methods. *Applied Mechanical Review*, 55(4):299–323, 2002.

[53] C. M. Rappaport. Exact and approximate underground wavefront shape determination from an above ground gpr source. In *2005 IEEE Antennas and Propagation Society International Symposium*, volume 3, pages 80–83. IEEE, 2005.

[54] V. Razevig, S. Ivashov, I. Vasiliev, A. Zhuravlev, T. Bechtel, and L. Capineri. Advantages and restrictions of holographic subsurface radars. In *Ground Penetrating Radar (GPR), 2010 13th International Conference on*, pages 1–6. IEEE, 2010.

[55] V. Rokhlin. Rapid solution of integral equations of classical potential theory. *Journal of Computational Physics*, 60(2):187–207, 1985.

[56] S. Sauter. *Über die Verwendung des Galerkinverfahrens zur Lösung Fredholmscher Integralgleichungen (On the use of Galerkin methods to solve Fredholm integral equations).* PhD thesis, Chistian-Albrechts-Universität, 1992.

[57] S. Sauter and C. Schwab. *Boundary Element Methods.* Springer Series in Computational Mathematics. Springer, 2010.

[58] D. M. Sheen, D. L. McMakin, and T. E. Hall. Three-dimensional millimeter-wave imaging for concealed weapon detection. *Microwave Theory and Techniques, IEEE Transactions on*, 49(9):1581–1592, 2001.

[59] T. Sigurdsson and T. Overgaard. Application of gpr for 3-d visualization of geological and structural variation in a limestone formation. *Journal of Applied Geophysics*, 40(1):29–36, 1998.

[60] I. H. Sloan and E. Stephan. Collocation with chebyshev polynomials for symm's integral equation on an interval. *The Journal of the Australian Mathematical Society. Series B. Applied Mathematics*, 34(02):199–211, 1992.

[61] O. Steinbach. *Stability Estimates for Hybrid Coupled Domain Decomposition Methods.* Springer-Verlag, 2003.

[62] E. Stephan. Boundary integral equations for screen problems in r^3. *Integral Equations and Operator Theory*, 10(2):236–2557, 1987.

[63] D. M. Sullivan. *Electromagnetic simulation using the FDTD method.* John Wiley & Sons, 2013.

[64] I. Terrasse and T. Abboud. *Modélisation des phénomenes de propagation d'ondes.* École Polytechnique, 2007.

[65] E. E. Tyrtyshnikov. Mosaic-skeleton approximations. *Calcolo*, 33(1-2):47–57, 1996.

[66] F. P. Valente and H. Pina. Iterative solvers for bem algebraic systems of equations. *Engineering analysis with boundary elements*, 22(2):117–124, 1998.

[67] P. D. Walker and M. R. Bell. Noniterative techniques for gpr imaging through a nonplanar air-ground interface. *IEEE transactions on geoscience and remote sensing*, 40(10):2213–2223, 2002.

[68] P. Wolfe. Eigenfunctions of the integral equation for the potential of the charged disk. *Journal of Mathematical Physics*, 12:1215–1218, 1971.

Synthèse en Français

Cette thèse s'inscrit dans le sujet des opérateurs intégraux de frontière définis sur le disque unitaire en trois dimensions, leurs relations avec les problèmes externes de Laplace et Helmholtz, et leurs applications au préconditionnement des systèmes linéaires obtenus en utilisant la méthode des éléments finis de frontière. On utilise aussi les résultats obtenus pour éteindre la portée des ces méthodes pour le préconditionnement des systèmes linéaires produits par des objets plats plus générals. Finalement, on montre la capacité de la méthode proposée dans la gestion de la complexité computationnelle associée à une nouvelle méthode de reconstruction des images en utilisant la diffraction d'ondes.

Chapitre 1: Propagation d'Ondes, Équations Intégrales de Frontière, Méthode des Éléments Finis de Frontière et Complexité Computationnelle

On décrit d'abord les méthodes intégrales pour résoudre les problèmes de Laplace et de Helmholtz en dehors des objets à frontière régulière lipschitzienne, et en dehors des surfaces bidimensionnelles ouvertes dans un espace tridimensionnel. On met le focus sur le cas du problème de Laplace. La formulation intégrale des problèmes de Laplace est décrite formellement.

On s'intéresse aux formes bilinéaires

$$\left\langle \mathcal{S}\lambda\,,\,\lambda^t\right\rangle_\Gamma \quad \text{et} \quad \left\langle \mathcal{N}\mu\,,\,\mu^t\right\rangle_\Gamma$$

pour l'opérateur de simple couche sur une distribution $\lambda \in H^{-1/2}(\Gamma)$

$$\mathcal{S}\lambda(\boldsymbol{y}) = \int_\Gamma G(\boldsymbol{x},\boldsymbol{y})\lambda(\boldsymbol{x})d\Gamma(\boldsymbol{x}), \quad \boldsymbol{y}\in\mathbb{R}^3,$$

et pour l'opérateur hyper-singulière sur une distribution $\mu \in H^{1/2}(\Gamma)$

$$\mathcal{N}\mu(\boldsymbol{y}) = \int_\Gamma \frac{\partial^2 G}{\partial \boldsymbol{n}_{\boldsymbol{x}}\partial \boldsymbol{n}_{\boldsymbol{x}}}(\boldsymbol{x},\boldsymbol{y})\mu(\boldsymbol{x})d\Gamma(\boldsymbol{x}), \quad \boldsymbol{y}\in\mathbb{R}^3,$$

définis pour une frontière Γ suffisamment régulière et pour la solution fondamental de l'équation de Laplace en trois dimensions, i.e.

$$G(\boldsymbol{x},\boldsymbol{y}) = \frac{1}{4\pi\left\|\boldsymbol{x}-\boldsymbol{y}\right\|}.$$

On décrit l'obtention des solution numériques en utilisant la méthode des éléments finis de frontière (BEM en anglais) et on s'intéresse aux matrices qu'en résultent de cette méthode. On décrit également la mise en œuvre d'une méthode numérique utilisant la méthode des éléments finis de frontière dans un cadre suffisamment ample. Les avantages et les défis inhérents à la méthode sont abordés : la complexité du calcul numérique (de mémoire et algorithmique), d'ordre $\mathcal{O}\left(N^2\right)$, et le mal conditionnement inhérentes à des systèmes linéaires associés, d'ordre $\mathcal{O}\left(h^{-1}\right)$, où N est le nombre de fonctions de base de l'espace discret utilisé et h est le paramètre de taille de la discrétisation de la surface Γ. Dans la suite de la thèse, on s'attaque au problème du conditionnement pour un type précis de surface Γ.

Chapitre 2: Opérateurs Intégraux et les Objets en Forme de Disque

Dans une deuxième partie on expose une technique optimale de préconditionnement (indépendante de la discrétisation) sur la base des opérateurs intégraux de frontière. On montre comment cette technique est facilement réalisable dans le cas de problèmes définis en dehors d'un objet régulier à frontière lipschitzienne, mais qu'elle pose des problèmes quand ils sont définis en dehors d'une surface ouverte dans un espace tridimensionnel. On montre que les opérateurs intégraux de frontière associés à la résolution des problèmes de Dirichlet et Neumann définis en dehors des surfaces ont des inverses bien définis. On montre également que ceux-ci pourraient conduire à des techniques de préconditionnement optimales, mais que ses formes explicites ne sont pas faciles à obtenir. Ensuite, on montre une méthode pour obtenir de tels opérateurs inverses de façon explicite lorsque la surface sur laquelle ils sont définis est un disque unitaire dans un espace tridimensionnel. Ces opérateurs inverses explicites seront, cependant, en forme des séries, et n'auront pas une adaptation immédiate pour leur utilisation dans des méthodes des éléments finis de frontière. On définit le disque comme

$$\mathbb{D} = \{\boldsymbol{x} = (x_1, x_2, x_3) \in \mathbb{R}^3 : x_3 = 0, x_1^2 + x_2^2 < 1\},$$

sur lequel on considerera aussi des coordonnées cylindriques $(\rho_{\boldsymbol{x}}, \phi_{\boldsymbol{x}})$ pour un point $\boldsymbol{x} \in \mathbb{D}$.

On considère les harmoniques sphériques définies pour un point $\boldsymbol{x}$ sur la sphère unité définie en coordonnées sphériques

$$Y_l^m(\theta_{\boldsymbol{x}}, \phi_{\boldsymbol{x}}) = \gamma_l^m e^{\mathrm{i}m\phi_{\boldsymbol{x}}} I\!P_l^m(\cos\theta_{\boldsymbol{x}}), \text{ pour } -l \leq m \leq l \text{ et } m \geq 0,$$

où

$$\gamma_l^m = (-1)^m \sqrt{\frac{l+1/2}{2\pi}} \sqrt{\frac{(l-m)!}{(l+m)!}}.$$

On définit des fonctions de base sur le disque comme

$$y_l^m(\boldsymbol{x}) = Y_l^m(\boldsymbol{x}^+), \quad \text{pour } \boldsymbol{x} \in \mathbb{D},$$

où $\boldsymbol{x}^\pm$ est la projection verticale supérieure/inférieure du point $\boldsymbol{x}$ sur la sphère unité. En considérant aussi une fonction de poids liée à la singularité des sauts des traces, $w(\boldsymbol{x}) = \sqrt{1-\rho_{\boldsymbol{x}}^2}$, et l'ensemble

$$\mathcal{Y} = \left\{ y_l^m \in C^\infty(\mathbb{D}) : y_l^m(\boldsymbol{x}) = Y_l^m(\boldsymbol{x}^+), \text{ for } \boldsymbol{x} \in \mathbb{D} \right\},$$

on définit les ensembles

$$\mathcal{Y}_s = \{y_l^m \in \mathcal{Y} : l+m \text{ pair}\}, \quad \mathcal{Y}_s^{1/w} = \left\{ \frac{y_l^m}{w} : y_l^m \in \mathcal{Y}_s \right\},$$
$$\mathcal{Y}_{as} = \{y_l^m \in \mathcal{Y} : l+m \text{ impair}\}, \quad \mathcal{Y}_{as}^{1/w} = \left\{ \frac{y_l^m}{w} : y_l^m \in \mathcal{Y}_{as} \right\}.$$

Un des principaux résultats est le développement en séries des fonctions sur les espaces $H^{1/2}(\mathbb{D})$, $H^{-1/2}(\mathbb{D})$, $\widetilde{H}^{1/2}(\mathbb{D})$, et $\widetilde{H}^{-1/2}(\mathbb{D})$.

Une fonction μ dans l'espace $\widetilde{H}^{1/2}(\mathbb{D})$ peut être développée dans la base $\mathcal{Y}_{as}$:

$$\mu(\boldsymbol{x}) = \sum_{l=0}^{\infty} \sum_{\substack{m=-l \\ l+m \text{ impair}}}^{l} \mu_l^m y_l^m(\boldsymbol{x}), \quad \mu_l^m = \int_{\mathbb{D}} \frac{\mu(\boldsymbol{x})\overline{y_l^m}(\boldsymbol{x})}{\sqrt{(1-\rho(\boldsymbol{x})^2)}} d\mathbb{D}(\boldsymbol{x}).$$

Une fonction g dans l'espace $H^{1/2}(\mathbb{D})$ peut être développée dans la base $\mathcal{Y}_s$:

$$g(\boldsymbol{x}) = \sum_{l=0}^{\infty} \sum_{\substack{m=-l \\ l+m \text{ pair}}}^{l} g_l^m y_l^m(\boldsymbol{x}), \quad g_l^m = \int_{\mathbb{D}} \frac{g(\boldsymbol{x})\overline{y_l^m}(\boldsymbol{x})}{\sqrt{(1-\rho(\boldsymbol{x})^2)}} d\mathbb{D}(\boldsymbol{x}).$$

Une fonction φ dans l'espace $H^{-1/2}(\mathbb{D})$ peut être développée dans la base $\mathcal{Y}_{as}^{1/w}$:

$$\varphi(\boldsymbol{x}) = \sum_{l=0}^{\infty} \sum_{\substack{m=-l \\ l+m \text{ impair}}}^{l} \varphi_l^m \frac{y_l^m(\boldsymbol{x})}{\sqrt{(1-\rho(\boldsymbol{x})^2)}}, \quad \varphi_l^m = \int_{\mathbb{D}} \varphi(\boldsymbol{x})\overline{y_l^m}(\boldsymbol{x}) d\mathbb{D}(\boldsymbol{x}).$$

Une fonction λ dans l'espace $\widetilde{H}^{-1/2}(\mathbb{D})$ peut être développée dans la base $\mathcal{Y}_s^{1/w}$:

$$\lambda(\boldsymbol{x}) = \sum_{l=0}^{\infty} \sum_{\substack{m=-l \\ l+m \text{ pair}}}^{l} \lambda_l^m \frac{y_l^m(\boldsymbol{x})}{\sqrt{(1-\rho(\boldsymbol{x})^2)}}, \quad \lambda_l^m = \int_{\mathbb{D}} \psi(\boldsymbol{x})\overline{y_l^m}(\boldsymbol{x}) d\mathbb{D}(\boldsymbol{x}).$$

En utilisant ces développements en série, on propose des noyaux intégraux comme séries formelles:

$$K_{as}^{ws}(\boldsymbol{x},\boldsymbol{y}) = \sum_{l=0}^{\infty} \sum_{\substack{m=-l \\ l+m \text{ impair}}}^{l} \frac{1}{\alpha_l^m} \left(y_l^m(\boldsymbol{x})\overline{y_l^m}(\boldsymbol{y}) + \overline{y_l^m}(\boldsymbol{x}) y_l^m(\boldsymbol{y}) \right),$$

$$K_{as}^{hs}(\boldsymbol{x},\boldsymbol{y}) = -\sum_{l=0}^{\infty} \sum_{\substack{m=-l \\ l+m \text{ impair}}}^{l} \alpha_l^m \left(\frac{y_l^m(\boldsymbol{x})}{w(\boldsymbol{x})} \frac{\overline{y_l^m}(\boldsymbol{y})}{w(\boldsymbol{y})} + \frac{\overline{y_l^m}(\boldsymbol{x})}{w(\boldsymbol{x})} \frac{y_l^m(\boldsymbol{y})}{w(\boldsymbol{y})} \right),$$

$$K_{s}^{ws}(\boldsymbol{x},\boldsymbol{y}) = \sum_{l=0}^{\infty} \sum_{\substack{m=-l \\ l+m \text{ pair}}}^{l} \frac{1}{\beta_l^m} \left(y_l^m(\boldsymbol{x})\overline{y_l^m}(\boldsymbol{y}) + \overline{y_l^m}(\boldsymbol{x}) y_l^m(\boldsymbol{y}) \right),$$

$$K_{s}^{hs}(\boldsymbol{x},\boldsymbol{y}) = -\sum_{l=0}^{\infty} \sum_{\substack{m=-l \\ l+m \text{ pair}}}^{l} \beta_l^m \left(\frac{y_l^m(\boldsymbol{x})}{w(\boldsymbol{x})} \frac{\overline{y_l^m}(\boldsymbol{y})}{w(\boldsymbol{y})} + \frac{\overline{y_l^m}(\boldsymbol{x})}{w(\boldsymbol{x})} \frac{y_l^m(\boldsymbol{y})}{w(\boldsymbol{y})} \right).$$

Dans ces noyaux, les coefficients α_l^m et β_l^m son définis comme

$$\alpha_l^m = \frac{\pi}{4} \left(\prod_{i=1}^{(l+m-1)/2} \frac{2i+1}{2i} \right) \left(\prod_{i=1}^{(l-m-1)/2} \frac{2i+1}{2i} \right), \text{ pour } l+m \text{ pair},$$

$$\beta_l^m = \frac{4}{\pi} \left(\prod_{i=1}^{(l+m)/2} \frac{2i}{2i-1} \right) \left(\prod_{i=1}^{(l-m)/2} \frac{2i}{2i-1} \right), \text{ pour } l+m \text{ impair}.$$

En définissant les opérateurs intégraux

$$\left(\mathcal{L}_s^{ws} u\right)(\boldsymbol{y}) = \int_{\mathbb{D}} K_s^{ws}(\boldsymbol{x},\boldsymbol{y}) u(\boldsymbol{x}) d\mathbb{D}(\boldsymbol{x}),$$

$$\left(\mathcal{L}_{as}^{ws} u\right)(\boldsymbol{y}) = \int_{\mathbb{D}} K_{as}^{ws}(\boldsymbol{x},\boldsymbol{y}) u(\boldsymbol{x}) d\mathbb{D}(\boldsymbol{x}),$$

$$\left(\mathcal{L}_s^{hs} u\right)(\boldsymbol{y}) = \int_{\mathbb{D}} K_s^{hs}(\boldsymbol{x},\boldsymbol{y}) u(\boldsymbol{x}) d\mathbb{D}(\boldsymbol{x}),$$

$$\left(\mathcal{L}_{as}^{hs} u\right)(\boldsymbol{y}) = \int_{\mathbb{D}} K_{as}^{hs}(\boldsymbol{x},\boldsymbol{y}) u(\boldsymbol{x}) d\mathbb{D}(\boldsymbol{x}),$$

on preuve que $\mathcal{L}_s^{hs} \circ \mathcal{L}_s^{ws} = -\mathcal{I}$ et que $\mathcal{L}_{as}^{ws} \circ \mathcal{L}_{as}^{hs} = -\mathcal{I}$ (où $\mathcal{I}$ est l'application identité). En suite on preuve que $K^{ws} = K_s^{ws}$ et que $K^{hs} = K_{as}^{hs}$, avec

$$K^{ws}(\boldsymbol{x},\boldsymbol{y}) = G(\boldsymbol{x},\boldsymbol{y}) \quad \text{et} \quad K^{hs}(\boldsymbol{x},\boldsymbol{y}) = \frac{\partial^2 G}{\partial \boldsymbol{n}_{\boldsymbol{x}} \partial \boldsymbol{n}_{\boldsymbol{y}}}(\boldsymbol{x},\boldsymbol{y}),$$

en donnant des expression pour les inverses de $\mathcal{S}$ et $\mathcal{N}$ sur le disque. Ces bases permettent de triangulariser les formulation variationnelles pour les problèmes de Dirichlet et de Neumann pour le disque en trois dimensions, donnant une méthode spectrale pour les résoudre.

Chapitre 3: Le Preconditionnement par Opérateurs Intégraux Modifiés pour des Objets Plats

Dans une troisième partie on montre comment certaines modifications aux opérateurs inverses mentionnés permettent d'obtenir des expressions variationnelles explicites et fermées, non plus sous la forme des séries, en conservant certaines caractéristiques importantes pour l'effet de préconditionnement cherché. Ces formes explicites sont applicables aux méthodes des éléments finis frontière. On obtient des expressions variationnelles précises et on propose des calculs numériques pour leur utilisation avec des éléments finis frontière. Ces méthodes numériques sont testées en utilisant différentes identités obtenues dans la théorie développée, et sont ensuite utilisées pour produire des matrices préconditionnantes. Leur performance en tant que préconditionneurs de systèmes linéaires associés à des problèmes de Laplace et Helmholtz à l'extérieur du disque est testée. Enfin, on propose extension de cette méthode pour couvrir les cas de surfaces diverses. Ceci est étudié dans les cas précis des problèmes extérieurs à des surfaces en forme de carré et en forme de L dans un espace tridimensionnel.

En considérant des noyaux modifiés,

$$\widetilde{K}_s^{ws}(\boldsymbol{x},\boldsymbol{y}) = \sum_{l=0}^{\infty} \sum_{\substack{m=-l \\ l+m \text{ pair}}}^{l} \zeta_l y_l^m(\boldsymbol{y}) \overline{y_l^m(\boldsymbol{x})},$$

$$\widetilde{K}_{as}^{ws}(\boldsymbol{x},\boldsymbol{y}) = \sum_{l=0}^{\infty} \sum_{\substack{m=-l \\ l+m \text{ impair}}}^{l} \zeta_l y_l^m(\boldsymbol{y}) \overline{y_l^m(\boldsymbol{x})},$$

$$\widetilde{K}_s^{hs}(\boldsymbol{x},\boldsymbol{y}) = -\sum_{l=0}^{\infty} \sum_{\substack{m=-l \\ l+m \text{ pair}}}^{l} \eta_l \frac{y_l^m(\boldsymbol{y})}{w(\boldsymbol{y})} \frac{\overline{y_l^m(\boldsymbol{x})}}{w(\boldsymbol{x})},$$

$$\widetilde{K}_{as}^{hs}(\boldsymbol{x},\boldsymbol{y}) = -\sum_{l=0}^{\infty} \sum_{\substack{m=-l \\ l+m \text{ impair}}}^{l} \eta_l \frac{y_l^m(\boldsymbol{y})}{w(\boldsymbol{y})} \frac{\overline{y_l^m(\boldsymbol{x})}}{w(\boldsymbol{x})},$$

où les coefficients modifiés sont

$$\zeta_l = \frac{2}{2l+1} \quad \text{et } \eta_l = \frac{2l(l+1)}{2l+1},$$

on définit également des opérateurs intégraux modifiés:

$$\left(\widetilde{\mathcal{L}}_s^{ws}\lambda\right)(\boldsymbol{y}) = \int_{\mathbb{D}} \widetilde{K}_s^{ws}(\boldsymbol{x},\boldsymbol{y})\lambda(\boldsymbol{x})d\mathbb{D}(\boldsymbol{x}),$$

$$\left(\widetilde{\mathcal{L}}_{as}^{ws}\varphi\right)(\boldsymbol{y}) = \int_{\mathbb{D}} \widetilde{K}_{as}^{ws}(\boldsymbol{x},\boldsymbol{y})\varphi(\boldsymbol{x})d\mathbb{D}(\boldsymbol{x}),$$

$$\left(\widetilde{\mathcal{L}}_s^{hs}g\right)(\boldsymbol{y}) = \int_{\mathbb{D}} \widetilde{K}_s^{hs}(\boldsymbol{x},\boldsymbol{y})g(\boldsymbol{x})d\mathbb{D}(\boldsymbol{x}),$$

$$\left(\widetilde{\mathcal{L}}_{as}^{hs}\mu\right)(\boldsymbol{y}) = \int_{\mathbb{D}} \widetilde{K}_{as}^{hs}(\boldsymbol{x},\boldsymbol{y})\mu(\boldsymbol{x})d\mathbb{D}(\boldsymbol{x}).$$

Un résultat central de la thèse est l'expression des formes bilinéaires associées aux ces opérateurs. En fait:

$$\left\langle \widetilde{\mathcal{L}}_s^{ws}\lambda\,,\,\lambda^t\right\rangle_{\mathbb{D}} = \int_{\mathbb{D}}\int_{\mathbb{D}} \frac{1}{4\pi}\left(\frac{1}{\|\boldsymbol{x}^+-\boldsymbol{y}^+\|}+\frac{1}{\|\boldsymbol{x}^--\boldsymbol{y}^+\|}\right)\lambda(\boldsymbol{x})\lambda^t(\boldsymbol{y})d\mathbb{D}(\boldsymbol{x})d\mathbb{D}(\boldsymbol{y}),$$

$$\left\langle \widetilde{\mathcal{L}}_{as}^{ws}\varphi\,,\,\varphi^t\right\rangle_{\mathbb{D}} = \int_{\mathbb{D}}\int_{\mathbb{D}} \frac{1}{4\pi}\left(\frac{1}{\|\boldsymbol{x}^+-\boldsymbol{y}^+\|}-\frac{1}{\|\boldsymbol{x}^--\boldsymbol{y}^+\|}\right)\varphi(\boldsymbol{x})\varphi^t(\boldsymbol{y})d\mathbb{D}(\boldsymbol{x})d\mathbb{D}(\boldsymbol{y}),$$

$$\left\langle -\widetilde{\mathcal{L}}_{as}^{hs}\mu\,,\,\mu^t\right\rangle_{\mathbb{D}} = \left\langle \widetilde{\mathcal{L}}_s^{ws}\overrightarrow{\mathrm{curl}}_{\mathbb{D}}\mu, \overrightarrow{\mathrm{curl}}_{\mathbb{D}}\mu^t\right\rangle_{\mathbb{D}} + \left\langle \widetilde{\mathcal{L}}_{as}^{ws}\left(\frac{1}{w}\frac{\partial\mu}{\partial\phi_{\boldsymbol{x}}}\right), \frac{1}{w}\frac{\partial\mu^t}{\partial\phi_{\boldsymbol{y}}}\right\rangle_{\mathbb{D}},$$

$$\left\langle -\widetilde{\mathcal{L}}_s^{hs}g\,,\,g^t\right\rangle_{\mathbb{D}} = \left\langle \widetilde{\mathcal{L}}_{as}^{ws}\overrightarrow{\mathrm{curl}}_{\mathbb{D}}g, \overrightarrow{\mathrm{curl}}_{\mathbb{D}}g^t\right\rangle_{\mathbb{D}} + \left\langle \widetilde{\mathcal{L}}_s^{ws}\left(\frac{1}{w}\frac{\partial g}{\partial\phi_{\boldsymbol{x}}}\right), \frac{1}{w}\frac{\partial g^t}{\partial\phi_{\boldsymbol{y}}}\right\rangle_{\mathbb{D}}.$$

Ces expression bilinéaires sont fermées, et donc calculables dans le cadre des méthodes des éléments finis de frontière. Les matrices qui en résultent, provenant des opérateurs avec des singularités dans leur noyaux similaires à celles des inverses de $\mathcal{S}$ et $\mathcal{N}$, sont adaptées pour être préconditionnantes. Plusieurs exemples numériques en montrent leur performance.

Chapitre 4: Application à la gestion de la Complexité Computationnelle dans la Test de Méthodes de Télédétection par Simulation

Enfin, les méthodes développés sont utilisés dans un exemple d'application. Sur la base de techniques et hypothèses de l'optique géométrique, on propose des améliorations à des méthodes existantes pour l'imagerie de la réflectivité du sous-sol en utilisant le radar à pénétration de sol. Étant basées sur des hypothèses de l'optique géométrique, ces méthodes doivent être évaluées par simulations numériques, ce qui entraîne la résolution d'un nombre très important de problèmes directs. Une analyse de complexité montre comment les techniques de préconditionnement proposées peuvent réduire la complexité algorithmique du problème global. Enfin, la capacité de résolution des méthodes proposées pour la formation des images du sous-sol est évaluée dans pour different scénarios d'intérêt.

Les méthodes traitées dans ce chapitre appartient aux méthodes de filtrage adaptative pour la reconstruction des images complexes de réflexivité $\mathcal{R}$ sur un surface Γ^R,

$$\mathcal{R}(\boldsymbol{y}) = \int_{\Gamma^H} \mathcal{F}(\boldsymbol{x}, \boldsymbol{y}) \mathcal{H}(\boldsymbol{x}) d\Gamma^H(\boldsymbol{x}), \quad \text{for } \boldsymbol{y} \in \Gamma^R,$$

où $\mathcal{H}$ est la fonction de diffraction (d'un objet irradié) mesurée sur une surface Γ^H, $\mathcal{F}$ est le filtre adapté, et Γ^I est une surface qui cache l'objet dont on veut faire un image de sa réflectivité.

université PARIS-SACLAY | École doctorale de mathématiques Hadamard (EDMH)

Titre : Aspects Théoriques et Numériques des Phénomènes de Propagation d'Ondes dans Domaines de Géométrie Complexe et Applications à la Télédétection

Mots-clés : Problème extérieur de Laplace, problème extérieur de Helmholtz, équations intégrales de frontière, méthode des éléments finis de frontière, préconditionnement par opérateurs, préconditionnement optimal, problèmes des surfaces ouvertes, problèmes de fissures.

Cette thèse s'inscrit dans le sujet des opérateurs intégraux de frontière définis sur le disque unitaire en trois dimensions, leurs relations avec les problèmes externes de Laplace et Helmholtz, et leurs applications au préconditionnement pour la méthode des éléments finis de frontière. On décrit d'abord les méthodes intégrales pour les problèmes de Laplace et de Helmholtz en dehors des objets à frontière régulière lipschitzienne, et en dehors des surfaces bidimensionnelles ouvertes. On décrit la mise en œuvre des éléments finis de frontière, la complexité du calcul numérique associé, et le mauvais conditionnement des systèmes linéaires. Ensuite, on décrit le préconditionnement optimal sur la base des opérateurs intégraux de frontière. Cette technique est facilement réalisable dans le cas de problèmes définis en dehors d'un objet à frontière lipschitzienne, mais elle pose des problèmes quand ils sont définis en dehors d'une surface ouverte. On montre que les opérateurs intégraux de frontière associés à la résolution des problèmes de Dirichlet et Neumann ont des inverses bien définies, et on montre également que celles-ci pourraient conduire à des techniques de préconditionnement optimales, mais que ses formes explicites ne sont pas faciles à obtenir. Ensuite, on présent une méthode pour obtenir de tels opérateurs inverses de façon explicite quand la surface est un disque unitaire. Ces opérateurs inverses explicites seront, cependant, en forme de séries, et n'auront pas une application immédiate avec des méthodes des éléments finis de frontière. On propose, ensuite, certaines modifications aux opérateurs inverses mentionnés permettant d'obtenir des expressions variationnelles explicites et fermées en conservant certaines caractéristiques importantes pour l'effet de préconditionnement cherché. Ces formes explicites sont applicables aux méthodes des éléments finis frontière. On obtient des expressions variationnelles précises et on propose des schémas numériques appropriés. Ces méthodes numériques sont testées et sont ensuite utilisées pour produire des matrices préconditionnantes. Leur performance en tant que préconditionneurs de systèmes linéaires est testée. Enfin, on propose une extension de cette méthode pour les cas de surfaces diverses. Les méthodes développées sont utilisées dans un exemple d'application. Sur la base de techniques et hypothèses de l'optique géométrique, on propose des améliorations à des méthodes existantes pour l'imagerie de la réflectivité du sous-sol en utilisant le radar à pénétration de sol.

Title: Theoretical and Numerical Aspects of Wave Propagation Phenomena In Domains of Complex Geometry and Applications to Remote Sensing

Keywords: Exterior Laplace problem, exterior Helmholtz problem, boundary integral equations, boundary element methods, operator preconditioning, optimal preconditioning, screen problems, crack problems.

This thesis is about some boundary integral operators defined on the unit disk in three-dimensional space, their relation with the exterior Laplace and Helmholtz problems, and their application to the preconditioning for the boundary element method. We begin by describing the integral method for the solution of the Laplace and Helmholtz problems on the exterior of objects with Lipschitz-regular boundaries and open two-dimensional surfaces in three-dimensional space. We describe the integral formulation in these cases, the boundary element method, its computational complexity and the inherent ill-conditioning of the associated linear systems. We describe optimal preconditioning based on operator preconditioning. We show that this technique is easily applicable when objects are Lipschitz-regular, but that its application fails for problems involving open surfaces. We show that the integral operators associated with the resolution of the Dirichlet and Neumann problems defined on the exterior of open surfaces have inverse operators that would provide optimal preconditioners but they are not easily obtainable. Then we show a technique to explicitly obtain such inverse operators for the unit disk. Their explicit inverse operators will be given in the form of a series and will not be immediately applicable in the use of boundary element methods. Then we show how some modifications to these inverse operators allow us to obtain variational explicit and closed-form expressions that conserve some characteristics that are relevant for their preconditioning effect. These explicit and closed forms expressions are applicable in boundary element methods. We obtain precise variational expressions for them and propose appropriate numerical schemes. The proposed numerical methods are tested and then used to build preconditioning matrices. Their performance as preconditioners for linear systems is tested for the case of the Laplace and Helmholtz problems for the unit disk. We propose an extension of this method that allows for the treatment of cases of open surfaces other than the disk. Finally, the methods developed are used in an application example. Based on techniques and assumptions from geometrical optics, we propose improvements to existing methods for the imaging of underground reflectivity using ground penetrating radar.

Université Paris-Saclay
Espace Technologique / Immeuble Discovery
Route de l'Orme aux Merisiers RD 128 / 91190 Saint-Aubin,
France